REPORT DOCUMENTATION PAGE

Form Approved
OMB No. 0704-0188

Public reporting burden for this collection of information is estimated to average 1 hour per response, including the time for reviewing instructions, searching existing data sources, gathering and maintaining the data needed, and completing and reviewing the collection of information. Send comments regarding this burden estimate or any other aspect of this collection of information, including suggestions for reducing this burden, to Washington Headquarters Services, Directorate for Information Operations and Reports, 1215 Jefferson Davis Highway, Suite 1204, Arlington, VA 22202-4302, and to the Office of Management and Budget, Paperwork Reduction Project (0704-0188), Washington, DC 20503.

1. AGENCY USE ONLY *(Leave blank)*	2. REPORT DATE	3. REPORT TYPE AND DATES COVERED
	May 31, 2007	Final: Feb. 9, 2004 to Feb.28, 2007

4. TITLE AND SUBTITLE	5. FUNDING NUMBERS
Deep Ultraviolet Laser Diode for UV-Resonance Enhanced Raman Identification	ARPA Order Q511/00
6. AUTHORS W. Hug, T.Moustakas, R.Treece, J.Smith, A.Bhattacharyya, R.Reid, J.Pankove, C.Brown, W. Nelson	Contract No. W31P4Q-04-C-R039
7. PERFORMING ORGANIZATION NAME(S) AND ADDRESS(ES) Photon Systems 1512 Industrial Park St. Covina, CA 91722	8. PERFORMING ORGANIZATION REPORT NUMBER 2003 DARPA FINAL
9. SPONSORING/MONITORING AGENCY NAME(S) AND ADDRESS(ES) U.S. Army Aviation & Missile Command AMSAM-AC-RD-AY Pam Brandebourg, (256) 842-7149 Redstone Arsenal, AL 35898-5280	10. SPONSORING/MONITORING AGENCY REPORT NUMBER
11. SUPPLEMENTARY NOTES	
12a. DISTRIBUTION/AVAILABILITY STATEMENT Unclassified	12b. DISTRIBUTION CODE

DISTRIBUTION STATEMENT A
Approved for Public Release
Distribution Unlimited

13. ABSTRACT *(Maximum 200 words)*

This proposal addresses the need for deep UV semiconductor lasers for use in UV resonance enhanced Raman spectroscopic identification of biological agents. The proposed approach avoids the problems of p-doping and ohmic contacts by using subminiature direct electron injection excitation of an InAlGaN heterostructure. We have demonstrated strong stimulated emission at 274nm using this approach with measured linewidth reduction from 16nm to 4nm and five orders of magnitude non-linear increase in intensity.

High levels of chemical specificity can be obtained using Raman spectroscopy without sample preparation, contact, or destruction. When Raman excitation occurs within the electronic resonance band of a material the scatter cross-sections can improve as much as eight orders of magnitude. For biochemical molecules such as nucleic and amino acids these absorption bands are very strong in the deep UV between about 220nm and 280nm. When Raman excitation is below about 250nm, there is a fluorescence-free region extending over 4000 wave numbers above the excitation wavelength providing very high detection sensitivities and low background noise.

It is the goal of this proposed program to demonstrate deep UV emission from a semiconductor laser and the ability to obtain deep UV resonance Raman spectra of analogs of hazardous biological agents.

14. SUBJECT TERMS	15. NUMBER OF PAGES
deep UV semiconductor laser Raman spectroscopy biological agent detection	214
	16. PRICE CODE CC

17. SECURITY CLASSIFICATION OF REPORT	18. SECURITY CLASSIFICATION OF THIS PAGE	19. SECURITY CLASSIFICATION OF ABSTRACT	20. LIMITATION OF ABSTRACT
Unclassified	Unclassified	Unclassified	Unlimited

NSN 7540-01-280-5500 Computer Generated STANDARD FORM 298
(Rev 2-89)

Prescribed by ANSI Std 239-18

298-102

"Deep Ultraviolet Laser Diode for UV-Resonance Enhanced Raman Identification of Biological Agents"

Final Report
May 31, 2007

Sponsored by
Defense Advanced Research Projects Agency (DOD)
(Controlling DARPA Office)

ARPA Order Q511/00

Issued by U.S. Army Aviation and Missile Command Under

Contract No. W31P4Q-04-C-R039

William F. Hug, Ph.D. Principal Investigator
Tel: 626 967-6431
w.hug@photonsystems.com

Photon Systems, Inc.
1512 Industrial Park St.
Covina, CA 91722-3417
www.photonsystems.com

"ESUVOS Development"
Effective Date of Contract: February 9, 2004

Contract Expiration Date: February 8, 2007

"The views and conclusions contained in this document are those of the authors and should not be interpreted as representing the official policies, either expressed or implied, of the Defense Advanced Research Projects Agency of the U.S. Government."

UNCLASSIFIED
"Approved for public release; distribution unlimited"

1.0 Table of Contents 3
2.0 Abstract, anticipated benefits, key words 3
3.0 Scientific and Technical Report 4
3.1 Executive Summary 4
3.2 Overview of the problem 8
3.3 Work breakdown between collaborating organizations 13
3.4 Photon Systems Results 13
3.4.1 Cathodoluminescence instrumentation development 14
Ebeam pumping of PARC material 66
3.4.2 Photolumiescence instrumentation development 76
3.4.3 AlGaN die facet coating development 78
3.4.4 ESUVOS device design development 85
3.4.5 Raman and native fluorescence detection and identification methods development 119
3.4.5.2 Univ. of Rhode Island Results 139
3.5 Boston University Results 141
3.6 Astralux Results 189
4.0 Distribution List 214

2.0 Abstract, anticipated benefits, key words

This program addresses the general need for low false alarm rate, non-contact methods for detection and identification of biological agents such as bacterial spores. This report addresses the particular need for deep UV semiconductor lasers for use in UV resonance enhanced Raman spectroscopic identification of biological agents. The approach avoids the problems of p-doping and ohmic contacts by using subminiature direct electron injection excitation of an InAlGaN heterostructure. High levels of chemical specificity can be obtained using Raman spectroscopy without sample preparation, contact, or destruction. When Raman excitation occurs within the electronic resonance band of a material the scatter cross-sections can improve as much as eight orders of magnitude. For organic molecules such as nucleic and amino acids and other biochemicals these absorption bands are very strong in the deep UV between about 220nm and 280nm. In addition, when Raman excitation below about 250nm is employed, there is a fluorescence-free region extending over 4000 wave numbers above the excitation wavelength providing very high detection sensitivities and low background noise.

It is the goal of this proposed program to demonstrate deep UV emission from a semiconductor laser and the ability to obtain deep UV resonance Raman and native fluorescence spectra of analogs of hazardous biological agents.

Anticipated Benefits/Potential Commercial Applications of the Research or Development

The Electron-beam Semiconductor Ultra-Violet Optical Source (ESUVOS) being developed here will enable a revolutionary reduction in size, weight and power consumption for UV resonance Raman and laser induced native fluorescence instruments for the detection and classification of biological agents on surfaces, in water and in the air. In addition, there is a broad commercial market need for deep UV sources that are small and efficient. The largest of these markets is likely in optical memory systems where the aerial data density is inversely proportional to the square of the source emission wavelength. However, other markets, while potentially smaller in quantity of demand, may have greater overall commercial impact, being the enabling technology for a wide array of analytical instruments. These instruments include biotechnology instruments used in clinical diagnostics, pharmaceutical research and product testing; environmental monitoring such as water, air and food quality; semiconductor development and processing; and a myriad of other applications where small spot sizes or photon-energy-specific excitation is needed or enabling.

List a maximum of 8 Key Words that describe the Project. Ultraviolet, semiconductor, laser, resonance Raman, native fluorescence, spectroscopy, biodetection.

3.0 Scientific and Technical Report

3.1 Executive Summary

This report summarizes the results of this two-year contract plus one-year extension to develop deep-UV-emitting electron beam pumped semiconductor lasers and UV resonance Raman analytical methods for detection and identification of bacterial spores and other potential biological threats. Contract period was March 2004 through February 2006 plus extension to February 2007.

This contract had two broad goals:

- develop a deep ultraviolet semiconductor laser emitting at a wavelength less than 250nm
- develop UV resonance Raman and native fluorescence spectroscopic methods for use in classification or confirmation of hazardous CBE agents.

The purpose of these developments is to provide technology to greatly improve limits of detection and false alarm rates for hazardous CBE agents in air, water and on surfaces. This report summarizes the efforts at Photon Systems, Boston University and Astralux, Inc., and University of Rhode Island toward these goals.

In broad terms this program has been a great success. Although, by the end of this contract, we had not yet demonstrated a working laser with emission wavelength below 250nm, we have made significant progress toward that goal and the goal of "greatly improving limits of detection and false alarm rates for hazardous CBE agents". The core reason for the lack of success in demonstrating a sub-250nm semiconductor laser is believed to be the inability to achieve adequately high electron-hole pairs within the active region of the semiconductor due to inadequate ebeam current density in combination with high optical losses within the active region. As a direct result of this DARPA contract and efforts enabled by the DARPA contract, we have:

1. Demonstrated internal quantum efficiencies for deep UV LED-type devices over 36% and coupling efficiencies over 70% at wavelengths less than 260nm. Present evidence at the time of the writing of this final report points to even higher QEs at shorter wavelengths. This compares to present results from other developers of deep UV LED devices of about 2%. We expect this will lead to miniature working devices with output over 2.5mW from a beam spot size less than 50um in diameter with input power about 10mW by the end of 2007 or early 2008. We call these devices electron-beam-pumped light emitting triodes or ELETs or simply LETs.
2. Demonstrated the benefits and methods of AlGaN film growth on A-plane sapphire to achieve common cleaving plane between substrate and film for edge emitting lasers.
3. Demonstrated that ebeam pumping did not pose a significant lifetime problem as an excitation method for deep UV semiconductor sources. In addition, we demonstrated the approximate voltages and current densities required to achieve threshold for laser operation in ebeam pumped devices. We demonstrated that the threshold power density was not significantly greater than in pn junction devices, but that the current density was about 500X lower and the voltage was 500X higher than pn junction devices.
4. We have developed data and analysis methods that demonstrate that an excitation wavelength of 235nm is the most ideal in being able to differentiate a wide range of biological, chemical and explosives materials using a combination of Raman and native fluorescence spectroscopic methods. This is a very important result and has led to ongoing following programs to further study this result. This result is contrary

to several previous results that have held that 280nm was the ideal excitation wavelength for detection and identification of biological materials.

5. We have demonstrated that the fusion of deep UV Raman and native fluorescence spectroscopic methods with excitation wavelengths under 250nm can provide vast enhancements in both sensitivity and specificity in the identification of a wide range of important CBE threats in a single sensor.
6. We have demonstrated, contrary to other government studies, that the methods developed by Photon Systems and it's collaborators using a combination of deep UV Raman and native fluorescence methods is capable of detecting and identifying trace concentrations of explosives on surface at working distances of several meters using a miniature, hand-held or robot mounted, battery powered sensor. This same sensor has also been demonstrated to be capable of simultaneously detecting and classifying trace levels of biological and chemical hazards.
7. We developed a deep UV photoluminescence spectrograph that is 500 times smaller and lighter, and 3000 times lower power consumption than commercially available instruments on the market with equivalent wide bandgap capability. We have successfully developed this instrument into a commercial product and have begun selling these instruments as of December 2006 at a price about 10X lower than other similar instruments on the market.

In addition, during this SBIR contract (both Phase I and II) we have presented fourteen (14) papers at major technical conferences, applied for two U.S. patents, and developed one major spin-off application. These results are as follows:

Conference presentations:

- Hug, W.F., R.D. Reid, R.Bhartia, and A.L.Lane, "Status of Deep UV Lasers for UV Resonance Raman and Native Fluorescence CBE Sensors", Invited Speaker, Conference on Lasers and Electro-Optics, PhAST 2, May 10, 2007.
- Hug, W. F., & R.D. Reid, "Status of Deep UV Lasers for UV Resonance Raman Spectroscopy", Invited Speaker, UV Resonance Raman Spectroscopy Symposium, 920-5, Pittcon, Feb. 27, 2007.
- W. Hug, R. Bhartia, A. Tsapin, A. Lane, P. Conrad, K.Sijapati, and R. D. Reid, "Water & surface contamination monitoring using deep UV laser induced native fluorescence and Raman spectroscopy", Proc. SPIE, Vol. 6378, Boston, MA. Oct. 2006.
- Hug, W.F., R. Bhartia, R. Reid, A. Tsapin, A. Lane, and P. Conrad, "Ultra-sensitive reagentless water contamination sensors using deep UV laser induced native fluorescence and resonance Raman spectroscopy", 2006 International Symposium of Spectral Sensing Research, Bar Harbor, ME. 29 May – 2 June, 2006.
- Bhartia, R. W.F.Hug, A.Lane, A. Tsapin, R. Reid, and P. Conrad, "Biochemical detection and identification false alarm rate dependence on wavelength using laser induced native fluorescence", Proc. SPIE, Vol. 6218, 62180J-1, Kissimmee, FL., Apr. 18-20, 2006.
- Bhartia, R.,E.C. Salas, W.F. Hug, K.Sijapati, A.Tsapin, A.Lane, R.Reid, and P.Conrad, "Native Fluorescence Spectroscopy: Wavelength Dependence in Differentiating Organic and Biological Compounds and Environmental Backgrounds", Pittsburgh Conference 2006, Orlando, FL., March 13-17, 2006.

- Hug, W.F., R. Bhartia, A. Tsapin, A.L. Lane, P. G. Conrad, K. Sijapati, and R.D. Reid, "Status of miniature integrated UV resonance fluorescence and Raman sensors for detection and identification of biochemical warfare agents", Proc. SPIE, Vol. 5994, Boston, MA., Oct. 22-26, 2005.
- Hug, W.F., R. Bhartia, A. Tsapin, A.L. Lane, P. G. Conrad, K. Sijapati, and R.D. Reid, "Status of miniature integrated UV resonance fluorescence and Raman sensors for detection and identification of biochemical warfare agents", SPIE Optics East, Boston, MA. Oct. 22-26, 2005.
- Hug, W.F., R.D. Reid, R.Bhartia, and T. Moustakas, "Ultraviolet resonance Raman spectroscopy for biological micro-sensing using ESUVOS", Solid State UV Technology, ed. J. C. Carrano and M.S. Shur, Int. J. High Speed Electronics and Systems, to be published.
- Hug, W.F., R.D. Reid, R. Bhartia, "Miniature Integrated UV Resonance Fluorescence and Raman Sensor for Detection and Identification of Biochemical Warfare Agents", Invited Speaker and Program Committee member, SPIE European Symposium in Security & Defense, London, UK, 25-28 October, 2004.
- Hug, W.F.,R.D. Reid, Pamela Conrad, Arthur L. Lane, and Rohit Bhartia, "Portable Integrated UV Resonance Fluorescence and Raman Chemical Sensor for in situ, Autonomous, Detection", 31st Annual Conference of the Federation of Analytical Chemistry and Spectroscopy Societies, Portland, OR., Oct. 3-7, 2004.
- Hug, W.F., William F. Hug, D. Reid, A Bhattacharyya, T. D. Moustakas, R. Treece, J. R. Smith and J. I. Pankove, "Status of Deep UV Semiconductor Sources for Laser Induced Native Fluorescence and Resonance Raman Spectroscopy" ", Invited Speaker, 31st Annual Conference of the Federation of Analytical Chemistry and Spectroscopy Societies, Portland, OR., Oct. 3-7, 2004.
- Bhattacharyya, A., T. Chen, T. Moustakas, R. Treece, J. Smith, J. Pankove and W. Hug, "Deep UV stimulated emission of electron-beam pumping of bulk AlGaN alloys", 8th Wide-Bandgap III-Nitride Workshop, Topic 11, Richmond, VA., Sept.29-Oct.1, 2003.
- Hug, W.F., R. Treece, J. Smith, A. Bhattacharyya, T. Moustakas, J. Pankove, J. Shaw and R. Reid, "Deep UV Laser Diode for UV Resonance Enhanced Raman Identification of Biological Agents", IEEE/LEOS Semiconductor Laser Workshop, CLEO Conference, Baltimore, MD, June 6, 2003.

U.S. Patent applications:

- Electron beam pumped semiconductor radiation source, 11/245,418, submitted Oct. 5, 2005
- Spectroscopic Chemical Analysis Methods and Apparatus, 11/245,486, submitted Oct. 5, 2005

Spin-off Idea:

And finally, Photon Systems developed a spinoff idea to employ mixtures of nanometer sized particles of AlGaN semiconductor materials to produce millions of individually addressable, remotely readable, covert, solar-blind digital optical tags (SBDOTS) which can be imbedded in chemicals such as explosives to provide traceability, as well as on individuals, vehicles, or other items of interest to be covertly traced.

The remainder of this report will provide the details of the work conducted under this DARPA SBIR contract.

3.2 Overview of the problem

Previous work as well as the efforts under this contract have demonstrated the benefits of using excitation wavelengths below 250nm to for the reagentless detection and identification of trace levels of CBE agents on surfaces, in water, or in air using non-contact, non-destructive, non-invasive methods including laser induced UV resonance Raman and native fluorescence spectroscopy. These methods can be employed in standoff detection and do not require any sample handling, processing, or the use of reagents or other consumable materials. These methods enable both high levels of sensitivity and specificity in identifying unknown materials.

The primary problem with these methods is the lack of a suitable source of narrow linewidth, deep ultraviolet radiation in a small, robust, high efficiency, low cost device. The holy grail of optical sources is traditionally considered to be pn-junction semiconductor devices including lasers and light emitting diodes. Traditionally these device provide reasonably high output powers, high source radiance, very miniature packages, high efficiency, and costs often under $0.10 for LEDs and under $10 for laser diodes. The push to make devices operating in the deep blue and UV have been continuing since the early 1990s until the present. To date the most popular short wavelength laser diodes are the GaN devices emitting in the range of 405nm, which are used in blue-ray optical memory devices and other application. To date, the manufacturing yield of these devices remains less than 10% and is the source of the continuing high cost of these devices. Typical 405nm laser diodes today from Nichea cost over $2500 each. And the cost has not come down is several years, despite increasing competition. The result of significant efforts in recent years under the DARPA SUVOS and other programs has been to reduce the emission wavelength of laser diodes to about 350nm, but with continuing low yield and short lifetimes. Light emitting diodes have fared much better with devices of a few mW and lifetimes over 1000 hours now available at wavelength as low as 280nm and prices under $250. The radiance of these devices, available from Sensor Electronic Technologies, is low, being about 2 W/cm^2. This compares to other somewhat less miniature, non-semiconductor, deep UV laser sources developed by Photon Systems with source radiance over 10^6 W/cm^2. Other deep UV LED sources have demonstrated output as low as 247nm but source radiance is less than 0.2 W/cm^2 and lifetimes of these device is still less than 100 hours.

Five major technical issues have blocked the ability to produce semiconductor lasers that emit at deep UV wavelengths. These roadblocks are:

- Inability to p-dope high aluminum content AlGaN materials
- Inability to make ohmic contacts to high Al content AlGaN materials
- Lattice mismatch with available substrate materials resulting in high defect density in active region
- Inability to cleave facets of good quality in available substrate materials
- Difficulty in forming wave-guiding layers in high Al content AlGaN

Because of one or more of these roadblocks, semiconductor lasers have been able to demonstrate emission only down to about 345nm, to date. And, at this wavelength, the lifetime is very limited. UV light emitting diodes have been demonstrated that emit at wavelengths as low as 247nm, but the output power and source radiance are very low, making these devices difficult or impossible to use to identify individual bacterial particles, on the fly, in bioaerosol sensors.

To avoid roadblocks associated with p-doping and ohmic contacts associated with pn-junction devices, our basic approach had been to use a ballistic electron beam to generate electron hole pairs in the active region of the AlGaN semiconductor material. In contrast to pn-

junction devices, each ballistic electron produces many hundreds of electron-hole pairs whereas only one pair is produced per electron in a pn-junction device. We believe this approach is a pragmatic solution that leapfrogs the most significant problems impeding the development of deep UV semiconductor lasers: p-doping and contact problems. This approach also allows us focus other important, but not as blocking, issues related to active region defects created by lattice mismatch, etc., facet quality, and waveguiding problems. If and when the problems of p-doping and ohmic contacts are solved for pn-junction AlGaN devices with Al-content above 60%, our approach will have enabled significant progress to be made on these other issues.

Figure 1 below shows the major materials families under development or use as semiconductor devices. The AlGaN family of materials has the greatest opportunity of achieving short emission wavelength. Pure AlN has a bandgap of 6.2 eV, corresponding to an emission wavelength of 200nm. Pure GaN has a bandgap of 3.6eV, corresponding to an emission wavelength of 350nm.

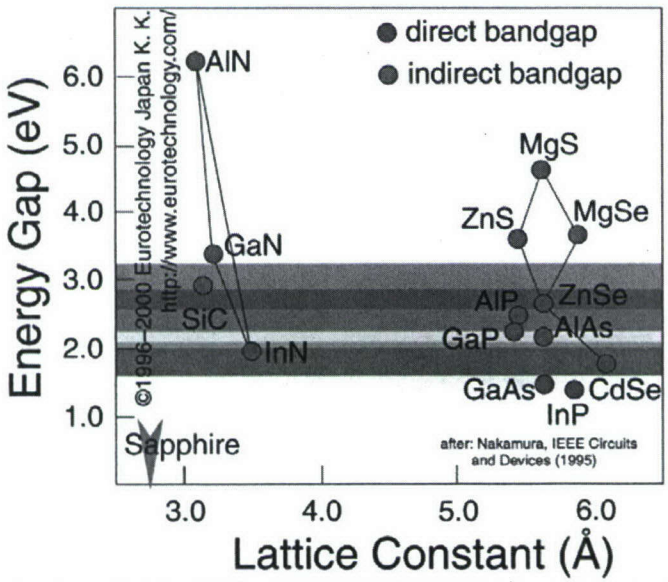

Figure 1. Bandgap of semiconductor material families of light emitting devices

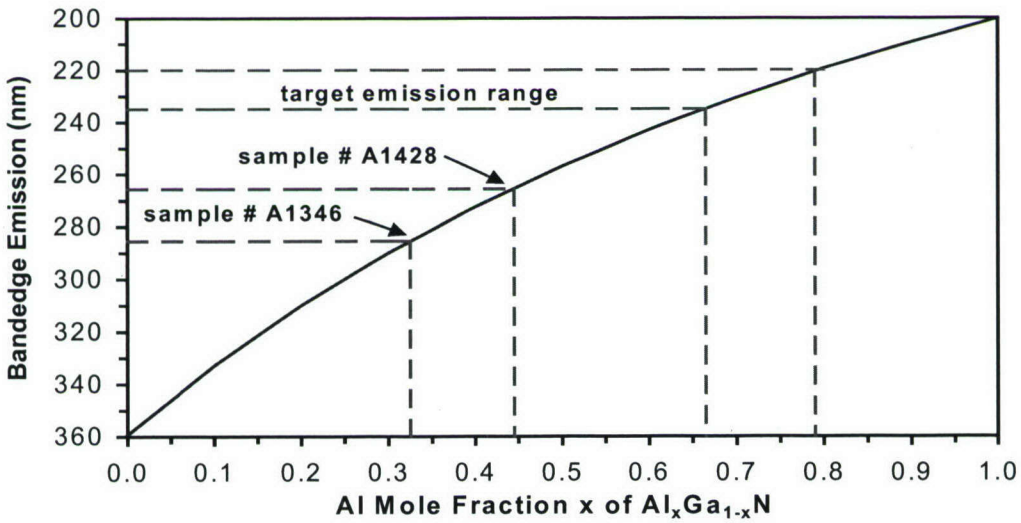

Figure 2. Vegard's Law for emission wavelength versus Al mode fraction for AlGaN

A schematic illustration of the concept for an edge emitting, electron-beam-pumped semiconductor Ultra-Violet Optical Source, or ESUVOS, is shown below in Fig. 3.

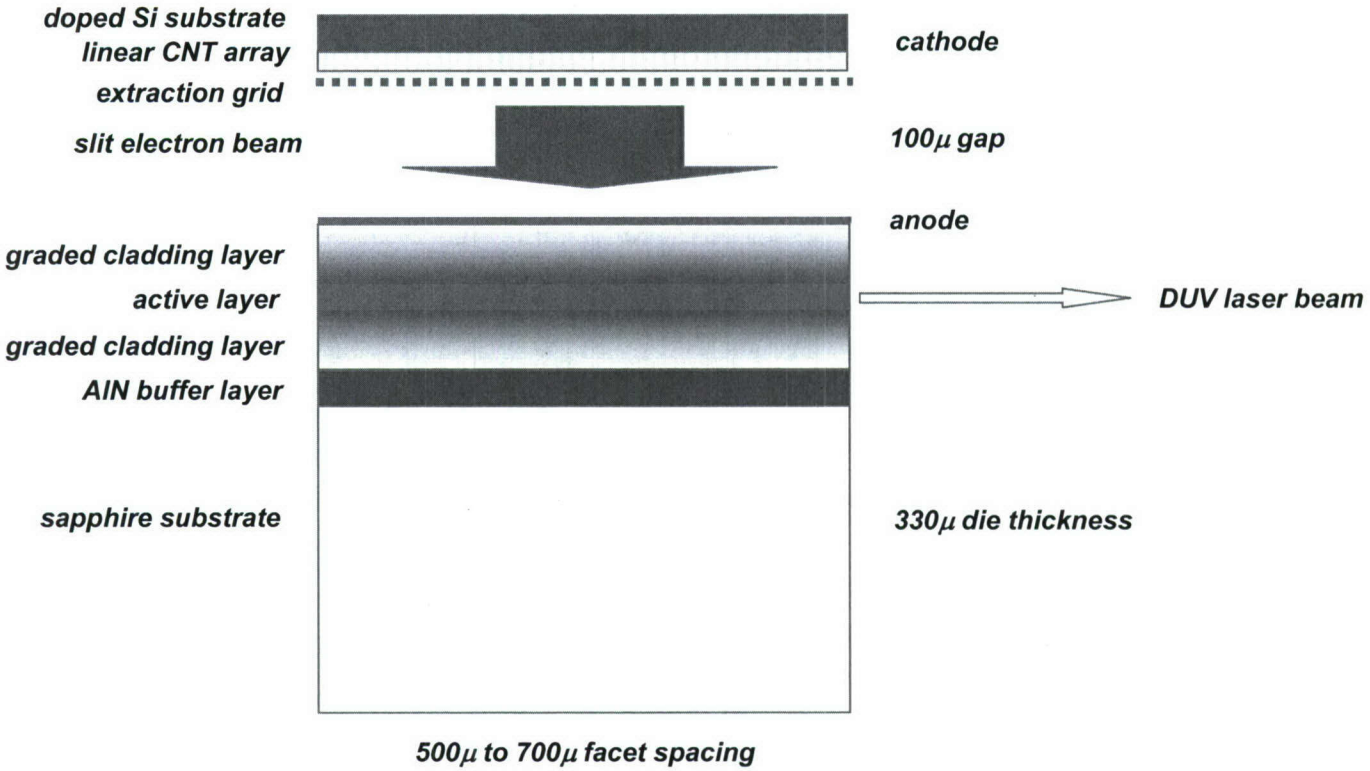

Figure 3. Schematic of edge emitting ESUVOS (Electron-beam-pumped Semiconductor Ultra-Violet Optical Source)

The concept is simple. A source of free electrons is controlled by an extraction grid and one or more focusing grids to provide a focused beam of electrons with rectangular cross-section onto the surface of an AlGaN film with cleaved facets at both ends. The source of free electrons illustrated in Fig. 3 is a carbon nanotube array. This source is field emitting and does not require heating to extract electrons from the substrate. Another field emission source of interest for this application is a diamond microtip array. The intended cross-section of the electron beam is approximately 750μm by 2μm with the 750μm dimension along the laser cavity optical axis and the 2μm dimension lateral to the laser cavity axis. The approximate current required to achieve laser threshold is estimated between 150μA to 1.5mA at a beam voltage about 7.5keV. Within this region, electron-hole pairs are generated in the active region of the semiconductor film with each ballistic electron producing several hundred up to perhaps 1000 electron-hole pairs.

Although our e-beam pumping approach avoids the above roadblocks, it brings other potential limitations that must be addressed if this approach is to succeed. These potential limitations related specifically to e-beam pumping include:

- Lifetime issues with direct electron beam pumping
- Alignment of the electron beam with respect to the optical axis
- Linearity of the electron beam along the optical axis
- Depth of field of the electron beam focus

Each of these issues will be addressed in the following discussion.

The two core pieces of evidence that the electron-beam excitation approach is a viable method of producing deep UV lasers are shown below. First, in Figures A, B, and C below, the linewidth is shown to decrease from about 16nm to 4nm as a result of two decade increase in electron beam pump current. Second, Fig. B shows a six order of magnitude increase in CL intensity as a result of a two order of magnitude increase in current, power, and power density. And finally, Fig. C shows that there is no catastrophic damage to the AlGaN film as a result of electron beam pumping.

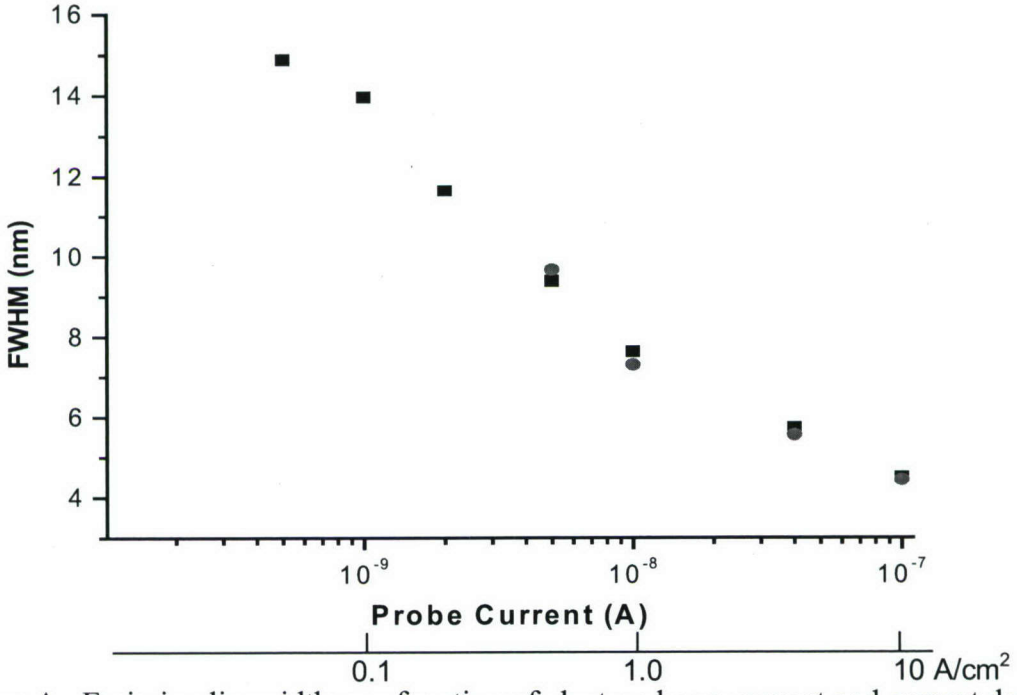

Figure A. Emission linewidth as a function of electron beam current and current density

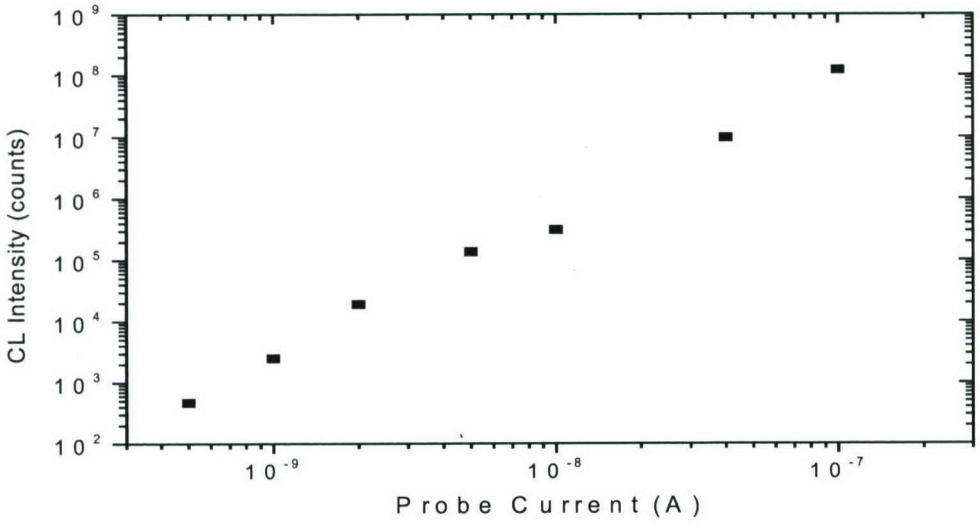

Figure B. Cathodoluminescence intensity as a function of electron beam current

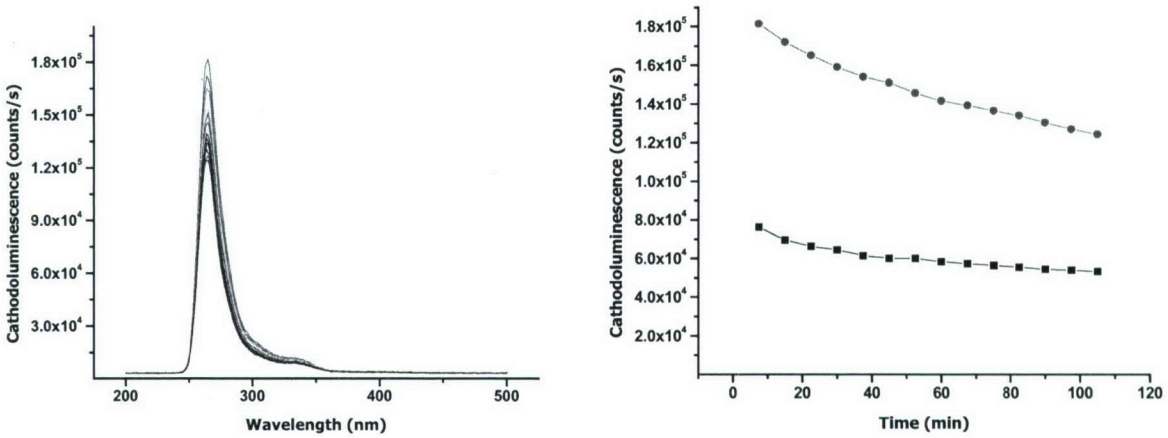

Figure C. CL Emission spectra and intensity versus time for 272nm CL

Nevertheless, with this evidence as proof of principle, we have yet to be successful in demonstrating laser emission using this technique. At present we attribute this lack of success to our inability to achieve a combination of high enough electron beam current density and current distribution over laser die to produce gain higher than losses in the active region of the devices built to date. We were informed by Dr. Steven LeBoeff of GE Central Research that he achieved laser emission in electron beam pumped devices in 2006 using a large ebeam source not available to Photon Systems. This was done under a DTRA funded program.

We began this project with the expectation that electron beam sources with sufficient current density were or would be available commercially from either Extreme Devices of Austin, TX., a manufacturer of high current density diamond microtip array field emission electron sources with integrated extraction and focusing grids, or from Xintek of Chapel Hill, NC., a manufacturer of carbon nanotube array field emission electron sources. Extreme Devices went bankrupt in early 2005 and the sources purchased from Xintek have not been able to achieve sufficient current density to achieve the deposited current density requirement on the AlGaN films. In addition to expending a significant effort in chasing these sources, we were left to develop our own thermionic electron sources as well as the entire gun including extraction and focusing grids. This was a significant redirection of the originally intended effort.

Also, early in the project, the original goal to etch facets using CAIBE methods was changed to cleaved facets because of a literature study at Astralux that showed the high levels of roughness of these surfaces would exacerbate optical losses, especially in the deep UV as a result of Rayleigh scatter law. The effort was then focused on growth of C-plane AlGaN films on A-plane sapphire, which share cleavage planes, and development of low loss, high reflectivity coatings for these facets. In addition to facet losses, bulk losses in AlGaN films and methods of waveguiding were the focus of much of the activity at Boston University.

Separate from the effort related to developing ESUVOS devices, a parallel effort was focused on development of UV Raman and native fluorescence spectroscopic methods to improve the ability to detect and identify biological and chemical threats. This work was conducted primarily at Photon Systems with some effort at the University of Rhode Island.

The remainder of this document describes the details of the effort both at Photon Systems and our three subcontractors: Boston University, Astralux, Inc., and University of Rhode Island.

3.3 Work breakdown between collaborating organizations

Photon Systems was the prime contractor and coordinator of this two-year SBIR contract plus one year extension. The effort involved three subcontractors: Boston University, Astralux Inc., and the University of Rhode Island. The work effort was broken down into the following:

Photon Systems, under the direction of Dr. William Hug, provided overall direction to the contract as well as development of: the cathodoluminescence instrumentation; photoluminescence instrumentation; process station and cooling stage development; high reflectivity AlGaN die facet coating development; ESUVOS device design development; and finally, development of combined Raman and native fluorescence methods for detection and identification of trace levels of concentration of chemical/biological/explosives materials.

Boston University, under the direction of Prof. Theodore Moustakas, was primarily responsible for AlGaN epitaxial film development and testing of samples. Their effort included development of films compatible with cleaving of substrate and AlGaN film to provide atomically smooth mirror facets for edge emitting devices.

Astralux, Inc., under the direction of Dr. Randy Treece, was primarily responsible for development of methods of cleaving, mounting, and testing of AlGaN die.

University of Rhode Island, under the direction of Prof. Christopher Brown, was responsible for a review of UV Raman marker band methods developed by Prof. Wilfred Nelson and evaluation of other methods for UV Raman data analysis to provide higher levels of specificity in identifying biological microorganisms.

3.4 Photon Systems Results

The Photon Systems activities were focused on the development of: the cathodoluminescence instrumentation; photoluminescence instrumentation; process station and cooling stage development; high reflectivity AlGaN die facet coating development; ESUVOS device design development; and finally, development of combined Raman and native fluorescence methods for detection and identification of trace levels of concentration of chemical/biological/explosives materials. Details of these efforts are described below.

Photon Systems summary of accomplishments;

1. Determined the approximate ebeam voltage and current density requirements to achieve threshold for laser emission
2. Developed very low loss, deep UV, multi-layer dielectric facet coatings for edge and surface emitting sources below the band edge of HfO.
3. Performed extensive modeling of electron guns with thermionic and field emitting sources
4. Designed and demonstrated several electron beam source geometries and methods to produce sufficient ebeam conditions to achieve laser threshold.
5. Designed and fabricated thermionic electron guns and ebeam controllers and provide them to our collaborators at Boston University and Astralux.
6. Developed a photoluminescence spectrometer to make wide bandgap photoluminescence spectral measurements for bandgaps up to 5.5 eV. Provided deep UV lasers to Boston University to enable them assemble their own instrument.
7. Demonstrated the need for UV Raman to be conducted at excitation wavelengths below 250nm to avoid fluorescence background from all target and substrate materials.

8. Demonstrated the value of simultaneous and combined UV Raman and native fluorescence to improve false alarm rates in the detection and identification of CBE agents.
9. Demonstrated the need for excitation wavelengths in the 230nm to 240nm range for ideal detection and identification of target materials using simultaneous UV Raman and native fluorescence methods

3.4.1 Cathodoluminescence instrumentation development

The purpose of this task was to develop electron gun instrumentation and to provide this instrumentation to our collaborators at Boston University and Astralux to assist in their testing of AlGaN. During the early part of the Phase I effort, preliminary values of current density and electron beam voltage needed to achieve threshold for lasing were developed using a scanning electron microscope at the Photonics Center at Boston University. Significant levels of linewidth narrowing, from 16nm to 4nm, occurred when an electron beam with a current density of $10A/cm^2$ at a beam voltage of 7.5 kV was focused on the surface of bulk AlGaN material with an Al content about 75%. The center wavelength of emission was about 274nm.

Ebeam pumping requirements overview

The ebeam pumping requirements to achieve laser emission are summarized as:

- Ebeam pumping density for lasing: 10^{-7} to 10^{-6} A/μ^2 = 10 to 100 A/cm^2.
- For 0.5μ x 750μ ebeam pumping stripe: 37μA to 370μA
- Pump power: 185mW to 2.7W at 5kV to 7.5kV beam voltage

We fully expect threshold for lasing to occur within the above limits and perhaps significantly below. In order to achieve near diffraction limited performance from the laser at about 240nm, the electron beam stripe width needs only to be about 0.3μ. However, in order to alleviate any tight ebeam focusing and alignment issues we plan to provide enough ebeam current to vastly overfill the minimum needed pumping area illustrated above. We are planning of providing up to perhaps 15mA of ebeam current at up to 10kV, or 150W of ebeam pumping power. In order to withstand this level of pumping power we will provide a pulsed ebeam pump with a ebeam pulse width about 100μs and a pulse repetition rate up to about 10Hz. We are currently not certain how tight a focus we expect to be able to achieve with the TE electron gun, but we expect to be able to achieve smaller than 20μ width or less. With a 20μ wide ebeam the alignment tolerance between the ebeam axis and the optical axis of the AlGaN die need only be about 30mr.

The CL source was originally planned to be a diamond microtip device from Extreme Devices. However, they went bankrupt in December 2003, shortly after the beginning of this program and their devices are no longer available. Before the beginning of the Phase 2 program we have been searching for alternative electron sources. The path we have chosen is to focus our efforts on traditional thermionic emission (TE) sources until we can find a suitable cold cathode field emission source. We evaluated carbon nanotube materials from Xintex with poor results. Although we will continue to evaluate opportunties for Field emitting (FE) electron sources our focus will be on making thermionic sources work

Although the original proposal divided the laser device development between edge emitting and surface emitting devices, Dr. Carrano suggested early in the Phase II effort that we focus our efforts entirely on edge emitters. This was a fortunate choice, since shortly after the

end of this DARPA contract it was discovered that there are not-well-known exclusion rules that make the possibility of surface emitters essentially impossible for AlGaN sources with high aluminum content. One of the problems with developing electron gun sources for edge emitters is that the electron beam needs to be rectangular with a very high aspect ratio.

Field Emission (FE) Electron Sources

Although it is not now our primary direction, it is worth a few words on the direction we presently believe we will be taking regarding a FE source. The reason we ultimately want to employ a FE source is related to size, weight and power consumption of both ESUVOS devices and their power supplies. TE sources require use a hot filament as an electron source and require a filament transformed as well as the high voltage source. This provides more bulk for the filament transformer and TE source itself and generate a heat dissipation requirement for the device. And they have higher overall power consumption. FE sources can be made much smaller and eliminate the added heat generation and dissipation requirement.

We are presently working with a group at JPL who are developing miniature carbon nanotube array electron sources for use in nanoklystron devices which have the same eventual size as our proposed ESUVOS devices, about 1 cubic millimeter. Both the nanoklystron and the ESUVOS require vacuum packaging since both are ballistic electron devices, so both device will share many technology issues. However, we do not hold out hope that such device will be perfected to a point we could employ this technology for the next year or so. Therefore we will continue to focus on the use of TE sources.

Thermionic Emission (TE) Electron Sources

The electron gun we have chosen to use for testing AlGaN films and devices and to make the initial sealed-off devices from is a commercial miniature electron gun assembly with a diameter of 1.6cm and an overall length less than 4cm. This gun assembly contains several grids and was quoted as capable of providing electron beam currents over 1mA in a collimated 250 μm diameter beam. Later we found this not to be the case. External to this assembly we provide the focusing lens and accelerator electrode. Photographs of the first thermionic emission electron beam pumped light emitting triode (TE ELET) device are shown below in Fig. 4.

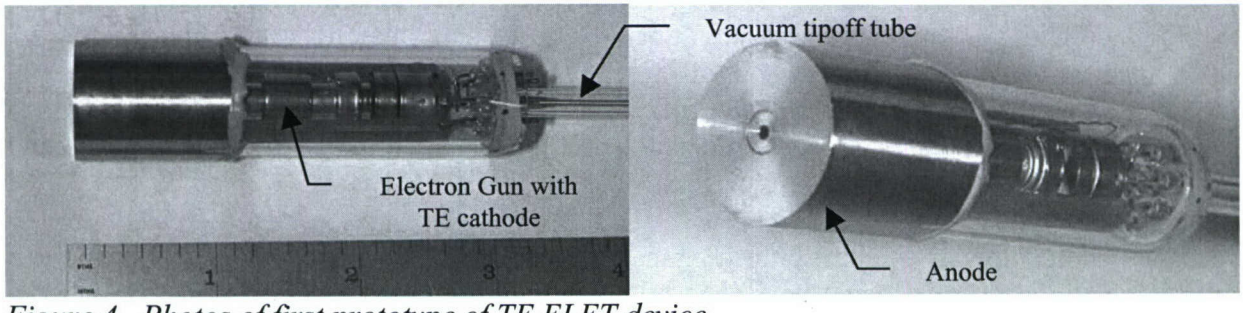

Figure 4. Photos of first prototype of TE ELET device

This present device is not a hard sealed device and will require operation on a vacuum station. We are currently working on smaller devices with all glass/metal/ceramic construction which can be sealed off. The basic body of this assembly will remain the same for both ELET and ELT devices. The head of the device will change depending on whether the device is an ELET or ELT. The ELET configuration, shown above, is very simple. The AlGaN sample is sealed film-side-down onto the electron beam aperture shown on the right above. The AlGaN

film is pumped from inside the device and emission occurs in a Lambertian distribution along the axis of the device. Performance information is not yet available. The breadboard power supply used an Emco 10KV power supply with a size about 2cc.

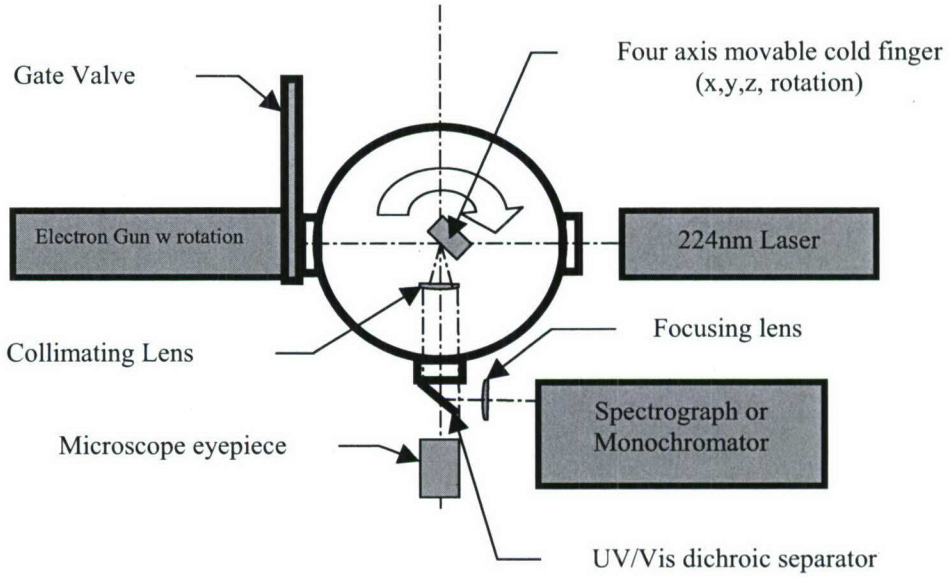

Figure 5. Diagram of CL/PL Lab Instrumentation

a. Drive Circuitry for the E-Gun.

All major hardware has been received. The first power supply is under construction. This has a +10 kV maximum output at 15 watts, which is estimated to be more than enough for the intended pulse mode. Pulse width will be board adjustable in the range of 100 μsec down to about 10 μsec . It is intended this to be more or less fixed during actual tests of AlGaN samples. Pulse repetition rate will be front panel adjustable from approximately 1 to 5 Hz. Output voltage is also adjustable from the front panel, with a 3-1/2 digit meter to monitor HVDC . Other outputs for test purposes include anode current at the e-gun, pulse trigger, and kV monitor.

b. E-Gun Vacuum Mounts

Five e-guns have been mounted in bored out 2.75"CF flanges.. The 22mm OD glass shell is sealed with vacuum epoxy into the flange. The seal has been under vacuum for about 3 weeks, at this time, and appears capable of maintaining pressures below 10^{-6} Torr.. Leak up after a one week interval was under one decade of pressure. We have been concerned that pins and base are sufficiently stress free for reliable operation. To date it looks good. It is planned to helium leak test all e-guns before shipping.

c. Further Modeling of E-Gun

A detailed model of the 22mm E-gun has been made with the slot lens placed at a plausible position out from the outboard end of the final factory installed lens (G5). The model spatial mesh resolution was 25 um, The circular approximation of the small dimension of the slot lens was used to test convergence of the beam and check for the amount of aberration.

The fine scale of the modeling grid means a very large number of field points, some 2.1 million in this model, and modeling the entire chamber area, will require about 40 million data points. This is turn requires about 10x that number (400 MB) of RAM in order to begin to compute the potential distributions. A reduced size ground enclosure was used for the first full set of lens models. The results are generally believable, but the closeness of the ground shell creates

unusual focus effects in front of the target area. It is expected that these will disappear when the full chamber is modeled.

d. E gun Lens Design Issues

Developing optimal focus involves a rather tedious iterative adjustment to the potential arrays of 6 focusing electrodes, while the accelerating potential is maintained at one value. Among the best-for-focus, configurations, it was clear that a beam spot size of less than 2 um would be possible with a fairly high electron throughput efficiency ~75% or more. So far it seems that the slot lens can generally be wherever is convenient, and seems to work well about 25mm out from the G5 final lens of the e-gun. We are using this approximate position for the design of the final electrodes and the MACOR insulating spacer.

A 3D rendering of the gun is shown below in Fig.6. One particularly nice feature to come out of this is the conclusion that the final lens, can be a fairly simple rectangular aperture. The larger it is, the less beam interception occurs and throughput efficiency is higher. So far there appears to be some degree of aberration in electron beam as it converges on the target. The 2 micron figure is the maximum spread of all electrons. A beam current density plot would be helpful here, and we expect to have those when the next round of modeling is completed.

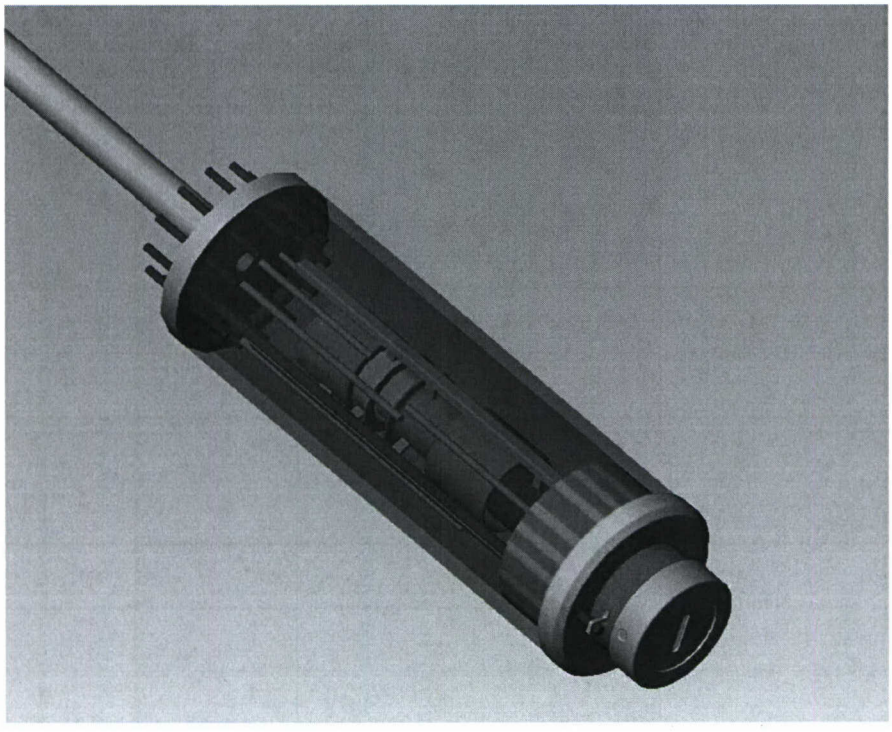

Figure 6. Electron Gun with electrostatic slit lens

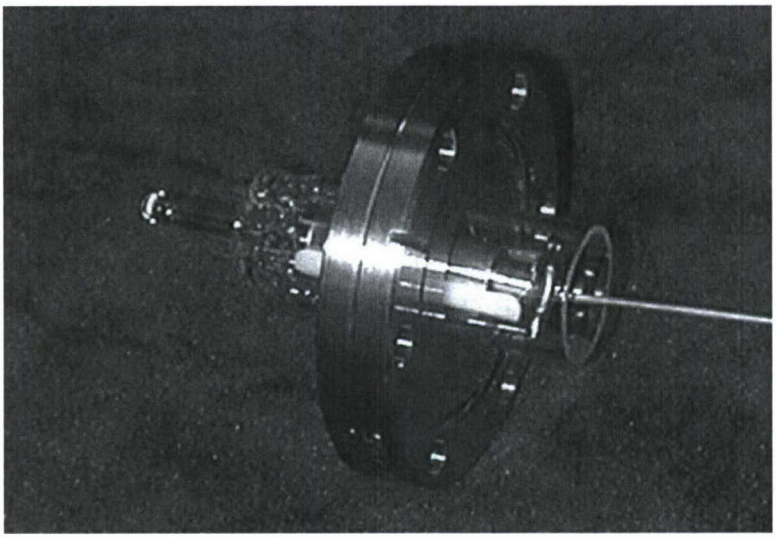

Figure 7. Photo of electron gun with electrostatic focus lens electrode.

e AlGaN Die – Sub Mount.

The sub mount is a simple rectangular beam (1 x 5 x 10 mm) of Cu W alloy, with one finely ground end face. Cu-W alloy is hard and brittle. About 25% of the pieces made had cracks and were considered unusable. Eight mounts have been sent to Astralux for their first attempts at Au coating and die mounting. Calculations indicate that if the AlGaN dies can be mounted so that their long edges lie within the edges of the slightly larger die end, then the angular alignment will fall within the adjustment

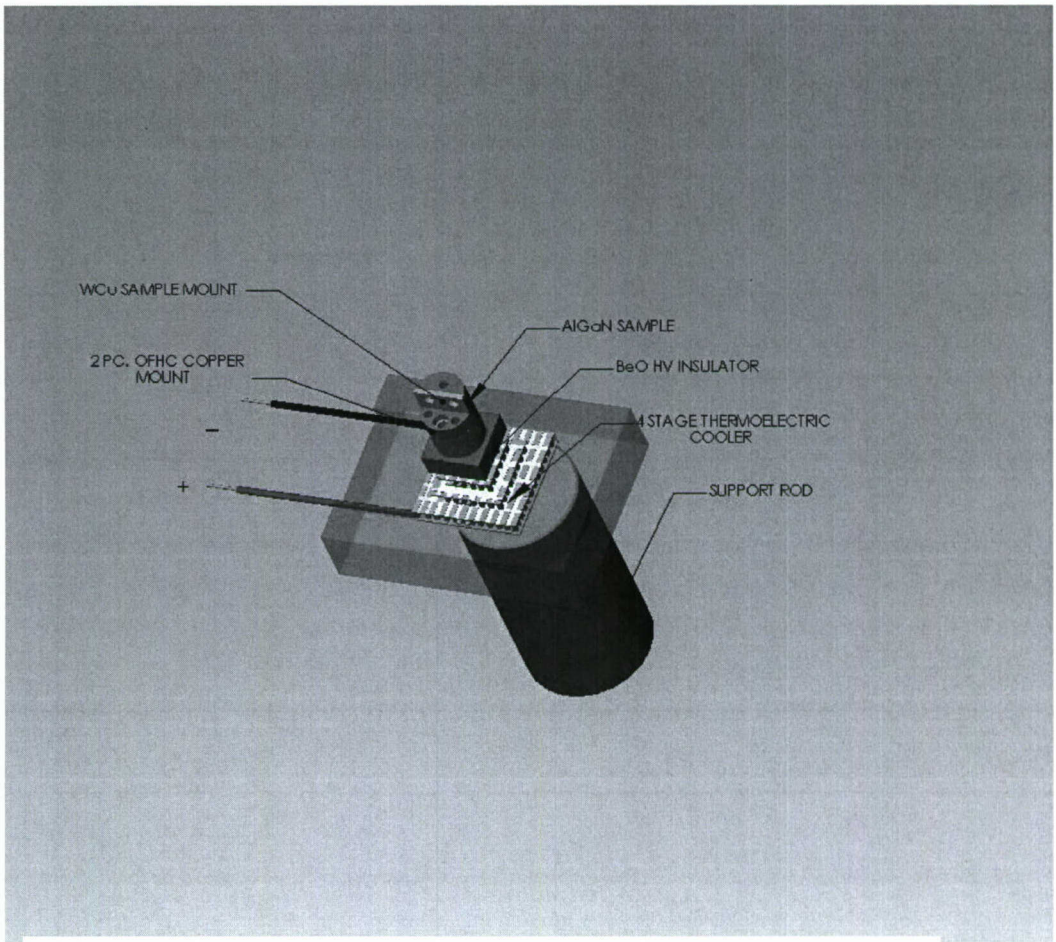

Figure 8. Die mounting apparatus with cooling.

range of the XYZ –rotational stage and the E-gun rotational stage.

The remainder of the thermal base mount is a two piece (see Fig.7) of OFHC Cu, which thermally grounds the sample to the TE cooler, through the BeO HV insulator.
When maintained at –100C, the base will provide sufficient heat capacity to fully sink the heat generated in the AlGaN during a beam pulse.

Electron Gun Controller: 1st Version

The pulsed electron gun controller was described in detail in the November Monthly Report. This report will focus on its status and procedures for alignment. More recent photos are shown below in Fig. 9.

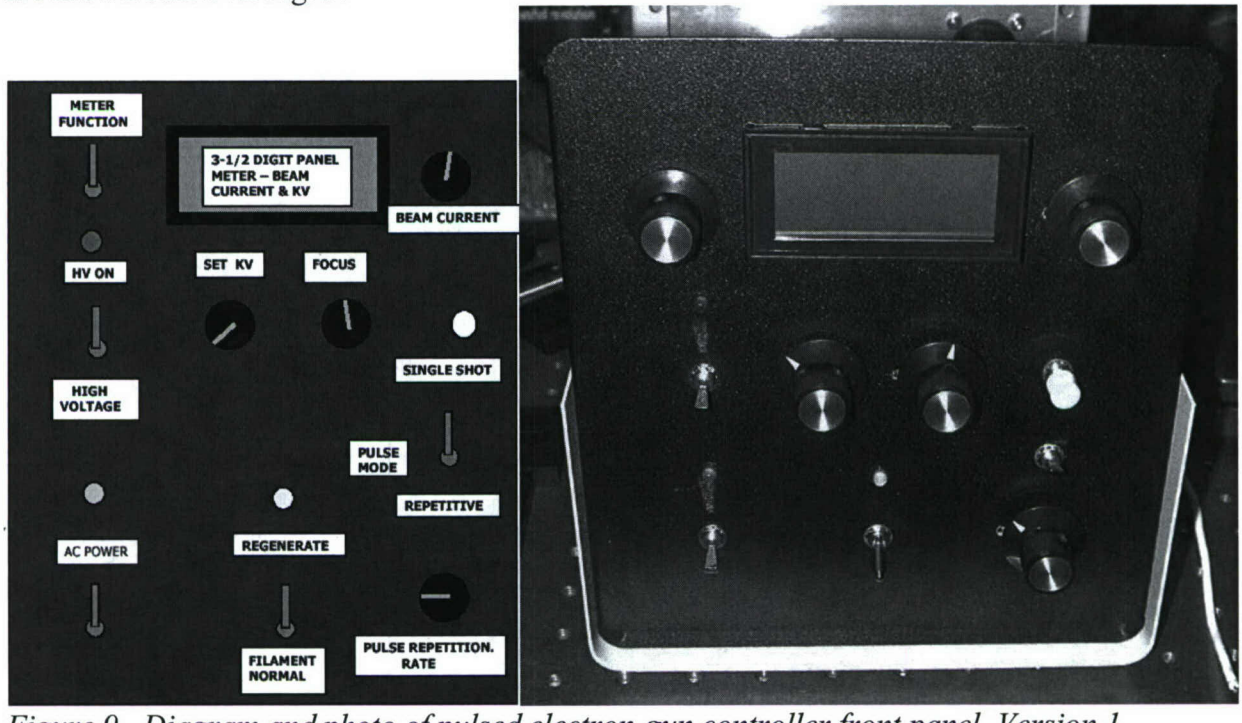

Figure 9. Diagram and photo of pulsed electron-gun controller front panel, Version 1

During a design review of the above controller during this reporting period, it was discovered that the grid control voltages could become interdependent if one or more control electrodes (grids) intercepted significant amounts of the electron beam. This condition can occur during the initial e-gun set-up. It causes the potential of an adjacent electrode to change when the potential on another electrode is being set. Given the sequential procedure for setting each electrode to a minimal beam interception potential (i.e.: minimal electrode current), the overall effect is to increase the number of iterations required for the focusing setup.

As the set –up and focus procedure was already somewhat tedious, it was decided to modify the focusing circuitry to providence independence of all grid voltages under all set-up conditions. At the same time it was felt appropriate to make a printed circuit board rather than continue with the vector board approach shown last month. The new circuit board with all design corrections is shown below in Fig. 10.

A few more refinements to the controls include changing the double pole Beam Current/KV mode switch, at the left of the LCD panel display, to a multi-position switch. This now enables the LCD display to read all electrode potentials, filament voltage and beam Kilo-

Volts. There are 3 spare positions for future functions if required. The table below lists the various switched functions, and identifies their corresponding board adjustment/calibration potentiometers.

Position	Function	Adjustment Pot location	Calibration Pot location
1	spare		
2	spare		
3	spare		
4	VG1	Panel(P7)	PWB(RT14)
5	VG2	PWB(RT5)	PWB(RT13)
6	VG3/VG5	PWB(RT3)	PWB(RT11
7	VG4	PWB(RT4)	PWB(RT12)
8	VG6	Panel(P6)	PWB(RT10)
9	Filament Volts	PWB(RT1)	PWB(RT15)
10	E beam KV	PWB(P4)	PWB(RT9)

The controller, at this time, does not provide a means to directly measure leakage currents to the various electrodes during set-up mode. The primary electron beam current is the anode

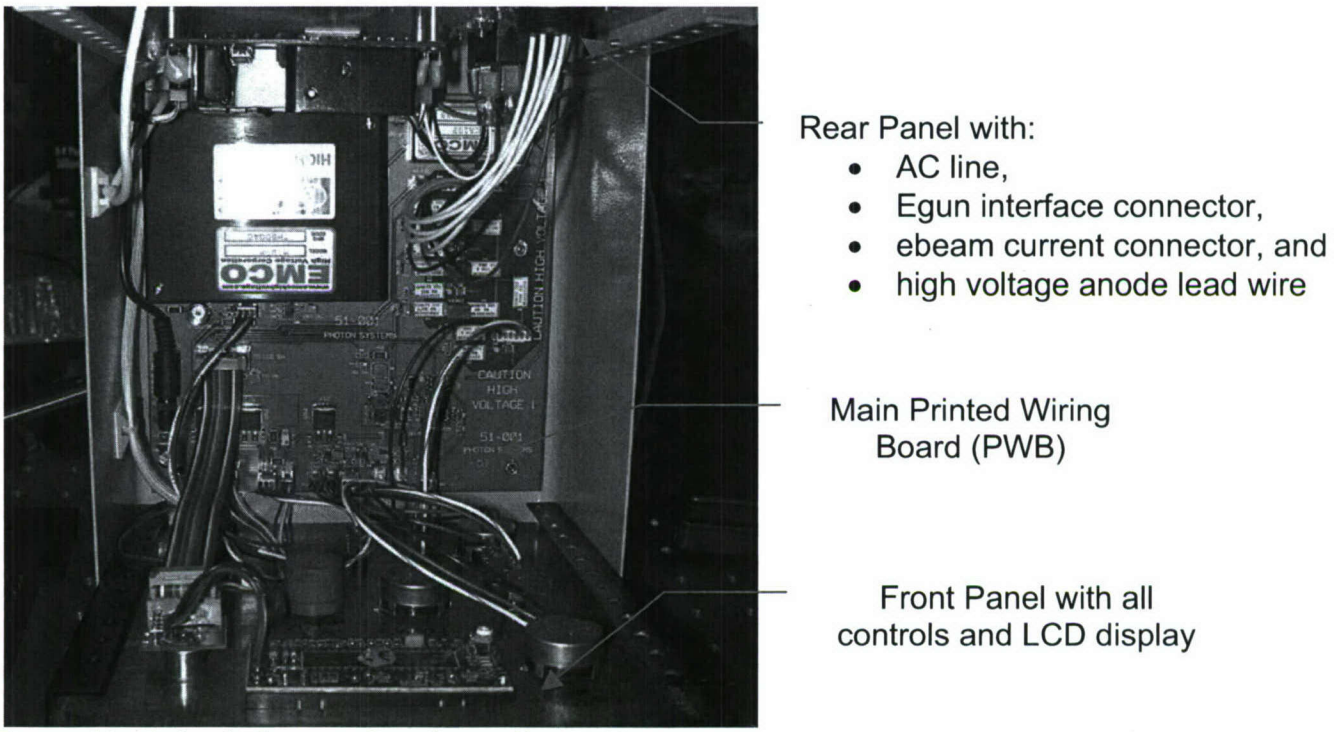

Figure 10. Pulsed Electron Gun Controller PWB

current. This is measured as a voltage drop across the 100 ohm resistance (R_{21}), and presented via a BNC connector on the rear panel. Either DC or pulsed current can be read in this way. The calibration factor is 10 mA per volt.

The board mounted potentiometers provide for calibration and range adjustment of each focusing electrode voltage, as well as the normal mode filament voltage. The function of the "calibration pot" is to set the accuracy of each measured voltage for the LCD display. The "adjustment pot" sets the actual voltage provided to the electrode.

During normal operation of the system, the voltages on G2, G3/G5 and G4 will remain fixed, while the "focus" voltage on G_6 will be adjusted, on the front panel, to maximize UV light output. The filament voltage setting is used to keep cathode emission in the space charge limited mode, so that there will be an adequate supply of electrons for the anticipated level of beam current.

In pulsed mode, pulse width and pulse repetition rate may be set. The pulse width controls the effective duty cycle of the electron gun. It is set by a board mounted potentiometer RT8. The pulse repetition rate is set on the front panel by potentiometer P8. A board mounted adjustment RT7 is used to provide the basic 0.2 to 1.2 second pulse interval (0.8 to 5 pps).

Figure 11, below shows the electron gun with the control/focus electrodes G1 through G6, and a beam trajectory plot for 100 electrons, launched from equally spaced points across the face of the cathode. The voltage settings for the electrodes cause one of the apertures of G3 to intercept a significant number of the electrons. Such a condition would cause G3 (and G5, since they are internally connected) to have a non-zero electrode current. Other combinations of electrode voltages can minimize the amount of beam interception that occurs. This is the trajectory model equivalent to the set-up and focusing process outlined later on in this report.

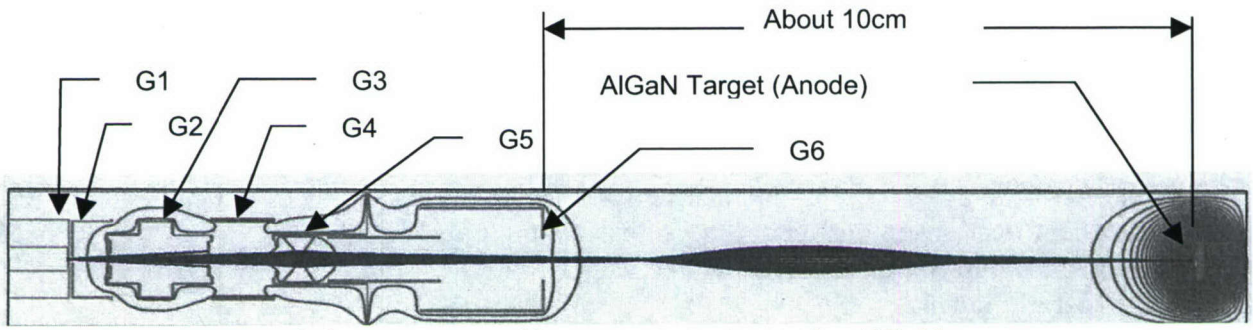

Figure 11. Diagram of electron gun and beam trajectories to the AlGaN target

Since each electron gun has small mechanical tolerances in the size and location of the electrodes, it will have a set of electrode voltages that give optimal focus. The Pulse Electron Beam (PEB) controllers will be calibrated and preset for one of the two electron guns included, before being sent to Boston University and Astralux Inc. Whenever the electron gun is changed, the various electrode voltages *may* need to be adjusted for optimal beam throughput.

At Photon Systems, we could provide these voltage settings, for each of the electron guns, by operating them in our test chamber. This will require conditioning the cathode first and then setting the voltages to provide optimal beam characteristics for the electron gun. The cathode will then be quite sensitive to moisture and atmospheric gas contamination, and may require regeneration after it is installed in other vacuum systems. It would be most desirable to avoid this. If the e-guns have reasonably similar characteristics, only one set of electrode voltage will be necessary for all. But this is not yet known.

Front Panel Controls:

As illustrated in Fig. 9, the external controls on the front panel of the controller are:

1. Line power on/off switch with green LED indicator light
2. HV power on/off switch with red LED indicator light
3. E beam voltage setting (0-10kV)

4. E beam current setting (0-15mA)
5. E beam focus voltage
6. Single versus repetitive pulse operation switch
7. Single shot push button
8. Pulse repetition rate (0.8 - 5Hz)
9. Pulse width (10-510μs) (R9)
10. Cathode heater normal operating temperature = yellow LED dim
11. Cathode heater regeneration mode = yellow LED bright
12. LCD display screen for electron beam voltage, and focus voltages

Continuous Mode:

By means of a board mounted jumper at plug (P19) the controller may be set to operate as a standard high voltage supply. In this mode of operation, the electron gun operates continuously. Beam current is set as before using the front panel control for beam current. Electron beam current will depend upon the heater filament setting, and the exact beam voltage. The primary HV supply can supply up to 1.5 mA of current to the anode(target), at full 10 kV output voltage. In continuous mode, caution must be exercised, since a well focused beam, could have a power density exceeding 15 kW /mm^2. Beam impingement on any electrode of the electron gun at these power levels would cause rapid heating, and possible distortion or even burn through of the electrode.

Continuous mode is most useful in the set-up and initial focusing operation of the electron gun and should be used at the lowest possible current. A nominal value of 10 to 50 μA is recommended.

On the next page is the latest schematic of the pulsed electron beam controller. Component identifications in this report, refer this version, Fig. 12.

b. Electron Beam Setup Procedure, Ver.1.0:

Hardware Installation:

a. Install the Pulsed Electron Gun Assembly on the vacuum system using a rotational feed-through stage, to enable the wide axis of the electron beam to be rotated. Position the electrostatic slit lens approximately horizontal.

b. Install the AlGaN Sample Test Assembly in the vacuum system with the centerline of the AlGaN die bar in the center of the electron beam axis. Make certain the die bar sample can be moved along it's entire vertical extent. We presently believe the AlGaN target can be used during the setup procedure, but it may be necessary to replace the AlGaN target with a scintillation target for greater visibility of the electron beam.

c. Connect the anode (HV) lead to the Sample Test Assembly. Connect the electron gun pigtail cable to the rear of the Controller.

d. Connect the TE cooler power leads and thermocouple leads and make sure they function in the vacuum system. The TE cooler requires 7.9VDC with a maximum current of 1.7A to achieve a temperature difference of 110^{0}C below ambient. The cooler is able to extract a maximum of 1.6W from the AlGaN sample. In the pulsed mode of operation, the maximum heat load is expected to be only a few mW.

e. Close the vacuum system and ensure a vacuum below about 10^{-6} Torr is achieved.

f. Connect the controller line cord to an 115VAC, 5A receptacle. Note: As a safety consideration, it is recommended that this be the last step before operation.

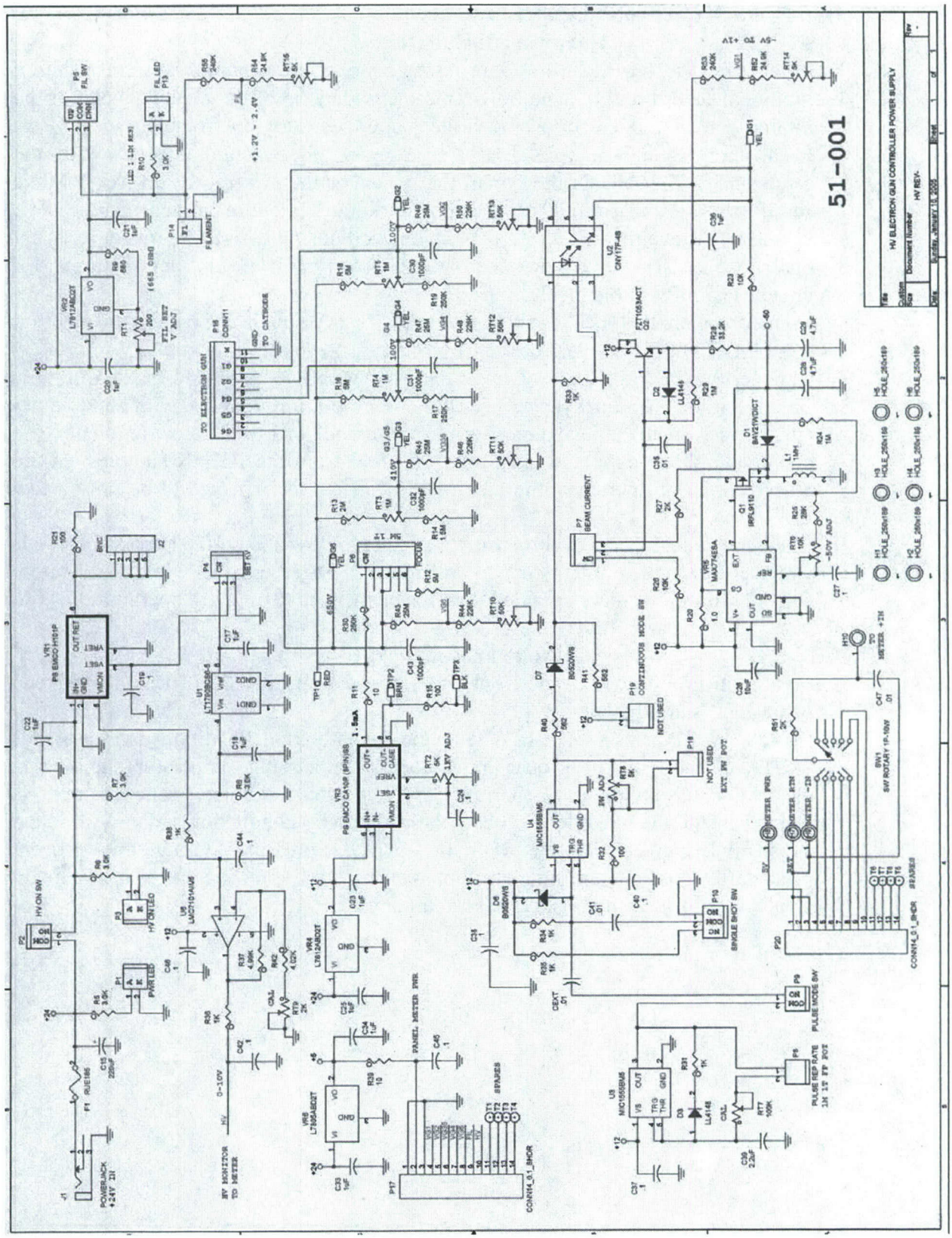

Figure 12. CL controller, Version 1.0

b. Electron Beam Setup Procedure, Ver.1.0:

Hardware Installation:

a. Install the Pulsed Electron Gun Assembly on the vacuum system using a rotational feed-through stage, to enable the wide axis of the electron beam to be rotated. Position the electrostatic slit lens approximately horizontal.

b. Install the AlGaN Sample Test Assembly in the vacuum system with the centerline of the AlGaN die bar in the center of the electron beam axis. Make certain the die bar sample can be moved along it's entire vertical extent. We presently believe the AlGaN target can be used during the setup procedure, but it may be necessary to replace the AlGaN target with a scintillation target for greater visibility of the electron beam.

c. Connect the anode (HV) lead to the Sample Test Assembly. Connect the electron gun pigtail cable to the rear of the Controller.

d. Connect the TE cooler power leads and thermocouple leads and make sure they function in the vacuum system. The TE cooler requires 7.9VDC with a maximum current of 1.7A to achieve a temperature difference of 110^0C below ambient. The cooler is able to extract a maximum of 1.6W from the AlGaN sample. In the pulsed mode of operation, the maximum heat load is expected to be only a few mW.

e. Close the vacuum system and ensure a vacuum below about 10^{-6} Torr is achieved.

f. Connect the controller line cord to an 115VAC, 5A receptacle. Note: As a safety consideration, it is recommended that this be the last step before operation.

Cathode Processing:

a. Switch on Line Power at the front panel of the controller (SW1/D1). The green panel LED should come on.

b. Switch the filament switch (SW3) to the Regeneration Position. This provides 24VDC to the filament to heat the cathode to outgassing temperatures and bring electron emission material (barium) to the cathode surface. The filament is located inside the cathode and heats the cathode by conduction. You will note a substantial increase in the vacuum chamber pressure during this process procedure. Continue until the vacuum system pressure recovers to a low vacuum. Typically this is accomplished in 5-10 minutes.

Initial Electron Beam Focusing:

Note: This set-up procedure is described here primarily for reference. The basic e-gun setup will be performed on each controller prior to shipping. This procedure is performed with the controller set in the Continuous Mode via Jumper on P19.

In order to read electrode currents, a micro-ammeter capable of being "floated" at up to 1kV potential is required. A convenient form of such a meter is a battery operated DVM with either direct reading μA scale or a mV DC voltage scale. A special adapter plug is used between the HV controller output and the E-gun cable for this procedure.

a. Switch the filament switch to Normal Position. This provides about 12-15 VDC to the filament for normal operation of the electron gun. This should be sufficient to provide 10mA or more needed during pulse mode for adequate excitation of the AlGaN sample. If greater current is needed, RT1 on the PWB can be set to a higher voltage. However, this will shorten the lifetime of the electron gun.

b. Set electrode voltages to these nominal values:
G1(extraction electrode) = 0 VDC
G2 = +100 VDC
G3/G5 = +400 VDC
G4 = +100 VDC
G6 = +500 VDC

c. Turn on high voltage (SW2). Red panel LED (D2) should come on.

d. Set HV to 3kV (R3). This is nominal. Other voltages can also be used

e. The general principle of beam optimization is to maximize the current to the target and minimize the sum of the currents to all control electrodes (grids). The total cathode current, $\mathbf{I_{cathode}}$, will be the sum of all grid currents plus the target current.

$I_{cathode} = \Sigma I_{gi}$ (for i=1-6) + I_{target}

f. Adjust V_{G1} to give I_{G1} = 1uA. Record VG1 and target current, I_{target}.

g. Adjust V_{G2} to give I_{G2} = 1uA. Record V_{G2}, I_{G1}, and I_{target}.

h. Adjust $V_{G3/G5}$ to give $I_{G3/G5}$ = 1uA. Record $_{VG3/G5}$ and I_{G1}, I_{G2} and I_{target}

i. Adjust V_{G4} to equal V_{G2}, and readjust $V_{G3/G5}$ to give $I_{G3/G5}$ = 1uA if necessary. Record $V_{G3/G5}$, I_{G1}, I_{G2}, $I_{G3/G5}$, and I_{target} .

j. Adjust V_{G6} (slit lens) to determine if it has any effect on I_{target}. It should be that I_{target} is approximately dependent on V_{G6}. Set V_{G6} to give I_{G6} = 1uA. Record V_{G6}, I_{G1}, I_{G2}, $I_{G3/G5}$, I_{G4} and I_{target}.

k. Check that $I_{cathode} = I_{G1}+I_{G2}+I_{G3/G5}+I_{G4}+I_{G6}$. It should be.

l. Repeat steps **f** through **k** as needed to get all grid currents as close to 1ua as possible. Record the voltages and currents on each grid as a "road map" along the way. This completes the preliminary setup. **NOTE:** Ideally the grid currents should be zero. The 1uA value brings us close to that condition. Any grids that have current less than 1ua are OK.

m. Now adjust V_{G1} (extraction grid) to cause beam "cut off". Cutoff occurs when $I_{cathode} = I_{target} = 0$. Record this voltage. Check that all grid currents are also zero at this point. If any grid currents are not zero, look for leakage somewhere in the circuitry and correct it. $I_{cathode}$ should be equal I_{target} plus the sum of the grid currents.

The above procedure is in a formative stage and may need to be modified as experience is gained. It forms the outline of the basic focus/setup process.

b. Electron Gun Source Assembly Status

Below is a photo of the front end of the pulsed electron gun with slit lens.

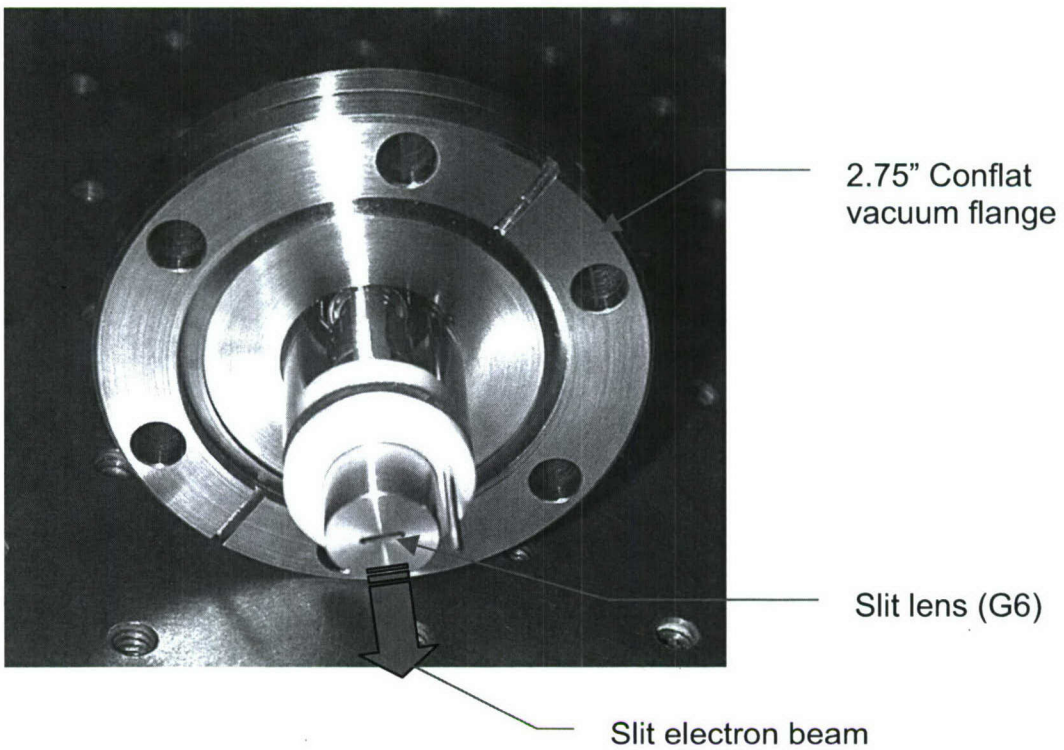

Figure 13. Photo of Electron Gun with Slit Lens mounted in 2.75" conflat vacuum flange

e Cleaved and Mounted A-plane AlGaN Samples and Test Assembly Status

The first AlGaN A-plane cleaved and mounted die bar was received from Astrulux during the month. We have examined the mounted as shown in the photos below.

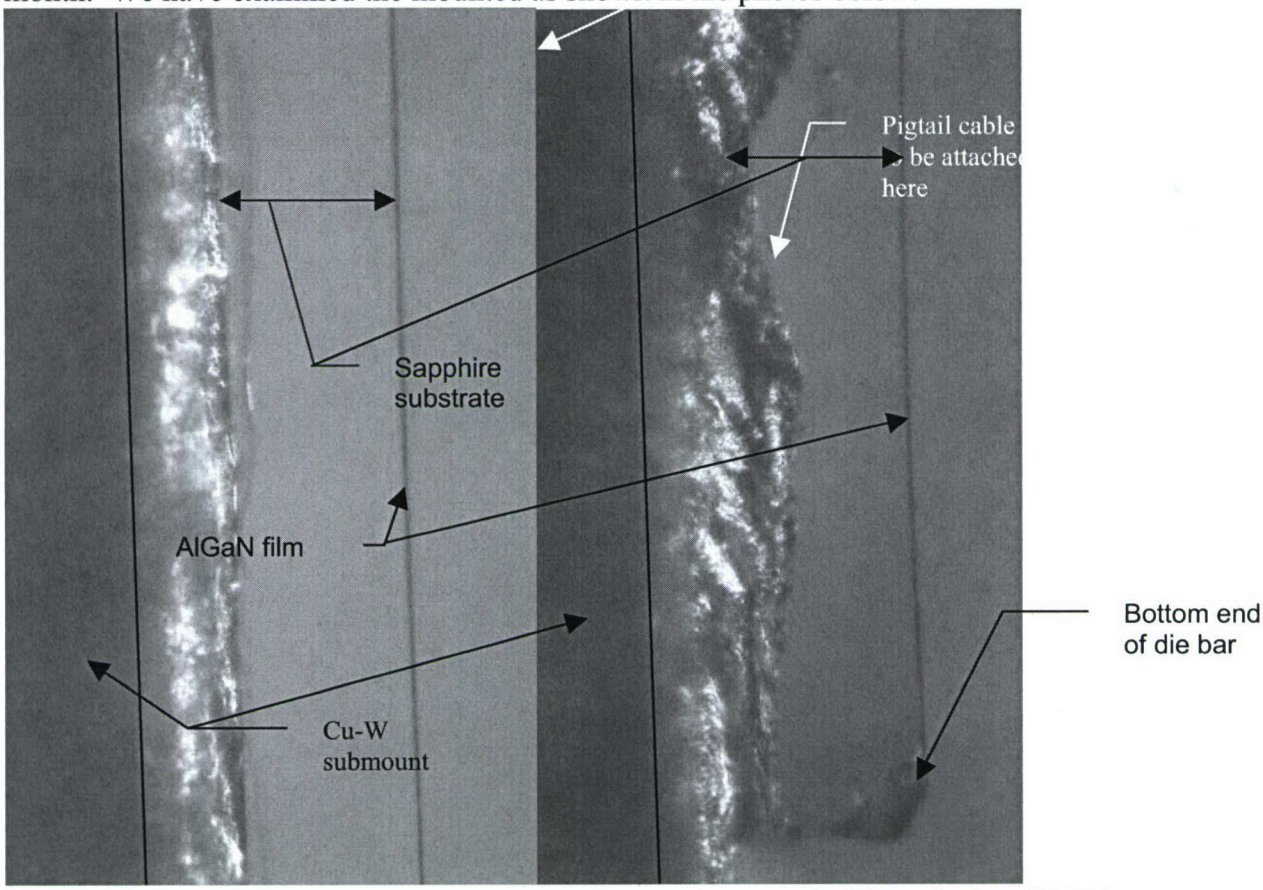

Figure 14. Two side views along laser optical axis of mounted AlGaN die bar (200X)

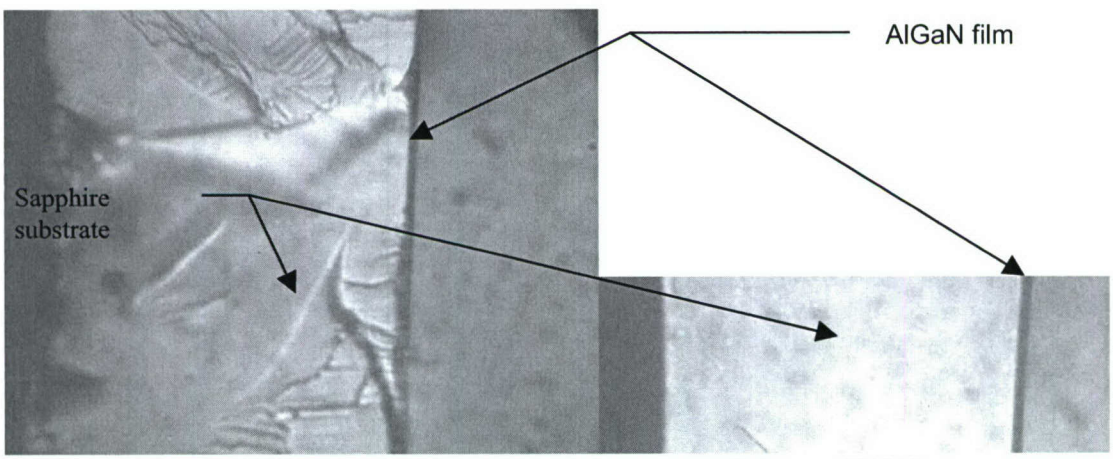

Figure 15. Two side views of defect and good regions of cleave (800X)

Some of the parts have been delayed in the machine shop but are expected by mid-January. The illustration below is in the same orientation as the photos above.

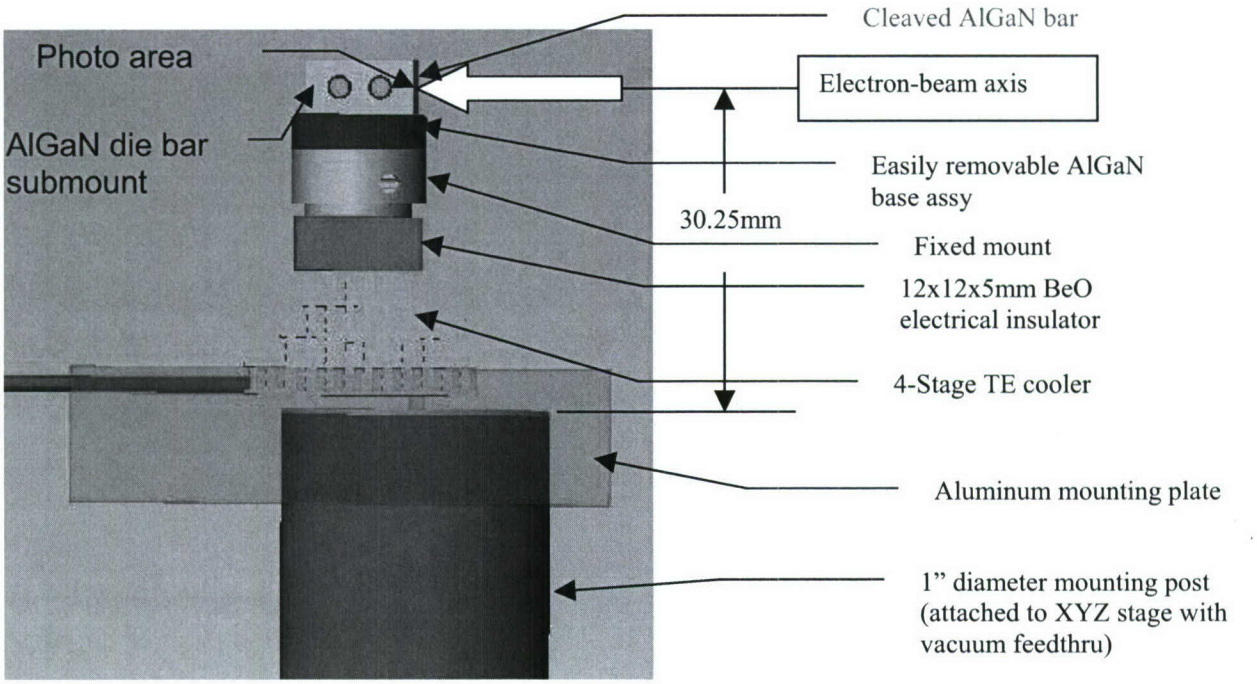

Figure 16. Die mounting assembly with cooling (laser axis out of page)

f. Vacuum Chamber.

The Vacuum Test Chamber is now fully functioning. Below is an overall view of the vacuum system.

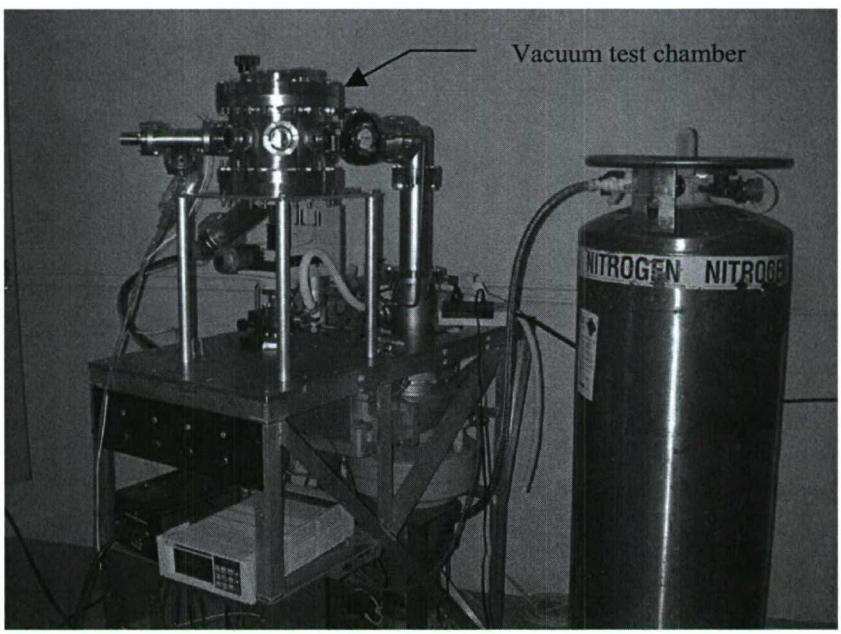

Figure 17. Overall view of vacuum test chamber for ESUVOS.

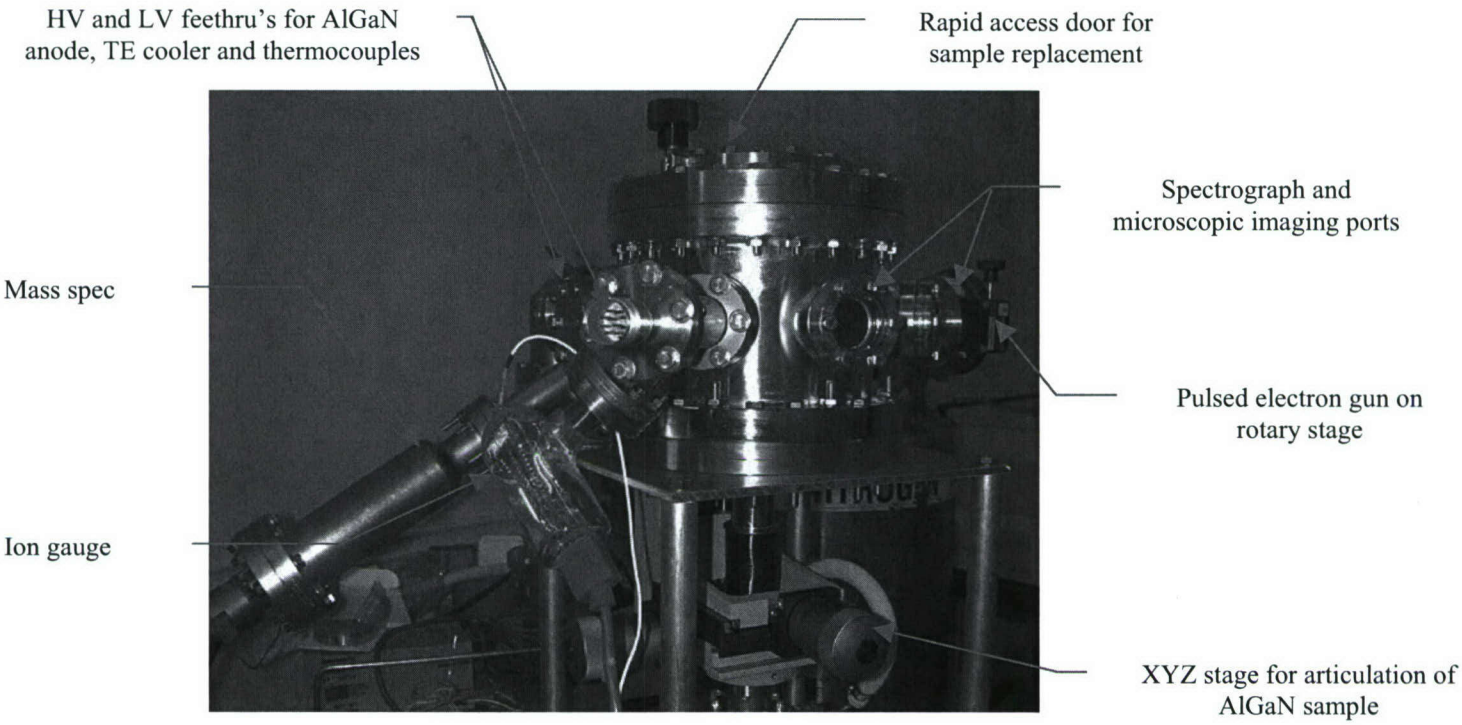

Figure 18. Closeup view of vacuum test chamber

The system is currently in the 10^{-7} Torr range and backout is continuing to prepare the system for testing of AlGaN samples.

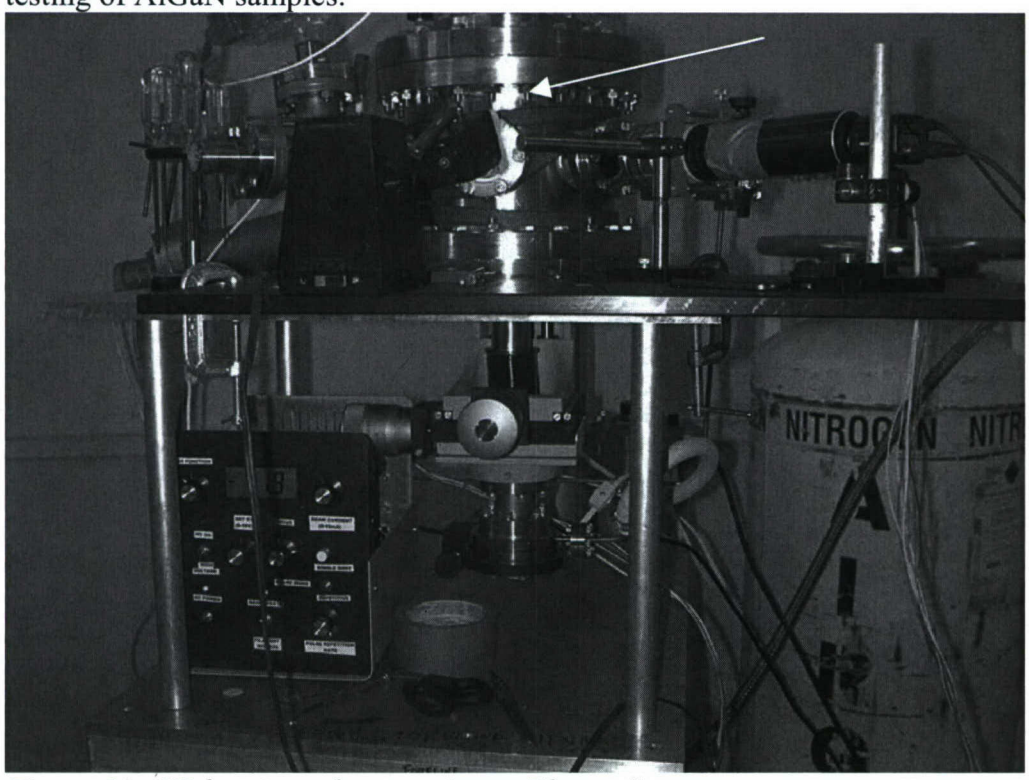

Figure 19. Wider view of test station at Photon Systems

Upgrade of pulsed slit beam CL instrument

We found several deficiencies with the first iteration of the pulsed electron gun CL instrument that we are in the process of correcting. The first, as well as present, instrument provide six independently controllable power supplies plus the filament supply. The cathode, K, is not shown in the diagram below since it is contained within G1. The grid controllers provide control voltages for the extraction grid, G1; focusing grid, G2; einseln lens G3/G5; focus grid, G4; slit lens grid, G6; and the AlGaN target anode, A. The high voltage supply for G3/G5 was inadequate to collimate the electron beam and allow proper focus using G2, G4 and G6 grid voltages. The ramification of this was that although we measured over 1mA of beam current at the cathode, this beam current was not being delivered to the AlGaN target due to leakages of current to various grids. This problem was not discovered immediately because the first iteration power supply did not have leakage current monitors for each power supply and relied too much of modeling of the electron beam using the SIMION 7 software acquired for this purpose. We are still getting familiar with this software and how to use it to accurately predict the performance of an electron beam.

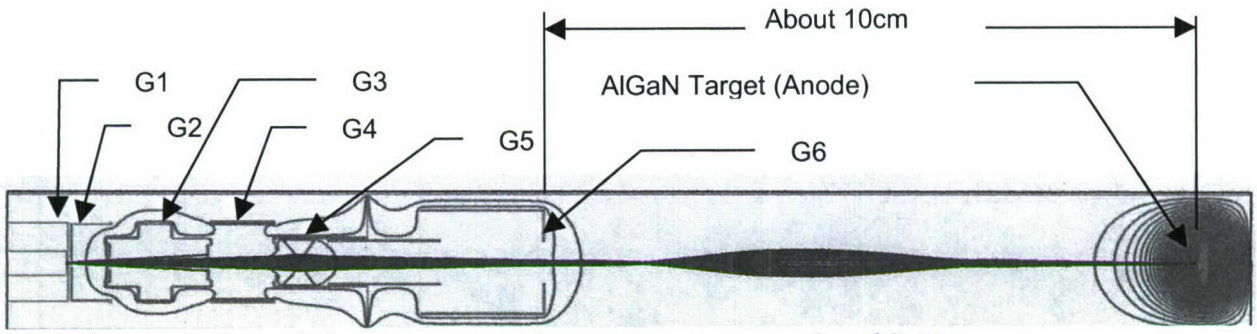

Figure 20. Diagram of electron gun and beam trajectories to the AlGaN target

Grid	Old VDC range	New VDC range	Nominal value
K	0	0	0
G1 (extraction grid)	-50 to +5	-50 to +5	0
G2 (focus grid)	0 to 500	0 to 500	385
G3/G5 (einseln lens)	0 to 500	0 to 10kV	3kV
G4 (focus grid)	0 to 500	0 to 1kV	70
G6 (slit grid)	0 to 500	0 to 10kV	3kV
Anode (AlGaN target)	0 to 10kV	0 to 10kV	5kV

As noted in the above table, two of the grid voltages must be closer to the anode voltage than previously predicted. As a result there was excessive current leakage to these grids and less than about 20μA of current was actually delivered to the AlGaN target, although more than 1mA emission was produced by the cathode, K. Unfortunately, to correct this problem, much of the controller and electron gun assembly needed to be redesigned. In the process, we are upgrading many features of the power supply including:

- Ability to measure both voltage and current simultaneously for each grid so that we can ensure minimum leakage current and maximum beam current delivered to AlGaN sample. This will greatly simplify the setup of the instrument since voltage and current for all grids will be visible simultaneously, allowing better adjustment of the grid voltages.
- Higher operating frequency (1kHz versus 10 Hz) and wider range of pulse widths. This will enable better compatibility with simple spectrographs like those available from Ocean Optics.
- Automatic timer for filament regeneration to eliminate burned out cathodes

The new ebeam controller is designed with three modules: the Filament and G2 pulser control board, 1kV and 10kV power supply boards. Below are a series of photo's of these new circuit boards. Schematics will not be included in this report but will be delivered with the instrument since they are too detailed to be readable in this report.

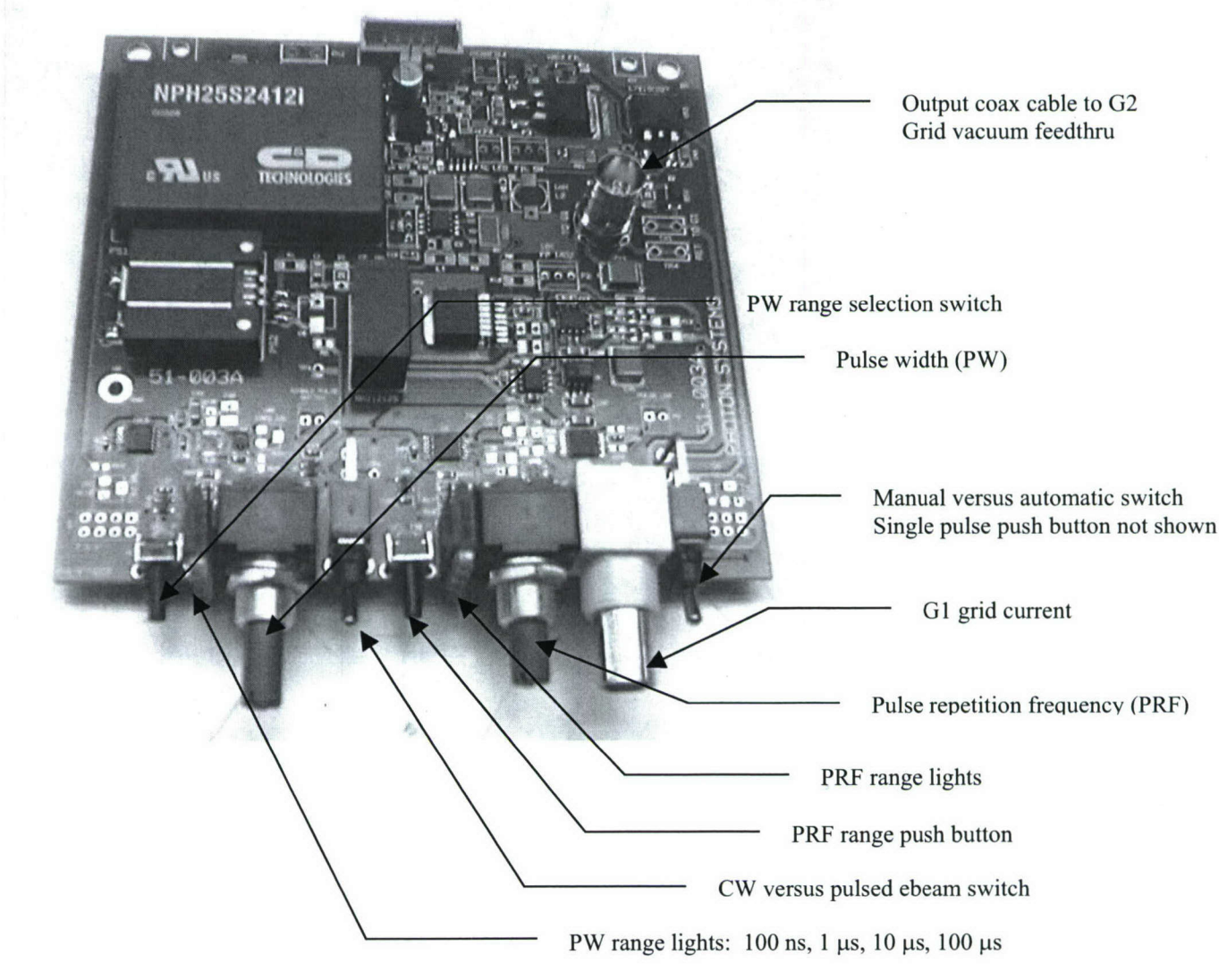

Figure 21. Photo of G1 grid control board (version 2)

The above photo shows the G2 grid control board, which also contains the filament operation and regeneration power supplies. The filament control switch (normal versus regeneration) is remote from this board and is not shown. Also not shown is the two step filament regen positions for 24VDC and 22.5VDC. Regen required processing of the filament for 2 minutes at 24VDC and about 30 minutes at 22.5VDC after being exposed to air. When the filament is placed in regen position, a timer limits the amount of time that the filament can be operated. This was done to eliminate the possibility that the filament would be burned out by leaving it on for too long a time.

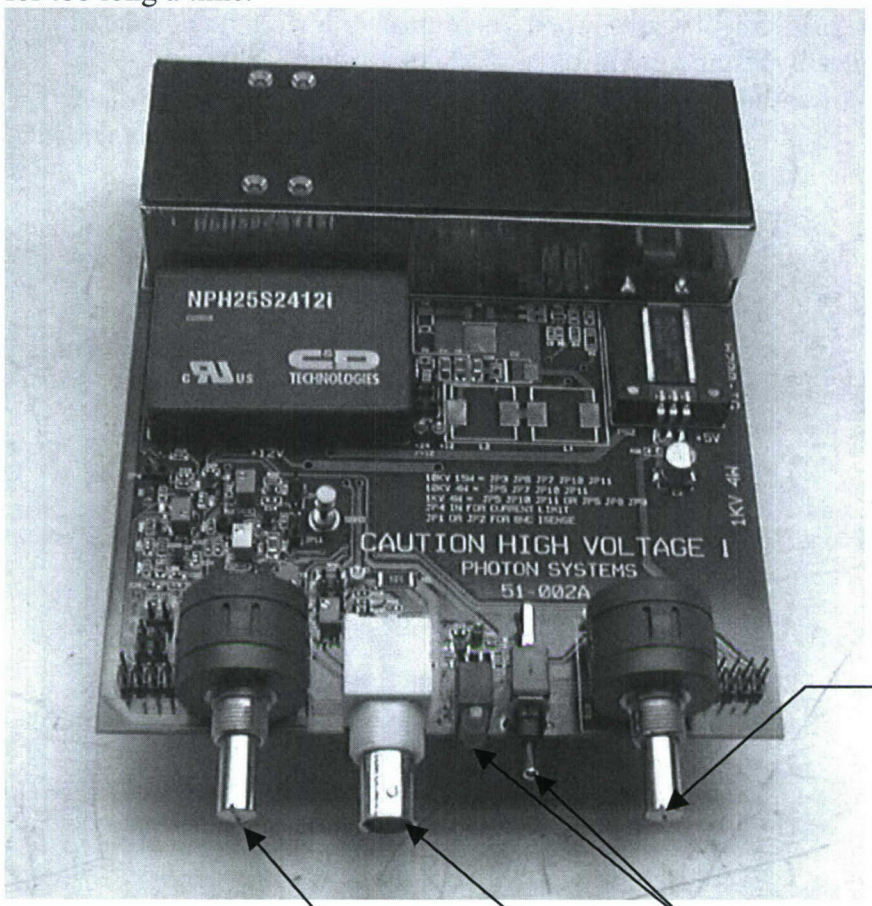

Figure 22. High voltage grid control power supply photo

The new high voltage power supplies shown above are a significant improvement over the first iteration power supply. First, these power supplies allow constant measurement of the leakage current as well as voltage using LCD displays shown in Fig. 23 below. A feature of this new design is the ability to set the leakage current, thus enabling this module to automatically set the operating voltage corresponding to this leakage current. We attempted to enable the circuit to select zero leakage current, thus automatically setting the optimum grid voltage, but the lowest

we could obtain was about 2 microamps, a small value compared to the approximately 1mA to 10mA anode current generated when optimized.

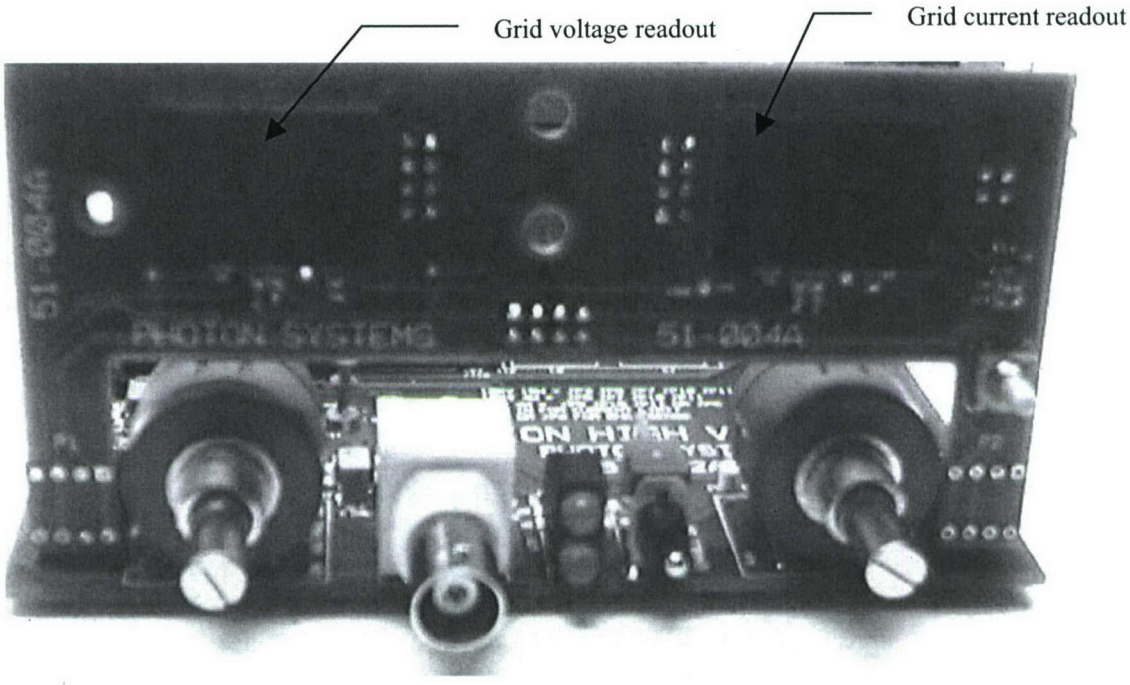

Figure 23. High voltage grid control power supply with voltage and current display circuit board attached

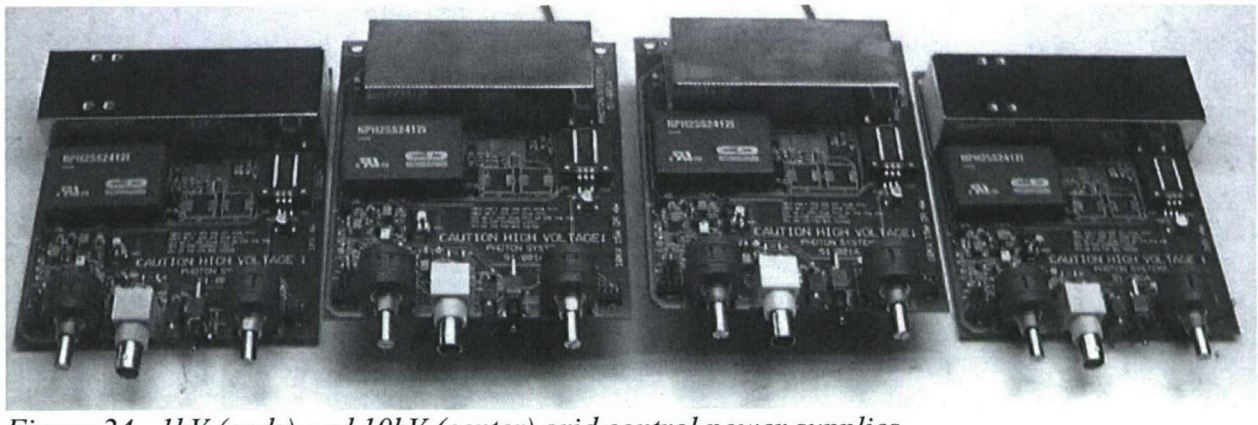

Figure 24. 1kV (ends) and 10kV (center) grid control power supplies

These grid control power supplies will be mounted in a chassis with three on either side, each including the voltage and current readout. This chassis is being built presently.

The procedures for setting up this ebeam controller will be similar to that give previously, but an update will be provided soon to take account of differences in the new controller.

Status of pulsed slit beam CL instrument

The first of the new high frequency slit electron guns and electron beam controllers (EBCs) was completed this month. A photo of the front panel is shown in Fig. 25 below.
The EBC provides voltages to various grids to control the shape of the electron beam on the target. It is desired to minimize the leakage current to any of the grids except the anode, which is the AlGaN target electrode, since any leakage reduces the maximum 1mA cathode emission.

The EBC front panel is divided into six sectors. Sectors 1 through 5 are identical in appearance, and offer control for the following:
Sector 1: G3/G5 power supply (einseln lens for beam collimation), nominally set at target voltage.
Sector 2: G6 -- slit beam focusing grid (voltage TBD)
Sector 3: Target (Anode), nominally at 5kV with a range from 3kV to 10kV.
Sector 4: G4 -- focus grid, nominally 400V
Sector 5: G2 -- focus grid, nominally 80 V
Sector 6: G1 (extraction grid) and filament voltage control as well as pulse width and pulse repetition rate. In addition, controls for Manual Firing (single shot) and Repetitive pulsing as well as CW (DC) and pulsed are also in this section. The filament control allows for activation and normal operation of the filament. Under normal operation the filament runs at 13.9V. Filament activation is done under the "Boost" setting at 22.5V and 24V according to a schedule given later. The extraction grid voltage, G1, controls ebeam current. G1= -35V provides extinction of the ebeam and G1= +5 provides maximum beam current. The displays in Sector 6 are for Filament Voltage (left) and G1 voltage (right).

Sectors 1 through 5 above are similar in appearance. Each section has a voltage and current display. The voltage displays are in kilovolts with the smallest reading of 1V. The current displays are in milliamps with the smallest reading of 1 microamp. Again, the goal of setting up the controller is to minimize the "leakage" current to any grid except the "anode" or "target".

The maximum voltages are 10kV on Sectors 1, 2 and 3, and 1kV on Sectors 4 and 5. Maximum currents are about 1mA. There are two potentiometers, a voltage and current pot for each sector. The voltage pot sets the grid voltage. The current pot sets the limit current for each sector power supply. To the upper right of each limit current pot is a white button. Pressing this button allows the "current limit setting" to be displayed. Otherwise the display shows the actual grid current when operating in CW or DC mode. During pulse operation, grid currents need to be measured using an oscilloscope. Each sector also has an on/off switch. The sector power supply is "off" when the toggle switch is "down". In the down position, the 2 LEDs to the left of the switch are green, showing they are "safe". In the "up" or "enable" switch position, the LEDs turn red, indicating that the power supplies are "on" or "hot". Use extreme caution is you see any "red" LEDs lit up since high voltage is being transmitted through the cable to the electron gun assembly in your vacuum system. Each section also has a BNC connector for reading the "leakage" current to each grid. The **BNC is calibrated to 1 volt per mA** of current.

This controller contains high voltage and high current power supplies and is very, very dangerous. Extreme caution is recommended.

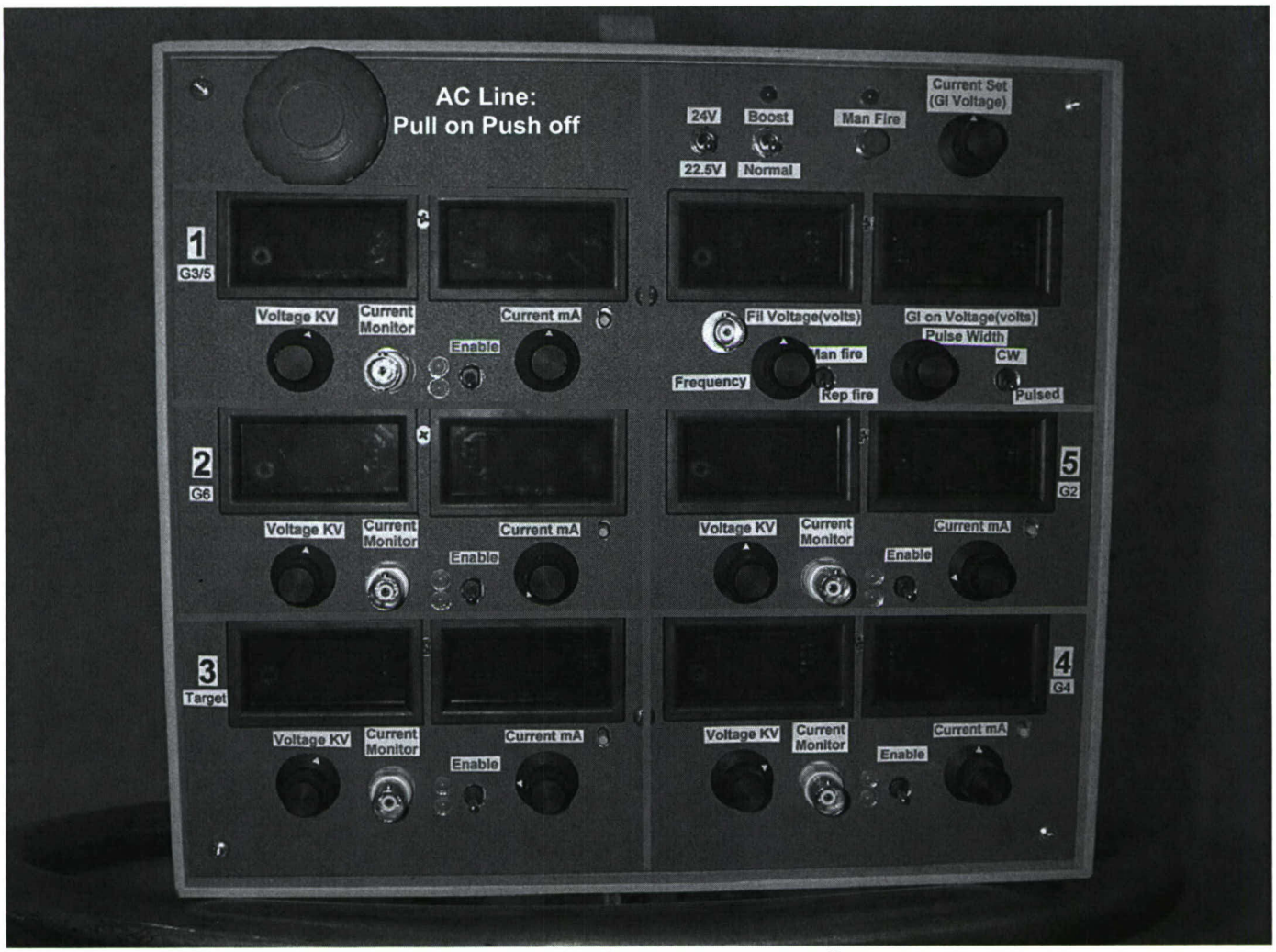

Figure 25. Photo of new high frequency slit electron gun controller

This controller contains high voltage and high current power supplies and is very, very dangerous. Extreme caution is recommended.

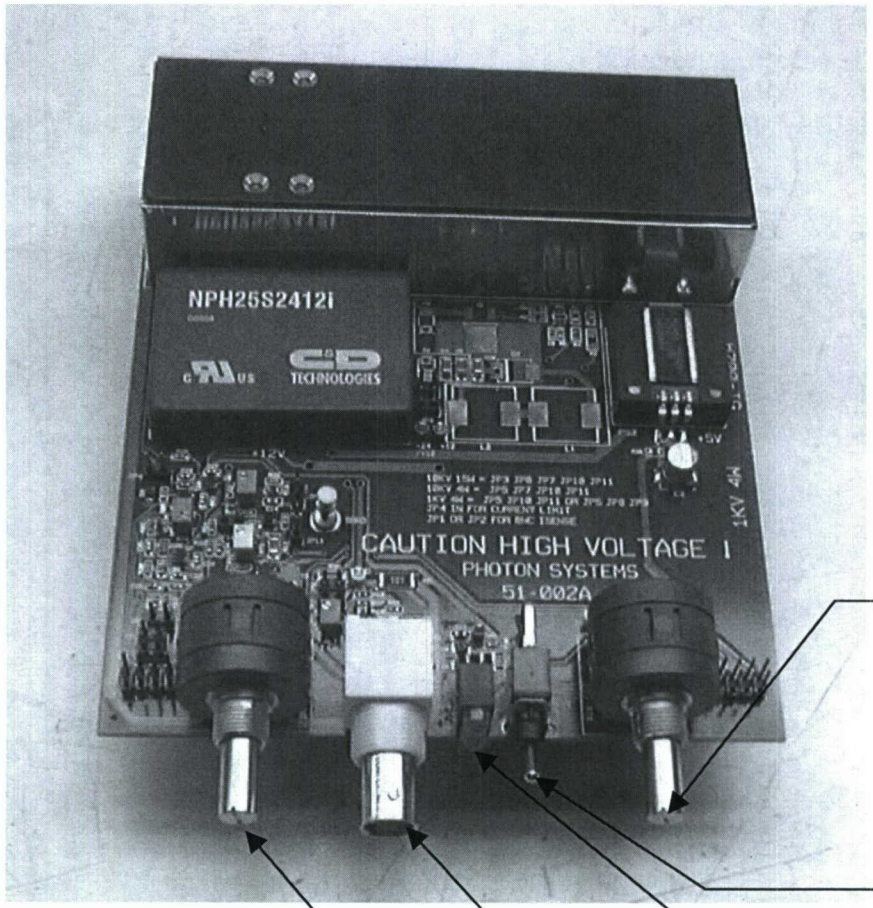

Figure 26. High voltage grid control power supply photo

A typical high voltage controller is shown above in Fig. 26.

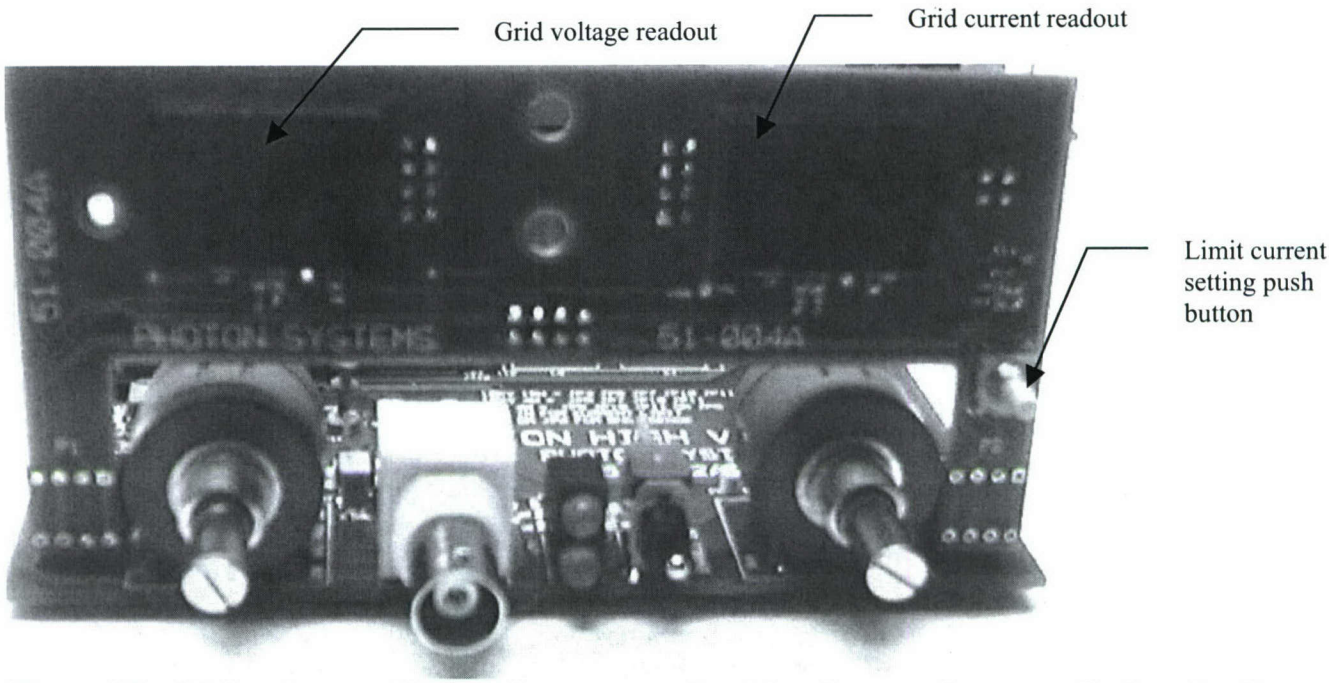

Figure 27. High voltage grid control power supply with voltage and current display circuit board attached

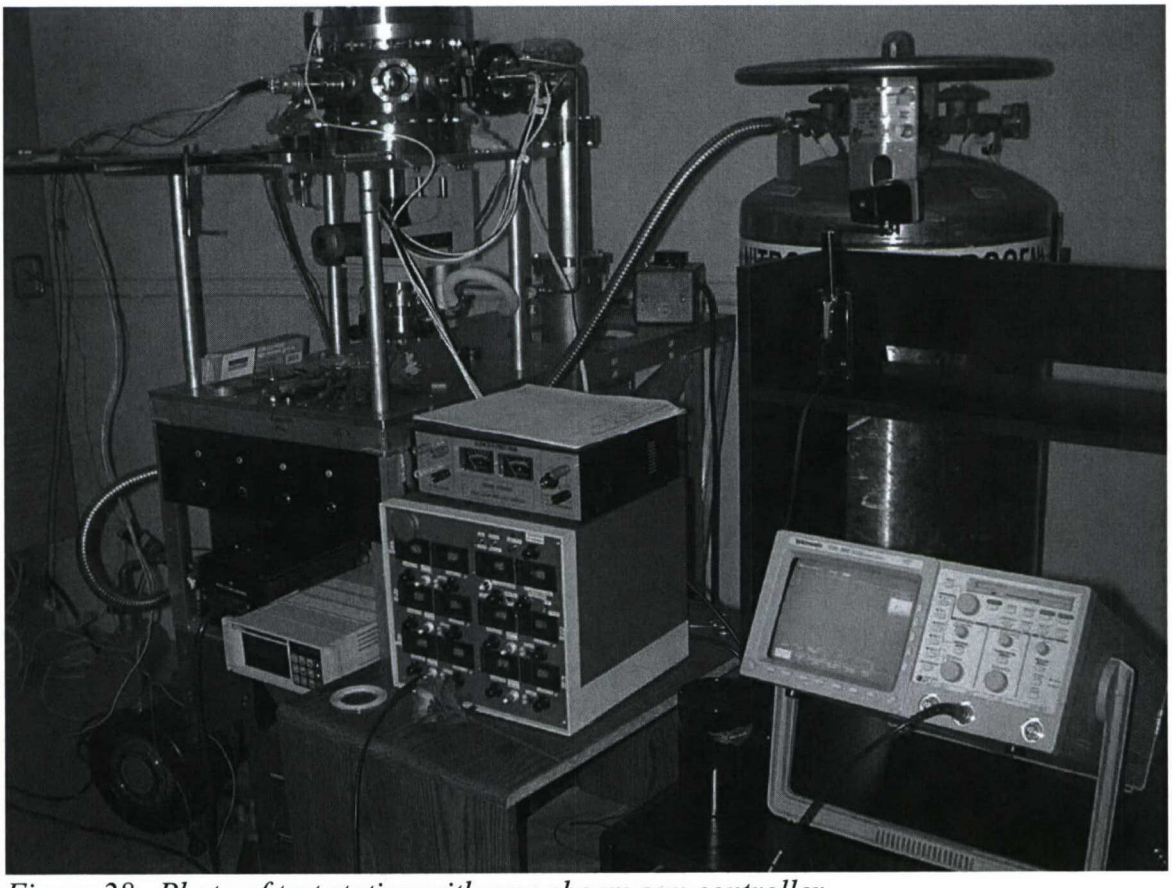

Figure 28. Photo of test station with new ebeam gun controller

First Startup Settings for Controller

Before plugging in the EBC into the AC line, make sure of the following settings. Make sure the large Red ON/OFF button is in the off (in) position. Make sure all power supplies are in the OFF or toggle switch down position and voltage knobs to minimum (full CCW). In Sector 6, set the filament to "normal", G1 voltage knob to minimum (full CCW). Set toggle switches to "Rep Fire" and "CW".

Filament Activation

With the settings as described above, filament activation is performed as follows:

1. Plug in the AC line cord.
2. Turn on the AC power by pulling out the large red button. The filament voltage display in Sector 6 should read 13.9V. The filament will heat up and begin to outgas binder materials. Allow this to proceed until your vacuum system has recovered to better than 10^{-6} Torr.
3. Switch the filament to the "Boost" position with boost voltage at 24V for 2 minutes.
4. Switch boost voltage to 22.5V for 8 minutes with G1 and G2 at 0 Volts.
5. With boost voltage still at 22.5V, set G1 = +15V, G2 = 0V, I max = 20mA max for 18 minutes.
6. Reset G1=0V, G2 = +400V for 8 minutes
7. Turn off G1 and G2 for cool down
8. Return filament voltage to normal, a 13.9V.

Initial Settings

Set the initial grid voltages in sequence to the following settings.

Grid	Old VDC range	New VDC range	Initial values
K	0	0	0
G1 (extraction grid)	-50 to +5	-50 to +5	-25
G2 (focus grid)	0 to 500	0 to 500	355
G3/G5 (einseln lens)	0 to 500	0 to 10kV	5kV
G4 (focus grid)	0 to 500	0 to 1kV	70
G6 (slit grid)	0 to 500	0 to 10kV	5kV
Anode (AlGaN target)	0 to 10kV	0 to 10kV	5kV

Following are some examples to illustrate the electron beam shape resulting from alteration of various grid voltages. Note that G6, which forms the slit beam, is not present in the following simulations. The following simulations are for a round electron beam only.

Figure 29, 1-3 (below). Variation of Anode/G3/G5: Increasing anode voltage produces smaller beam on target

1) Anode/G3/G5 = 1kV

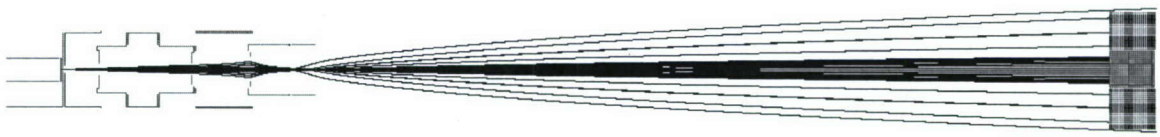

2) Anode/G3/G5 = 5kV

3) Anode/G3/G5 = 10kV

Figure 30, 1-5 (below). Variation of G1: Higher G1 voltage produces larger current extraction. Extinction occurs below about –30V. +3V corresponds to about 1mA of beam current

1) G1=-20V

2) G1 = -15V

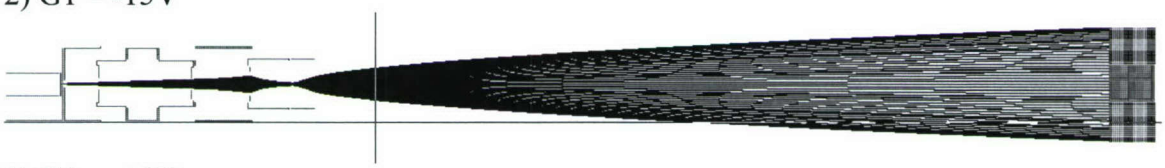

3) G1 = -10V

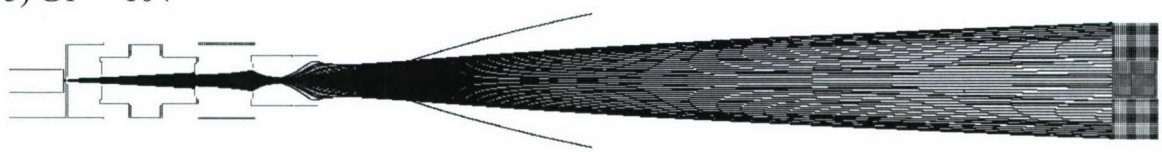

4) G1 = -5V

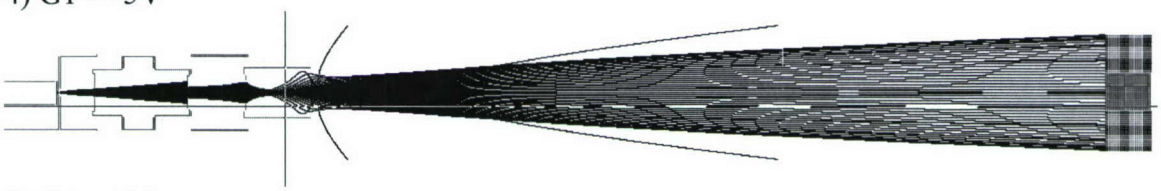

5) G1 = 0V

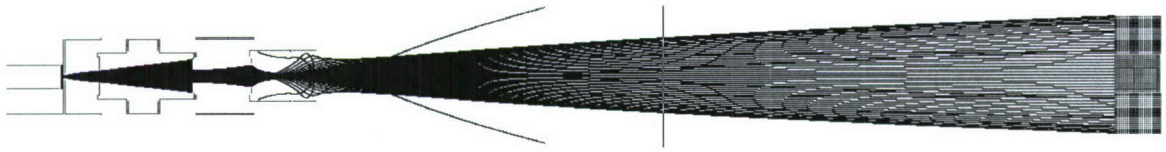

Figure 31, 1-6 (below). Variation of G2 Voltage: Optimum G2 voltage is about 355V

1) G1 = 10kV

2) G2 = 1000V

3) G2 = 500V

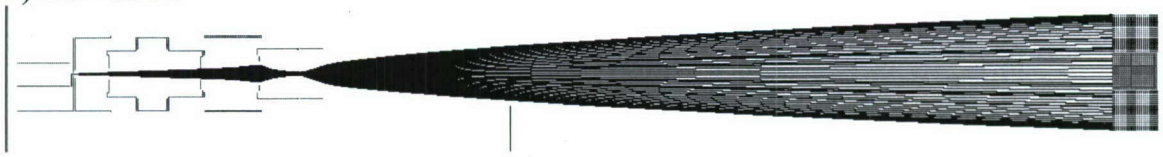

4) G2 = 385V

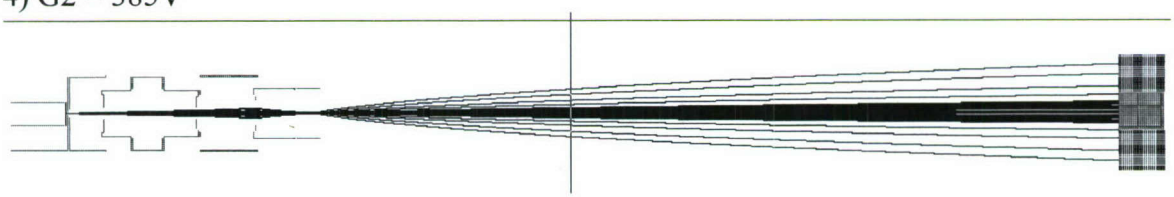

5) G2 = 355V

6) G2 = 350V

Gets cutoff at G2 = 345V

Figure 32, 1-4 (below). Variation of G4 Voltage: G4 voltage has little effect. This is also true of G3/G5.

1) G4=70V

2) G4=100V

3) G4=1000V

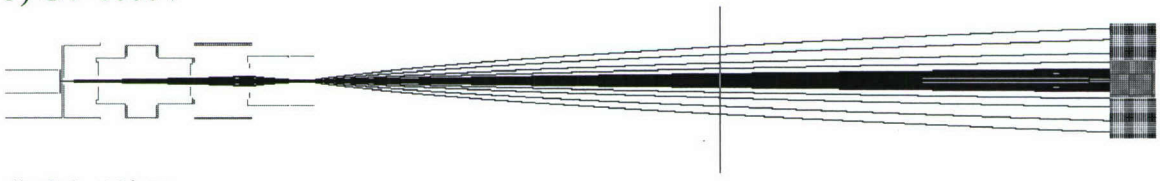

4) G4=10kV

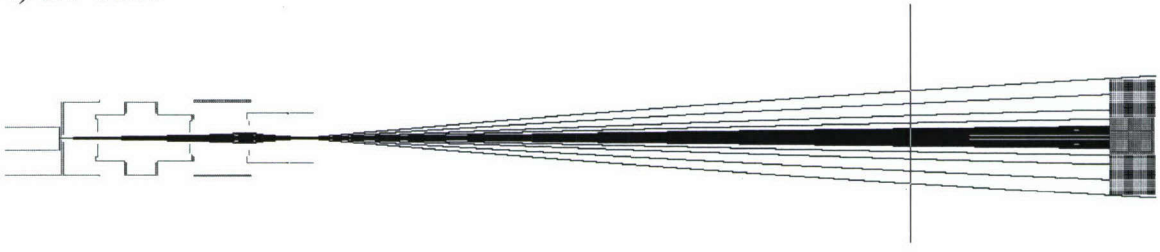

As illustrated above, the extraction and focusing of electrons from the cathode by G1 and G2 form the core of the electron gun. Figure 8, below, shows the iso-potential lines in the regions of the cathode, G1 and G2. The spacing between the cathode, G1, and G2 are 100μm, or about 0.004". The cathode is at ground potential and the beam current increases as G1 is increased from extinction below about –35V to about 1mA at +5V. Electron beam focus varies as G2 is varied. At G2 = 385V the beam has a focus near the exit of G5 and gradually spreads to the anode target. We have not yet added the slit lens grid, G6, to develop the focus at the anode.

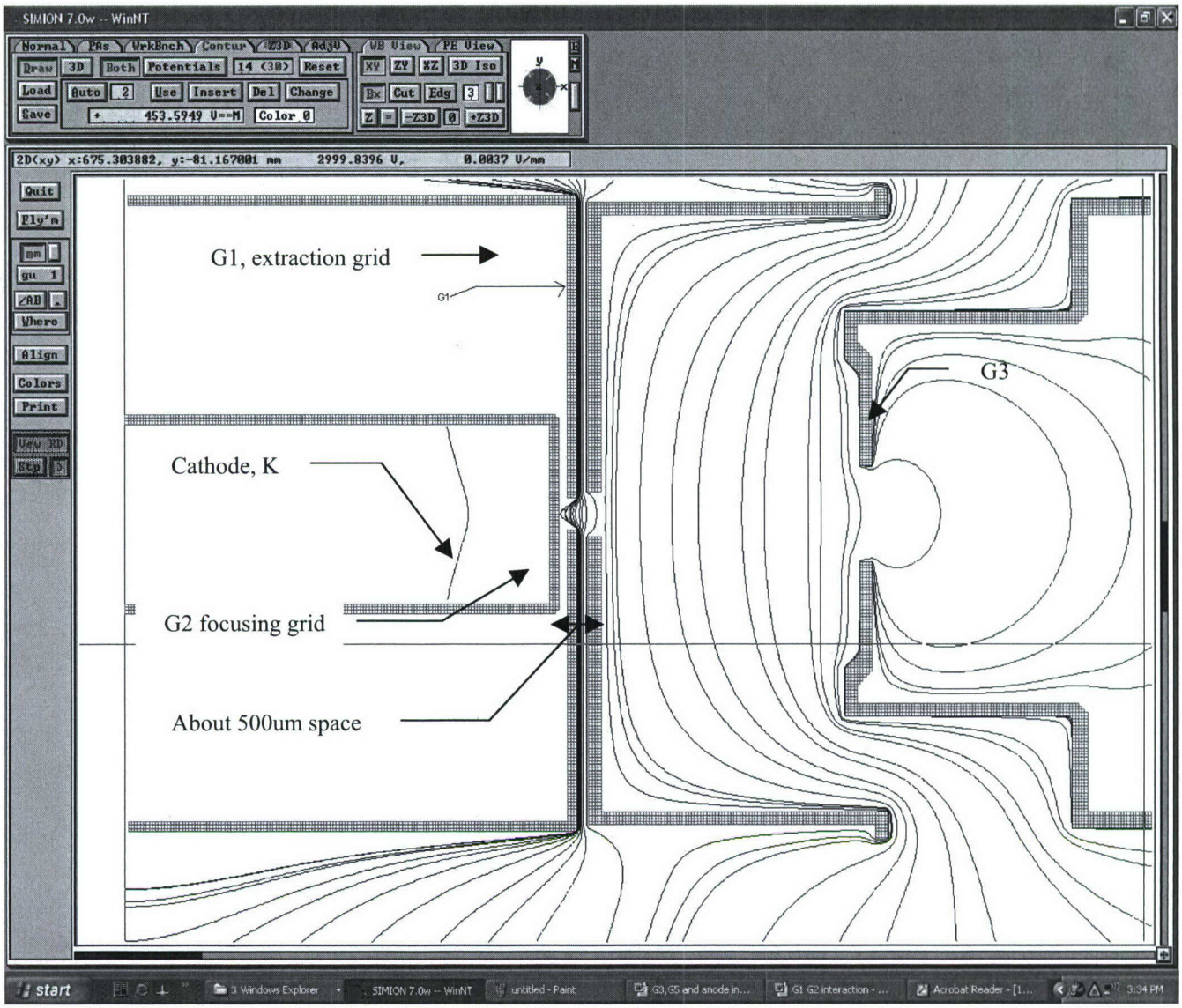

Figure 33. Iso-potential lines in vicinity of cathode, G1 and G2

E-Gun installation and operation instructions

A. ASSEMBLY

Below is a photo of the electron gun components including the hermetic feedthrough with teflon mating adapter socket, gun assy including the cathode and G1 through G5, 19mm glass sleeve, a Makor G6 mount, G6 slit grid, and the G6 lead wire.

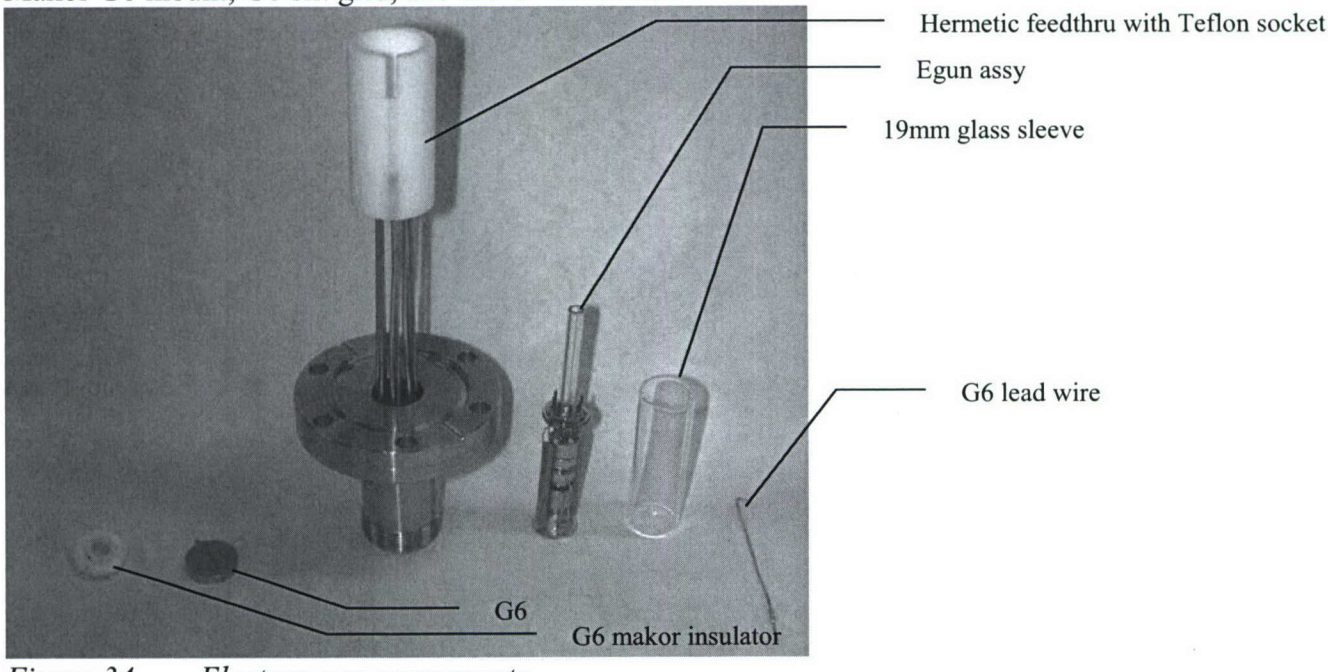

Figure 34. Electron gun components

The assembly is shown below in Fig. 35.

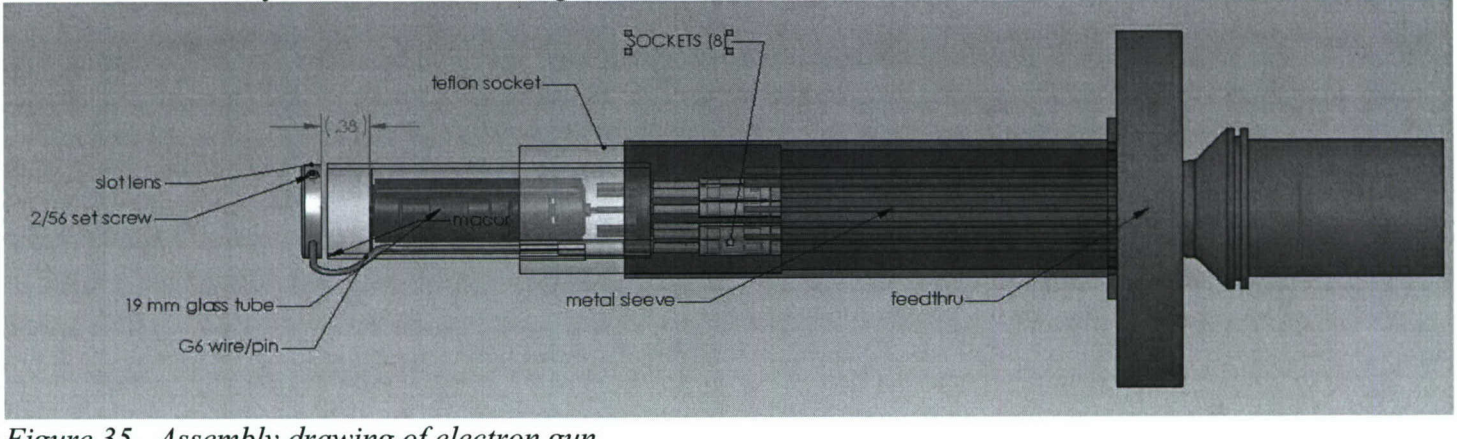

Figure 35. Assembly drawing of electron gun

A1. CLEAN ALL PARTS (EXCEPT E-GUN) TO REMOVE FINGER OILS, ETC.
A2. INSTALL TUBE SOCKET ONTO FEEDTHRU PINS (WEAR FINGERCOTS)
NOTE: (clip off center 2 leads so they do not short to the outside pins)
A3. INSTALL SST TUBE OVER SOKET ONTO FEEDTHRU BASE WITH 2-56 SOCKET HEAD SCREWS (make sure slots are aligned)
A4. INSTALL EGUN INTO SOCKET (NOTE PIN GAP ALIGNMENT.

NOTE: (engage pins into sockets by pushing down on the glass base with a probe (see picture))

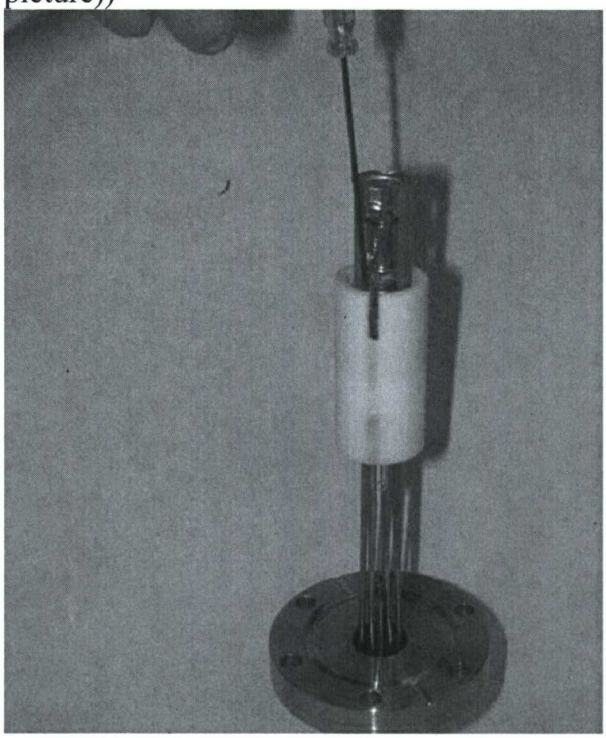

Figure 36. Photo of seating of electron gun in socket

A5.PUSH GLASS TUBE DOWN TO BOTTOM OF SOCKET.
A6. INSTALL MACOR CAP AND G6 CAP (IF USED)
NOTE: (lightly tighten 2-56 set screw onto macor endcap
A7.INSTALL G6 WIRE INTO SOCKET AND WIRE INTO G6 (PUSH FIT)
A8.INSTALL FEEDTHRU BASE ONTO ROTARY PORT WITH Cu GASKET
NOTE: (make sure long edge of G-6 slot is parallel to bottom of chamber)
A9.INSTALL THERMOCOLLER ASS'Y (WITH DIE) ONTO COOLING POST.
A10. HOOKUP:

a) thermocooler wires (watch polarity)
b) HV lead push into hole in cu mount
c) Fiber optic from feedthru to side of die (1/4-1/2")

A11. PUMP SYSTEM DOWN AND CHECK FOR LEAKS
A12. WHILE LOOKING THRU BACK VIEWPORT, ALIGN DIE TO CENTER OF GUN (APPROX)
A13. HOOKUP H.V. P.S. WIRES TO FEEDTHRU PER SKETCH
NOTE: (make sure sleeving is pushed down to the bottom of each feedthru pin)

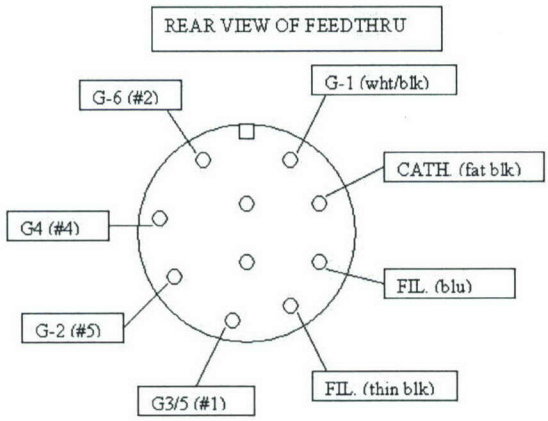

Figure 37. Hermetic feedthru pin designations

B. OPERATION

This controller contains high voltage and high current power supplies and is very, very dangerous. Extreme caution is recommended.

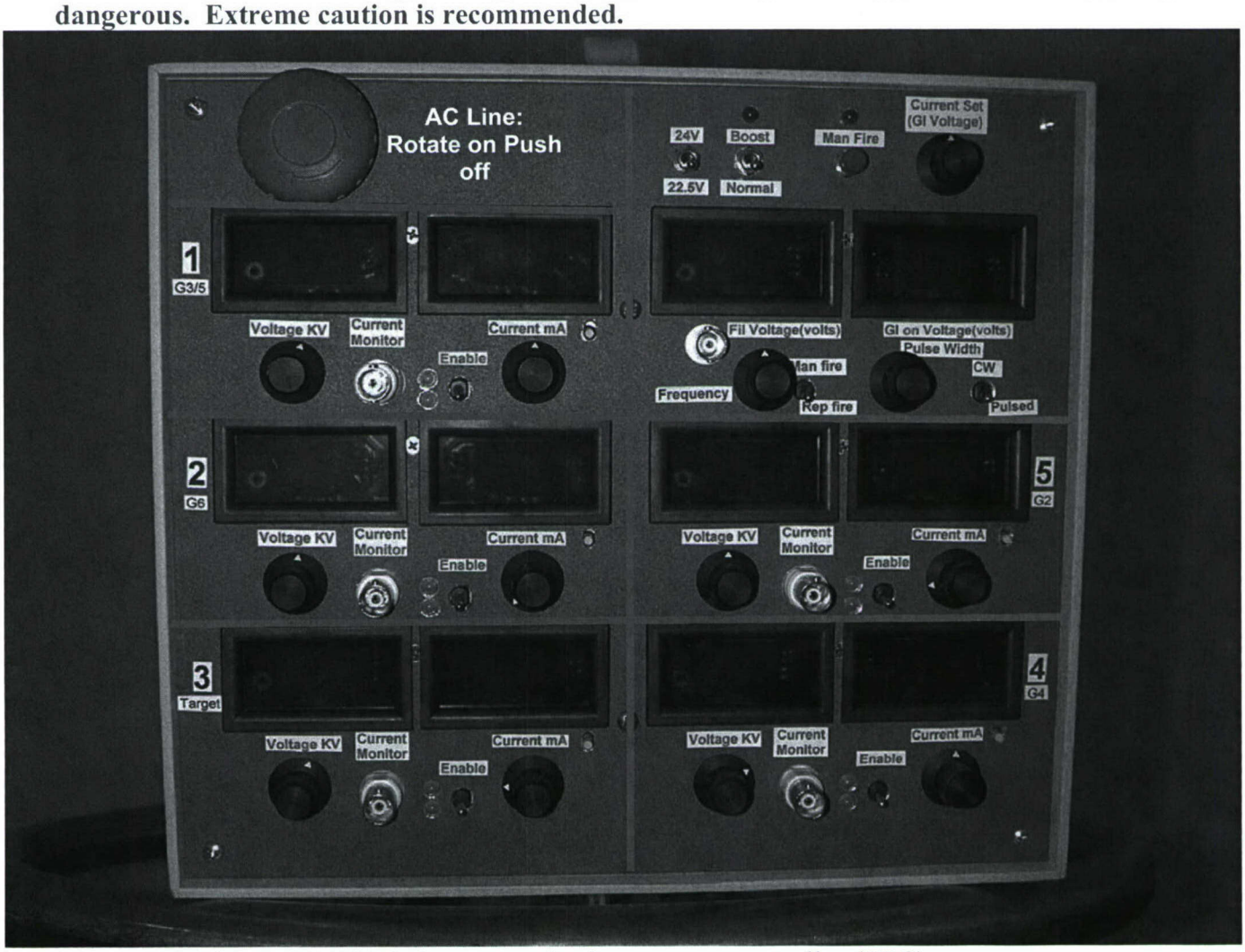

Figure 38. Photo of new high frequency slit electron gun controller (EBC)

This controller contains high voltage and high current power supplies and is very, very dangerous. Extreme caution is recommended.

Sectors 1 through 5 above are similar in appearance. Each section has a voltage and current display. The voltage displays are in kilovolts with the smallest reading of 1V. The current displays are in milliamps with the smallest reading of 1 microamp. Again, the goal of setting up the controller is to minimize the "leakage" current to any grid except the "anode" or "target".

The EBC front panel is divided into six sectors. Sectors 1 through 5 are identical in appearance, and offer control for the following:
Sector 1: G3/G5 power supply (einseln lens for beam collimation), nominally set at target voltage.
Sector 2: G6 -- slit beam focusing grid (voltage TBD)
Sector 3: Target (Anode), nominally at 5kV with a range from 3kV to 10kV.
Sector 4: G4 -- focus grid, nominally 400V
Sector 5: G2 -- focus grid, nominally 80 V
Sector 6: G1 (extraction grid) and filament voltage control as well as pulse width and pulse repetition rate. In addition, controls for Manual Firing (single shot) and Repetitive pulsing as well as CW (DC) and pulsed are also in this section. The filament control allows for activation and normal operation of the filament. Under normal operation the filament runs at 13.9V. Filament activation is done under the "Boost" setting at 22.5V and 24V according to a schedule given later. The extraction grid voltage, G1, controls ebeam current. G1= -35V provides extinction of the ebeam and G1= +5 provides maximum beam current. The displays in Sector 6 are for Filament Voltage (left) and G1 voltage (right).

B1. FILAMENT ACTIVATION.

NOTE: (vacuum should be <1.0 E–6 Torr)
NOTE: set all enables to off (down),
all current sets to max(clockwise)
Set G-1 to low (counter clockwise)
set pulser to CW,
set filament voltage: normal, 13.9V
make sure Filament and HV connectors(back) are tight

a) TURN ON P.S. (red button clockwise).
b) Filament: normal---------- 1min
c) Filament: Boost ---------- 2min
d) Filament: Boost ,G1=0,G2=0---------- 10min
e) Filament: Boost ,G1=+3.8V,G2=0--------- 20min
f) Filament: Boost ,G1=-0.7,G2=400--------- 10min
g) Filament: Boost ,G1=-0.7,G2=0---------- 2min
h) Filament: Normal ,G1=-0.7,G2=0---------- 2min
i) PS : off

NOTE: When you first activate you should notice water vapor, CO,CO2,H2 as byproducts if you use a mass spectrograph or residual gas analyzer on your vacuum system.

B2. GUN OPERATION (NO G-6)

NOTE: (ocassionaly the beam will "fade out", just switch filament to normal for 10 sec., then back to boost)

a) TURN ON P.S. AND SET FILAMENT TO BOOST.
b) SET G-1 TO -16V,REP FIRE,CW,COAX TO SCOPE,ROTATE KNOBS CLOCKWISE. (LATER you will set to 100hz,10us)
c) ENABLE G2 235V (1KV MAX)
d) ENABLEG4 274V (1KV MAX)
e) ENABLE G3/5 4.0KV (10KV M)
f) ENABLE TARGET 5.0KV (10KV MAX)
g) SLOWLY TURN UP G-1 TO 0V AND WATCH FOR EBEAM GLOW NEAR OR ON THE DIE (may need to dim lights)
h) ADJUST THE VERTICAL AND GROSS FEEDS TO ADJUST LOCATION OF THE E-BEAM ON THE DIE.
i) G3/5 WILL PRODUCE MORE TARGET CURRENT BUT WILL SPREAD AND MOVE THE BEAM.
j) ADJUST G-4 TO REFOCUS THE BEAM
k) G2 ADDS MORE CURRENT BUT SPREADS THE BEAM (refocus the beam with G3/5-G4)
l) TO SHUT OFF, SHUT OFF TARGET SWITCH, THEN G-3/5, G-4, G-2, FILAMENT TO NORMAL, PUSH RED BUTTON.

C. EBEAM PULSE CURRENT MONITORING: SCOPE SET-UP

CURRENT PULSE CALIBRATION (1mV/ua)
WITH A DUAL CHANNEL SCOPE CAN SET UP TARGET CURRENT CHANNEL WITH THE G-1 PULSE CHANNEL (g-1 modulates the electron flow)

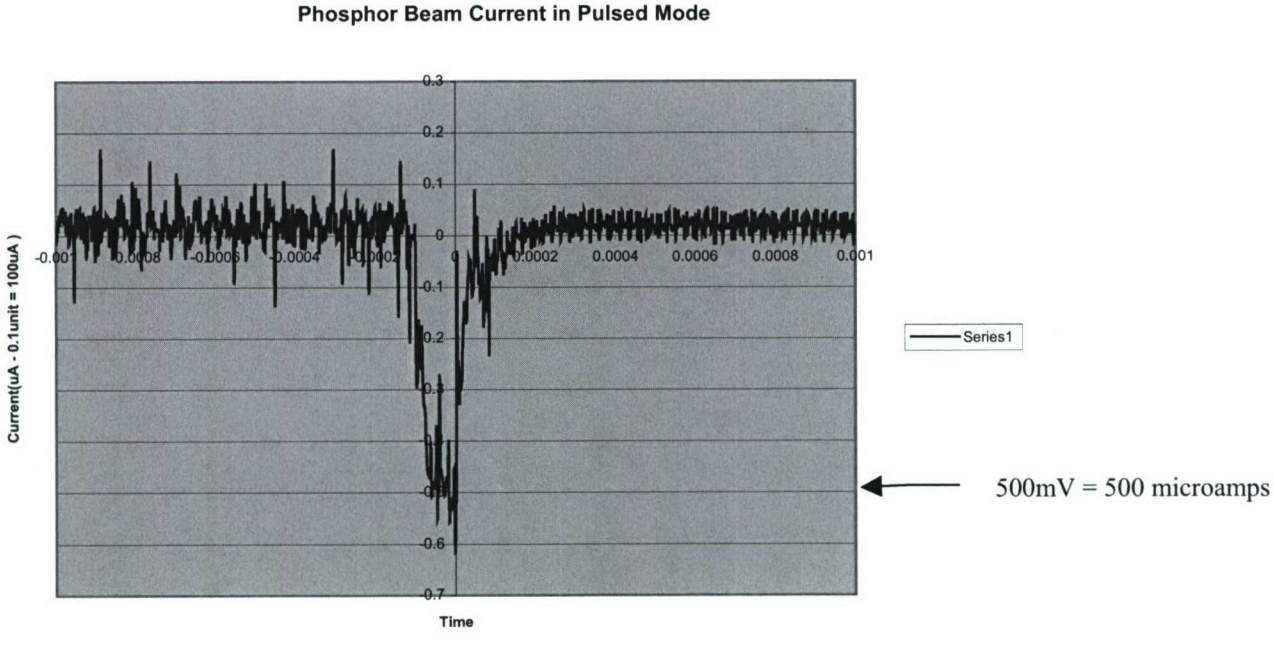

Figure 39. Oscillogram of target current pulse

D. Target Setup and Cooling

We have found that the best arrangement for initial alignment is to have wide area AlGaN target above, but in the same plane as, the AlGaN die bar target. The transmissive AlGaN target is needed for initially locating the electron beam and making sure it is where you think it is. With the die bar directly below you can simply move the die bar vertically into position.

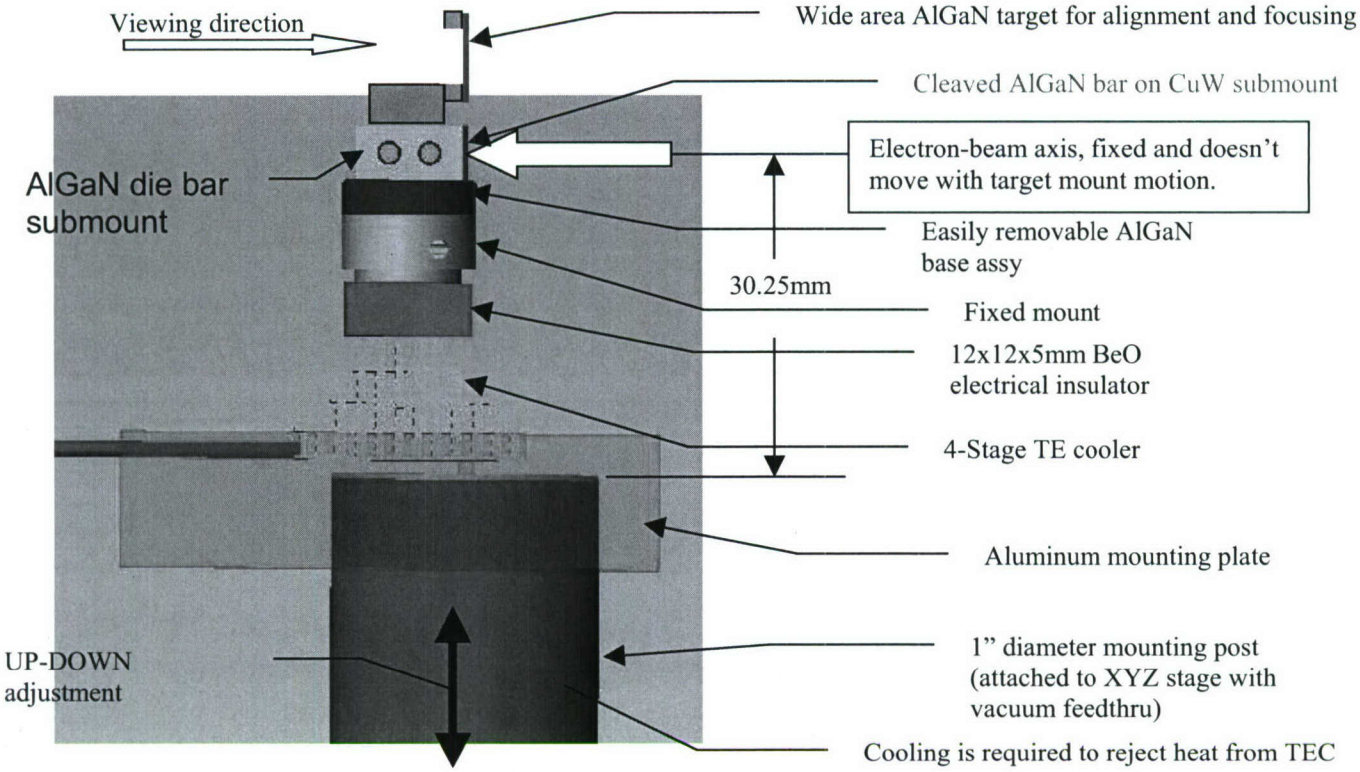

Figure 40. Die mounting assembly with cooling (laser axis out of page)

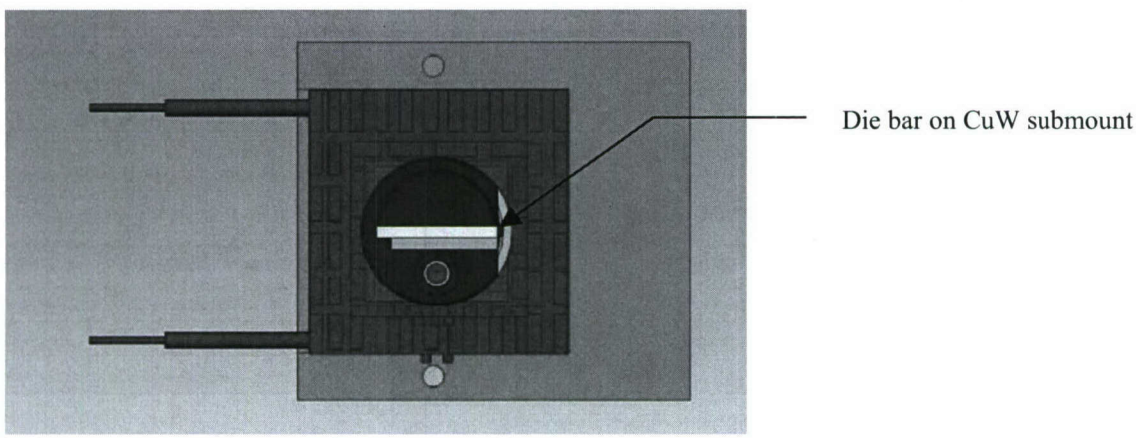

Figure 41. Top view of die bar mounting

E. Emission spectra examples from transmissive sample, BU1452

IMAGE 2 FIL. 22.5V, G1 0V, G2 313V, G3/5 2.6KV, G4 10V, G6 2.8KV, TAR 5.36KV

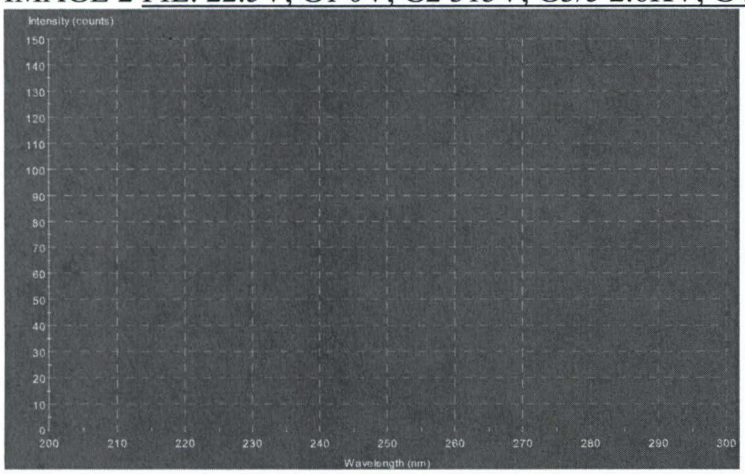

Note CL changes with Target Voltage as the mean penetration distance increases

IMAGE 3 FIL. 22.5V, G1 0V, G2 313V, G3/5 2.6KV, G4 10V, G6 2.8KV, TAR 8.0KV

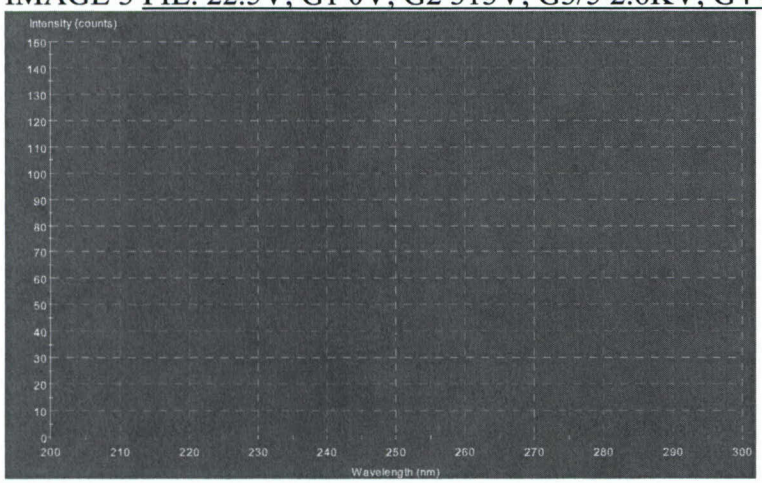

IMAGE 4 FIL 22.5V, G1 0V, G2 313V, G3/5 2.6KV, G4 10V, G6 2.8KV, TAR 10 KV

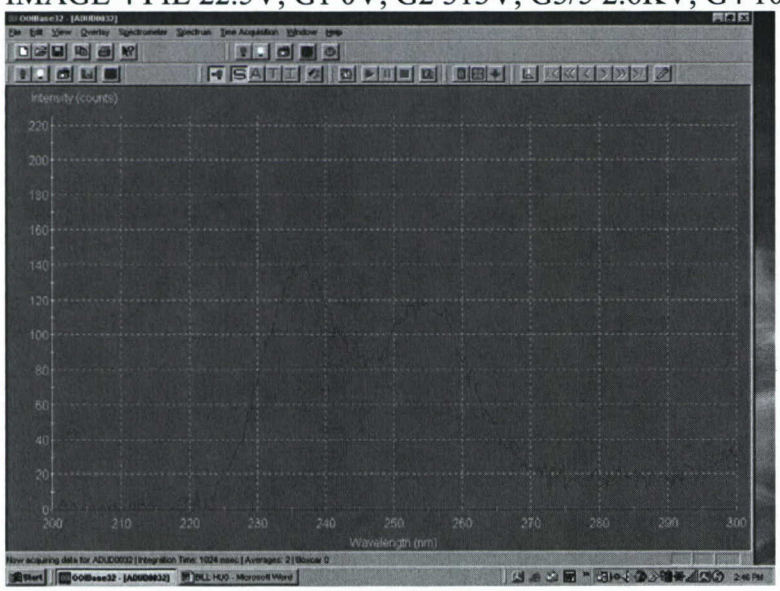

Figure 42. CL spectra of BU1452 at various target voltages, i.e. penetration depths

Status of miniature electron beam pumped source development

We have begun modeling miniature ebeam pumped devices with dimensions on the order of a few millimeters in size, without the vacuum envelope. Including the vacuum envelope the size will be in the order of one or two cubic centimeters. The devices being modeled include edge emitting laser triodes (EELTs), vertical cavity surface emitting laser triodes (VCSELTs), and light emitting triodes (LETs) employing either thermionic or field emission electron sources. We are looking at thermionic sources since they are readily available and do not require development. Modeling of a miniature EELT that has a thermionic electron source is shown below for the narrow focus direction. The overall length from cathode to AlGaN target is 2.2 mm. Laterial focus is less than a few μm in this model. In the other axis, the electron beam has a width about 750 μm, corresponding to the cavity spacing of the AlGaN die.

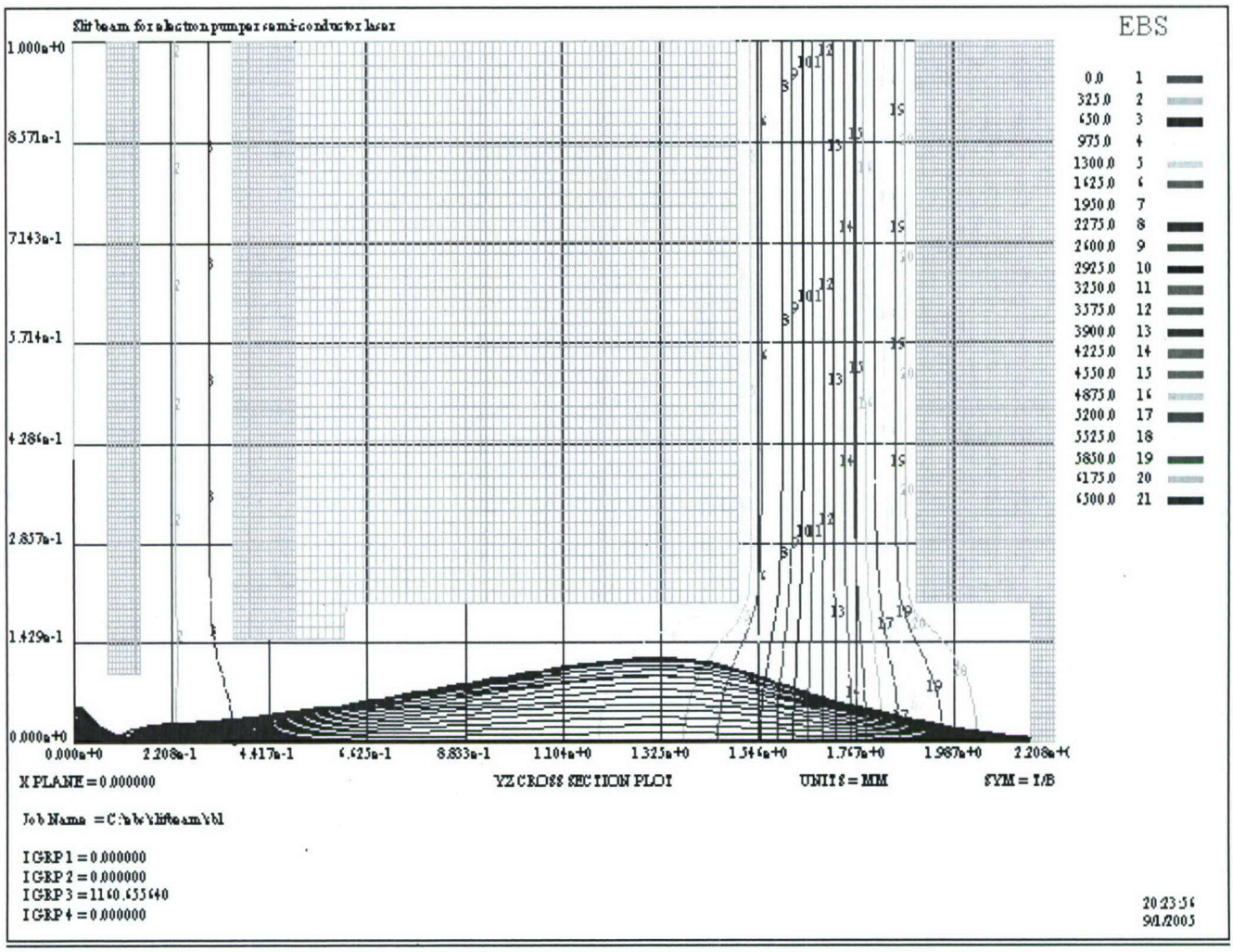

Figure 43. Lateral electron beam profile of miniature, 2.2mm thermionic electron gun assembly for EELT

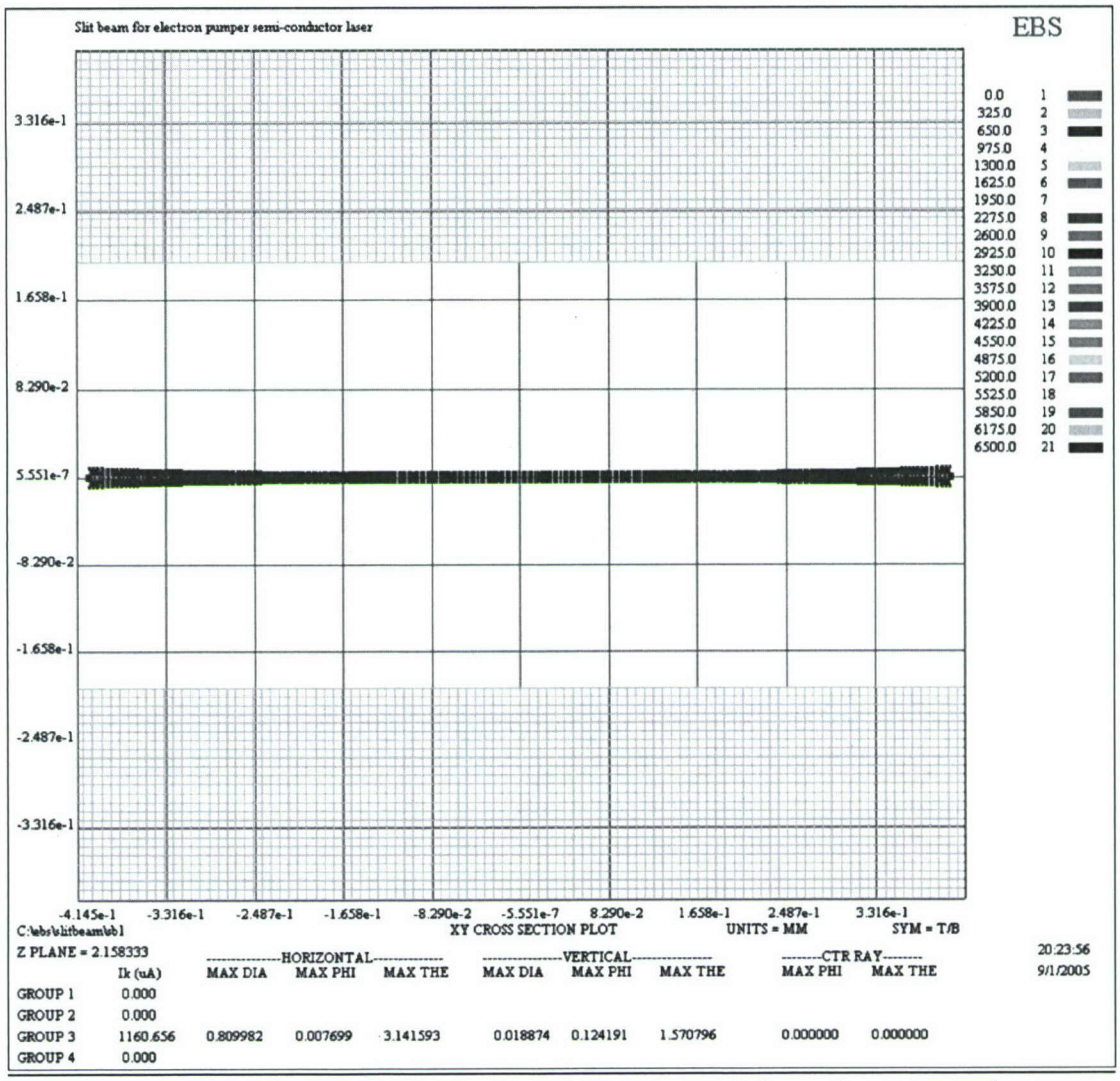

Figure 44. End-on electron beam profile of miniature, 2.2mm thermionic electron gun assembly for EELT

The end-on electron beam distribution is shown above in Fig. 44 where the beam spread in the lateral direction is less than a few micrometers and the uniformity along the long optical cavity axis is excellent.

Laboratory ebeam system status

The redesigned and rebuilt laboratory ebeam systems have finally been shipped to our collaborators at Boston University and Astralux last month. We also expect to ship a third ebeam system to Dr. Mike Wrabach at Army Research Labs in the future.

There were many more issues than anticipated both from the point of view of theoretical performance of the instrument, but also related to detailed debugging issues related to internal electromagnetic interference and related instrument operation issues. We are still working to optimize the forming of the ebeam to the desired characteristics. An photograph of the ebeam on an AlGaN die bar is shown if Fig. 45, below. The beam conditions for Fig. 45 were: Filament

Voltage – 24V (Boost); G1 = -0.4V; G2 = 332V; G3 = G5 = 6300V; G4 = 0V; G6 = 1.86kV; Target = 5kV. Target current was 500uA. Distance from G6 to target is about 19mm. In Fig. 1 we have outlined the die bar in red. The photo was taken at an oblique angle with the electron gun on the right. The visible wavelength CL is shown as an angled stripe with the width being the width of the AlGaN bar, about 750um, and the height estimated to be less than 75um. The height is estimated based on the 750um width, where the height appears to be less than 10% of the width. The current density on the target at these settings is about 0.9A/cm^2. This current density measurement is based on observation of visible light emission from the AlGaN target. We are actually measuring emission from subbands and/or impurities. In addition, the video image is clearly saturated in the ebeam image area. The sum of all of these effects is that the beam dimensions as measured here are expected to be large exaggeration of the actual electron beam dimensions, because of lateral spreading of the visible light in the target. The spread is expected to be a fixed value so that it will affect the height (small dimension) greater than the width. We believe the actual current density could be 5 to 10 times greater than the values estimated here using imaging in visible light.

Figure 46 is a photograph of a frontal view of the electron beam where the camera is imaging the back of an AlGaN segment about 4mm by 4mm. The setup was made to view the ebeam shape without distortions based on observation perspective. The AlGaN target was only a few mm in front of the G6 slit grid. We have found that we need a voltage on G4 lower than zero in order to more fully focus the beam in both vertical and horizontal directions. We are presently modifying our in-house ebeam controller to provide negative voltages on this grid. If successful, we will retrofit the ebeam guns at our collaborators facilities.

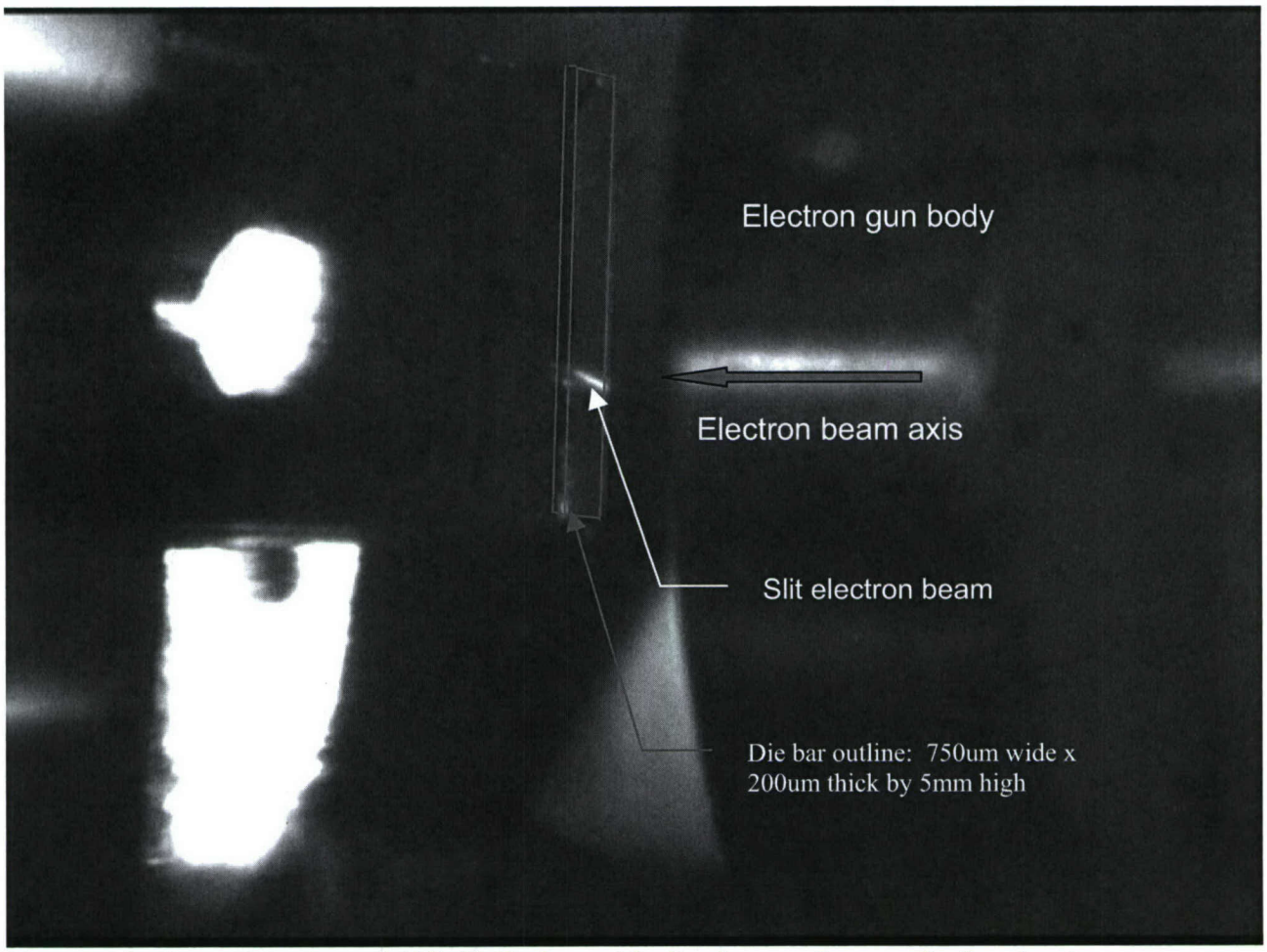

Figure 45. Isometric view of AlGaN die bar with slit electron beam. Peak pulse beam current about 600uA into a 750um x 75um electron beam at the AlGaN target

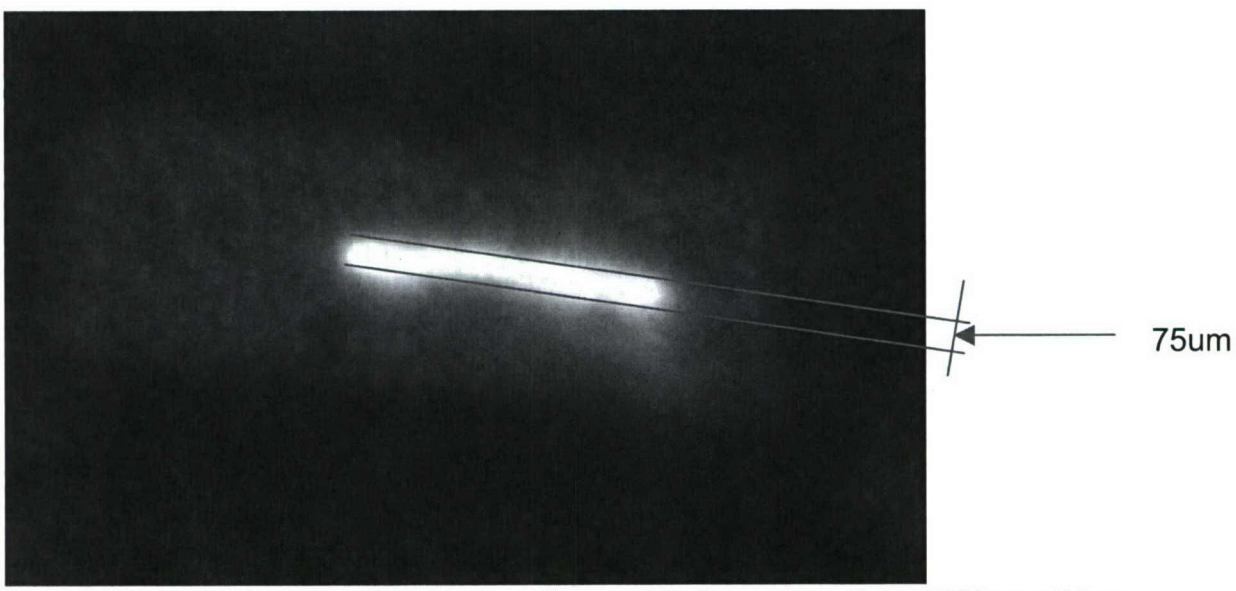

Figure 46. Frontal image of slit electron beam with dimensions about 1150um x 75um

The beam conditions for Fig. 46 were: Filament Voltage – 24V (Boost); G1 = -0.7V; G2 = 550V; G3 = G5 = 5400V; (IG3 = 550uA) G4 = 0V; G6 = 3.77kV; Target = 5.5kV. Target current was 600uA. Target distance from G6 to target was about 6mm. We expect to be able to reduce the leakage current on G3/G5 by making G4 go negative. This should enable substantially over 1mA of target current, corresponding to a current density from 1.5 to over 2.5 A/cm^2. Also, these values do not account for the lateral spreading of observed visible emission and the actual delivered current densities could be much higher than estimated above.

Earlier in this program we measured strong simulated emission at a beam current density below $10A/cm^2$ on bulk AlGaN with about 74% aluminum operating at 100^0K with no resonator facets. We could already be near this level of ebeam current density. We are awaiting delivery from Astralux of mounted AlGaN die bars with high reflectivity facet coatings to begin laser tests. We are also attempting to increase the delivered beam current density by up to factor of 10 above present levels. We will also attempt to make more quantitative measurements of the actual ebeam dimensions.

We are attempting to obtain the best correlation between theoretical modeling and empirical measurements of the electron beam characteristics. This is important to enable optimization of the laboratory CL instrument as well as to assist in the design of the miniature electron beam source to be employed in the eventual ESUVOS device. We are using two theoretical modeling programs: Simion 7.0 and EBS.

Description of EBS simulations:
Using the EBS electron beam simulation software we have completed 5 simulations relating to the Clinton DM2001 einzel electron gun used to energize a semiconductor laser. The purpose of this work is to characterize the electron beam in its current form and to suggest easy changes that can improve performance by reducing spot size and increasing current density at the target.

Description of simulations:
1. Standard target position at Z =4.325", VG3 = 6kV, no G6 grid
2. Standard target position at Z =4.325", VG3 = 6kV, with G6 grid
3. Standard target position at Z =4.325", VG3 = 12kV, with G6 grid
4. Short target position at Z =2.135", VG3 = 6kV, with G6 grid
5. Short target position at Z =2.135", VG3 = 12kV, with G6 grid

All jobs were computed using the EBS left/right symmetry model in two connected jobs. The beam forming region job extends from cathode surface to about 0.1" inside the G3 where the electric field has reduced to near zero. The connecting lens job extends from 0.1 inch inside the G3 to just beyond the target. The target consists of a vertical stack of basic rectangular and cylindrical shapes from the WCu die mount down to the copper mount. The entire target and beam shield are set at G5 potential. Focus voltages are generally set for smallest vertical dimension just short of the target.

Results:

SIM #	VG3	Target Z (inches)	VG4 (volts)	VG6 volts)	Spot size (Inches)	Current Density at target (A/cm2)	I Target (uA)	I G5 (uA)	I G6 (uA)
-	6kV	4.325	-200	NA	0.124 x 0.124	0.029	863	19.7	NA
A	6kV	4.325	0	3900	0.260 x 0.017	0.039	153	33.4	494.5
B	6kV	2.135	0	2000	0.149 x 0.016	0.075	271	33.4	533.2
D	12kV	4.325	0	4000	0.224 x 0.018	0.053	256	0	425.7
C	12kV	2.135	-800	2200	0.085 x 0.016	0.203	679	0	338.1

Target potential at 6kV, Cathode current approx. 1.0 mA. Sim C is illustrated below.

1.Spot size and current density improvement.

Increasing VG3 and moving the target closer to the gun effect a reduction in spot size and an increase in current density at the target. The combination of the two results in an almost 7 times increase in current density at the target. Positioning the target closer to the gun exit effectively reduces linear magnification of the main lens system resulting in a smaller magnified cross over contribution to spot size. Increasing G3 potential improves beam quality in the gun by reducing beam size within the lens system. Higher G3 potential also allows more of the beam to pass through the G6 aperture resulting in more beam available to energize the target.

2. Beam clipping on grids.

Beam clipping occurs on the G5 grid when the G3/G5 potential is too low. This gun was designed to operate with the G3/G5 potential at 12KV. Using G3 of 6KV yields a beam divergence angle entering the G3 that is too large and results in the beam clipping the entrance aperture of the G5 grid. The G4 voltage potential also has a great effect on the amount of beam that is collected on G6 as well as G5. The DM2001 design operates with G4 potential near 0.0 volts to focus the round beam several inches away from the gun exit. As this potential becomes more negative the lens action will cause more convergence of the beam resulting in closer focal distance and more beam passing through the apertures and less collecting on grids.

3. Quadrupole action of G6 slotted aperture grid.

The rectangular aperture of the G6 grid creates a quadrupole lens the nature of which is to converge the beam in the vertical plane while diverging the beam in the horizontal (perpendicular) plane. Thus the potential of G6 has a great effect on beam focus in the vertical plane.

4. Beam/target shield

All simulations were done with the beam/target shield included in the model. This allowed for a reasonable job size since the vacuum chamber need not be included in the model. The shield has a square cross section and measures about 1.25 inches on a side. The beam shield, target and G5 grid are electrically connected and set at a potential of 6kV providing a 6KEV beam energy at the target for all jobs. For jobs C and D the G3 would be connected to its own power supply and set at 12KV.

Simulation C: DM2001 gun with G6 beam shaping grid
VG3 = 12kV, short target distance Target at Z = 2.135

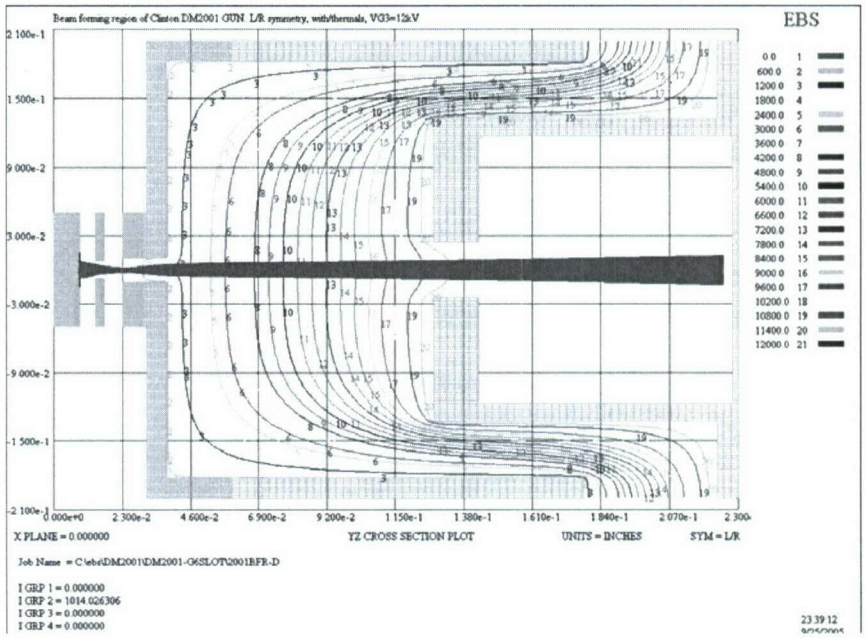

Figure 47. YZ cross section plot of the beam forming region of DM2001. The G3 potential is set at 12kV. Cathode bias condition are Vco = 80 volts, VG2 = 590 volts, drive for about 1000 uA = 60 volts. Actual potentials are K=20 V, G1=0, G2=590, G3=12kV. According to the information supplied by Clinton the G1 thickness is coined down to 0.0032 inches. VG3 = 12kV

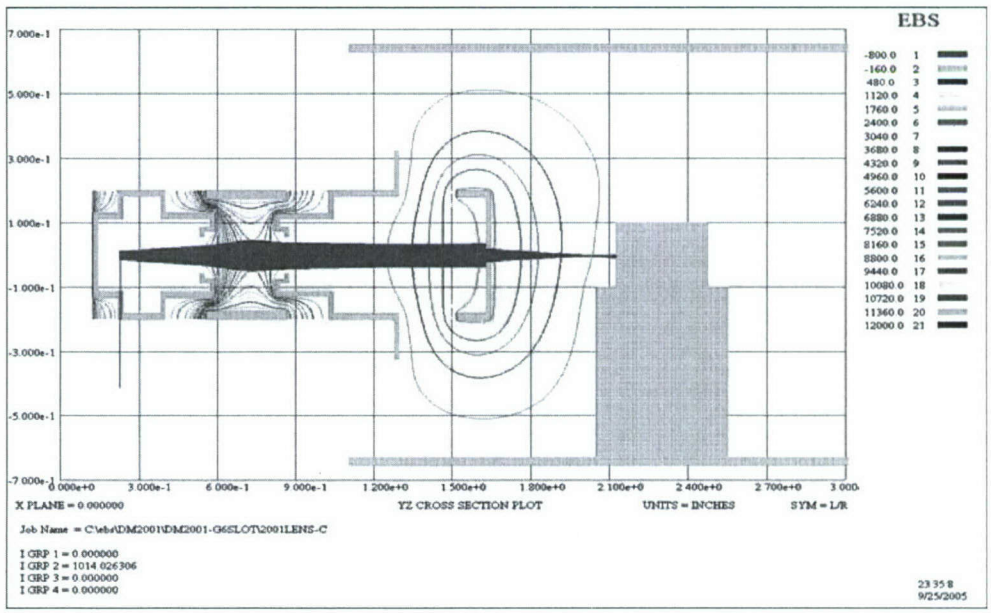

Figure 48. In this simulation the G3 potential has been increased to 12kV and the target position has been moved close the gun exit at Z = 2.125 inches. This combination gives the best results in terms of smallest spot size and resultant highest current density.
The plot shows a vertical cross section of gun, target and G6 grid with rectangular aperture. In this simulation the G6 potential is set at 2200 Volts to focus the beam in the vertical plane just short of the target. We have also reduced the G4 potential to –800 volts. This also helps to focus the beam and allow more current to pass through the G6 aperture and reach the target.

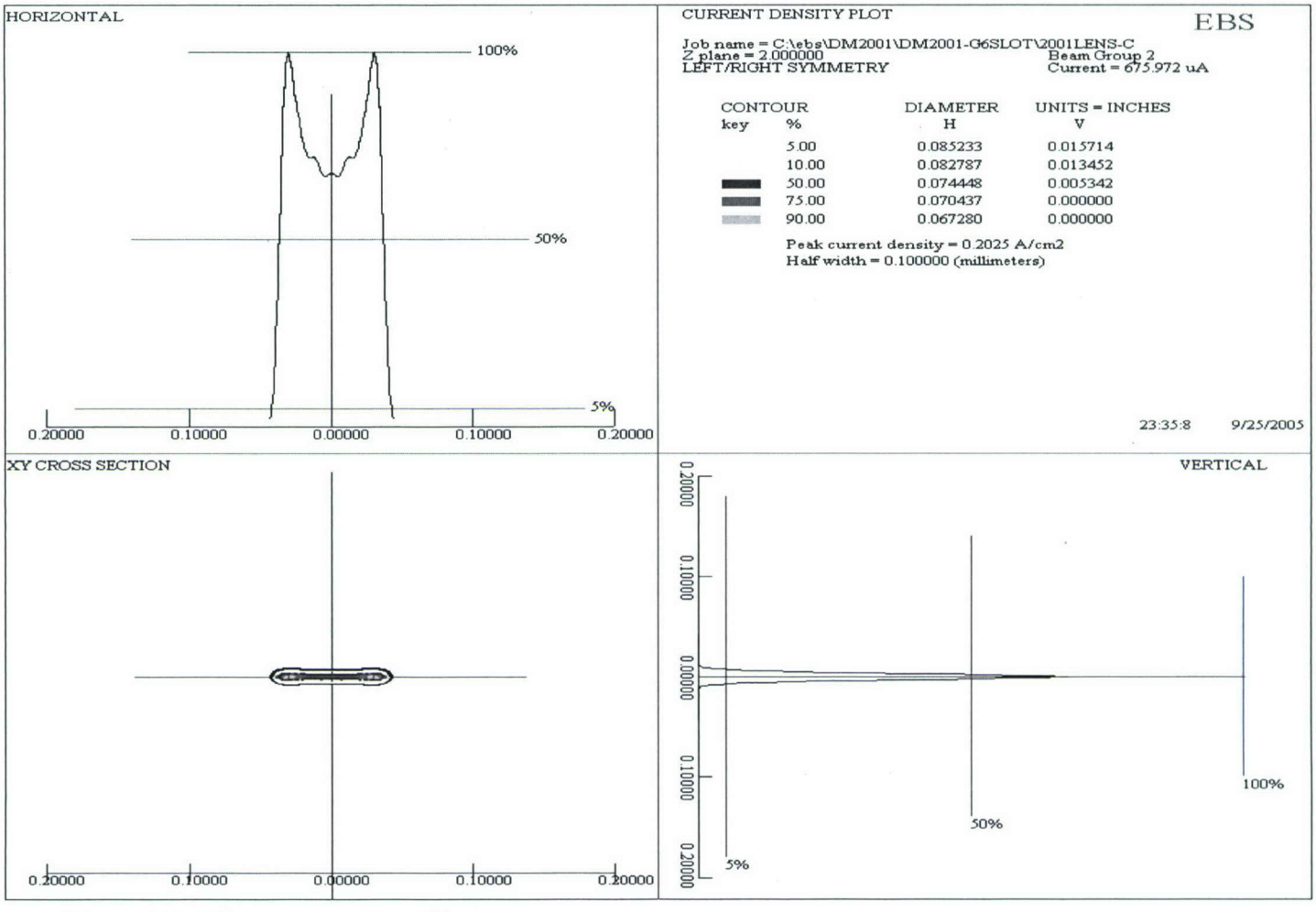

Figure 49. Ebeam current profiles.

Below in Figure 50 are a series of 22 comparisons between theoretical simulations and empirical results for our laboratory 6-grid egun using Simion 7.0 and EBS software. Grid voltages are listed on the left. To the right are the modeling results of Simion 7.0. In the middle are EBS, and finally, on the right, are photos of the ebeams on an AlGaN target for the same set of grid voltages used in the simulations. The scale of the Simion 7.0 and EBS are not the same. The Simion 7.0 simulation is done at 50 μm per division compared to 500 μm per division for the EBS program. The photographs have a vertical field of view (black screen height) about 3810 μm. The ebeam photos are skewed from the simulations with a rotation of the axis of the ebeam about 10 degrees counterclockwise from the horizontal.

We have previously determined that we could not achieve the total current and current density results needed for pumping AlGaN die by operating our electron guns under "normal" cathode conditions. We have therefore been employing the cathodes under a "boosted" condition where the cathode is operated at higher than normal temperatures and therefore provide higher than normal current density. In this manner we have been able to achieve total current in excess of 1mA, compared to the normal cathode beam current about 100 μA.

G1 = -0.7 G2 = 550 G4 = -1400 G6 = 1000 G3/G5 = 5400 TARGET = 5500	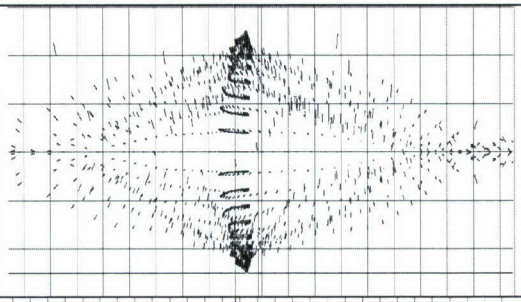	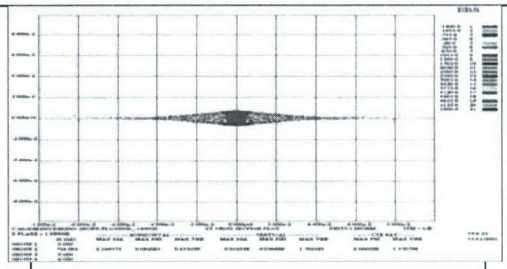	
G1 = -0.7 G2 = 550 G4 = -1000 G6 = 1000 G3/G5 = 5400 TARGET = 5500	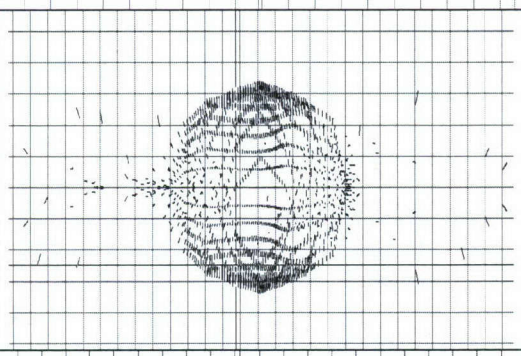	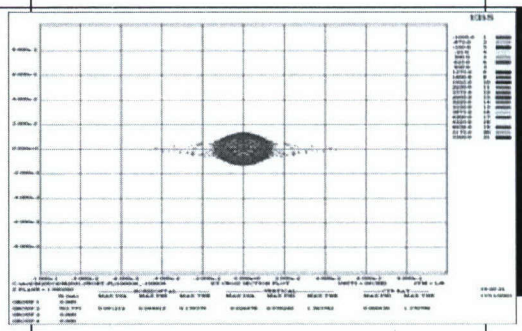	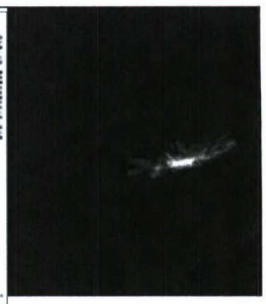
G1 = -0.7 G2 = 550 G4 = -600 G6 = 1000 G3/G5 = 5400 TARGET = 5500	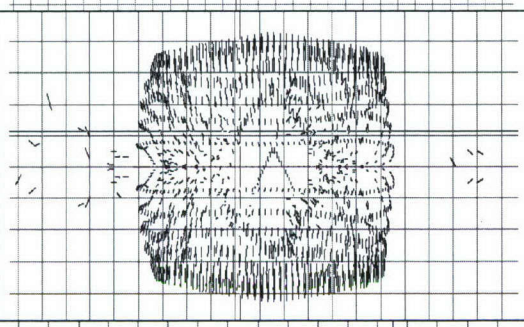	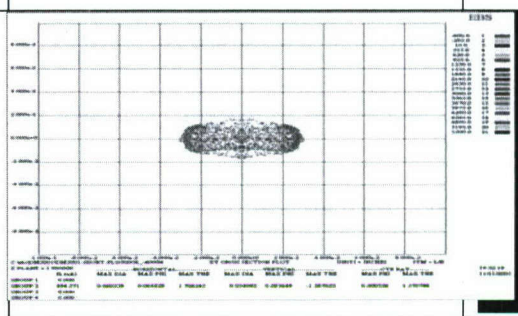	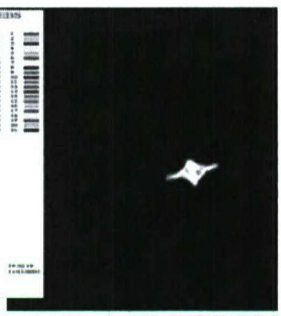
G1 = -0.7 G2 = 550 G4 = -200 G6 = 1000 G3/G5 = 5400 TARGET = 5500	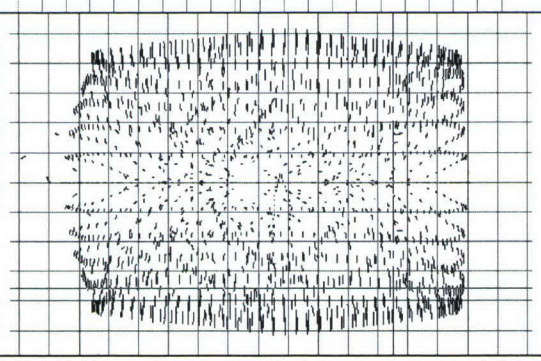	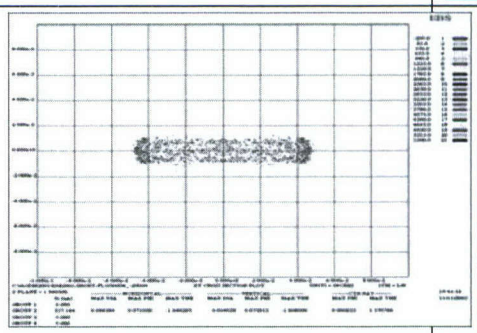	

G1 = -0.7
G2 = 550
G4 = +200
G6 = 1000
G3/G5 = 5400
TARGET = 5500

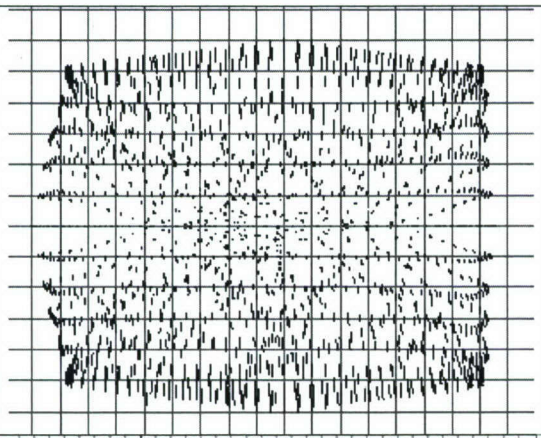

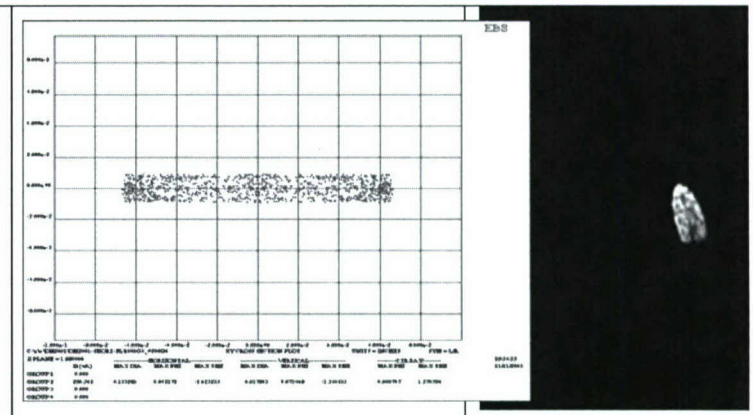

G1 = -0.7
G2 = 550
G4 = -1400
G6 = 2333
G3/G5 = 5400
TARGET = 5500

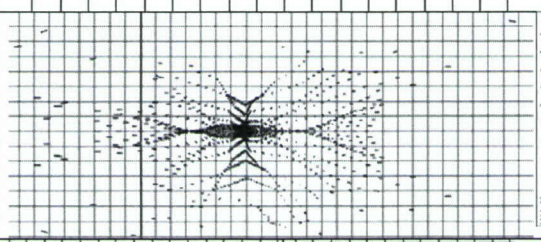

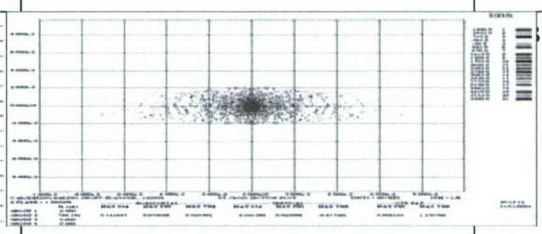

G1 = -0.7
G2 = 550
G4 = -1000
G6 = 2333
G3/G5 = 5400
TARGET = 5500

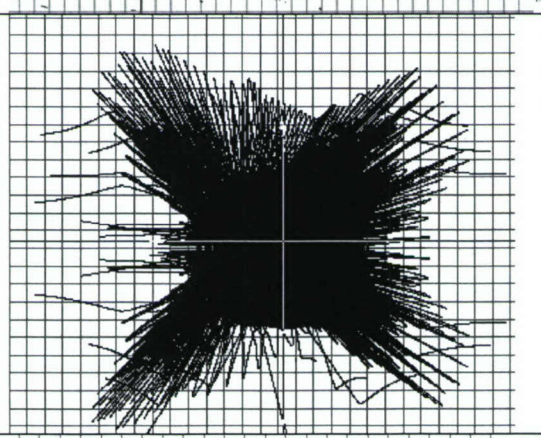

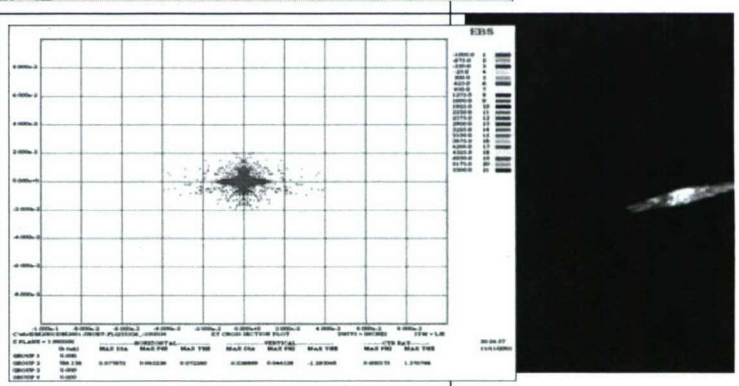

G1 = -0.7
G2 = 550
G4 = -600
G6 = 2333
G3/G5 = 5400
TARGET = 5500

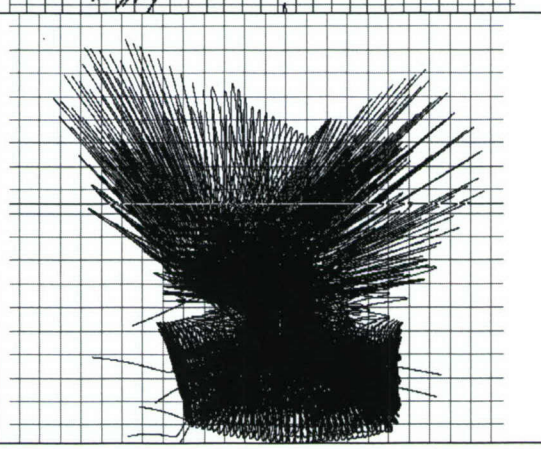

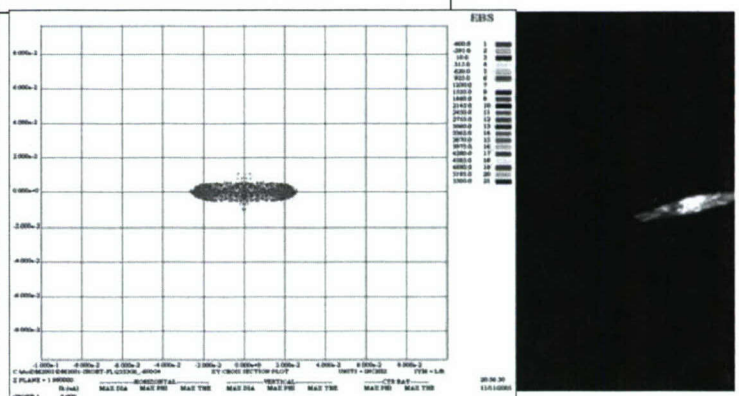

G1 = -0.7
G2 = 550
G4 = -200
G6 = 2333
G3/G5 = 5400
TARGET = 5500

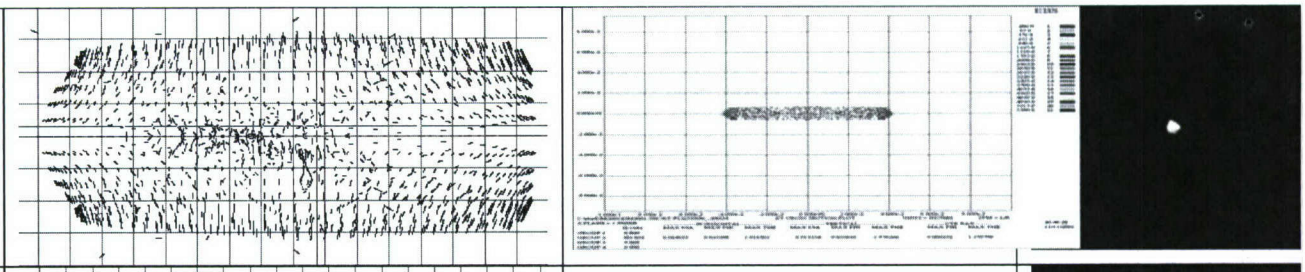

G1 = -0.7
G2 = 550
G4 = +200
G6 = 2333
G3/G5 = 5400
TARGET = 5500

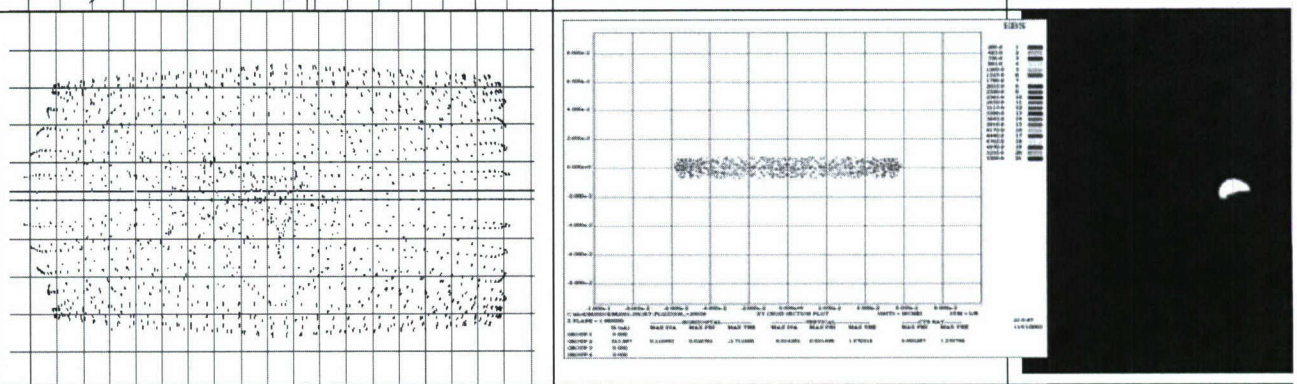

G1 = -0.7
G2 = 550
G4 = -1400
G6 = 3666
G3/G5 = 5400
TARGET = 5500

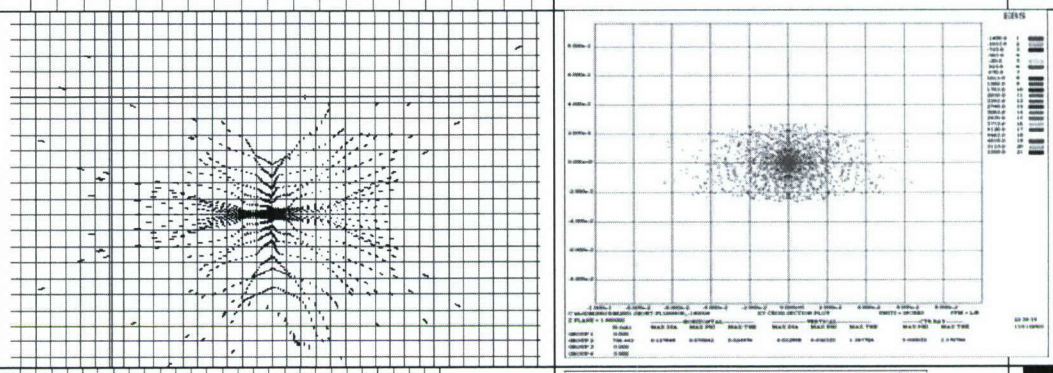

G1 = -0.7
G2 = 550
G4 = -1000
G6 = 3666
G3/G5 = 5400
TARGET = 5500

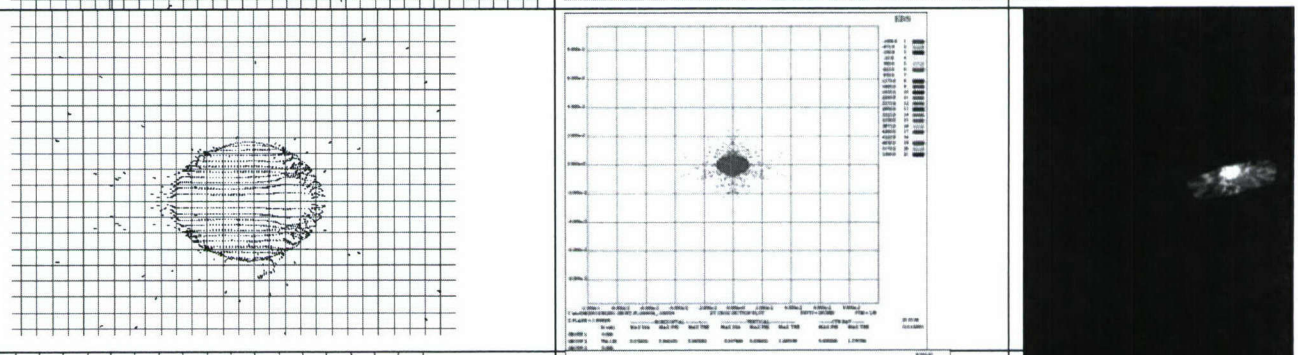

G1 = -0.7
G2 = 550
G4 = -600
G6 = 3666
G3/G5 = 5400
TARGET = 5500

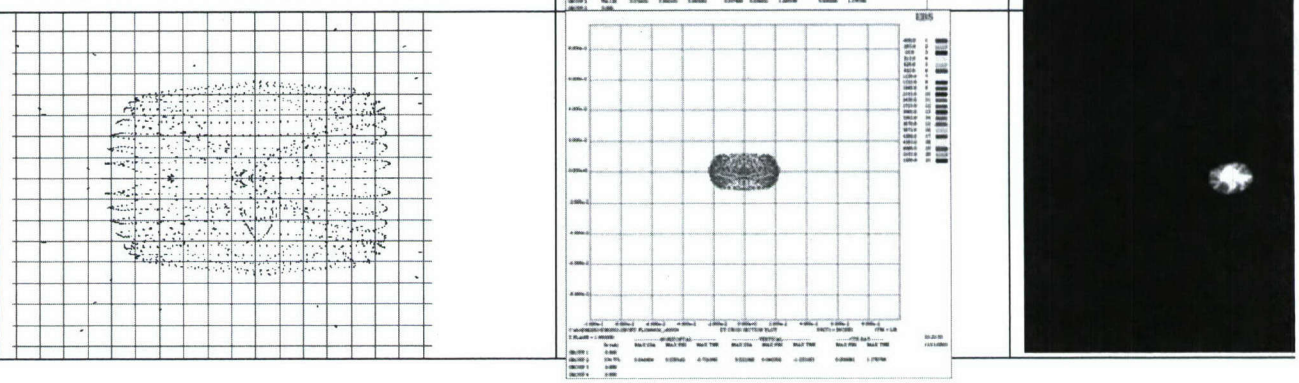

G1 = -0.7
G2 = 550
G4 = -200
G6 = 3666
G3/G5 = 5400
TARGET = 5500

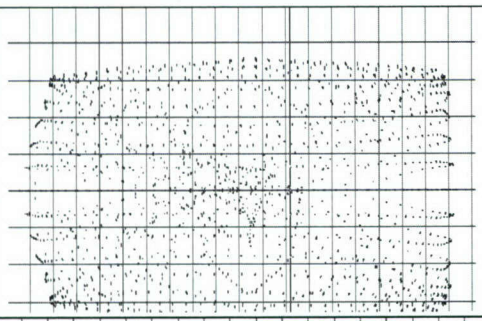

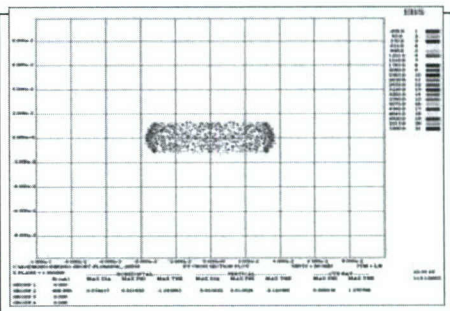

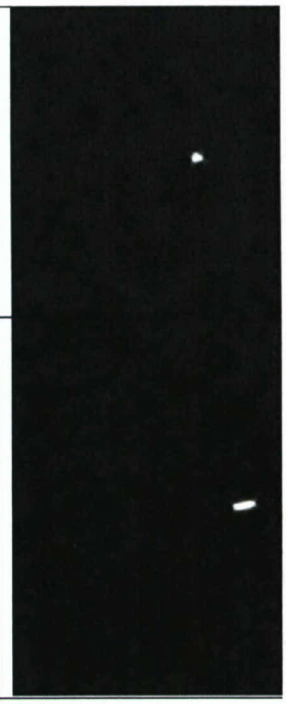

G1 = -0.7
G2 = 550
G4 = +200
G6 = 3666
G3/G5 = 5400
TARGET = 5500

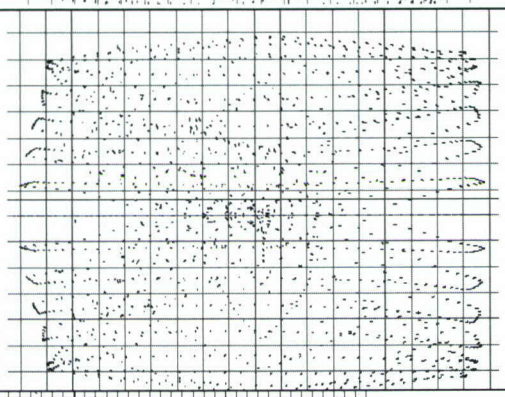

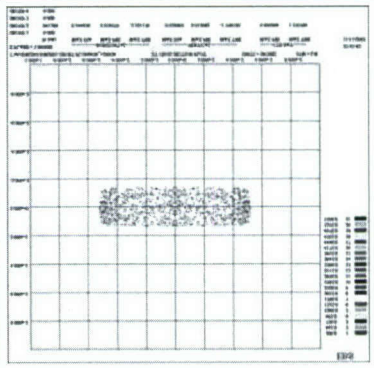

Obs 16

G1 = -0.7
G2 = 550
G4 = -1400
G6 = 5000
G3/G5 = 5400
TARGET = 5500

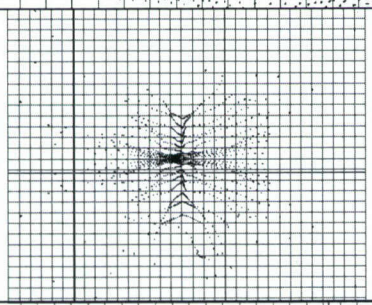

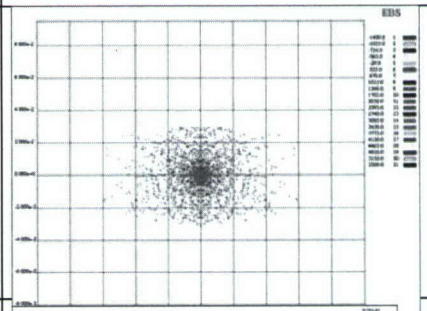

G1 = -0.7
G2 = 550
G4 = -1000
G6 = 5000
G3/G5 = 5400
TARGET = 5500

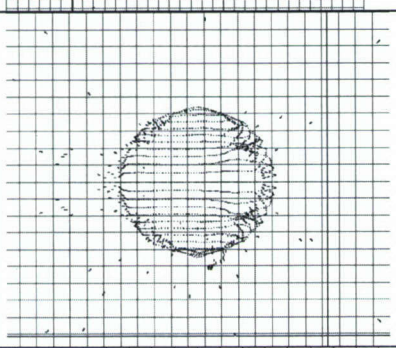

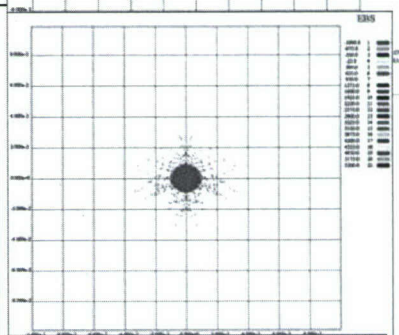

G1 = -0.7
G2 = 550
G4 = -600
G6 = 5000
G3/G5 = 5400
TARGET = 5500

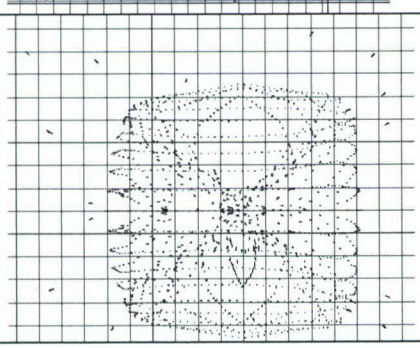

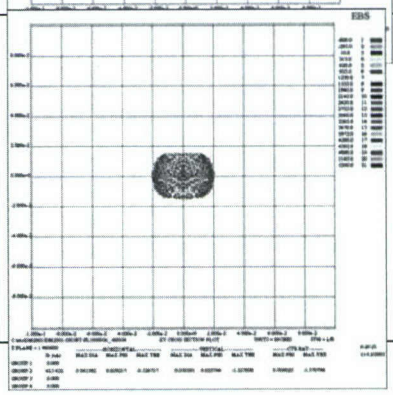

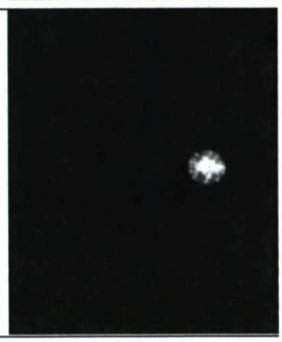

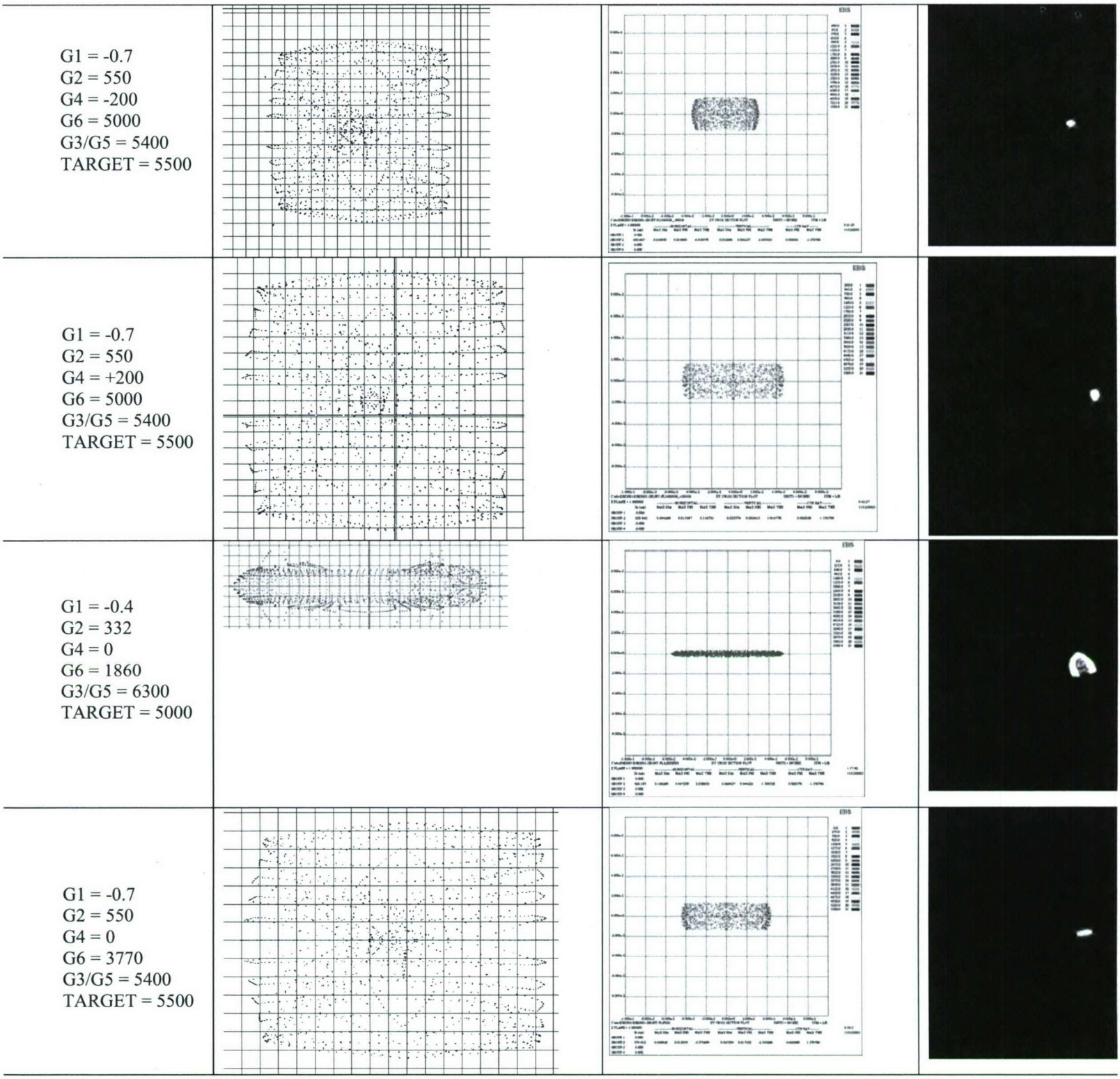

Figure 50. Comparison of theoretical simulations and recorded ebeam images

The modeling results appear to be most accurate only at very low beam current values where electron-electron repulsion is low. In the above data of Fig. 50, there is a broad sense of agreement between the empirical and theoretical results. However, in some cases there appears to be little similarity between the two. We are still attempting to understand how to apply theoretical boundary conditions at the cathode surface which represent the differences between "normal" and "boost" conditions of operation. We are also attempting to understand at what current densities the theoretical models break down. In some cases, as shown in the final example in Fig. 50, the electron beam behaves nearly as expected, although the scale is not accurate.

Below are Simion 7.0 and EBS simulations plus a phot in the same scale with the grids at G1 = -0.7, G2 = 550, G4 = 0, G6 = 3770, G3/G5 = 5400, and TARGET = 5500.

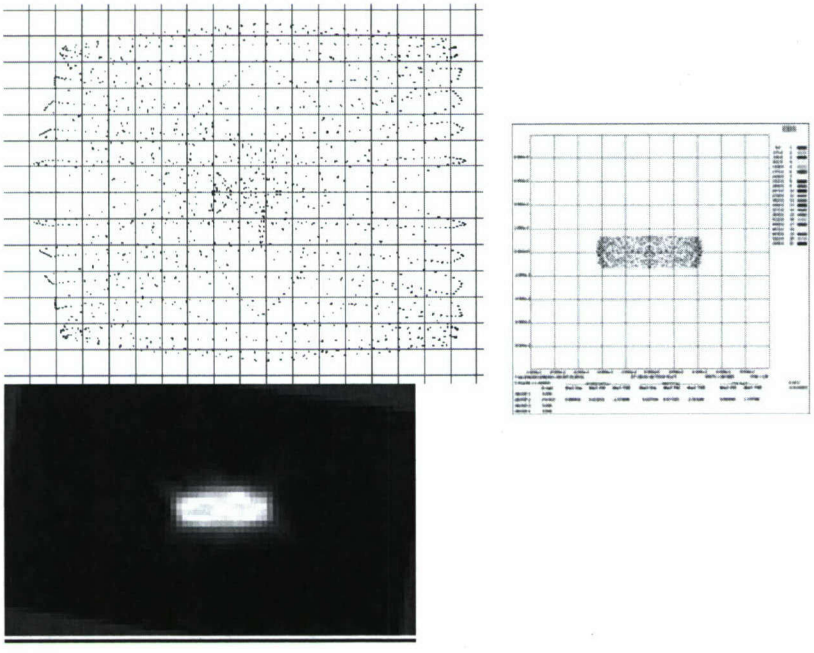

Figure 51. Reformating of last data set from Fig. 50.

The shape of the ebeam and model are very similar above except that the dimensions are wrong. The image of the ebeam at the right above is about 100 μm high by 250 μm wide compared to about 800 μm high by 2000 μm wide for the EBS simulation and 850 μm high by 850 μm wide for the Simion 7.0 simulation. The shape of the ebeam is best predicted by the EBS simulation, but the dimensions in both cases are off by a large margin. Effort will be put into discovering the cause of the disparity. We believe some of the errors may be due to the method by which the cathode boundary conditions are specified.

Laboratory ebeam system status

During November we began to obtain ebeam geometry results from the laboratory ebeam system using the new negative HV supply for G4. This enabled us to achieve higher current densities that with the prior power supply. Following is a discussion of this effort.

Ebeam Reproducibility

Shown below in Fig. 52 is the ebeam image shown in our September report (No. 20).

Figure 52. Ebeam image from Sept. 2005 report. The conditions were: Filament=24V (boost), cathode = 0, G1=-.7, G2=590, G3/G5=2.1kV, G4=0, G6=2kV, Target=5.5kV, Target current= 600uA. G3/G5 current = 1mA.

The ebeam dimensions in Fig. 52 are about 75 μm high by 1150 μm wide. The target current in this area corresponds to 0.70A/cm^2. In November we reproduced these conditions with some variations. Below is an ebeam image with conditions the same as Fig. 52 above, except that the filament was operated at normal versus boost voltage and G3/5 = 590V versus 2.1kV in Fig. 52.

Figure 53. Operating conditions: Filament = 13V (normal) LEFT and 24V (boost) RIGHT. G1 = -0.7V G2 = 590V, G3/5 = 590V (1mA on G3/5), G4 =0V, G6 = 2kV, Target = 5.5kV. Target current = nil on left and 300 uA on right.

These images corresponds closely to the image in the September report and will be the best achievable with present ebeam controller until we replace the G4 power supply with a negative going power supply.

After testing the reliability, we tried getting the beam spot as close to the required beam spot dimensions as possible, i.e. 750um by <100um. The results are shown below.

Figure 54. Filament = 24V(boost), G1 = -0.7V G2 = 325V, G3/5 = 5.0kV,G4 =-226V, G6 = 2.2kV, Target = 5.74kV , Target current = 600uA

Approximate ebeam spot dimensions in Fig. 55 are 770 um wide by 136 um high. By adjusting G2 we obtained the following ebeam image at 900uA target current.

Figure 55. Filament = 24V(boost), G1 = -0.7V G2 = 438V, G3/5 = 5.0kV, G4 =-226V, G6 = 2.2kV, Target = 5.74kV, Target current = 900uA.

Approximate ebeam spot dimensions are 800 um by 158 um. This corresponds to about 0.79A/cm^2 as measured in the image. As mentioned previously, we believe the actual current density is somewhat higher due to blooming and saturation in the present images. Currently be believe these are the most optimum value for operating the present electron guns.

Filament: 24V (boost)
G1 = -0.7V
G2 = 438V
G3/5 = 5kV
G4 = -226V
G6 = 2.2kV
Target = 5.75kV

Electron Beam Pumping of PARC Material

A sample of GaN material was provided by Dr. Noble Johnson of PARC for testing with e-beam pumping. The structure of this material is shown in Fig. 55A.

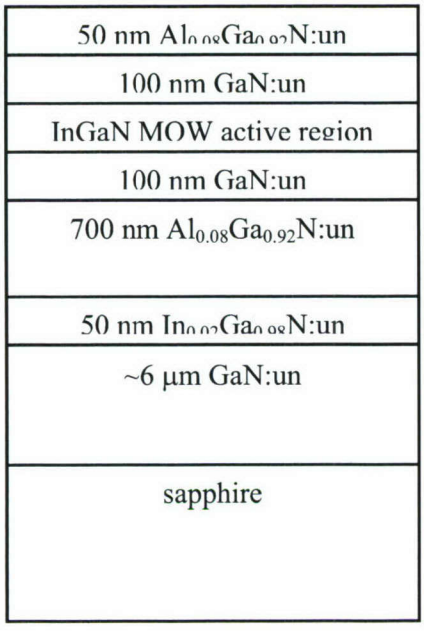

B2802 active region:

- *Five 35A $In_{0.08}Ga_{0.92}N$ MQWs*
- *65A $In_{0.01}Ga_{0.99}N$ barriers*
- *Wavelength ~393 nm (shorter towards edge)*
- *P_{th} ~70-100 kW/cm^2*

***Figure 55A**. Structure of PARC GaN sample*

This material was demonstrated to lase under optical pumping at 266nm by Dr. Mike Wrabach of ARL. It is the goal of these tests to demonstrate laser emission also under electron beam pumping. Figure 55B below shows a typical emission spectra using a 266nm femtosecond laser pump with average power in the range of a few mW and a peak power nearly 1GW, in a 50 micrometer diameter spot, producing an excitation power density near $4x10^{13}$ W/cm^2.

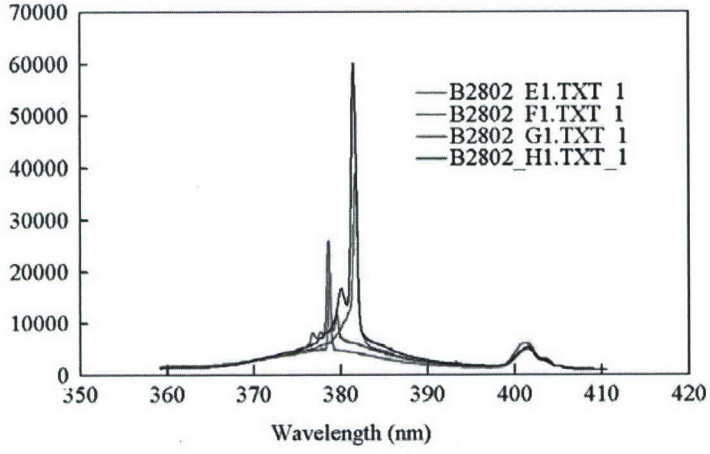

Figure 55B. Emission spectra of PARC GaN sample under optical pumping at 266nm

The PARC sample is made up of many die on a wafer segment shown in the sketch below in Fig. 55C. Each die was formed by CAIBE etching.

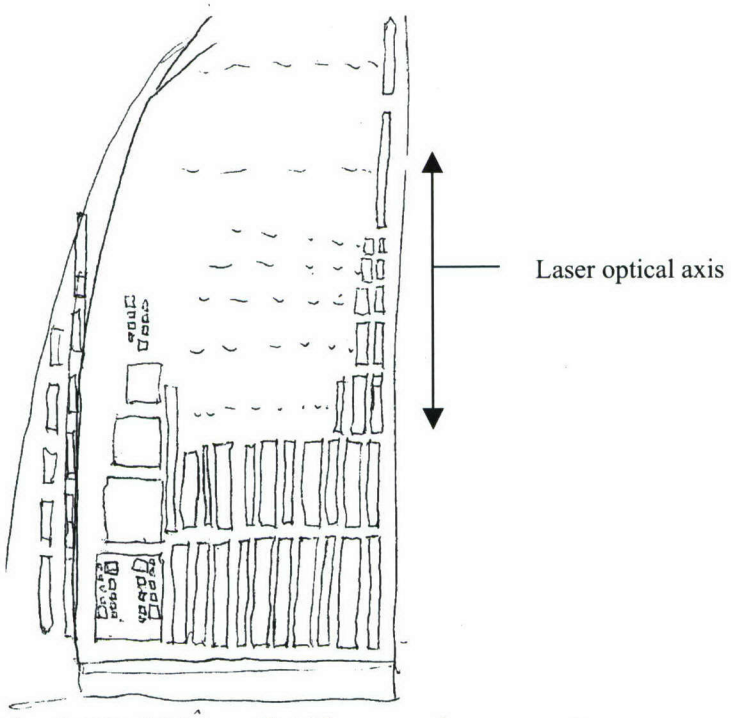

Figure 55C. Sketch of PARC 380nm GaN laser wafer segment

We have just begun this testing and have only preliminary results to date. We have demonstrated emission about 385nm with e-beam pumping, but have not optimized the ebeam pumping or the optical collection optics and alignment. Based on the information from Dr. Johnson, threshold for lasing occurs at a pump power between 70kW/cm^2 and 100kW/cm^2. For our ebeam operating at a beam voltage between 5kV and 10kV, this corresponds to between 7A/cm^2 and 20A/cm^2 of ebeam current density. For our 1mA beam the beam area must be less than between 5,000 μ^2 and 20,000 μ^2 to achieve laser threshold. Since these die are several millimeters long and hundreds of um wide, we will only pump a small region of each die. More will be reported on this in the next monthly report.

Design of an electron gun with planar electron beam geometry

The following is a continuation of the larger, more general design document reported above. The scope here is to determine the emission capabilities of fine wire directly heated thermionic cathodes, in an electron gun configuration more or less similar to the earlier design study. The target current densities are unchanged, at 1 to 10 μA/μm^2 over a rectilinear region approximately 2μm by 750μm.

As before, the output of the electron source may be controlled either by the cathode temperature (heater current) or by bias potential between cathode and lens electrode. The lens focal length is voltage controlled, and produces a rectangular cross section beam of constant long dimension (width) and variable aspect ratio (height).

The thermionic source material was Tungsten with 2% Thorium, at three different diameters, 1 mil (25 um), 5 mil (125um) and 6 mil (150um) . These filament diameters are available from sources for Electron Microscope cathodes and thus are more or less available "off the shelf". The squared-off design is a minor modification of a standard inexpensive glass based "hairpin" style SEM cathode.

For the thermionic emission equations and other technical background, the reader is referred to the appropriate sections of the earlier report.

Overview and Objectives

Basic Design Premises

The electron sources under consideration here have the same specifications as previously analyzed cathodes. They need to produce a current density at the target from 1 to 10 μA per μm^2 , with a target footprint of approximately 2 by 750 μm. The cathodes are directly heated with filament diameters of 1, 5, and 6 mils (25, 125, and 150 um respectively). The filaments are Tungsten wire with 2% Th, which when activated after the cathode is under high vacuum, can produce a cathode with a work function between 2.5 and 2.6 eV. This results in a filament temperature about 900 K lower than for pure Tungsten. Table 1 is similar to that in the earlier report but has the different cathode areas for the fine filament wires.

Table 1
Electron Source Requirements

Target Current Density (j) :	1 to 10 $\mu A/\mu m^2$ [100 – 1000A/cm^2]
Target Size:	2μm high x 750μm long
Target Area (A) :	1500 μm^2 [1.5x 10^{-5} cm^2]
Target Current (I = j A) :	1.5 to 15mA
Diameters of Cathodes:	0.0025 cm; 0.0125 cm ; 0.015 cm
Length Of Cathode:	0.075 cm
Cathode Surface Areas:	5.89x10^{-4} cm^2; 2.945 x$10^{-3}$$cm^2$; 3.534x$10^{-3}$ cm^2
Cathode material:	Tungsten – with 2% Th.

Target Current Density

Equation (1) derives the required target current based on the target dimensions and estimated current density. The target beam current is the product of target current density times effective target area, or the beam footprint at the target.

(1) $$\mathbf{I_{target} = j_{target} \times A_{target}}$$

$$\mathbf{I_{target} = (1 - 10\ uA/\mu m^2) \times (\ 1500\ \mu m^2\ )}$$

$$\mathbf{I_{target} = 1.5 - 15\ mA}$$

Reserve margin requirements are the same proportionally as before, and would allow for some beam overfill of the target at target plane. A suitable reserve margin is best determined from experimental results, as excessive current on the target will result in increased substrate (target) heating and device degradation.

The minimum cathode current must be large enough to supply whatever current is intercepted by the beam shaping electrodes plus the target beam current.

From equation (1), the cathode must provide a current of at least 1.5 to 15 mA. From Table 1 the surface areas of the three different diameter cathodes are 5.89x10^{-4} cm^2; 2.945 x$10^{-3}$$cm^2$; 3.534x$10^{-3}$ cm^2 , which give current densities of Using equation (2) the cathode current densities are shown to be in the range of

(2) $$\mathbf{J_{cathode} = I_{source} / Area_{cathode}}$$

$$\mathbf{= (1.5\ to\ 15\ mA)/\ 5.89x10^{-4}\ cm^2}$$

$$\mathbf{J_{cathode} = \underline{2.547\ to\ 25.47\ A/cm^2\ for\ 1\ mil\ diameter}}$$

$$\mathbf{= (1.5\ to\ 15\ mA)/\ 2.935x10^{-3}\ cm^2}$$

$$J_{cathode} = \underline{0.511 \text{ to } 5.11 \text{ A/cm}^2 \text{ for 5 mil diameter}}$$

$$= (1.5 \text{ to } 15 \text{ mA}) / 3.534 \times 10^{-3} \text{ cm}^2$$

$$J_{cathode} = \underline{0.423 \text{ to } 4.23 \text{ A/cm}^2 \text{ for 6 mil diameter}}$$

Figures 56 – 60 below show the variation in cathode emission as a function of temperature and heater current for each of the candidate filament diameters.

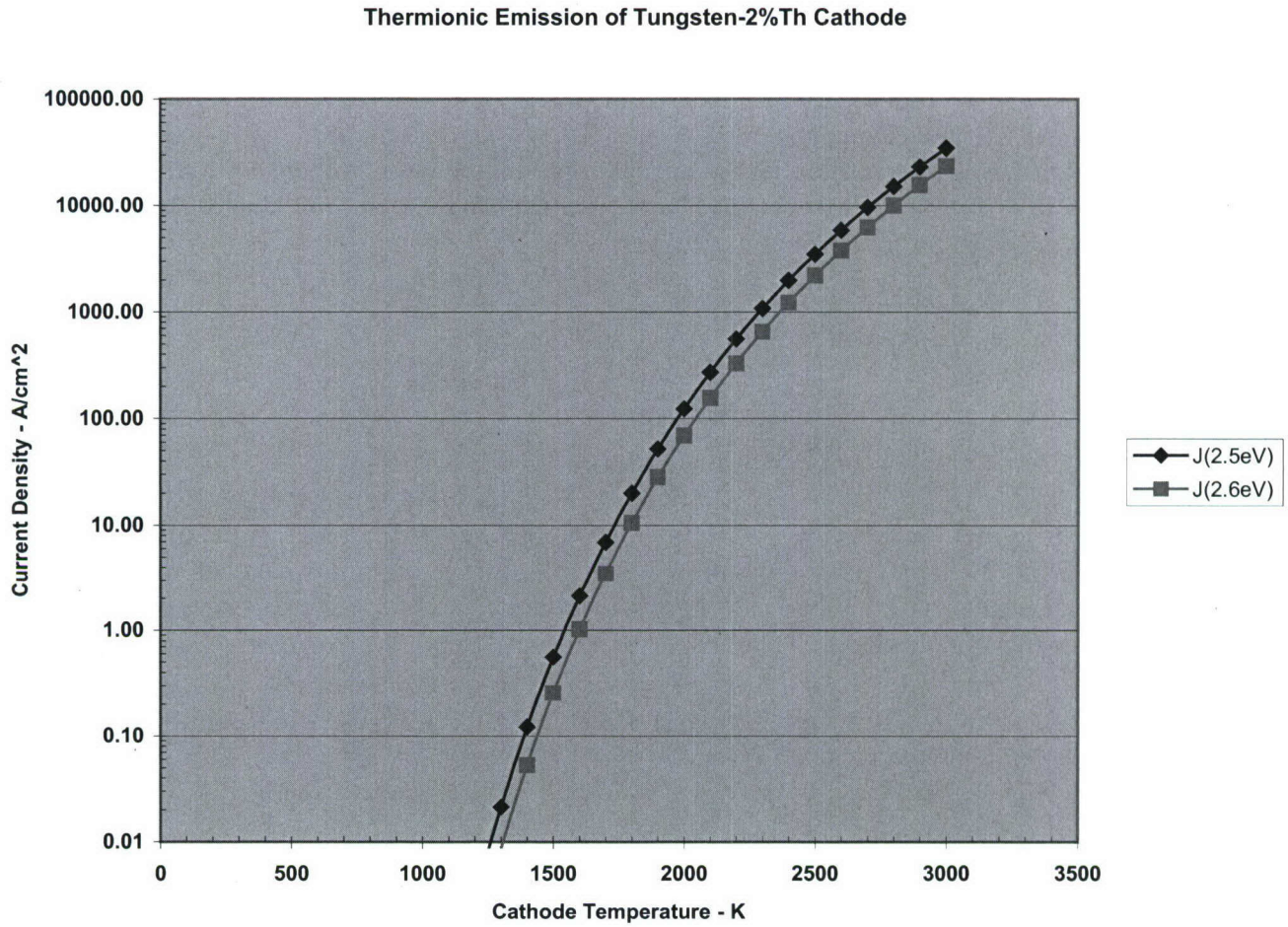

Figure 56: Thermionic current density available from a Tungsten –2% Th source for various source temperatures. Note the required current densities for the e-gun require cathode temperatures in the 1500 – 1700 K range.

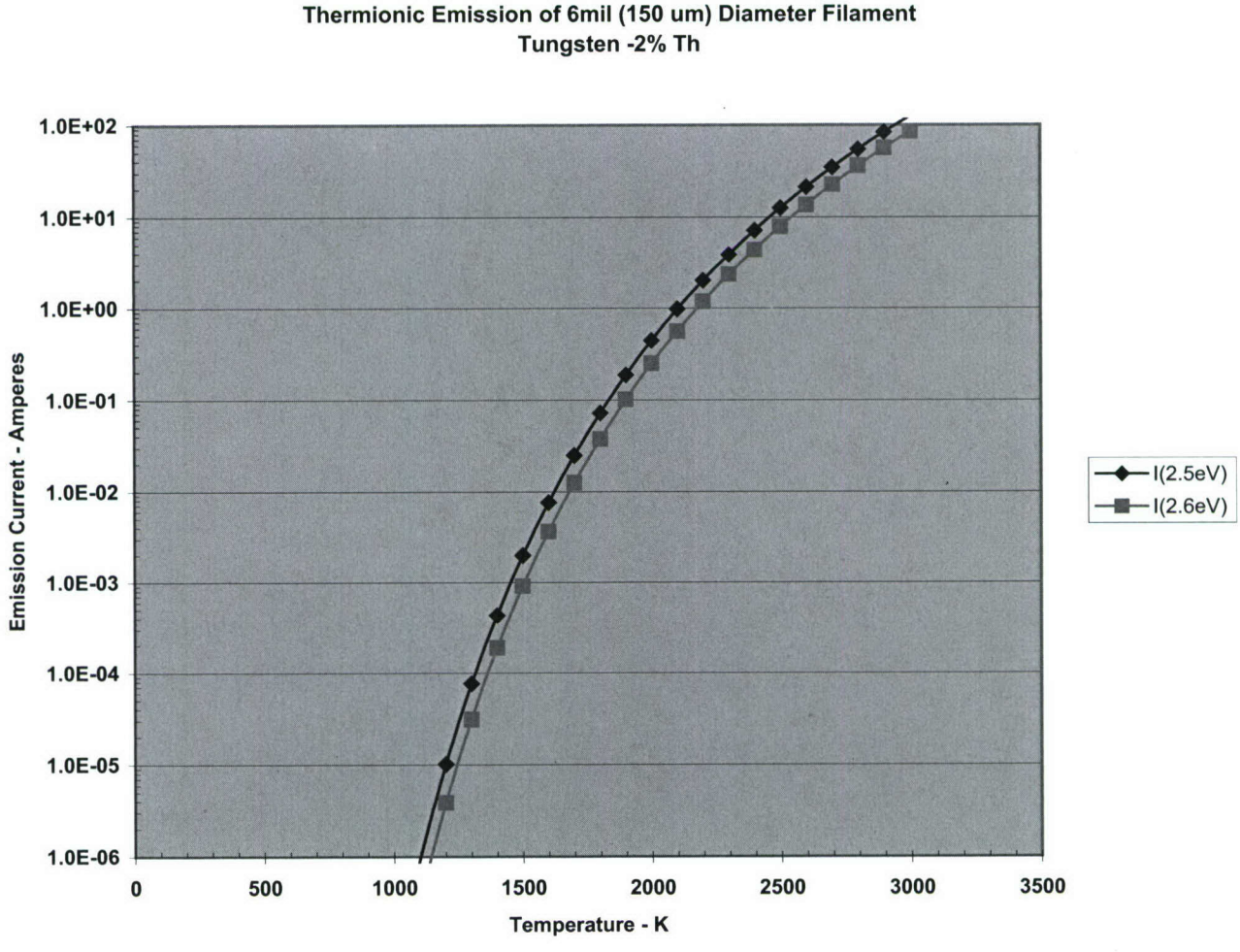

Figure 57: *Emission Current for the 6 mil (150UM) diameter cathode, versus temperature. Again it can be seen the desired cathode currents are reached at temperatures around 1500-1600 K.*

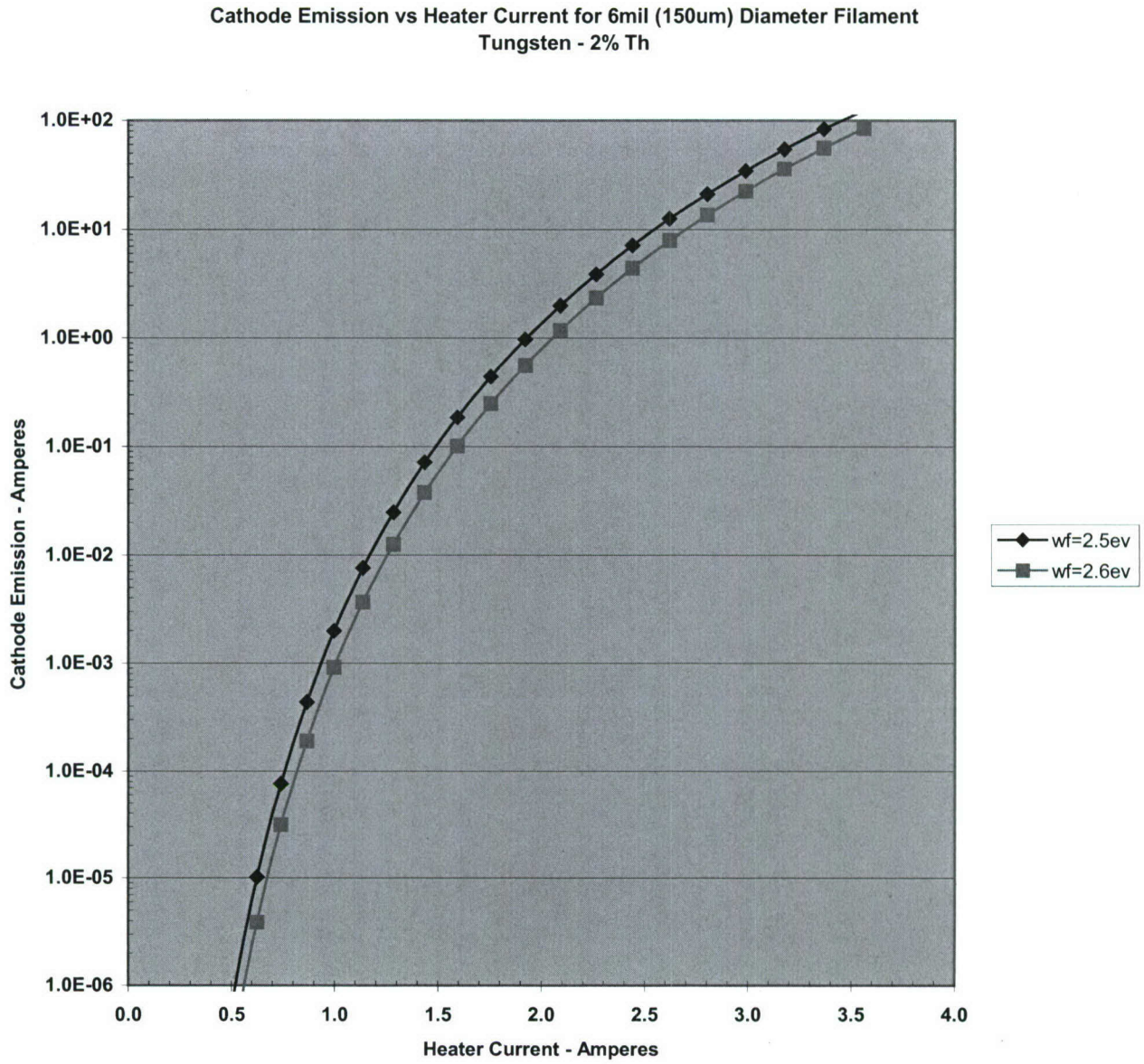

Figure 58: *Cathode emission versus heater current for the 6 mil (150 um) diameter filament.*

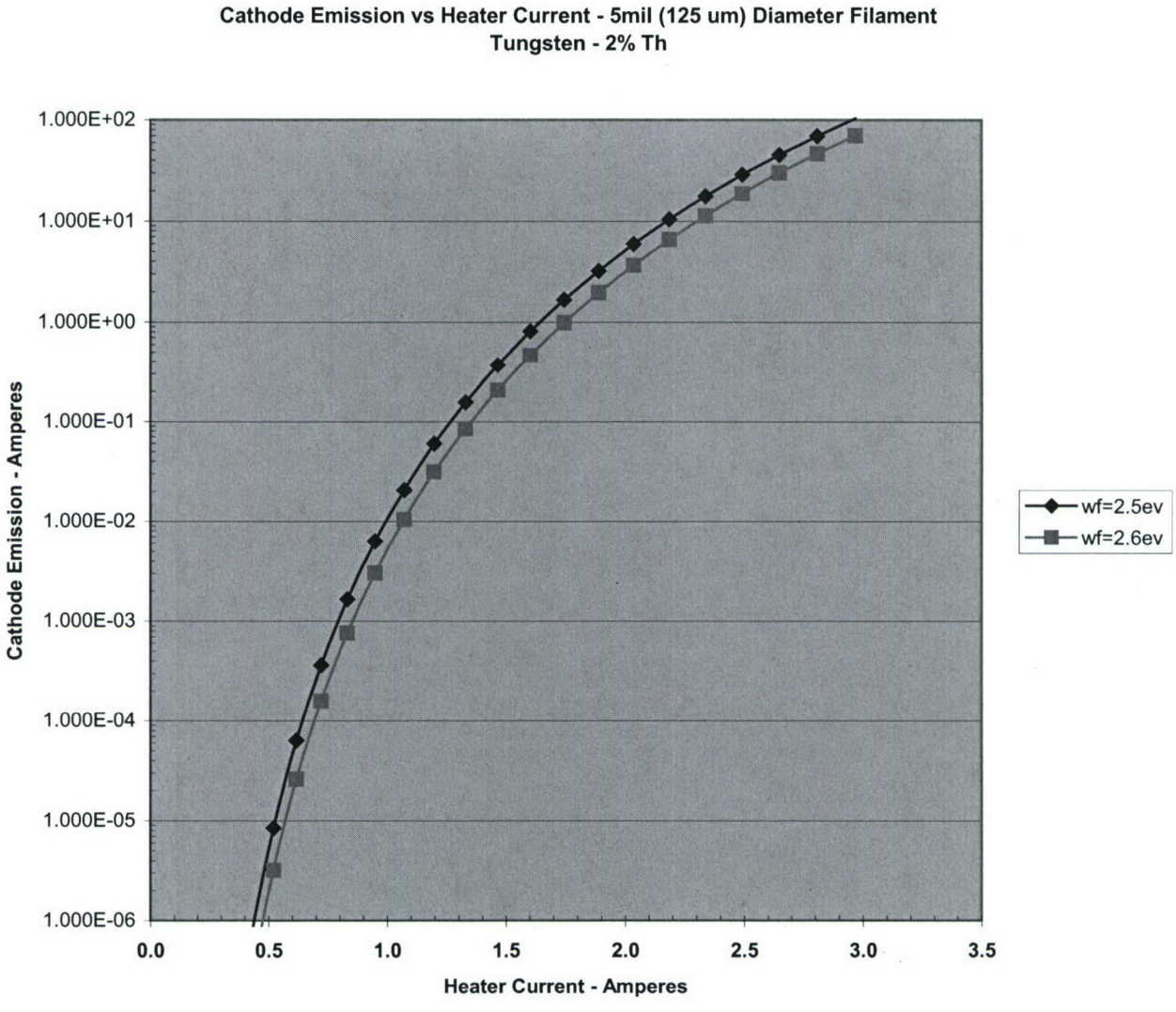

Figure 59: *Cathode emission versus heater current for the 5 mil (125 um) diameter filament.*

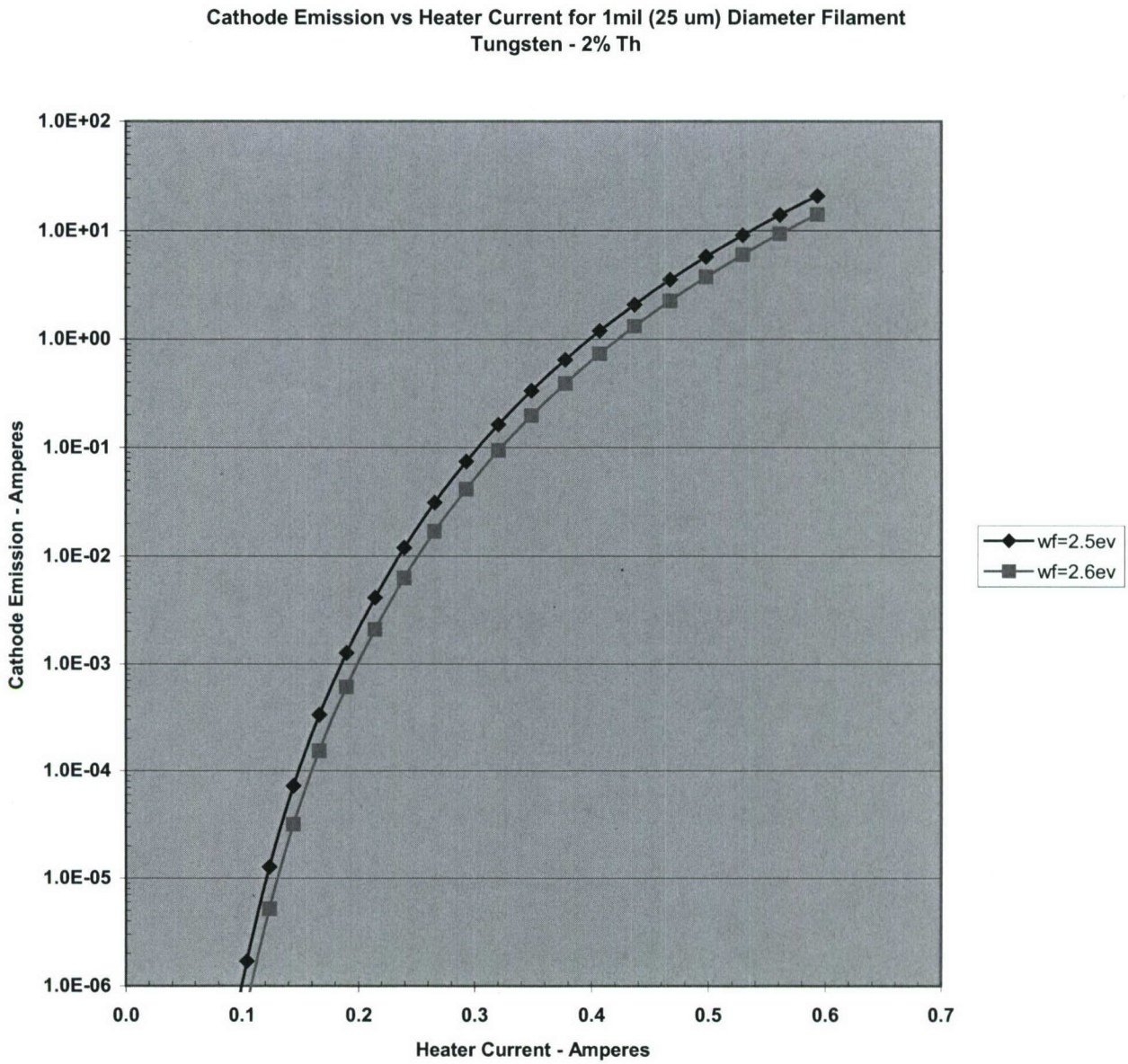

Figure 60: *Thermionic emission versus heater current for the 1 mil (25 um) diameter filament. Although this curve does not show it, reference to figure 1 and the current density shown in equation 2, indicates the finest filament must operate at the highest temperature (around 1700 K) to obtain to desired current density.*

Physical Design of the Cathode

A standard filament configuration was sought among the various shapes in common use for electron microscopes. Figure 60 shows a modified standard design from Kimball Physics on an EAI base. The base has Kovar pins that allow the Tungsten filament wires to be mounted easily with spot welds.

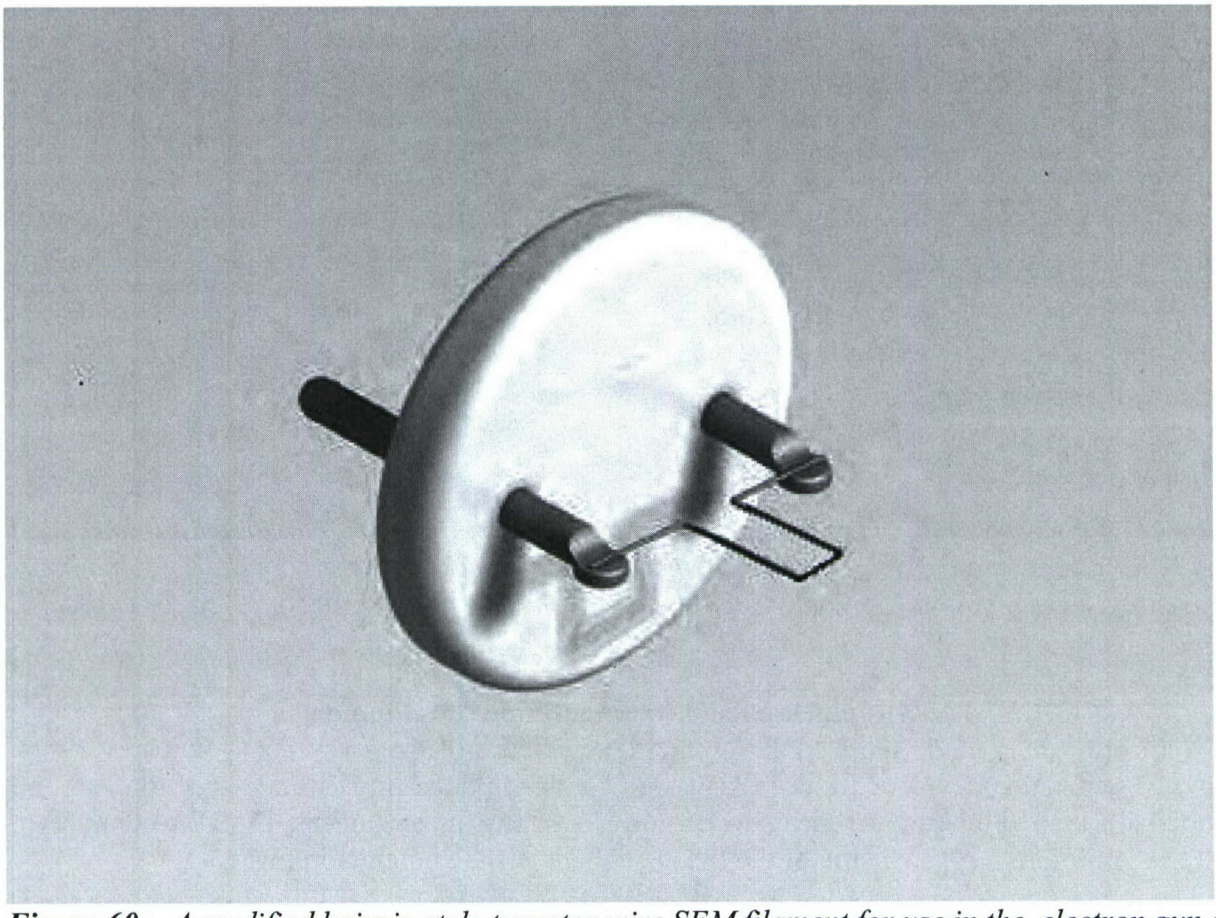

Figure 60: *A modified hairpin style tungsten wire SEM filament for use in the electron gun of a ESUVOS device. The filament wire is tungsten with 2% Th for lower emission temperatures. The filament is spot welded to the Kovar posts. The filament shape must be produced while heating the tungsten to avoid breakage.*

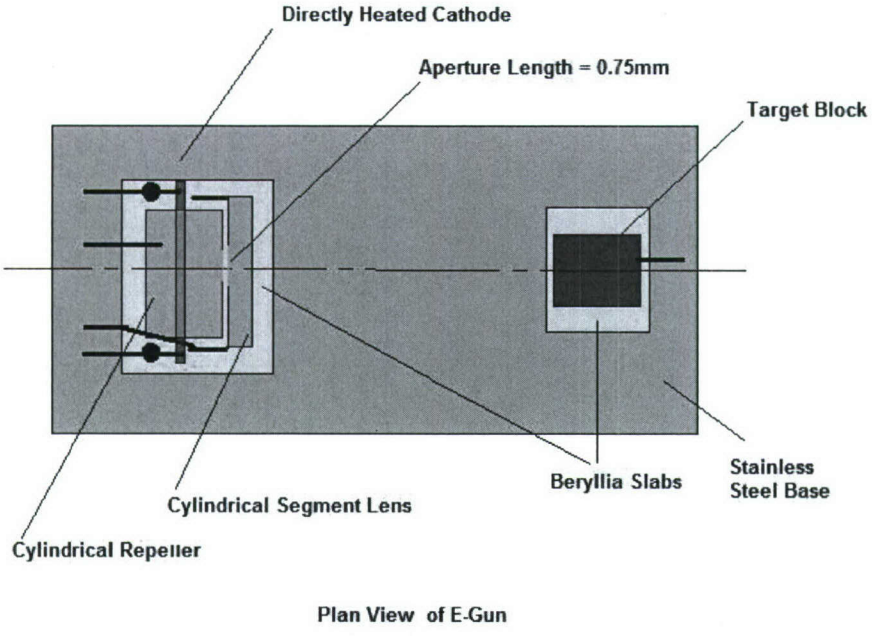

Figure 61 *A conceptual layout of the miniature electron gun. The new modified hairpin shaped filament would replace the longer thicker cathode and fit closely at the rear of the 0.75 mm long slot opening. The close spacing allows a low extraction/control voltage to be used for emission setting.*

3.4.2 Photoluminescence instrumentation development

In order to provide more tools for the development of deep UV semiconductor lasers, Photon Systems also developed a deep UV wide bandgap photoluminescence spectrometer and provided a laser and other components to Boston University, as part of this DARPA contract, to assist in their efforts. A schematic of the PL instrument is shown below in Fig. 62.

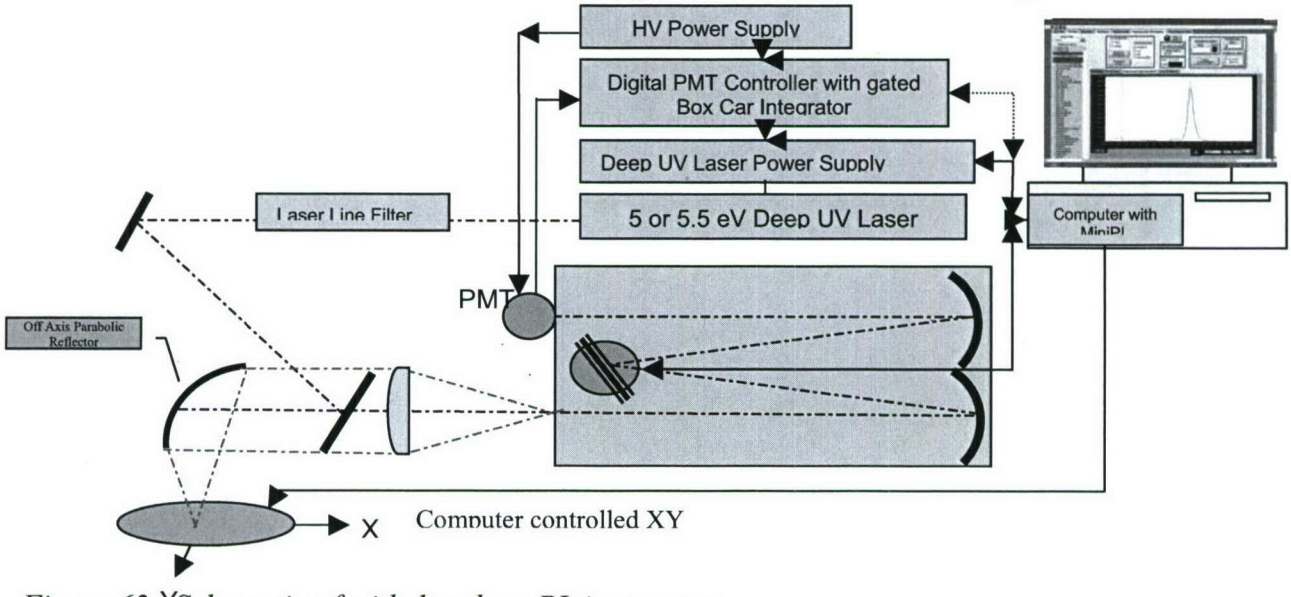

Figure 62. Schematic of wide bandgap PL instrument

This instrument uses one of two different deep UV lasers manufactured by Photon Systems: a 224.3nm HeAg or a 248.6nm NeCu laser. The features of this instrument are:

- Room Temperature PL
- 5.5 eV (224.3nm) or 5.0 eV (248.6nm) laser excitation
- measurement of excitation and emission energy for direct QE measurement
- Highly portable 15 x 18 x 36cm, < 8kg
- High Resolution 0.2nm (multi slits included).
- Computer controlled Grating selection and Calibration
- 1200 g/mm holographic grating std. (300nm peak)
- 3600 g/mm holographic grating for High Res PL or Raman optional (250nm peak)
- Digital PMT controller with gated box car Integrator & Averager for low noise digital PMT output measurement
- < 20Watts (90-240VAC) input
- Fully integrated, self contained, system
- LabView interface and control of laser, spectrograph, PMT, spectral data
- Analysis software included, FWHM, Peak, Side lobe identification, spectral subtract, normalize etc.
- Up to 50 mm diameter sample size
- X-Y-Z stage manual sample control 50mm standard
- 50mm X-Y motorized stage including mapping software optional.

The optical layout and photo of the complete instrument is shown below in Fig. 63.

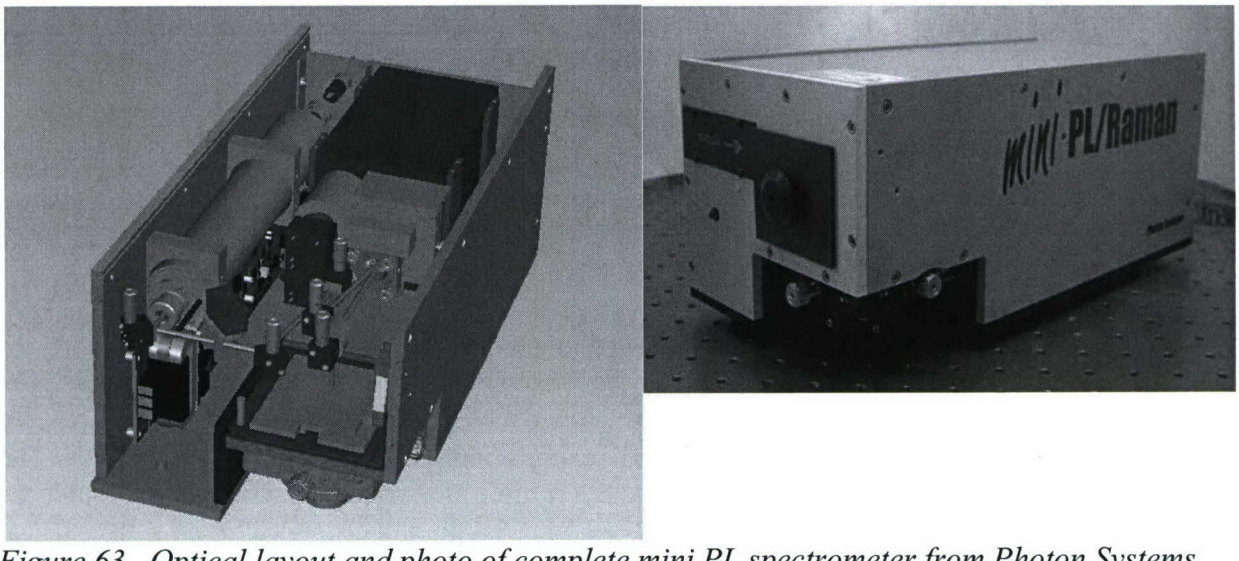

Figure 63. Optical layout and photo of complete mini PL spectrometer from Photon Systems

This instrument is 500 times smaller and lighter and 3000 times lower power consumption than comparable instrument on the commercial market today. This instrument was just introduced to the commercial marketplace in December 2006 and selling well.

3.4.3 Process station & cooling stage development

The vacuum station used to test devices has gone through several iterations during this program. We began with an oil diffusion pump systems with a scroll forepump and liquid nitrogen trap. The LN_2 was also used to cool the stage on which AlGaN targets were mounted. We used this vacuum system for most of the program and replace it with a turbomolecular pump system in mid 2006 because of issues with contamination of AlGaN targets with carbonatious deposits, presumed related to oil contaminants in the old diffusion pump system.

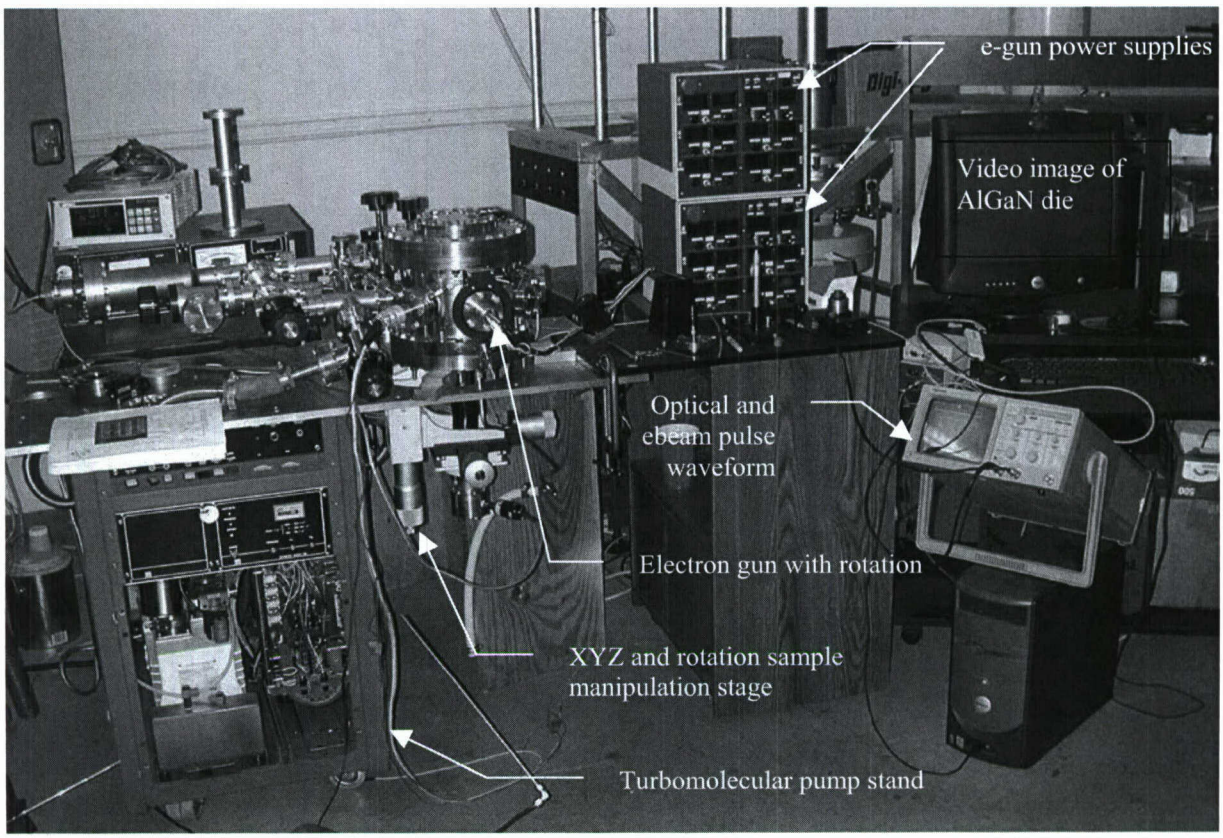

Figure 64. Laboratory test station for AlGaN die, electron sources, guns and EVCSEL devices

3.4.3 AlGaN die facet coating development

Some changes in direction occurred in various aspect of the die development over the duration of the program as a result of knowledge gained and decisions made along the way. We have not changed our fundamental direction of using a ballistic electron beam to avoid the problems of p-doping and making ohmic contacts on high aluminum content AlGaN materials needed for deep UV emission. However, epitaxial film development has changed somewhat in direction. Epitaxial film development was originally focused on the growth of C-plane AlGaN films on C-plane sapphire substrates. This approach assumed we could generate optical cavity facets of adequate quality using reactive ion etching (RIE) or chemically-assisted ion beam etching (CAIBE). In order to optimize the performance of ESUVOS devices it is essential to minimize optical losses other than cavity coupling losses. Optical losses include: bulk gain region losses due to defects and waveguiding losses; Fabry-Perot mirror cavity facet surface quality, facet reflectivity, and facet angle or mode walkoff. The relationship between gain and losses at threshold, G_{th}, for lasing is given by:

$$G_{th} = (1/L)\ln(1/R) \qquad \text{Eq. 1}$$

where L is the cavity length and R is the non-specular reflection losses of the two identical end facets[1]. Mirror facet losses consist of scatter, R_s, and absorption losses, R_a, and reflectivity losses, R_r. Additional optical losses must also include alignment losses, R_A. Scatter losses are due primarily to surface roughness of the facets while absorption and reflectivity losses are due to facet surface chemistry and/or coatings. Alignment losses are due to angular alignment errors in the facets (primarily in the vertical or sagittal direction) and result in increased wave-guiding losses due to misalignment of the mirror axis with the optical axis of the wave-guide. Misalignment of facets in the tangential direction lead to walk-off losses.

Natural Facet Reflectivity

A value for the natural reflection coefficient, R_r, for uncoated GaN was measured in the above reference to be 15% while the theoretical value, assuming a perfect interface between air and GaN and a typical refractive index for GaN of 2.4 is 17%, given by

$$R_r = (n-1)^2/(n+1)^2 = 17\% \qquad \text{Eq. 2.}$$

We plan to provide multi-layer dielectric coating of facets to reduce these reflectivity losses and enable laser emission at lower threshold gain levels. A more detailed analysis of the index of refraction of AlGaN films is described later.

Facet Formation

Considerable effort at Astralux was put into evaluating the potential for using Chemically-Assisted Ion Beam Etching (CAIBE) to generate the facets for deep UV lasers. A literature review on dry-etching of III-nitrides for facet formation was performed. The following items are relevant to the ESUVOS work:

- Most III-nitride dry-etch techniques rely on Cl-based chemistry, which provides enhancement of etch rate due to the formation of volatile etch products.[2] This enhancement is particularly important for difficult to etch $Al_xGa_{1-x}N$ materials.
- To achieve vertical sidewall profiles it is necessary to have separate control of the physical and chemical etch components.[3] Conventional RIE does not permit this.
- Chemically-assisted ion beam etching (CAIBE) allows this control. ICP-RIE has also been shown to provide vertical sidewalls. We have an arrangement to use the CAIBE-facility at Colorado State University and are looking into ICP-RIE facilities. We will utilize the technique and facility that will best meet our needs.
- CAIBE-etched facets have been reported to have sidewall roughness ranging from ~ 5 to 50 nm from SEM examinations. [2] One group has reported lasing at 375nm from CAIBE-etched GaN with facets having 50 nm roughness, verticality within $\pm 2^0$, and a

[1] F. Binet, et.al., "Realization and optical characterization of etched mirror facets in GaN cavities", App.Phys.Lett., **72**, 8, 960, 23 Feb. 1998.
[2] A.T. Ping, M. Asif Khan, and I. Adesida, Semicond. Sci. Technol. **12**, 133 (1997).
[3] I. Adesida, C. Youtsey, A.T. Ping, F. Khan, L.T. Romano, and G. Bulman, MRS Internet J. Nitride Semicond. Res. **4S1**, G1.4 (1999).

reflection coefficient of 15%.[4] This reflection coefficient is reasonably close to the theoretical value of 17% for the GaN-air interface.

- Facet quality requirements will be dictated in part by the gain coefficients (g) for our materials, which have not been measured yet. However, g might range anywhere from 50-100 cm^{-1} for low Al-content bulk $Al_xGa_{1-x}N$ [5] to perhaps one to two orders of magnitude larger for MQW samples. Gain on the order of 3000 cm^{-1} has been observed for InGaN/GaN QW lasers[6], and the Riken group has evidence that AlGaN-based MQWs have similar PL intensities as InGaN-based QWs, at least at low temperatures.[7]

Need for Change in Direction to Cleaved and Coated Facets

As semiconductor devices are produced that operate at shorter and shorter wavelengths, losses become increasingly important in the optimization of device design. Since facet scatter losses are proportional to the inverse 4th power of laser wavelength, the equivalent surface roughness specification for a laser at 250nm would be about 5 times lower than for a 375nm laser. The surface roughness spec for a 230nm would be about 7 times lower. Lack of parallelness of the facet surface vector to the optical axis cause serious optical losses also with a 4th power wavelength dependency. Wave-guiding losses due to decreasingly small index of refraction differences between the guiding and active layers as wavelengths decreases are largely unexplored to date.

Because of the uncertainty in the values of gain described above, and the increasing losses at short wavelengths, we have chosen to focus our efforts on an alternate method of achieving facets of excellent surface quality: cleaving. Cleaving atomically smooth facets of GaN or AlGaN on sapphire has not been demonstrated on traditional C-plane sapphire substrates although significant efforts have been expended to do so. However, in a publication in 1999 the (1102) cleavage plane of sapphire was shown by T. Moustakas' group at BU to extend to the GaN lattice as the (1120) plane, facilitating the formation of cleaved facets[8]. Early in this program, in late April 2004, we shifted our focus from etching to cleaving to form facets for our deep UV ESUVOS ELD devices.

Facet Coating:

Threshold gain is related to the cavity length and mirror losses by $g_{th} = \alpha_{int} + [1/2L]^* [\ln(1/R_1R_2)]$ where R1 and R2 are the reflectivity of the two end facets on the laser cavity. The natural, uncoated, facet reflectivity is given by $R_i = (n-1)^2/(n+1)^2 = 18\%$ (n = 2.5) per facet or 3.2% for a round trip. Facets will be coated at 97% to increase round-trip reflectivity to over 94%, an increase over 30X. Internal losses, α_{int}, include scatter losses from facets and defects in the active layer and waveguiding losses, where α_{int} is proportional to $1/\lambda^4$. Surface roughness at 230nm needs to be 65 times lower than at 650nm or 10 times lower than 400nm for the same optical loss.

---

[4] F. Binet, J.Y. Duboz, N. Laurent, C. Bonnat, P. Collot, F. Hanauer, O. Briot, and R.L. Aulombard, Appl. Phys. Lett., **72**, 960 (1998).
[5] J. Holts, L. Eckey, A. Hoffmann, O. Ambacher, M. Stutzmann, J. Crystal Growth, **189/190**, 692 (1998).
[6] Y.K. Song, et. al., Appl. Phys. Lett. **72**, 1418 (1998).
[7] H. Hirayama, Y. Enomoto, A. Kinoshita, A. Hirata, and Y. Aoyagi, **80**, 37 (2002).
[8] D. Doppalapudi, et.al. "Epitaxial growth of gallium nitride thin films on A-plane sapphire by molecular beam epitaxy", J.App.Phys., **85**,7, 3582, 1999.

Our initial coating run will use a coating with 97% reflectivity at 240nm ±10nm on each end of the bar. The symmetry is chosen to minimize coating run cost. To harden facets against optical damage, the following will be done: Ion treatment of facets to remove surface oxides and contaminants and smooth; forming native nitrides to eliminate dangling bonds and form a barrier on facets, seal and prevent reoxidation. The initial coating will use a HfO_2/SiO_2 dielectric coating stack since the planned emission wavelength is above 230nm. Future coatings for devices below 230nm will use Al_2O_3/SiO_2 because of a band edge for HfO2 at 230nm

Refractive Index of AlGaN Active Region

The optical constants of AlGaN alloys are far from being well established, with different values presented by various authors. The structural and chemical impurities present in the material, especially for high AlN mole fraction, play a significant role in generating this ambiguity. The presence of atomic order is also an important factor.

Here we have obtained the refractive index of AlGaN alloys from two different sources. Fig 65 shows the refractive index alloys obtained using algorithms from Brunner at al.[9]. In this paper, the samples used were grown by PAMBE, which may make these results more relevant to our devices. In this work, $Al_xGa_{(1-x)}N$ alloys covering the range $0<x<1$ were grown, and the refractive index was measured from optical transmission measurements

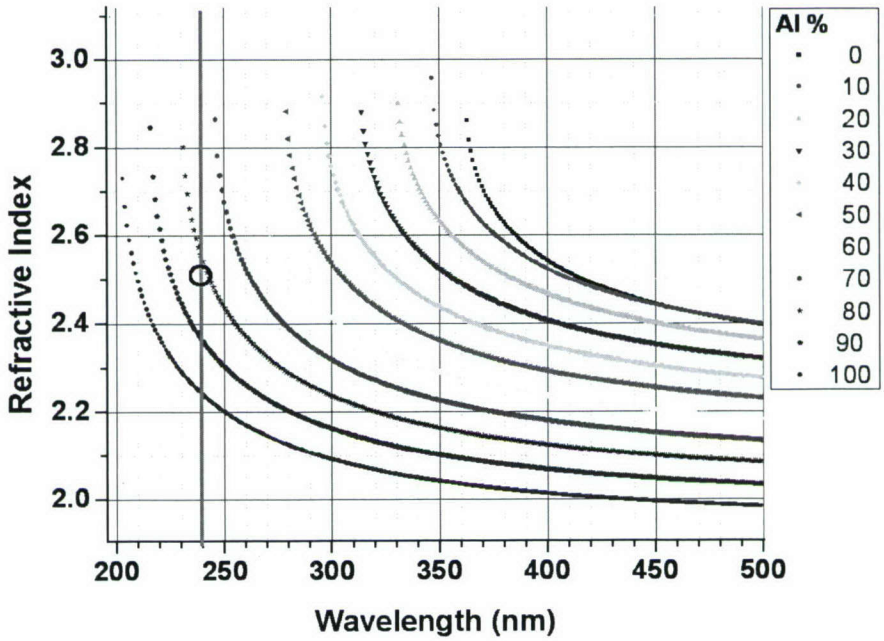

Fig 65: Refractive index as a function of AlGaN composition (Brunner et. al.)

[9] D. Brunner, H. Angerer, E. Bustarret, F. Freudenberg, R. Ho¨ pler, R. Dimitrov, O. Ambacher, and M. Stutzmann J. Appl. Phys. **82,** 5090 (1997)

The refractive index for AlGaN alloys with AlN mole fraction between 80% and 85%, which has been employed in our laser structures, is found to be about 2.5 at 240nm. It was seen however, that the fitting parameters provided in the paper, which we have used in order to extrapolate the refractive index data in the region close to 240nm, have quite large error bars. Therefore the data obtained by use of the given algorithm may also have a significant inaccuracy.

A more advanced approach was made by Tisch et. al [10], using spectroscopic ellipsometry. Here the samples were grown by MOCVD. The refractive index data was obtained using a 4-layer model, which took into account the buffer layer, the substrate, and the surface roughness. Also, the effect of band-tailing was taken into account, which generates a complex dielectric function, the imaginary part gaining prominence in the vicinity of the band-gap.

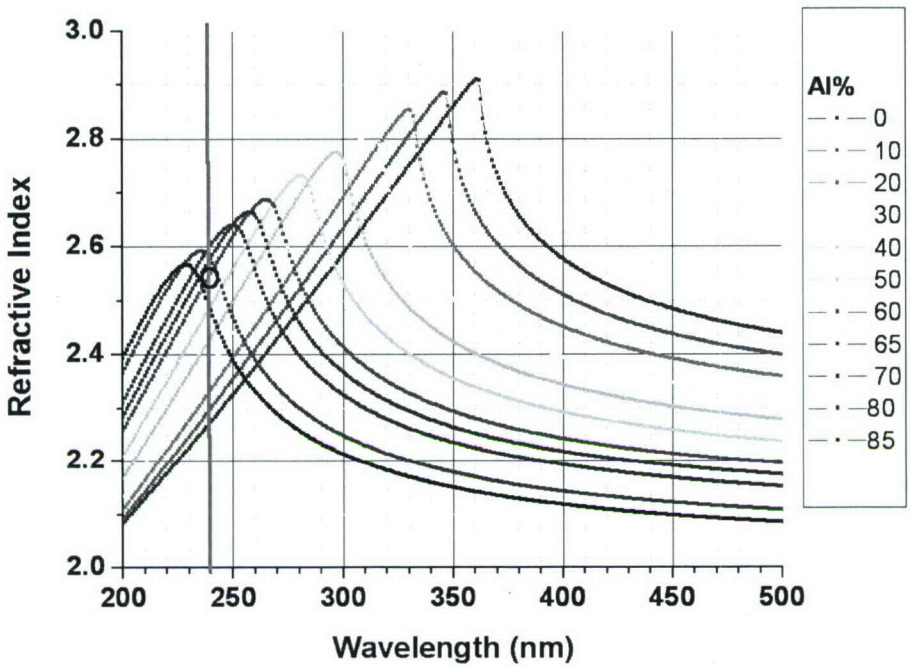

Fig 66: Refractive index as a function of AlGaN composition (Tisch et. al.)

The refractive index data however was presented in this paper for AlGaN alloys up to only 65% Al, and the curves obtained for higher Al content in Fig 8 was obtained by extrapolation using the algorithm provided. For AlGaN alloys with AlN mole fraction between 80 and 85%, the RI was found to be about 2.55.

From Fig 65 and 66, it is seen that the relevant refractive index for our laser structures is between 2.5 and 2.55 at 240nm.

[10] U. Tisch, B. Meyler, O. Katz, E. Finkman, and J. Salzman, J. Appl. Phys. **89,** 2676 (2001)

High Reflectivity Facet Coatings

Below is a graph of the high reflection coating applied to the end facets of the AlGaN die. These coated die were received in late 2005 and were be shipped to Astralux for die mounting on CuW submounts supplied by Photon Systems.

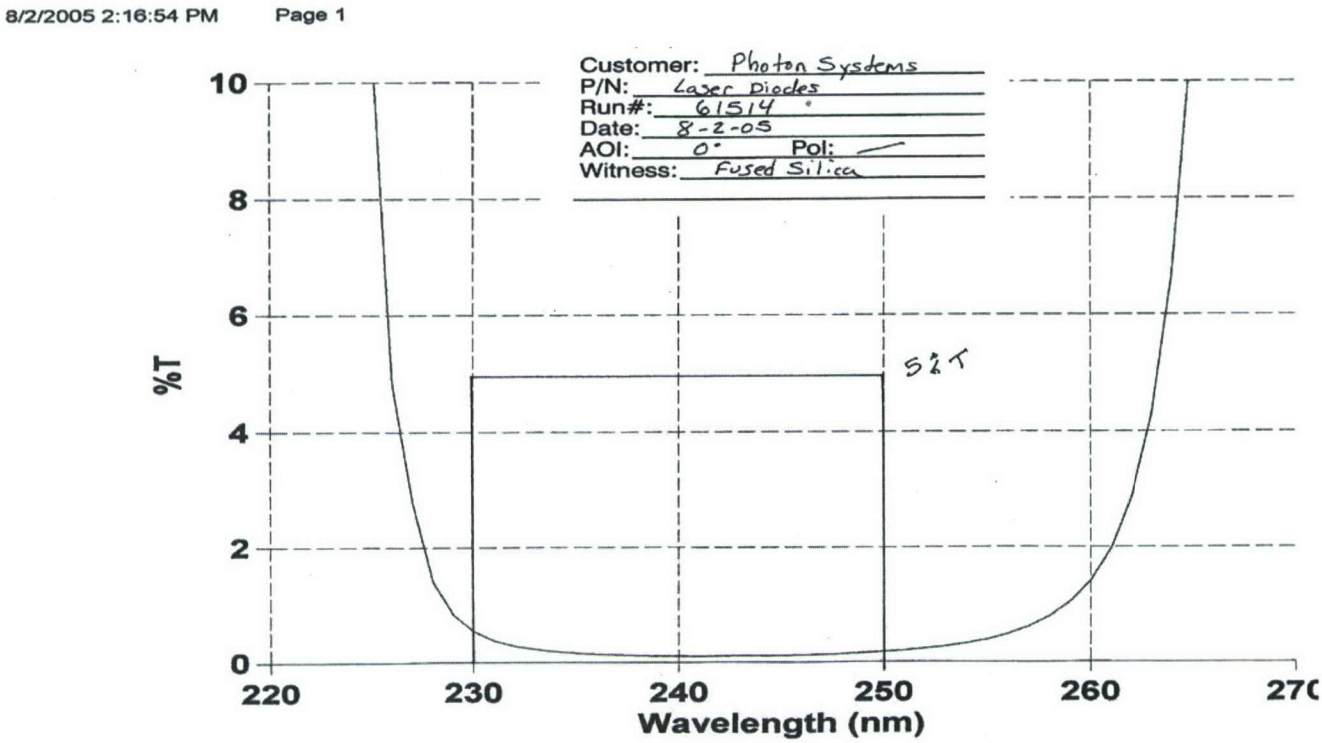

Figure 67. Transmission spectra of AlGaN end facet coatings

The threshold gain, gth, need to achieve lasing is give below

$$g_{th} = a_{int} + [1/2L][\ln(1/R_1R_2)]$$

where R1 and R2 are the reflectivity of the end facets. From Fig 10 above it is seen that the reflectivity is in the 0.1% or 10^{-3} range so, which allows enables laser action with much higher losses than normally allowed.

Summary of Key Parameters for Coated-facet $Al_xGa_{1-x}N$ Dice

A summary of key parameters for the coated-facet $Al_xGa_{1-x}N$ dice is shown in the table below. The die identification numbers correspond to the wafer numbers assigned by BU. The growth parameters are nominal values reported by BU. λ_{max} values were measured by CL spectroscopy at BU and/or Astralux for wafer samples prior to die processing. Cavity lengths were measured at Astralux using a calibrated length scale under an optical microscope.

Table . Summary of key growth, spectral, and processed parameters for the coated-facet $Al_xGa_{1-x}N$ dice produced to date in Phase II.

Die #	Layer Structure	Active Layer Al Content (%AlN)	Active Layer Thickness (nm)	CL λ_{max} (nm)	Approx. Cavity Length (μm)	Backside Metallization
1644e	GRINSCH	75	300	247-256	804	yes
1671e	GRINSCH-MQW	70	140 (50 MQWs)	231-233	824	no
1671m	GRINSCH-MQW	70	140 (50 MQWs)	231-233	766	yes
1671n1	GRINSCH-MQW	70	140 (50 MQWs)	231-233	773	no
1671n2	GRINSCH-MQW	70	140 (50 MQWs)	231-233	796	no
1683b	GRINSCH	80	250	240-250	1032	yes
1683c	GRINSCH	80	250	240-250	827	yes
1683d	GRINSCH	80	250	240-250	787	yes
1683e	GRINSCH	80	250	240-250	1150	yes
1787v	GRINSCH	78	170	238-240	773	no
1787w	GRINSCH	78	170	238-240	823	no

A total of eleven dice from four wafers had edge facets coated at MLD Technologies. The AlN content ranged from 70-80%, resulting in λ_{max} values from 231-256 nm. Some variation in λ_{max} for each wafer was observed as a function of position on the wafer and also excitation conditions. There is a significant amount of variation in cavity lengths due to poor control during notch formation, with most of the dice having lengths ~ 800 +/- 30 μm. Six of the dice have Cr/Au backside metallizations for identification of the epitaxial-side of the die, as well as to facilitate possible eutectic die bonding. From topview inspection under low magnification, the dice labeled 1671m and 1671n1 have the best cleaved edges with no significant imperfections visible at 100X magnification.

In the short-term, we plan to begin mounting the dice on submounts using Ag conductive adhesive rather than a eutectic solder because of shorter turnaround times for the first method and problems with high-vacuum compatibility for the solder/flux system used previously.

3.4.4 ESUVOS device design development

In order to make useful miniature ESUVOS devices it was understood early in the Phase I SBIR contract that field emitting electron sources would be needed. This would eliminate the issues with thermionic electron sources that included excess device power and heat related to heating the cathode and the related increase in size, weight, and power consumption of devices. Unfortunately, as of the writing of this final report, no supplier of field emission electron sources has been identified that can provide the required current density.

The original device design direction was not the most compact configuration possible. However, it was relatively easy to fabricate since it is an open frame design similar to a traditional butterfly pack used in the opto-electronics industry and employed an off-the-shelf diamond microtip array field emission electron source from Extreme Devices. The overall, finished device, view is shown below in Fig. 68. The laser beam is emitted from the side of the package through a brazed in sapphire window. Sapphire has the same thermal expansion coefficient as Kovar and provides an excellent hermetic seal.

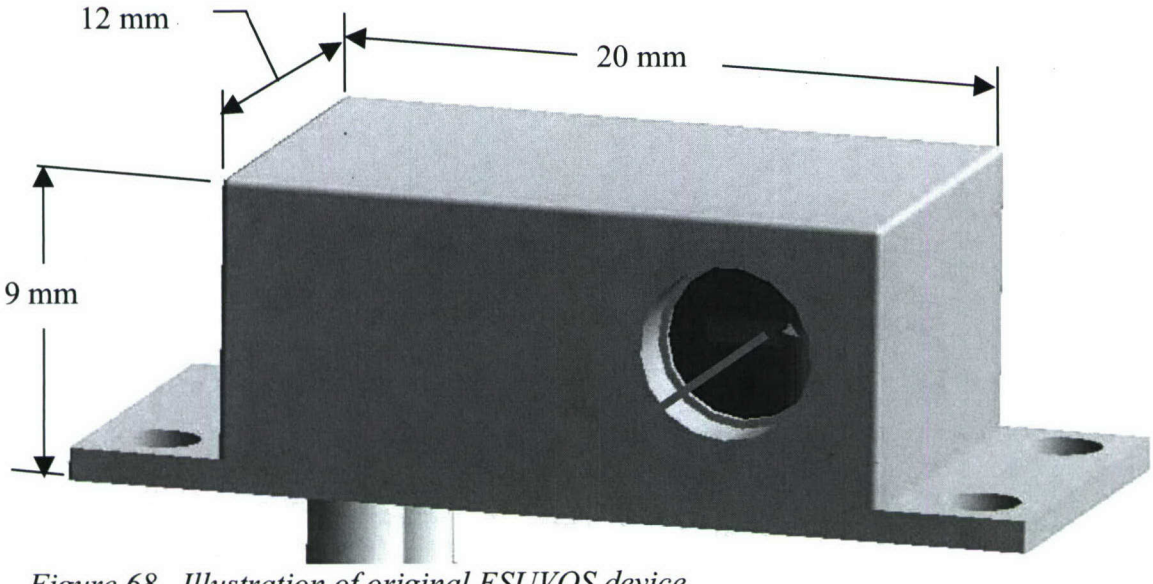

Figure 68. Illustration of original ESUVOS device

Below in Fig. 69 is an illustration of the internal assembly of the device with the copper substrate for the AlGaN die, electrostatic focusing lens, diamond microtip field emission array electron source and voltage divider resistors.

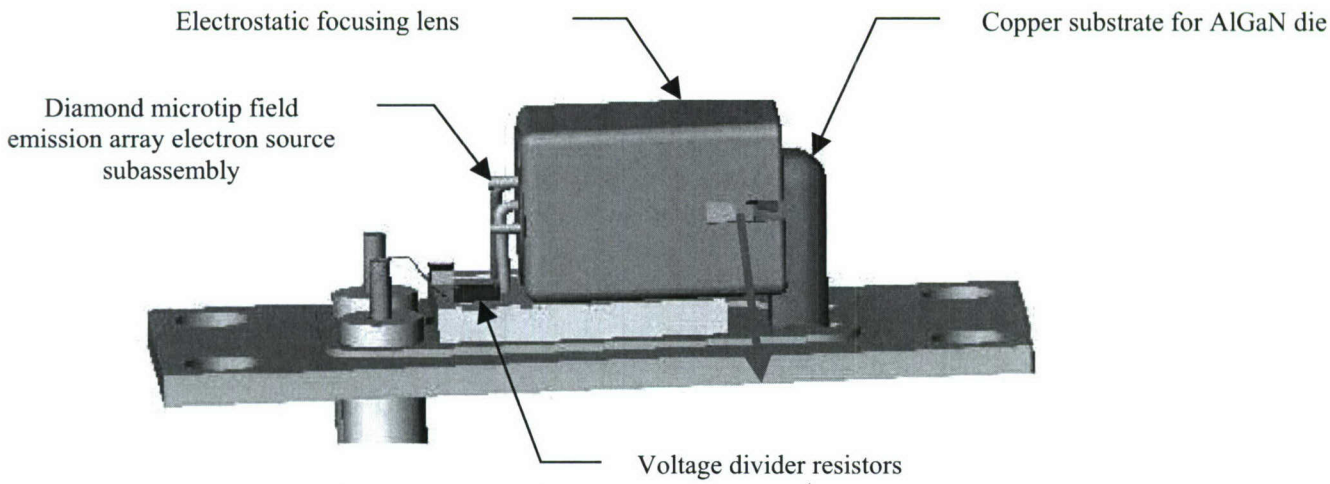

Figure 69. Internal components of ESUVOS

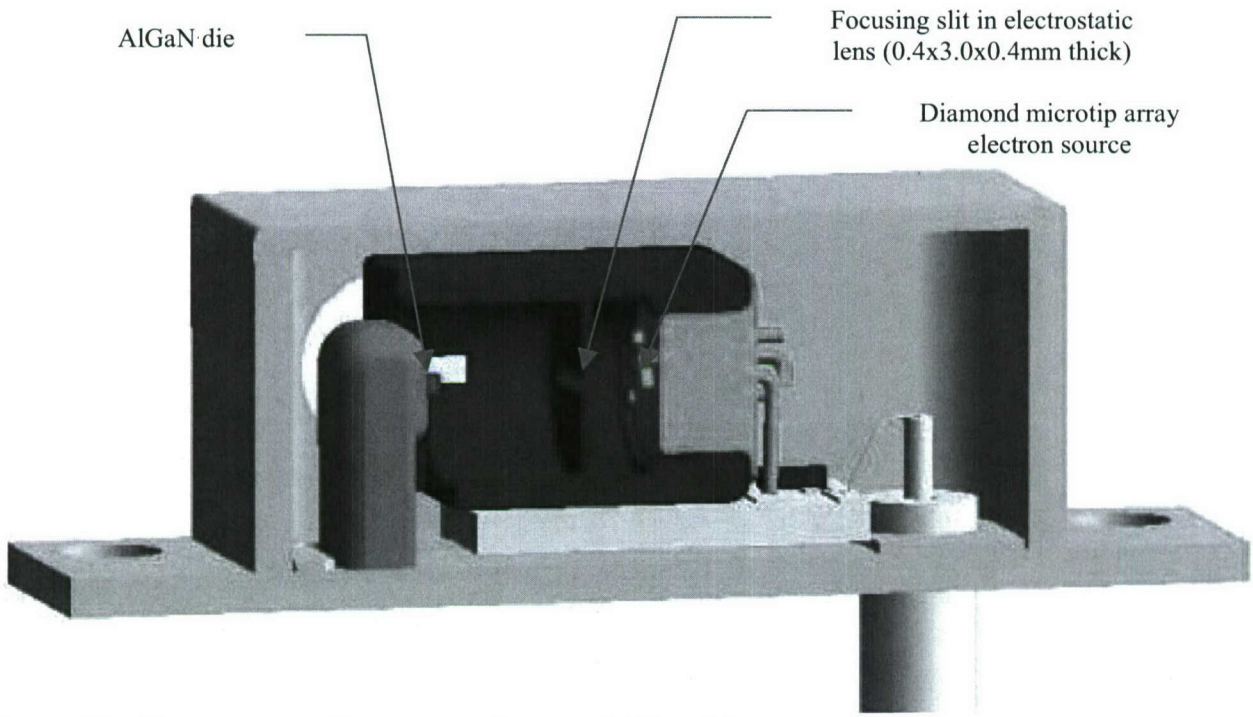

Figure 70. Cross-section illustration of original ESUVOS

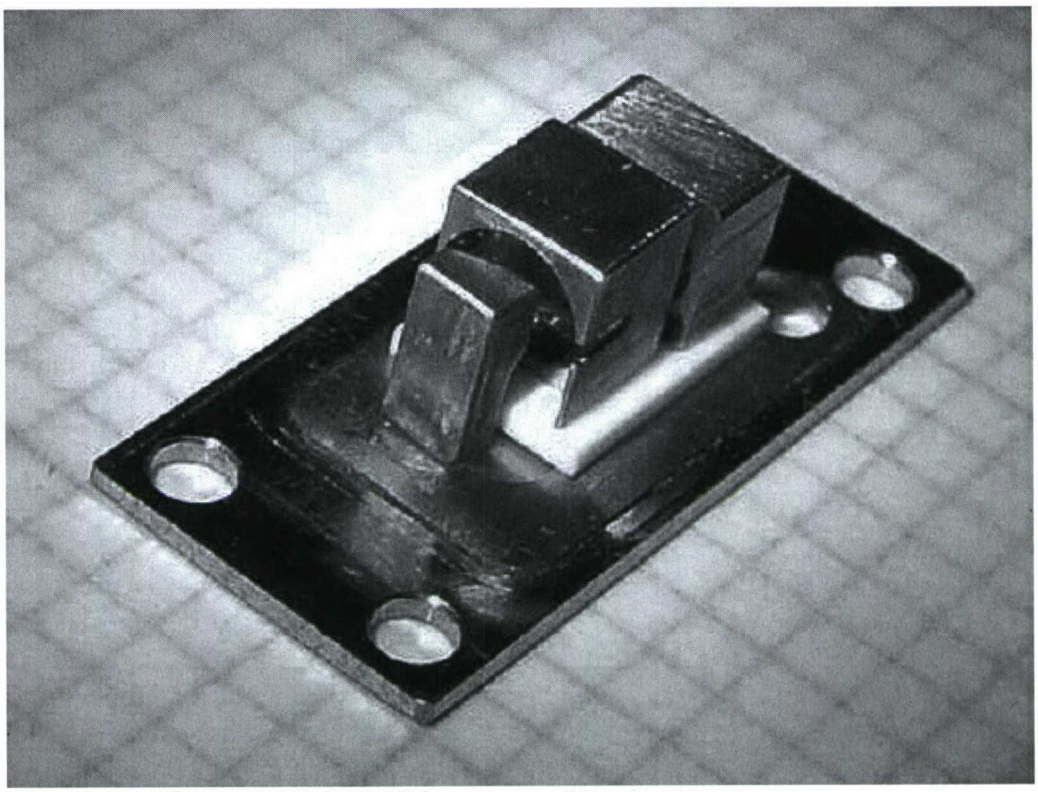

Figure 71. Photo of original ESUVOS base assembly

As described previously, Extreme Device, Inc., went bankrupt at the beginning of this Phase II contract and alternate plans needed to be developed for miniature devices using thermionic emission electron sources. Thus, the following is an analysis of what would be required to build a miniature thermionic emission electron gun for ESUVOS.

A. Summary

The following describes the design and evaluation of a miniature thermionic electron source and electrostatic lens system capable of producing a target current density from 1 to 10 $\mu A/\mu m^2$ over a rectilinear region approximately 2μm by 750μm. The output of the electron source may be controlled either by the cathode temperature (heater current) or by bias potential between cathode and lens electrode. The lens focal length is voltage controlled, and produces a rectangular cross section beam of constant long dimension (width) and variable aspect ratio (height).

The focus of this study is development of a thermionic egun design although it is eventually intended that a field emission source will be used to minimize power consumption and heat dissipation. This study does not address any thermally related issues caused by electron impact of the target material. The baseline design will employ Tungsten with 2% Thorium as the cathode although the general formulas developed in Sections 3 and 4 are sufficient to allow evaluation of other materials.

Design of the electrostatic lens was guided by a basic consideration to keep things as simple as possible, while developing a practical control strategy. Simply put, the lens would be designed to operate with lowest possible voltages for a given target potential and focal length. A set of design curves has been developed here that should make possible the construction of

devices with differing dimensions and hence focal lengths, while still obtaining the necessary beam current density at the target.

The electrostatic lens designs were then modeled using SimIon 7.0 an Ion Trajectory Software package published by the Idaho National Engineering and Environmental Laboratory (INEEL).

Finally, a simplified conceptual design is shown on a miniature electron optic bench, set up to function like an optical bench. Such an arrangement should allow evaluation of the various parts with the least investment in setup and pump down time.

Depending upon the success of the prototype in the UV application, future developmental work could involve design of a cold cathode or field emission source and with the requisite power supply and controls. Production and maintenance of the required high vacuum micro-environment will be an important challenge in the packaging of such a device.

B. Overview and Objectives

Basic Design Premises

The electron source under consideration was specified to produce a current density at the target from 1 to 10 μA per μm^2, over a narrow line of approximately 2 by 750 μm. The source material was also specified to be tungsten with a 2% thorium content This material has a significantly lower work function than pure tungsten, which results is a lower cathode temperature for the same output current. The actual cathode material was cylindrical in cross section and 0.5 mm in diameter. A nominal design length was to be about 1.2 cm. The cathode would be heated by passing a current through the cathode rod. These basic specifications constitute the basic design parameter of the source, and guided the general development of the following information. Table 1 summarizes the electron source requirements.

Table 1
Electron Source Requirements for edge emitting ESUVOS

Target Current Density (j) :	1 to 10 $\mu A/\mu m^2$ [100 – 1000A/cm^2]
Target Size:	2μm high x 750μm long
Target Area (A) :	1500 μm^2 [1.5x 10^{-5} cm^2]
Target Current (I = j A) :	1.5 to 15mA
Diameter of Cathode:	0.5 mm [0.05 cm]
Length Of Cathode:	1.2 cm
Cathode Surface Area:	0.1885 cm^2
Cathode material:	Tungsten – with 2% Th.

Target Current Density

The required target current density is established by focusing the electron beam. The target beam current is the product of target current density times effective target area, or the beam footprint at the target.

(1) $$\mathbf{I_{target} = j_{target} \times A_{target}}$$

$$\mathbf{I_{target} = (1 - 10\ uA/\mu m^2) \times (\ 1500\ \mu m^2\ )}$$

$$\mathbf{I_{target} = 1.5 - 15\ mA}$$

Some amount of reserve margin is desirable in case the beam overfills the target at target plane. A suitable reserve margin is best determined from experimental results, as excessive current on the target will result in increased substrate (target) heating and device degradation.

Source Current

The gross source current must obviously equal the target beam current plus any intercepted part of the beam (clipping) caused by the beam overfilling the lens aperture(s). Further, with a cylindrical source as provided here, the emission will be distributed around the circumference of the source. Use of a *repeller* electrode at a potential slightly negative to the cathode, will reverse backwards emitted electrons.

If the repeller surrounds the cathode concentrically, except for an opening in the direction facing the lens aperture, then the electrons are collected from all regions of the periphery and presented to the lens, which approximately doubles the actual cathode current density.

From Table 1, the cathode must provide a current of at least 1.5 to 15 mA. Also from Table 1 the surface area of the cathode is 0.1885 cm^2. Using equation (2) we determine the cathode current density to be in the range of

(2)

$$\mathbf{J_{cathode} = I_{source} / Area_{cathode}}$$

$$\mathbf{= (1.5 \text{ to } 15\ mA)/\ 0.1885\ cm^2}$$

$$\mathbf{= 7.958 \text{ to } 79.58\ mA/cm^2}$$

The lens must then focus this current down to a line 2 microns high by 750 microns long. Ideally the lens will not intercept any of the electrons, keeping the source current and component heating to a minimum.

The next section will present the basic equations for thermionic emission of electrons and results for a range of cathode types.

C. Characteristics of Thermionic Sources

Thermionic Emission - The Richardson-Dushman Equation

Electron emission from a heated metal is governed by the temperature of the metal surface and by the work function of the metal. Equation (3) is a standard form of the Richardson –Dushman equation which relates the cathode current density **J** to the cathode temperature (**T**) in Kelvins and the cathode work function φ

(3)

$$\mathbf{J = A\ T^2\ exp\ [-\varphi/\kappa T\ ]}$$

The constant **A** is derived from basic physical parameters, as follows and has the value of approximately **120**, although Rosebury, [1] states the value is 60.2 for all pure metals, and can be "much higher" for impure metals. When **J** is in amperes per square meter, **A** is determined from equation (4).

(4) $$A = 4\pi m\kappa^2 eh^3$$

$$= 1.19909 \text{ X } 10^6 \text{ amperes/m}^2$$

$$\underline{A = 119.909 \text{ A/cm}^2}$$

where **m** is electron mass = 9.11×10^{-31} kg, **e** = electronic charge 1.6×10^{-19} coulomb, **k** = 1.38×10^{-23} joules/Kelvin, and **h** is Planck's constant 6.626×10^{-34} joule-sec. The difference in value of A given by Rosebury and that shown in (4) above is in the coefficient of 2 or 4 in front of pi. We use here the lower figure to be conservative. The significance of the two values for the constant, is virtually lost in the enormous effect of the exponential term in equation (3).

Data obtained using equation (3) is shown in Table 2 and Figure 1., for several values of work function, corresponding to common cathode materials. Temperatures range from 1000 K through 3000K. Current densities are in amperes per cm^2 .

Table 2.
Values of Thermionic Current Density for various Work Functions.
The Richardson Coefficient A is 60.2.
Current density is in Amperes/cm^2

T - K	1.00 eV	1.50 eV	2.50 eV	2.60 eV	4.25 eV
1.000E+03	5.581E+02	1.699E+00	1.575E-05	4.944E-06	2.454E-14
1.100E+03	1.937E+03	9.985E+00	2.655E-04	9.257E-05	2.613E-12
1.200E+03	5.545E+03	4.435E+01	**2.836E-03**	**1.080E-03**	1.298E-10
1.300E+03	1.368E+04	1.586E+02	**2.132E-02**	**8.744E-03**	3.579E-09
1.400E+03	2.999E+04	4.780E+02	**1.215E-01**	**5.310E-02**	6.215E-08
1.500E+03	5.977E+04	1.256E+03	5.541E-01	2.559E-01	7.446E-07
1.600E+03	1.102E+05	2.948E+03	2.108E+00	1.022E+00	6.595E-06
1.700E+03	1.905E+05	6.305E+03	6.905E+00	3.492E+00	4.553E-05
1.800E+03	3.120E+05	1.248E+04	1.995E+01	1.048E+01	2.552E-04
1.900E+03	4.878E+05	2.311E+04	5.187E+01	2.818E+01	1.200E-03
2.000E+03	7.332E+05	4.046E+04	1.232E+02	6.901E+01	4.861E-03
2.100E+03	1.065E+06	6.747E+04	2.707E+02	1.559E+02	1.731E-02
2.200E+03	1.502E+06	1.079E+05	5.562E+02	3.285E+02	5.518E-02
2.300E+03	2.065E+06	1.662E+05	1.078E+03	6.512E+02	1.596E-01
2.400E+03	2.773E+06	2.480E+05	1.983E+03	1.224E+03	4.242E-01
2.500E+03	3.650E+06	3.595E+05	3.488E+03	2.194E+03	1.046E+00
2.600E+03	4.719E+06	5.081E+05	5.891E+03	3.773E+03	2.414E+00
2.700E+03	6.002E+06	7.019E+05	9.599E+03	6.249E+03	5.250E+00
2.800E+03	7.524E+06	9.500E+05	1.514E+04	1.001E+04	1.083E+01
2.900E+03	9.309E+06	1.262E+06	2.321E+04	1.556E+04	2.131E+01
3.000E+03	1.138E+07	1.650E+06	3.465E+04	2.355E+04	4.017E+01

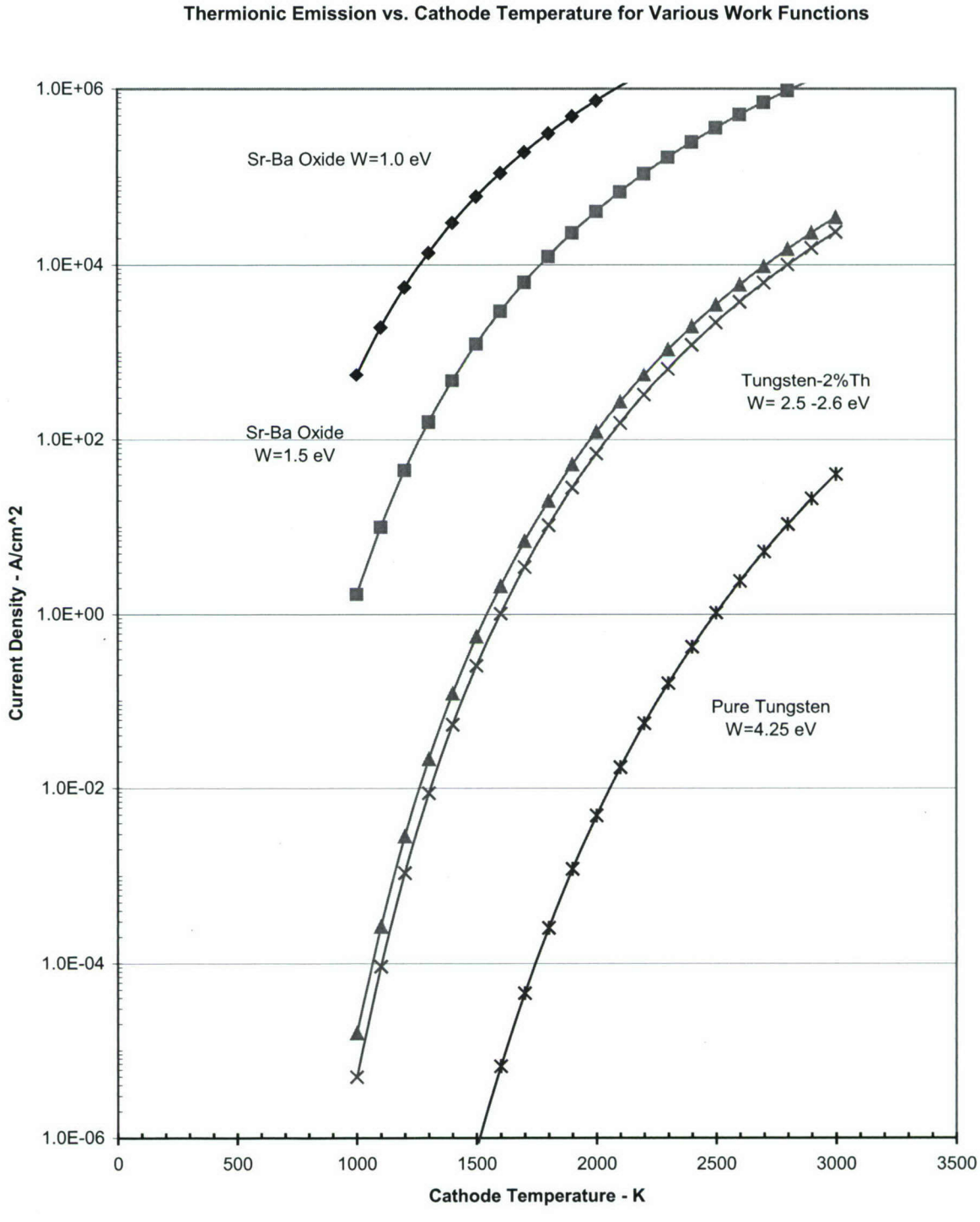

Figure 72. *Thermionic emission current density plotted versus surface temperature for several values of work function. It can be seen that 2% thoriated tungsten with a work function of 2.5 to 2.6 eV provides the required range of emission current density (7.958 to 79.58 mA/cm^2 at temperatures near 1400 K. For comparison, a tri-carbonate cathode would achieve the same current densities below 1000 K .*

Child-Langmuir Space Charge Limitations

The Richardson-Dushman equation contains the tacit assumption that all emitted electrons are drawn away from the cathode surface by the anode field, so that no build up of charge occurs. If the anode field is not strong enough, the emitted electrons will develop a local field that will reduce the cathode emission. Under such conditions the current is said to be space charge limited. The Child-Langmuir equation describes the relation between anode - cathode potential and the resulting current density at the cathode. The equation is sometimes known as the 3/2's power law, because of the voltage dependent term.

(4) $$J = 4/9\ \varepsilon_\circ\ (2e/m)^{1/2}\ V^{3/2}\ d^{-2}$$

where $\varepsilon_\circ = 8.85 \times 10^{-12}$ F/m, the permitivity of vacuum; **e** is the electronic charge; **m** is the mass of the electron, **V** is anode to cathode voltage in volts, and **d** is the anode to cathode spacing in meters. Table 3 gives values of current and current density for an assumed anode to cathode spacing of 1 cm, over a range of voltages from 1.0 V to 50,000 volts. Figure 2 plots these data.

Table 3

Space Charge Limited Current and Current Density for the 2% Th –Tungsten cathode at a spacing of 1 cm. These data are calculated for a uniform electric field between cathode and anode.

VOLTAGE V – volts	Cur. Density j - a/cm^2	Current I- amps
1.000E+00	2.340E-06	4.411E-07
2.000E+00	6.619E-06	1.248E-06
5.000E+00	2.616E-05	4.931E-06
1.000E+01	7.400E-05	1.395E-05
2.000E+01	2.093E-04	3.945E-05
5.000E+01	8.273E-04	1.559E-04
1.000E+02	2.340E-03	4.411E-04
2.000E+02	6.619E-03	1.248E-03
5.000E+02	2.616E-02	4.931E-03
1.000E+03	7.400E-02	1.395E-02
2.000E+03	2.093E-01	3.945E-02
5.000E+03	8.273E-01	1.559E-01
1.000E+04	2.340E+00	4.411E-01
2.000E+04	6.619E+00	1.248E+00
5.000E+04	2.616E+01	4.931E+00

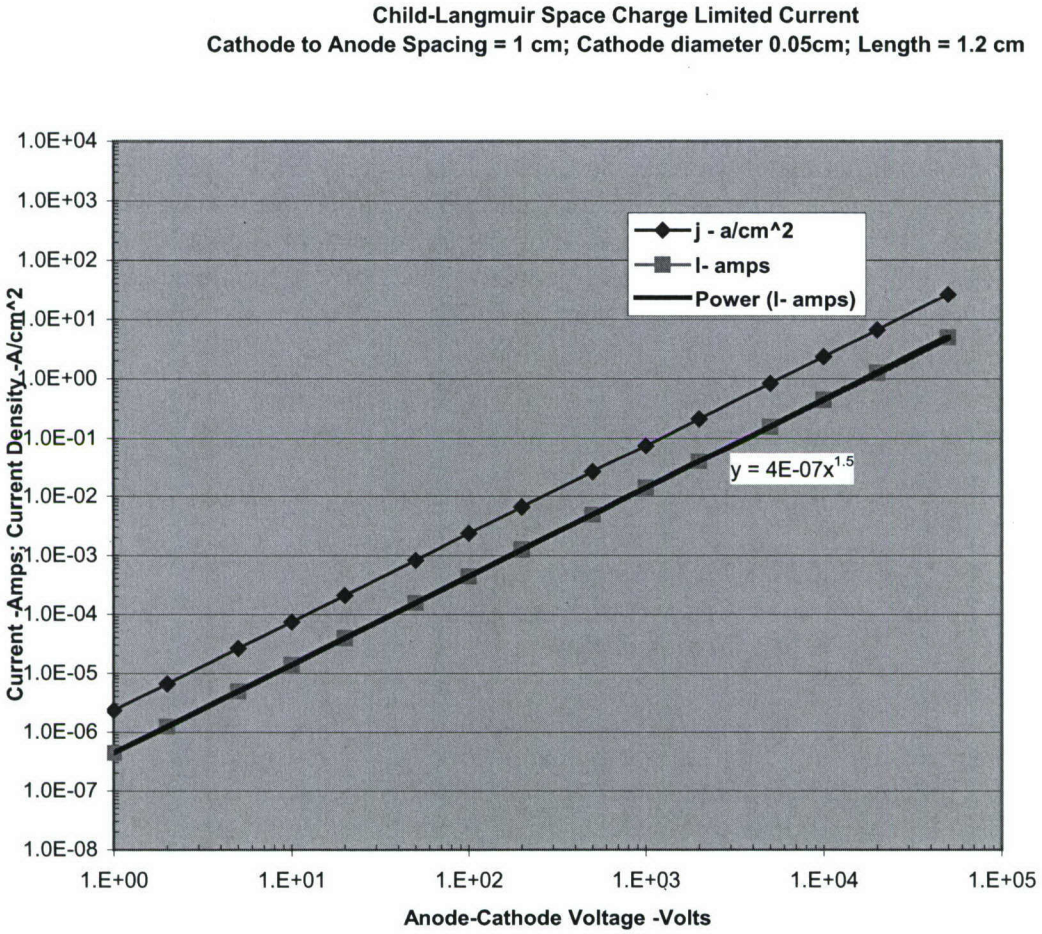

Figure 73 *The Child – Langmuir space charge limited current and current density is plotted against Anode – Cathode voltage. For the current densities required, (7.58 to 75.8 mA/cm^2), voltages in the range of 200 to 1000 volts are necessary. This sets the minimum values for anode voltage and indicates that at low focus voltages, the cathode current density may be space charge limited.*

For a cylindrical cathode and anode arrangement, the electric field is non-uniform, varying as 1/r. For a 1cm anode spacing (1 cm radius anode electrode), with the 0.05 cm diameter cathode (0.025 cm radius), the electric field given by equation (5a & 5b) below is seen to be

(5a) $\mathbf{E_{cath}}$ **= V/(r x ln(R/r))**
= V/(.025 x ln(1/.025))
= V/(.025 x 3.6888)
= <u>10.843 volts /cm per volt</u> at the cathode surface.

(5b) $\mathbf{E_{anode}}$ **= V/(1.0x3.6888)**
= <u>0.27 volts/cm per volt.</u> at the anode surface.

The uniform field of planar electrodes of similar spacing

(6) $\mathbf{E_{unif} = V/D}$
$\mathbf{= V/1.0}$
$\mathbf{=}$ **1 Volt/cm per volt, throughout the region.**

Comparing (5a), (5b) and (6), it can be seen that the uniform field of the planar configuration falls between the electric fields at the cathode and anode in the cylindrical configuration. To determine whether a space charge limitation occurs with cylindrical configuration, we compare the mean electric fields of the two configurations. For the uniform field geometry, the electric field is the same everywhere. For the cylindrical geometry, we use the geometric mean field which is the square root of the cathode/anode electric field ratios. From equations 5a and 5b above,

(7) $\mathbf{E_{mean\text{-}geo.} = [\, E_{cathode} / E_{anode} \,]^{1/2} \times E_{anode}}$

$\mathbf{= [\, 10.8/0.27 \,]^{1/2} \times E_{anode}}$

$\mathbf{= 6.32 \times 0.27}$ **V/cm per volt**

$\mathbf{= 1.707}$ **V/cm per Volt.**

which is greater than the uniform field of the planar geometry. This shows the cylindrical geometry should not be restrictive from space charge considerations. By using the current density under uniform field conditions, to set the cathode current density under cylindrical field conditions, a comfortable margin of safety is given for the necessary extraction voltage.

D. Design of Thermionic Sources

Source Drive Current, Voltage and Power

To determine the current required to bring the cathode up to the temperature for thermionic emission, we consider the cathode to be in thermal equilibrium with its surroundings. That is to say the power dissipated in the resistive heating is in balance with the power conducted and radiated away from the cathode structure.

For a conservative simplicity, it is common to ignore conducted heat transfer, as a first approximation, since it will depend heavily on the exact manner in which the cathode is mounted in the device.

By considering thermal radiation to be the only heat removal mechanism, we obtain the lowest figures for cathode heating power.

The Stefan-Boltzmann equation describes the radiative heat transfer from a surface of specified temperature and emissivity.

(8) $\mathbf{P_{radiated} = \sigma\varepsilon\,(\,T_H^4 - T_{amb}^4\,)}$ **watts/cm^2**

σ, the Stefan-Boltzmann Coefficient = 5.6696 x 10^{-12} w/cm^2 /K^4 ; **ε** is the surface emissivity; $\mathbf{T_H}$ is the high temperature surface (cathode) while $\mathbf{T_{amb}}$ is the ambient temperature. A black body radiator has an emissivity of 1.000.

Data from equation **(8)** and actual measured radiated power are shown in figure 74., below, and in Table 4.

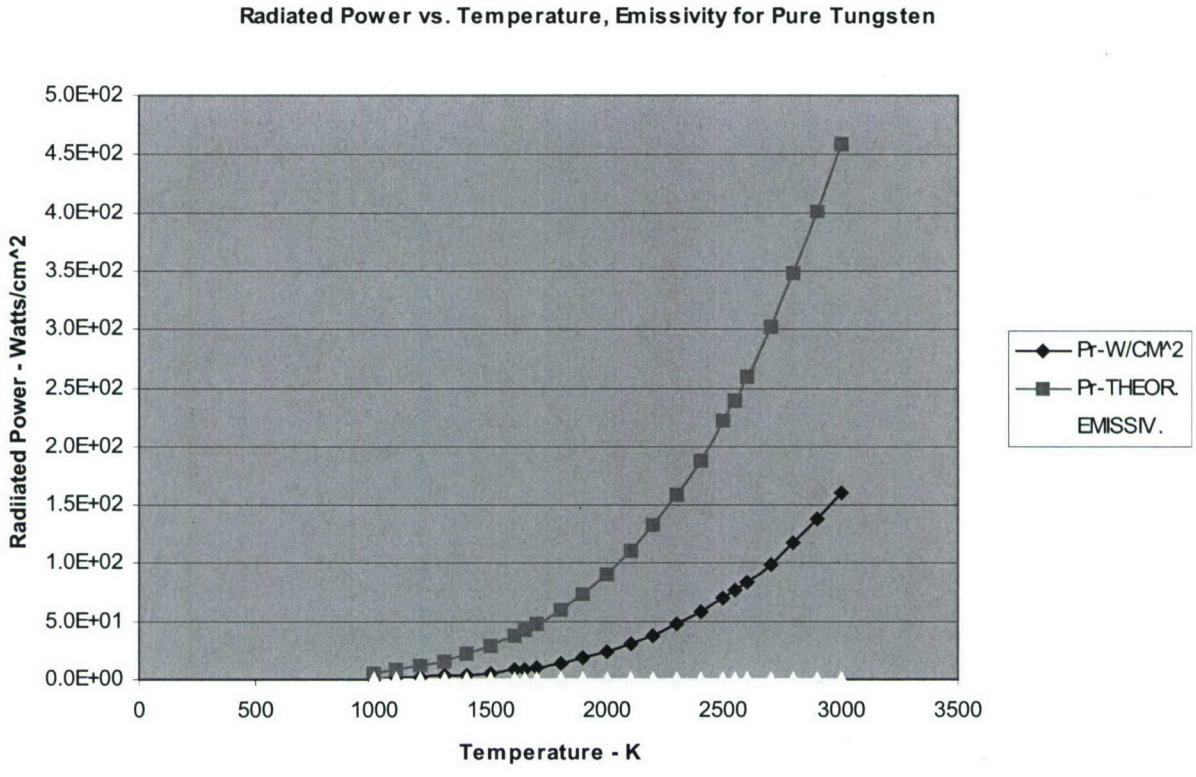

Figure 74. *Radiated Power from Tungsten at temperatures from 1000 to 3000K. The upper curve is for emissivity of 1.00, the lower curve is measured radiated power.*

Table 4
Theoretical and Measured Values of Radiated Power in Watts / cm^2 for Tungsten.

Temperature K	**Measured W/CM^2**	**Theoretical W/CM^2**
1.000E+03	6.020E-01	5.624E+00
1.100E+03	1.027E+00	8.255E+00
1.200E+03	1.660E+00	1.171E+01
1.300E+03	2.570E+00	1.615E+01
1.400E+03	3.830E+00	2.173E+01
1.500E+03	5.520E+00	2.866E+01
1.600E+03	7.740E+00	3.711E+01
1.700E+03	1.062E+01	4.731E+01
1.800E+03	1.419E+01	5.947E+01
1.900E+03	1.864E+01	7.384E+01
2.000E+03	2.404E+01	9.067E+01
2.100E+03	3.050E+01	1.102E+02
2.200E+03	3.820E+01	1.328E+02
2.300E+03	4.720E+01	1.586E+02
2.400E+03	5.770E+01	1.881E+02
2.500E+03	6.980E+01	2.214E+02
2.600E+03	8.380E+01	2.590E+02
2.700E+03	9.960E+01	3.013E+02
2.800E+03	1.176E+02	3.484E+02
2.900E+03	1.378E+02	4.010E+02
3.000E+03	1.605E+02	4.592E+02

The ratio of theoretical to measured emission is the definition of surface emissivity at that temperature. Figure 75 plots the ratio of the curves in figure 74.

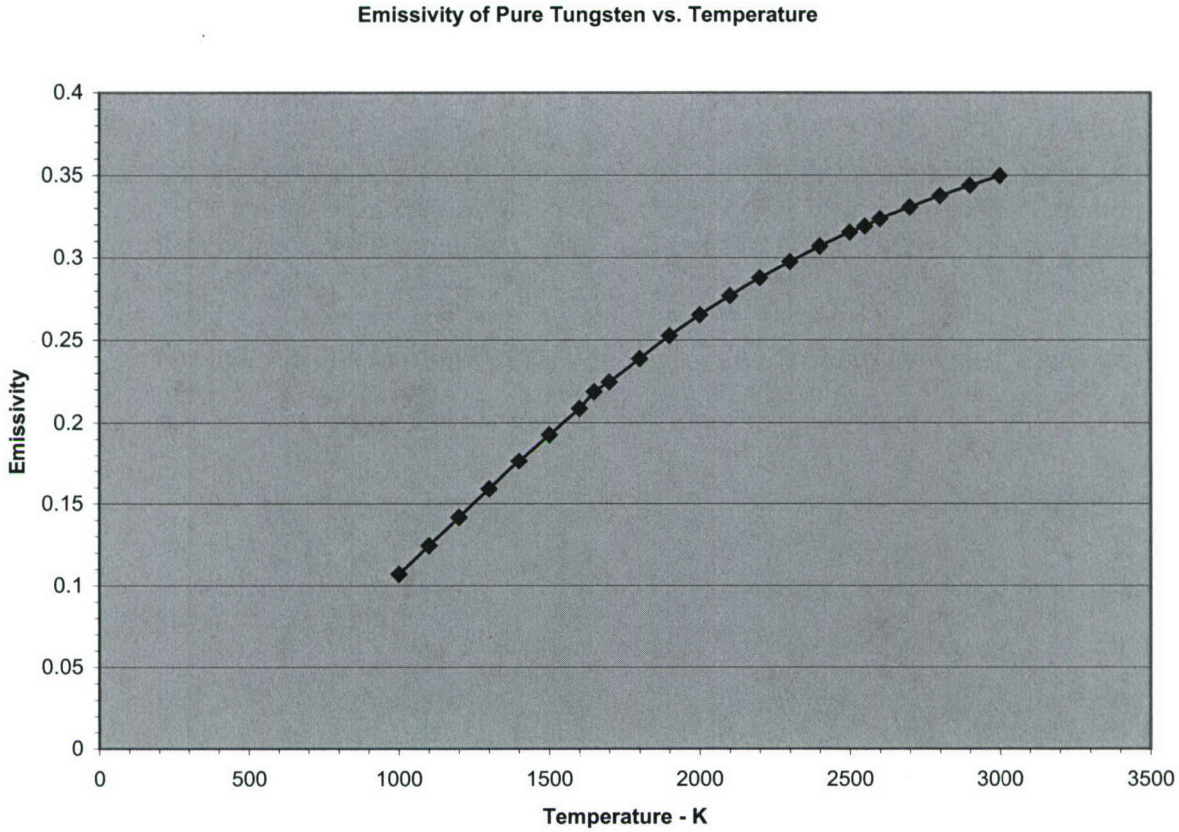

Figure 75. *Emissivity of Tungsten between 1000 and 3000 K.*

To determine the electrical power required to heat the cathode to a particular temperature, a heat balance equation is set up between the input power in equation (9) and the radiated power in equation (8). This is shown in equation (10), next.

(9) $P_{resistive} = I^2 R(T_H)$

$= I^2 Rho(T_h) L/A_{xcath}$

(10) $P_{resistive} = P_{radiated}$

$I^2 R(T_H) = \sigma\varepsilon A_s (T_H^4 - T_{amb}^4)$

where $R(T_H)$ is electrical resistance at the cathode temperature, and $Rho(T_H)$ is electrical resistivity at the cathode temperature, L is cathode length, and A_{xcath} is the cross sectional area of the cathode.

Figure 76 shows the tabulated values of resistivity for pure Tungsten, and calculated values of Tungsten alloy with 2% Thorium, over the temperature range from 1000 to 3000 K. It can be seen that the relationship between resistivity and absolute temperature is essentially linear for

both, from temperatures in excess of about 300K. A simplified expression, valid in the range of 1000 – 3000 K is given by curve fit, in (11) for pure Tungsten.

(11) $$\textbf{Rho (T)} = 3 \times 10^{-8}\, T - 10^{-5} \quad \textbf{ohm cm.}$$

Note the point of "inferred" zero resistance, at 300 K is not a physical result. At this temperature, Tungsten actually has a resistivity of approximately 5.49 x 10^{-6} ohm cm. By restricting temperatures to above 1000 K, however, the expression is sufficiently accurate for design use here.

As no tabulated data were found for the resistivity of 2% Thorium alloy tungsten, an

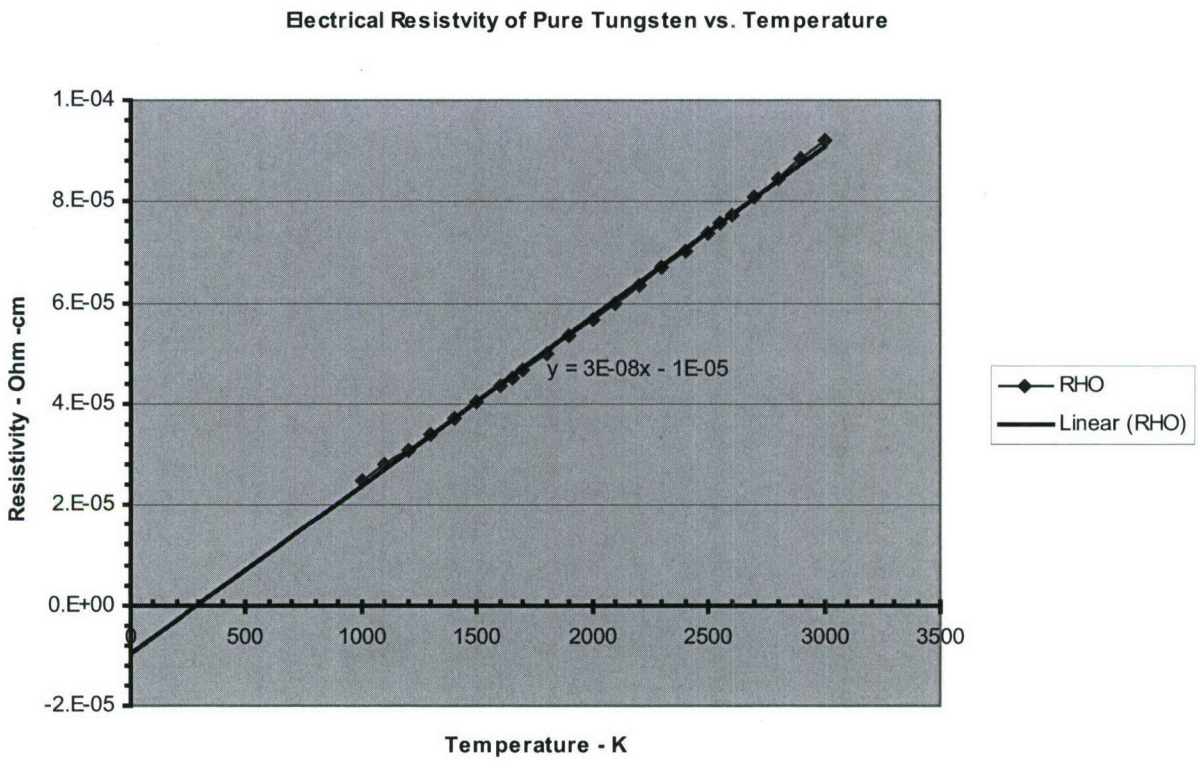

Figure 76. *The variation of resistivity of pure Tungsten as a function of temperature is nearly linear, at higher temperatures, having a curve fitted equation of Rho(T) = (0.03T – 10) micro-ohm cm. An "inferred" zero resistivity, is shown by the intercept at about 300K . Use of this point simplifies calculations of high temperature resistivity.*

equivalent resistivity at 20 C was calculated by combining the two resistivities in proportion to the alloying ratios. Using values at 20 C, the effective resistivity is a weighted average of 98% Tungsten at 5.49 micro-ohm cm and 2% Thorium at 14.7 micro-ohm cm. The result, shown in (12) is approximately 3% higher than pure tungsten.

(12) $\mathbf{Rho_{w\text{-}2\%Th} = [0.98 \times 5.49 + 0.02 \times 14.7] \times 10^{-6}\ ohm\text{-}cm}$
$\mathbf{= 5.674 \times 10^{-6}\ ohm\ cm.\ \ at\ 20\ C}$

(13) $\mathbf{Ratio = 5.674/5.49 = 1.0335}$

Some variation in Tungsten resistivity occurs depending on heat treatment and processing. This refinement, noted here, is not used in the cathode heating power equations. The effect of a small increase in overall resistivity is helpful toward lowering cathode heater current.

The 2% Thorium in the tungsten alloy presumably makes some effect on surface emissivity, too, but no data were found for that effect. Thorium reduces the effective work function to about 59% of the value for pure Tungsten (from 4.25eV to about 2.5eV), which may be indicative of the magnitude of emissivity change. This being the case, the predicted currents for reaching a particular cathode temperature should be used with some caution, as they may be low.

Combining equation (10) with (12) the temperature coefficient of resistivity, and solving for current gives the full expression for heater current under radiative heat balance.

(14) $$I^2 = \frac{\sigma\varepsilon\, A_{xcath}\, A_s\, (T_H^4 - T_{amb}^4)}{Rho(T_H)\, L}$$

(15) $$I^2 = \frac{3\times10^{-8}\, (\sigma\varepsilon\, A_{xcath}\, A_s\, (T_H^4 - T_{amb}^4))}{(T_H - 333.3)\, L}$$

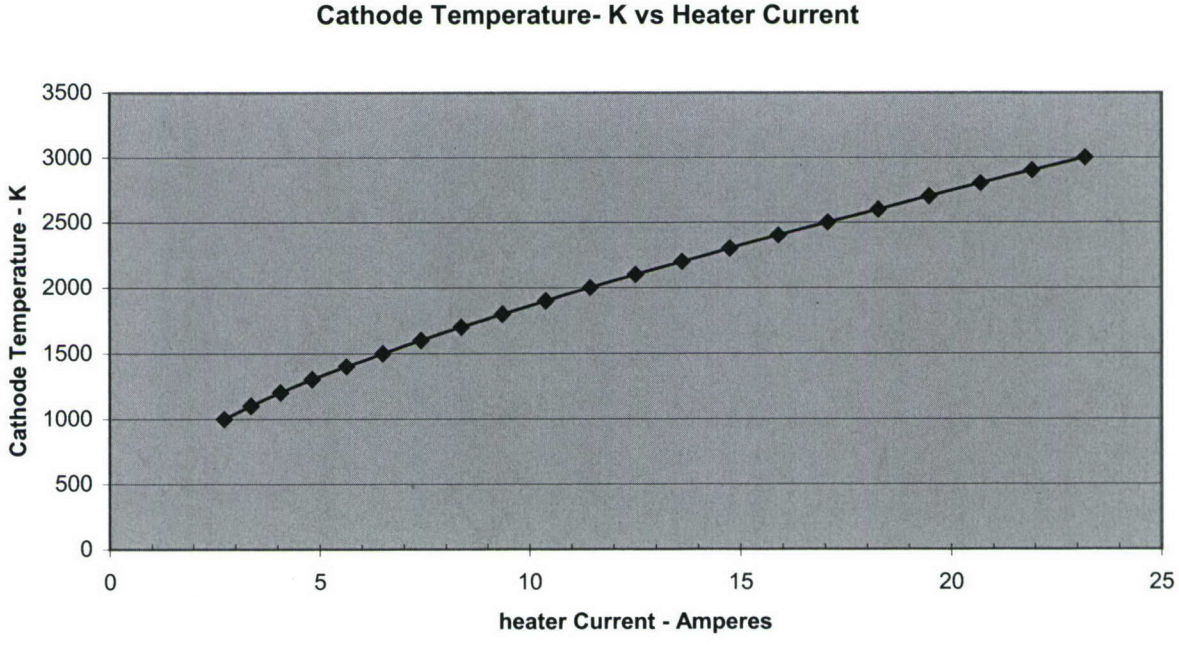

***Figure** 77. Cathode Temperature vs Heater Current for the 0.5 mm dia. Tungsten Cathode. Figure 77 plots the results of equation (15) for the specified 0.5mm diameter Tungsten-2%th directly heated cathode. Results for smaller diameter heaters would be above the curve drawn.*

Vapor Pressure Considerations

One last item of consideration is the vapor pressure of the heated tungsten cathode. At high temperature, it can be a factor that affects the useful life of a sealed system. At cathode temperatures, above 2500 K the evaporation rate of the cathode material, can be high enough to overwhelm getters or even a pumped system. The evaporated cathode material (Tungsten) will coat insulating surfaces, creating conducting paths that will short out the anode potential. Figure 7 plots tabulated vapor pressure data for pure Tungsten over the temperature range of 1000 to 3000 K. A pressure of 10^{-8} Torr is a practical *upper* limit for a sealed vacuum system. Pressures as high as even 10^{-6} Torr may be practical for a continuously pumped system for testing purposes.

These pressures set maximum operating temperatures for the cathode of 2400 and 2600 K respectively. Thermionic limits are much lower, in the range of 1400 to 1500 K, making the cathode evaporation insignificant.

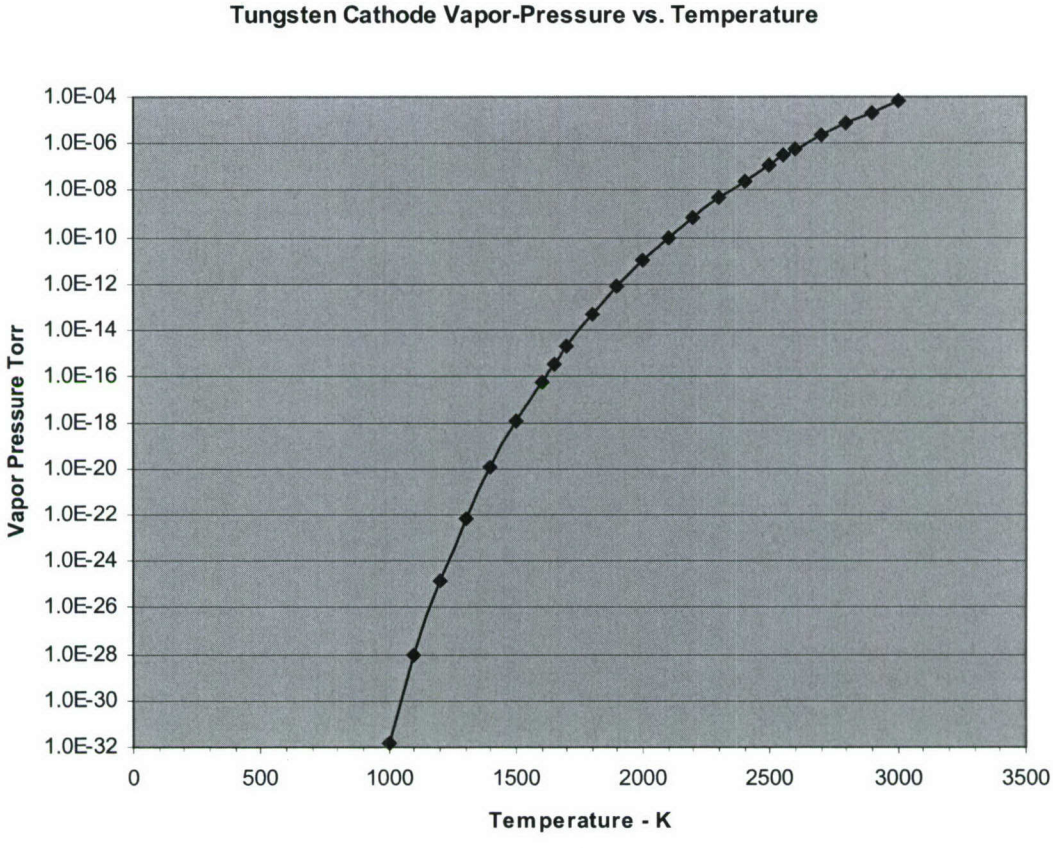

Figure 78 *The vapor pressure of tungsten increases very rapidly as the temperatures rise above 1000K. Cathode temperatures in excess of ~2400 K will cause vapor pressures that would compromise the vacuum conditions in a sealed system. Above about 2600 K, even a continuously pumped system, could be overwhelmed. A Tungsten cathode with 2% Th would operate below 2000K and create no evaporation problems.*

Operating Parameters of Tungsten w/2% Thorium Cathode

It is useful in designing the electron gun to have an expression relating cathode ***heater current*** to the cathode ***emission current***. This requires combining the Richardson-Dushman equation (3) and the general heat balance equation (15). Multiplying equation (3) by $\mathbf{A_s}$ the surface area of the cathode, gives (16), the cathode emission current as function of Temperature.

(3)
$$\mathbf{J_{cath}} = A\,\mathbf{T^2}\ \mathbf{exp}\ [-\varphi/\kappa\mathbf{T}\ ]$$
$$\mathbf{I_{cath}} = \mathbf{J}\ \mathbf{A_s}$$

(16)
$$\mathbf{I_{cath}} = \mathbf{A_s}\,A\,\mathbf{T^2}\ \mathbf{exp}\ [-\varphi/\kappa\mathbf{T}\ ]$$

In order to combine equations (15) and (16), it is necessary to first obtain a solution in one of them for temperature T. Then that expression can be substituted into the remaining equation to make the general relational expression.

However, neither equation (15) or (16) is easily solved for T. The presence of the thermal variation of resistivity in the denominator of (15) turns the 4th power expression for T into a general third order polynomial in T, for which the roots need to be extracted. One possible simplification is to neglect $T_{amb.}$ in the numerator, which then leaves only an expression in $T_H{}^4$. This gives an error of 1% or less for temperatures above 1000 K. But the basic difficulty in extracting the roots of T_H still remain.

Equation (17) shows the general form that results, neglecting $(T_{amb}\ )^4$. Possible solutions for T are the roots of the polynomial in T. Each has to be tried, to find the correct root.

(17)
$$\mathbf{I(T_H)} = \frac{B\,[\,\mathbf{T^4}\,]}{(\mathbf{T} - a)} = B\,[\,\mathbf{T^3} + a\mathbf{T^2} + a^2\mathbf{T} + a^3 + (a^4)]$$

This will have roots of $T=a_1$, $T=a_2$, $T = a_3$, only one of which will have physical meaning.

Equation (16) has the form $y = x^2 \exp(-1/ax)$. A common strategy would be to simplify the exponential term using a series expansion, and retain only the first order term. Such an expansion converges very slowly when x is > 1. In this case the exponential term, has values from ~29 at 1000 K to 9.66 at 3000 K. This leaves equation (16) also as a non-linear expression in T.

Equation (18) expresses the desired relationship symbolically, but numerical methods are required to solve this expression explicitly.

(18)
$$\mathbf{I_{emssion}} = F\,\{\,\mathbf{I_{heater}}\}$$

A different method was chosen to obtain a relation between cathode heater current and cathode emission current.

The method used was to solve the Richardson-Dushman equations (15) and (16) at fixed temperatures, a technique conveniently done with a spreadsheet. The results for cathode heater current and cathode emission current at these temperatures are then extracted and compared. The results are given in Table 5 for the temperature range 1000 to 3000 K, and plotted in Figures 79a and 79b.

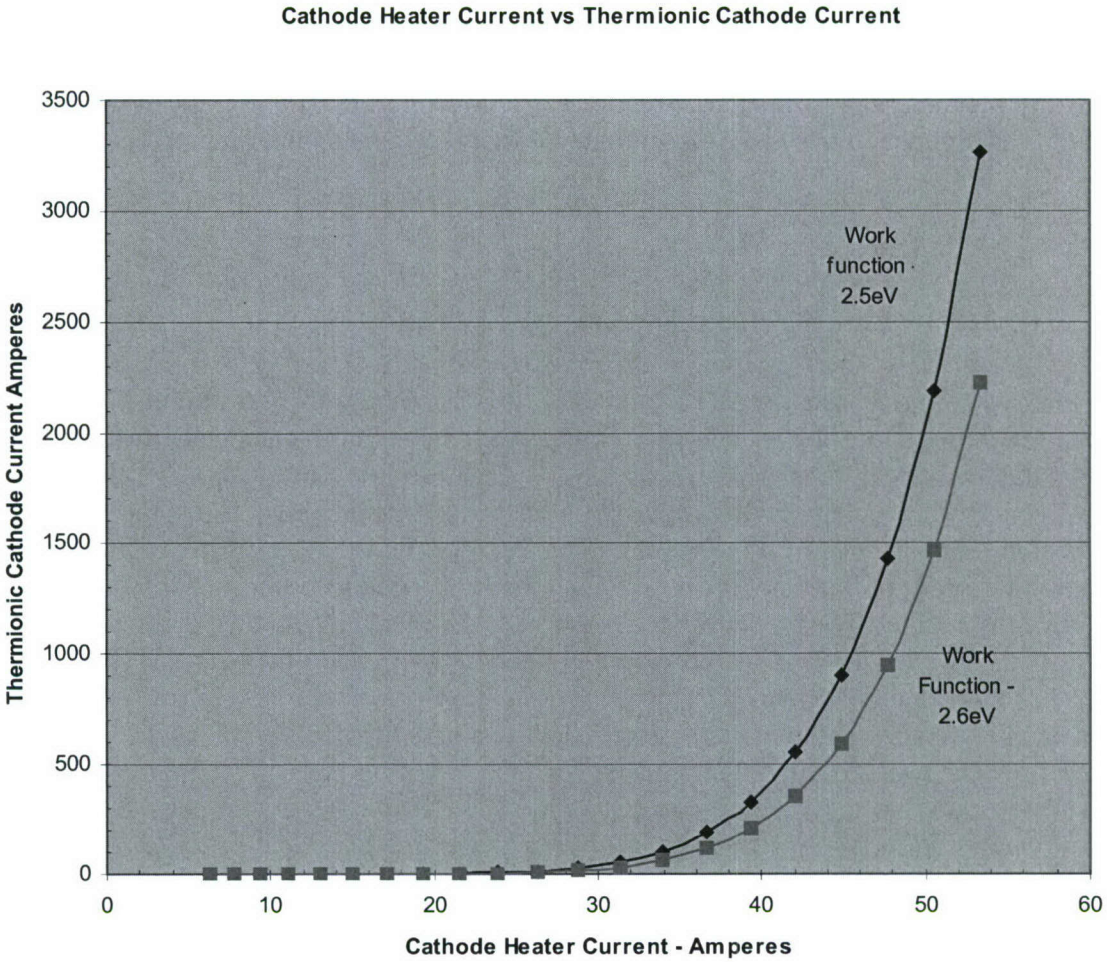

Figure 79a. *Cathode heater current in amperes is plotted against the Thermionic Limited Cathode current in amperes. Values are for a Tungsten –2%Th cathode, 0.5mm diameter and 1.2 cm long.*

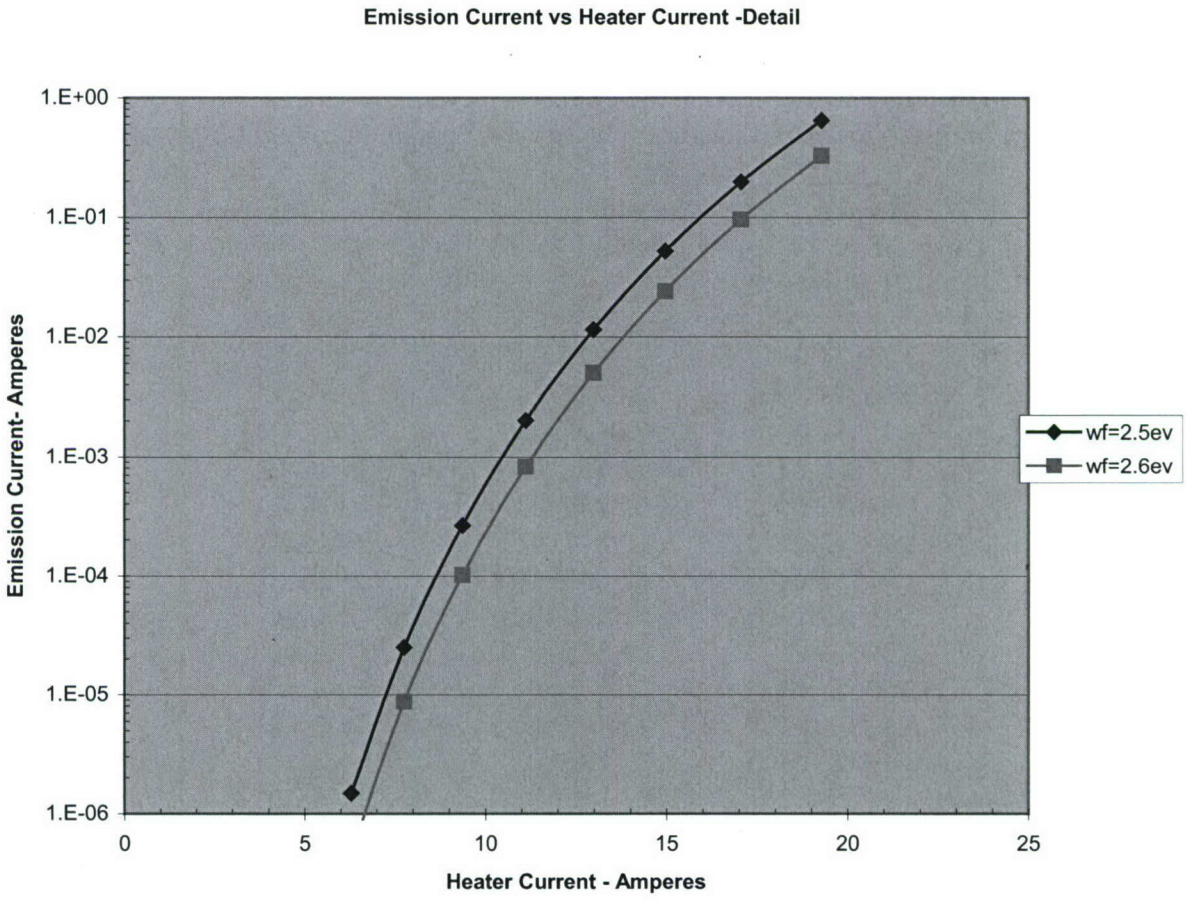

Figure 79b. *Low level emission current is shown as a function of heater current for work functions of 2.5 and 2.6 eV representative of a cathode 0.5 mm diameter, and 1.2 cm long, using Tungsten with 2% Thorium.*

Table 5

The cathode heater current in amperes required to produce the indicated cathode emission in amperes from two different work function materials. The work functions shown are representative of tungsten with 2% thorium. The cathode temperature is from 1000K to 3000K.

Heater Current Amperes	**Cathode Emission - A φ = 2.5 eV**	**Cathode Emission-A φ = 2.6 eV**
6.286E+00	1.485E-06	4.660E-07
7.755E+00	2.502E-05	8.724E-06
9.363E+00	2.673E-04	1.018E-04
1.111E+01	2.010E-03	8.241E-04
1.298E+01	**1.145E-02**	**5.004E-03**
1.496E+01	**5.223E-02**	**2.412E-02**
1.705E+01	**1.987E-01**	**9.631E-02**
1.927E+01	**6.508E-01**	**3.292E-01**
2.154E+01	1.881E+00	9.878E-01
2.391E+01	4.888E+00	2.656E+00
2.635E+01	1.161E+01	6.504E+00
2.883E+01	2.551E+01	1.469E+01
3.138E+01	5.242E+01	3.096E+01
3.397E+01	1.016E+02	6.137E+01
3.662E+01	1.869E+02	1.153E+02
3.931E+01	3.287E+02	2.068E+02
4.207E+01	5.553E+02	3.556E+02
4.484E+01	9.047E+02	5.890E+02
4.766E+01	1.427E+03	9.436E+02
5.052E+01	2.188E+03	1.467E+03
5.342E+01	3.266E+03	2.220E+03

The last item to calculate is the heater voltage necessary to drive the cathode current. This is simply found by multiplying the heater current in (14) by cathode heater resistance at each heater temperature. Equation (19) gives the expression.

(19) $$V(T) = I_{cathode}(T) \times R_{cathode}(T)$$

Table 6 and figures 80a & b show the results for the 0.05 cm diameter x 1.2 cm long Tungsten-2% Thorium cathode. Because this specific cathode has a rather large cross section, the currents are high and voltage low. To drive such a cathode, a low voltage high current AC filament transformer could be used.

A better thermionic design would use a coiled-coil thoriated tungsten wire filament for lower current and higher voltage. For a given cathode type, a specific emission current density sets the required cathode temperature, which in turn sets the radiated power, and heater power. Thus the heater power is a more or less fixed parameter for a given cathode material, once the

emission current is specified. For a small device, a large heater power, will create a serious design challenge with regard to heat removal. This underscores the importance of a non-thermionic electron source.

Table 6

Heater Voltages for a Tungsten -2% Th. cathode, 0.5 mm diameter and 1.2 cm long. The

Heater Voltage Volts	Emission Current - A $\varphi = 2.5$ eV	Emission Current - A $\varphi = 2.6$ eV
9.577E-02	1.485E-06	4.660E-07
1.324E-01	2.502E-05	8.724E-06
1.773E-01	2.673E-04	1.018E-04
2.314E-01	**2.010E-03**	**8.241E-04**
2.950E-01	**1.145E-02**	**5.004E-03**
3.690E-01	**5.223E-02**	**2.412E-02**
4.539E-01	**1.987E-01**	**9.631E-02**
5.510E-01	**6.508E-01**	**3.292E-01**
6.588E-01	1.881E+00	9.878E-01
7.796E-01	4.888E+00	2.656E+00
9.125E-01	1.161E+01	6.504E+00
1.058E+00	2.551E+01	1.469E+01
1.217E+00	5.242E+01	3.096E+01
1.389E+00	1.016E+02	6.137E+01
1.576E+00	1.869E+02	1.153E+02
1.776E+00	3.287E+02	2.068E+02
1.992E+00	5.553E+02	3.556E+02
2.221E+00	9.047E+02	5.890E+02
2.467E+00	1.427E+03	9.436E+02
2.727E+00	2.188E+03	1.467E+03
3.005E+00	3.266E+03	2.220E+03

emission currents are in amperes for work functions of 2.5 and 2.6 eV.

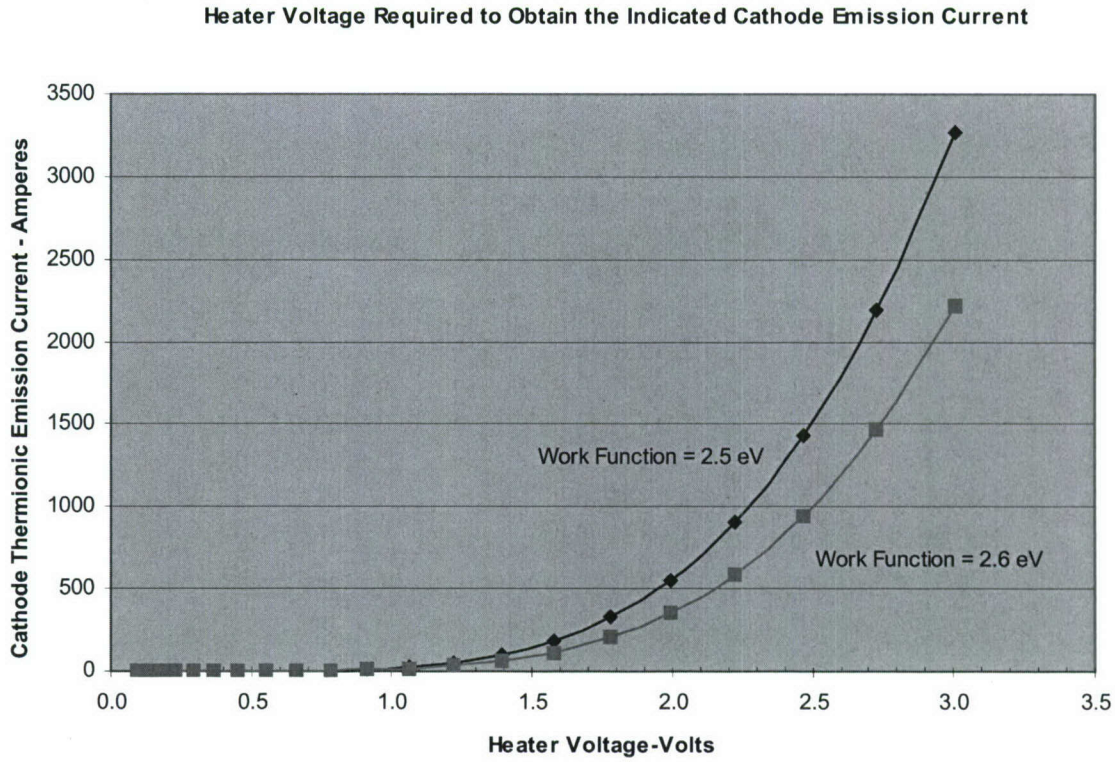

Figure 80a- *Cathode Emission Current as a function of Heater voltage.*

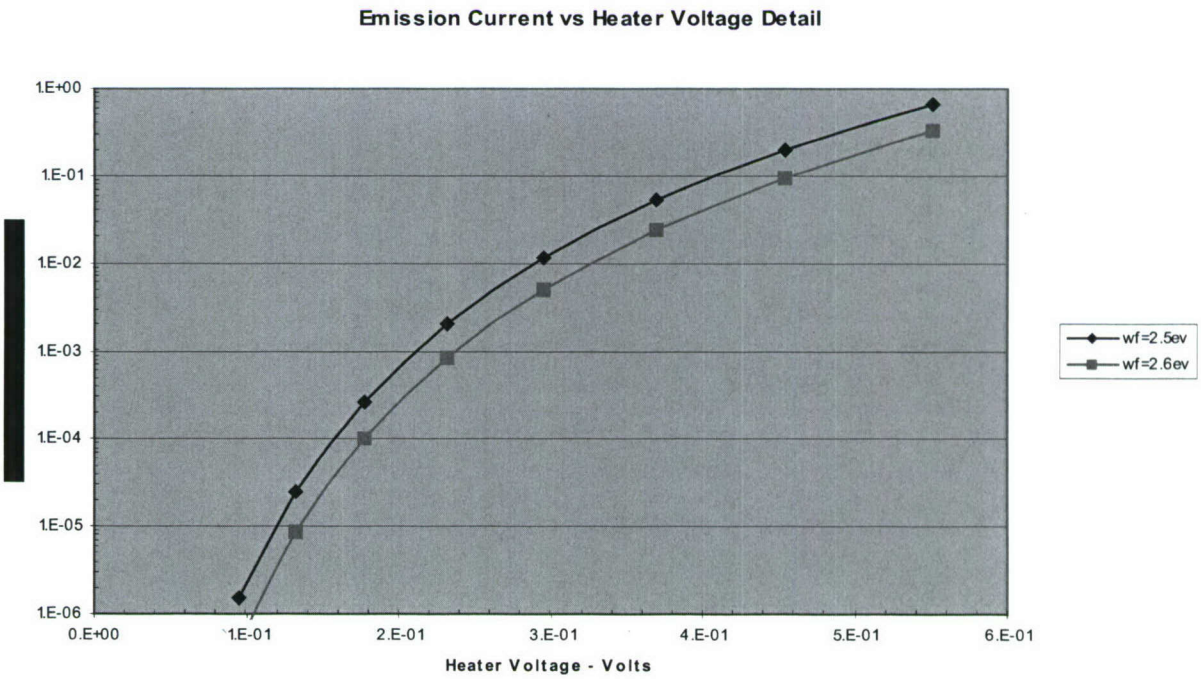

Figure 80b. *Low emission current detail showing heater voltages required for the work function of 2.5 and 2.6 eV corresponding to a Tungsten, with 2% Thorium cathode.*

E. The Electrostatic Lens

Aperture Lens Formulae and Parameters

The electrostatic lens functions somewhat differently from an optical "thin lens". The electric fields around the lens element and the lens voltage together provide its refractive power. Their combined influences are analogous to optical media curvature and index of refraction.

An aperture type lens is a simple structure that can give good results if the focal length is not too small relative to the lens aperture diameter. Equations (20a) and (20b) give the relationship between focal length, lens voltage and the electric fields in front of and behind the lens aperture, for circular and rectangular aperture lenses.

(20a) $$\textbf{F.L.} = 4\,V_{lens} / (E_b - E_a)$$ **Circular Aperture**

For a rectangular beam cross section, a rectangular lens aperture seems a good choice.

(20b) $$\textbf{F.L.} = 2\,V_{lens} / (E_b - E_a)$$ **Rectangular Aperture**

As shown in figure 81, V_{lens} is the voltage on the lens element, E_b and E_a are the electric fields in front and behind the aperture, respectively. The distance units for focal length, are the same as for the electric field, i.e.: mm and volts/mm, etc.

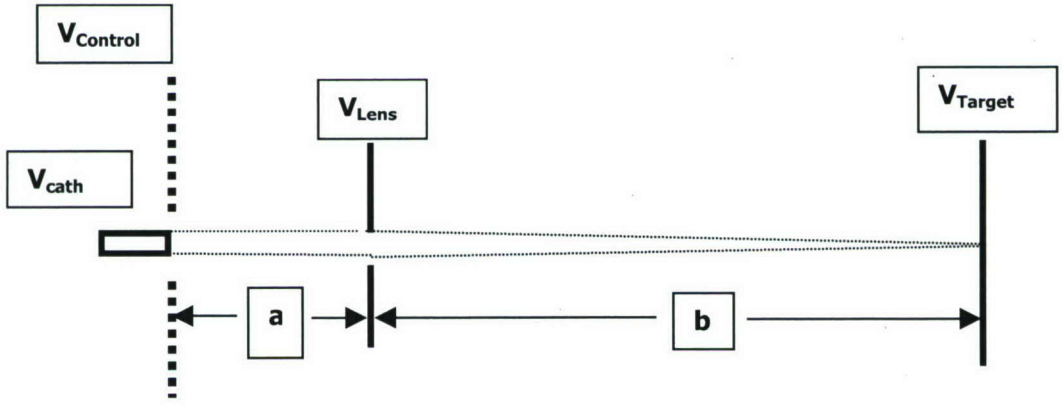

Figure 81. *A simple electron source seen from the side, with an aperture lens between the cathode and the anode or target.*

As with thin optical lenses, electrostatic aperture lenses produce aberrations to the ideal refractive path as the off axis-distance increases. When the incoming beam is significantly non-paraxial, (diverging or converging, for example) the electron trajectories leaving the aperture, may resemble a folded or twisted sheet, making a common focus nearly impossible to achieve. To minimize this effect, two things are necessary in a simple lens system: (a) use a lens opening substantially larger than the beam dimensions, and (b) restrict the incoming beam divergence (convergence). Whether the lens produces a good quality focus at short or long focal lengths, depends on the specifics of geometry, for the electron gun being modeled. As will be seen in the comparison examples that follow, the simple aperture lens formulas, give reasonably good agreement with the modeled systems, over a limited range of focal lengths.

The circular aperture lens focuses uniformly in all radial directions, while the rectangular aperture or "slot lens" focuses only in the short dimension, and near the edges of the slot in the long dimension. If the slot is sufficiently long, so that the beam is away from the slot edges in the long dimension, then the beam will be focused only in the short dimension, leaving the wide dimension unaffected.

From equation (20a &b) it can be seen that the expression for focal length involves the potentials and separation distances of all three electron gun elements – cathode, lens and anode. Cathode and anode potentials are present in the front and back electric fields, E_a and E_b . It is convenient to rearrange equations (20a & b) to express the lens voltage as a ratio of target voltage, and express the lens focal length as multiples of the cathode to lens distance.

If the cathode is considered to be at or near ground potential, then $V_{cathode}$ is ~ 0. Equation (21a,b) are the simplified expressions that result.

(21a) $$\mathbf{F.L.} = \frac{4\,V_L}{\frac{(V_T - V_L)}{a} - \frac{V_L}{b}} = a$$ **Circular**

(21b) $$\mathbf{F.L.} = \frac{2\,V_L}{\frac{(V_T - V_L)}{a} - \frac{V_L}{b}} = a$$ **Rectangular**

$\mathbf{V_T}$ is the target voltage, and $\mathbf{V_L}$ is lens voltage.

Rearranging (21) gives the following form which is plotted in figure 82. Table 6 lists specific values of the variables.

(22a) $$V_L/V_T = \frac{1}{(5 + a/b)}$$ **Circular Aperture**

(22b) $$V_L/V_T = \frac{1}{(3 + a/b)}$$ **Rectangular Aperture**

The expressions in 22a &b allow a set of dimensionless curves to drawn (figure 82) from which various combinations of voltage and focal length can be determined. To use these curves with the cathode voltage at other than zero voltage, the cathode voltage is simply added (or subtracted) from both lens and target(anode) voltages.

Table 7

Focal Lengths as a ratio of Cathode to Lens distance versus the ratio of Lens to Target Voltage for Circular and Rectangular Aperture Lenses. The focal length is taken to be the distance from lens to target.

Ratio of Focal Length to Lens-Cathode Dist. (A/B)	**Lens to Target Voltage Ratio Round Aperture**	**Lens to Target Voltage Ratio Slot Aperture**
1.000E+00	1.667E-01	2.500E-01
2.000E+00	1.429E-01	2.000E-01
3.000E+00	1.250E-01	1.667E-01
4.000E+00	1.111E-01	1.429E-01
5.000E+00	1.000E-01	1.250E-01
6.000E+00	9.091E-02	1.111E-01
7.000E+00	8.333E-02	1.000E-01
8.000E+00	7.692E-02	9.091E-02
9.000E+00	7.143E-02	8.333E-02
1.000E+01	6.667E-02	7.692E-02
1.100E+01	6.250E-02	7.143E-02
1.200E+01	5.882E-02	6.667E-02
1.300E+01	5.556E-02	6.250E-02
1.400E+01	5.263E-02	5.882E-02
1.500E+01	5.000E-02	5.556E-02
1.600E+01	4.762E-02	5.263E-02
1.700E+01	4.545E-02	5.000E-02
1.800E+01	4.348E-02	4.762E-02
1.900E+01	4.167E-02	4.545E-02
2.000E+01	4.000E-02	4.348E-02
3.000E+01	2.857E-02	3.030E-02
4.000E+01	2.222E-02	2.326E-02
5.000E+01	1.818E-02	1.887E-02
1.000E+02	9.524E-03	9.709E-03

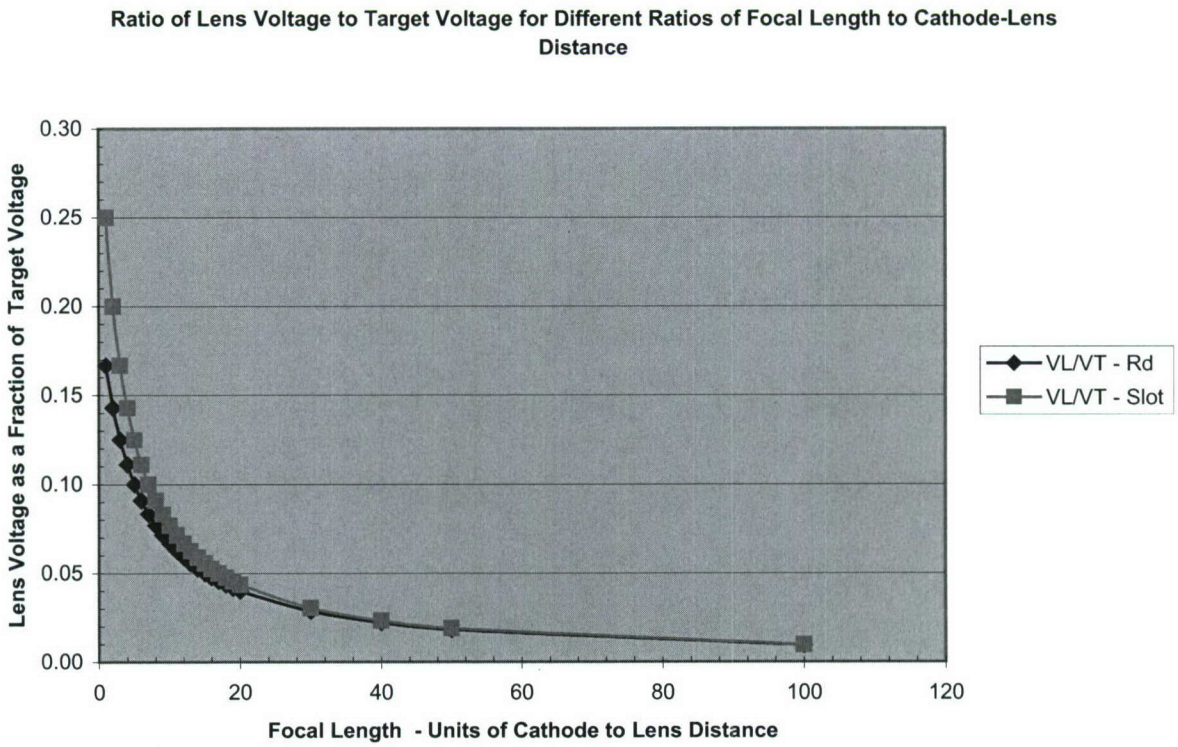

Figure 82. *The ratio of lens voltage to target voltage is plotted against the focal length of the lens, expressed in units of the cathode to lens distance.*

Electron Trajectory Model Comparisons

Electron trajectories of several arrangements of electron source, beam current control, lens and target as analyzed above were then modeled using the SIMION 7.0 software package and the results compared to the theoretical predictions.

Figures 83 (a-e) show the set of potential arrays that were analyzed. In general, all configurations match the schematic view shown in figure 82. The simulation in (83a), gave quite good results and was then modified to include a cut-off or extractor electrode. This electrode would be used to control beam current, and to provide a convenient means to pulse the beam. The extractor electrode can also function as an auxiliary lens. In these simulations, it was only modeled in the on /off modes because of the added complexity to the analysis.

In general, a geometric scale of 1 graphical unit (GU) per 25 microns was used. The overall dimensions were chosen to agree with the earlier geometry assumed for the thermionic source analysis, and with some consideration to fabrication issues. The geometry of this simple electron source is scalable, so that if dimensions and voltages are proportionally changed, the electron gun performance is unchanged. Thus results from one model may be transferred to any proportionally scaled system.

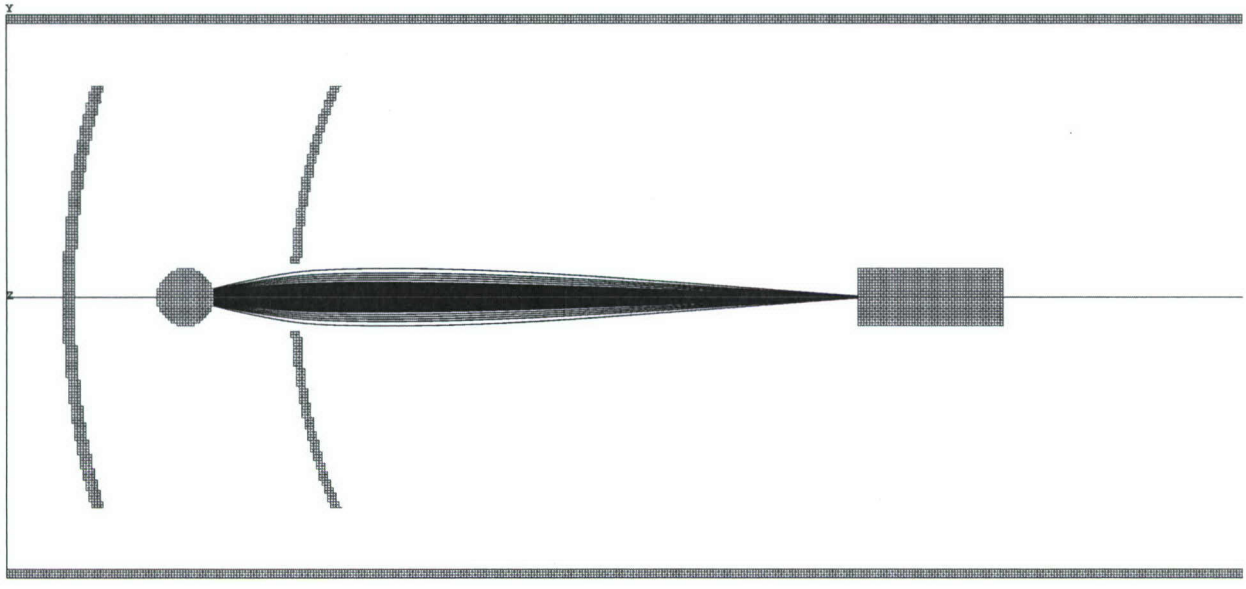

Figure 83 a: *Linear E gun with cylindrical repeller and lens. Target is at 300 Graphical Units to the right of the origin - (1 GU = 25 um) . The repeller is at the far left, cathode shown next and lens to the right of cathode. With* $V_{repeller}$ *and* $V_{cathode}$ *= 0 V,* V_{lens} *= +110V, and* V_{target} *= 7500 V, this arrangement gives a line width of 0.044 GU or about 1.1 um wide.*

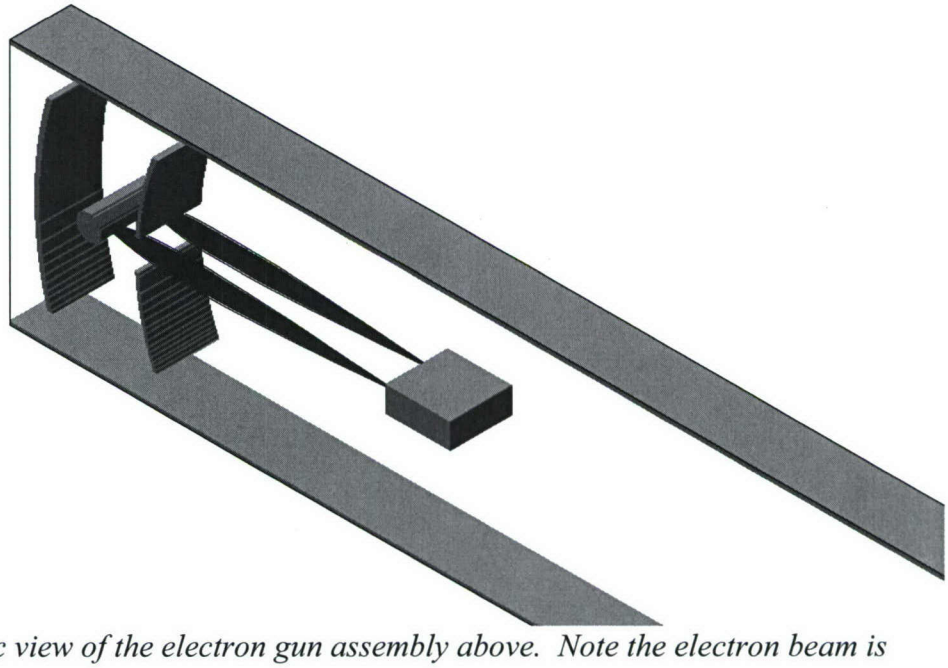

Figure 83 b: *Isometric view of the electron gun assembly above. Note the electron beam is shown at each end of the source .*

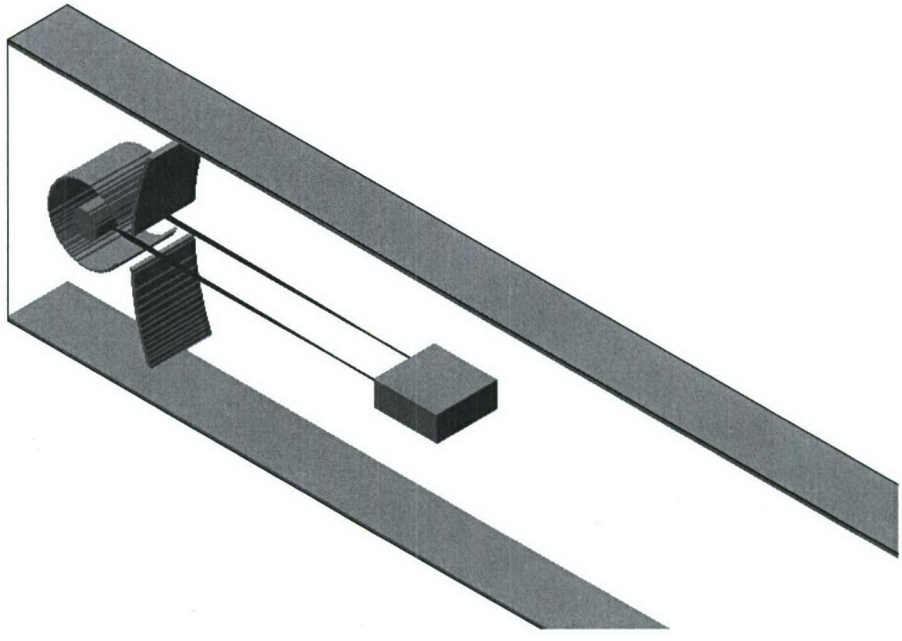

Figure 83c: *Electron Gun with enclosing repeller and lens. With $V_{repeller} = 0$, $V_{cathode} = +21.2$ V, $V_{lens} = +84.5$ V, $V_{target} = 7500V$, beam width is ~ 2.6 um on target, with 70.5% of electrons in the primary focus. The target is at 300 GU (7.5 mm) from the origin.*

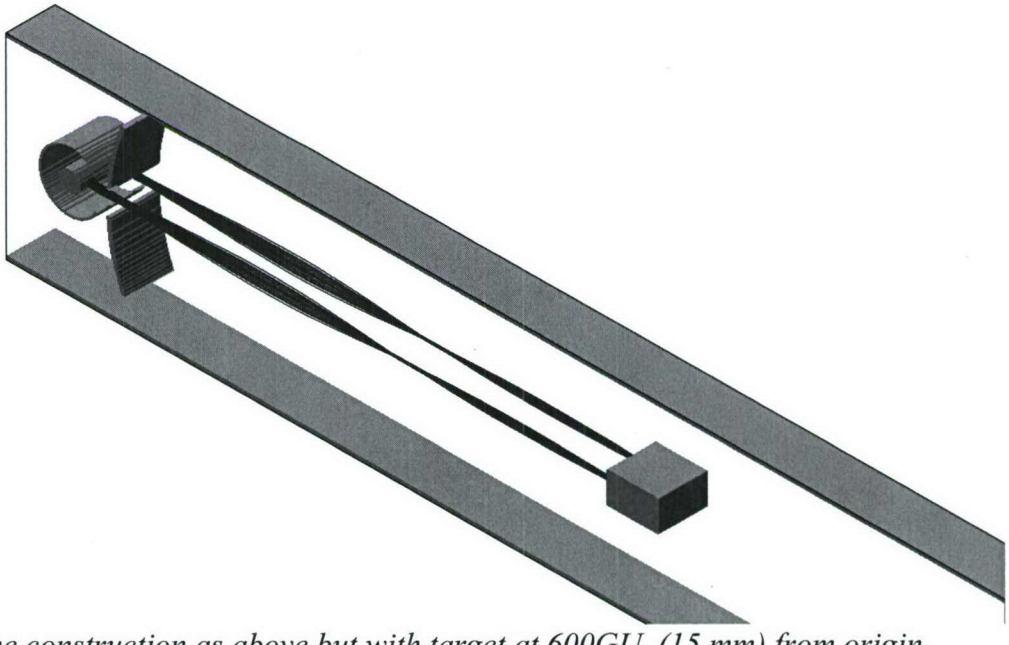

Figure 83 d. *Same construction as above but with target at 600GU (15 mm) from origin. Notice the double crossover in the electron trajectories. This is caused by the grounded enclosure proximity. Best focus conditions occur at $V_{repeller} = 0V$; $V_{cathode} = +1.0V$; $V_{lens} = +780$ V and $V_{target} = +7500V$. Beam width at the target with these voltages is 0.155 GU (3.93 um), with 83.6% of electrons in the prime focus.*

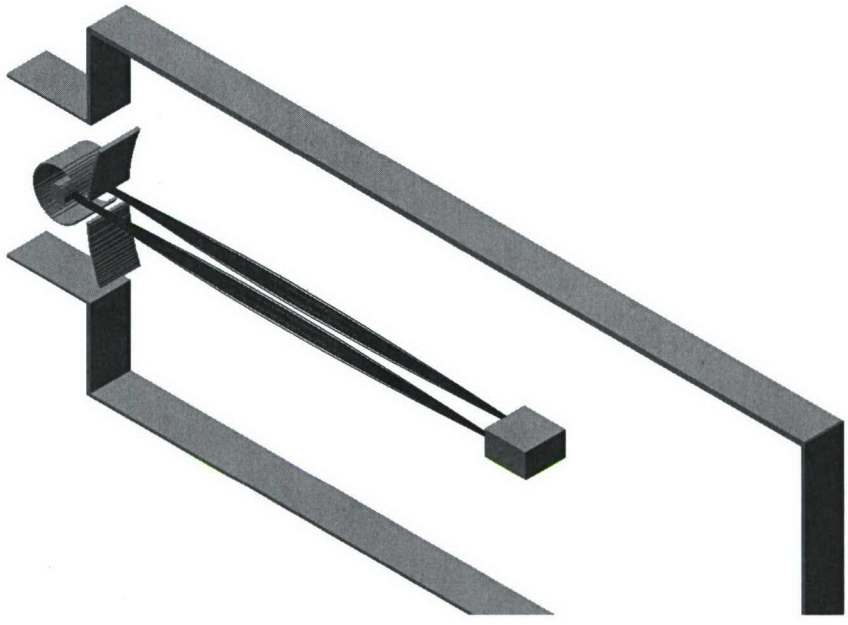

Figure 83 e. *Same geometry as in 12d, but the ground enclosure is twice the width in the region of the electron beam. Comparing the two geometries, the double crossover is now gone. The beam primary focus is at the target. The result indicates that container geometry will be important, since 13d shows the primary focus (1st crossover) occurs about where the short focus was in 13 c. The aspect ratio of the ground structure must evidently be about 1:3 width to length to avoid the extra beam crossing.*
Focus conditions above are: $V_{repeller} = 0V$; $V_{cathode} = -17V$; $V_{lens} = +730V$; $V_{target} = +7500V$, *with 80.3% of the electrons in the prime focus.*

The examples of modeling, shown in figures 12 a-e, are the end results of several hundred refinements, essentially performed by trial and error, after the initial approximations were set up from the aperture lens formulas.

In figures 83(a-e) the extractor electrode has been omitted. It was found that the repeller can function approximately as the control grid, although it does affect the focus, the same as would a control electrode.

Figure 84a shows the beam as the repeller approaches cutoff, while figure 83b shows the electron fold-back that occurs at cutoff, a voltage of –5.5 volts. The repeller should be physically small and not closer than needed to the cathode, limit both its temperature, and capacitive coupling to the cathode. For low duty cycle pulsing, the repeller should work well as a gate electrode.

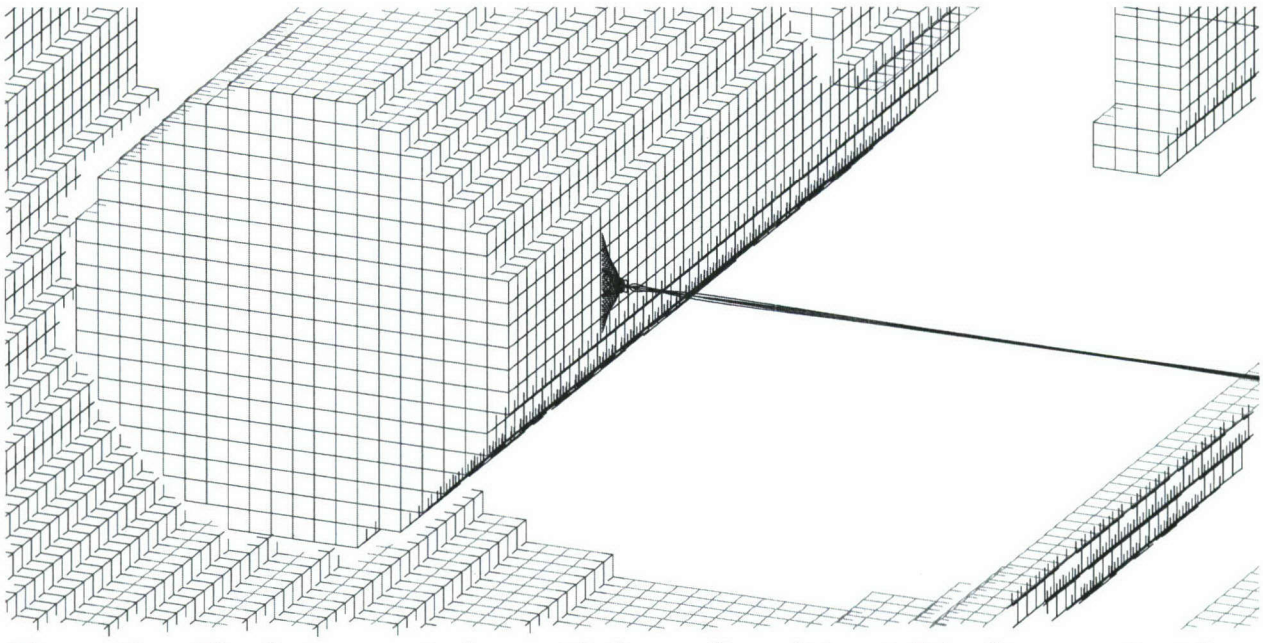

Figure 84 a. *The electron gun is shown with the repeller voltage at -5.4 volts, approximately 98% of cutoff voltage. The other potentials are the same as in figure 11d, above.*

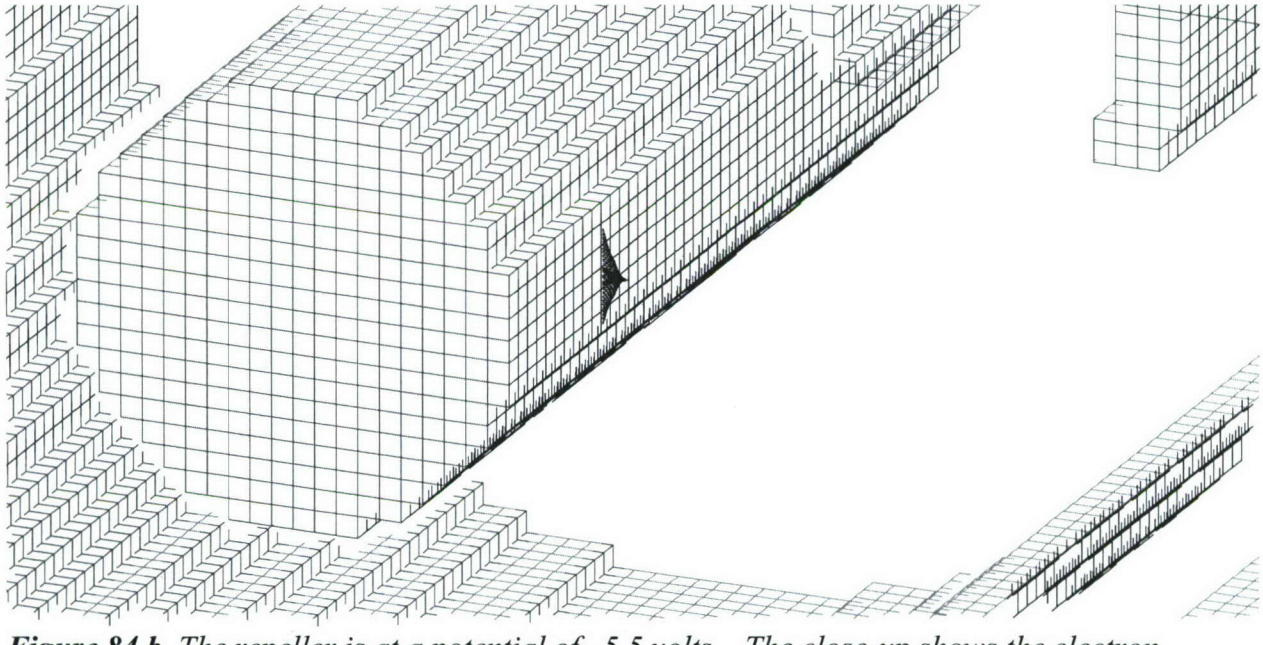

Figure 84 b. *The repeller is at a potential of –5.5 volts. The close-up shows the electron foldback occurring at the cathode surface.*

For control of the beam current, the repeller voltage will need to be coupled to that of the lens electrode to maintain optimal focus at the target. An optically derived output signal may be needed to provide indications of lasing. Alternatively, a microprocessor could provide both the control logic and analog signals to accomplish the coupled response.

Several conclusions can be drawn from these results.

1. The repeller or cathode enclosure has only limited useful effect in focusing. It can fine tune the focus by modifying the cathode to lens field.

2. Focus is better at short focal lengths. Narrower beam widths are achieved at short focal lengths. This is consistent normal optical theory.

3. The grounded enclosure must be far enough removed from the beam path to avoid secondary focusing effects

4. The field around the target electrode functions as a lens. The target electrode shape must be considered in the design.

5. The repeller can function efficiently as a gating electrode to pulse the beam. It is less effective as a beam current control because of its effects with the lens on beam focus.

F. Conceptual Physical Design

General Considerations

The beam trajectory data in Section 5 can be directly scaled for use as a proof of concept electron gun for the ESUVOS or related projects. The system is modeled in a space of 600 x 400 x 50 graphical units which represent 25 um (0.001") each. The Z dimensions were kept as small as possible to shorten computing time, and graphical presentation time. For a real device, the z dimension should be approximately the same as the Y dimension or 400 GU.

Thus on a 1:1 scale, the modeled volume of the electron gun would be, approximately 1.50 cubic centimeters or about 1.5 x 1.0 x 1.0 cm. This represents the smallest electrostatic volume which avoids beam focus problems, (the double crossover trajectory). A larger size perhaps twice these dimensions might be more practical for a first device, especially considering the heater wattage.

Increasing the outer shell volume will not significantly alter the focus quality, but may materially improve thermal issues.

It is recommended that the initial device be fabricated on a metallic base having high mechanical stability, with a removable metallic enclosure for electrostatic shielding. The unit can be conveniently placed into a larger evacuated chamber for bake-out and testing. The electrode materials other than the target electrode, need to be non-magnetic stainless steel. Otherwise, beam steering may occur, even if the parts are initially demagnetized.

The target electrode should be of good thermal conductivity and mechanical stability. Tungsten- copper alloy can be used effectively here. In pulse mode of operation, with low duty cycle, the target will not heat excessively. For higher duty cycle, supplementary cooling may be necessary. The entire device can be mounted to a "cold finger" for extended operation at or below ambient. Extended low temperature operation, my require the cathode to have more thermal isolation so that proper levels of thermionic emission can be maintained.

Table 7 summarizes the various data for the proof of concept design. Data for a short (7.5 mm) and a long (15 mm) focal length device are shown. Some data, (heater current for example), derives from original specifications for the cathode material type and size. Figure 14 shows a conceptual design with the basic (minimal) dimensions discussed above.

It should be noted that the focusing voltages shown are based on the electron beam simulations that gave the tightest focus. These should be considered a starting point for the setup of the test device. Similarly, the heater voltages. These are entirely derived from calculated values of resistivity for pure tungsten, modified to estimate the effects of 2% thorium alloy. The actual heater voltage required will depend on the electrical and mechanical design applied to the heater assembly, and the specific heater(cathode) material.

The simulations shown indicate no beam current is intercepted by either the repeller or the lens electrode. This should remain true for voltages close to the values shown for best focus.

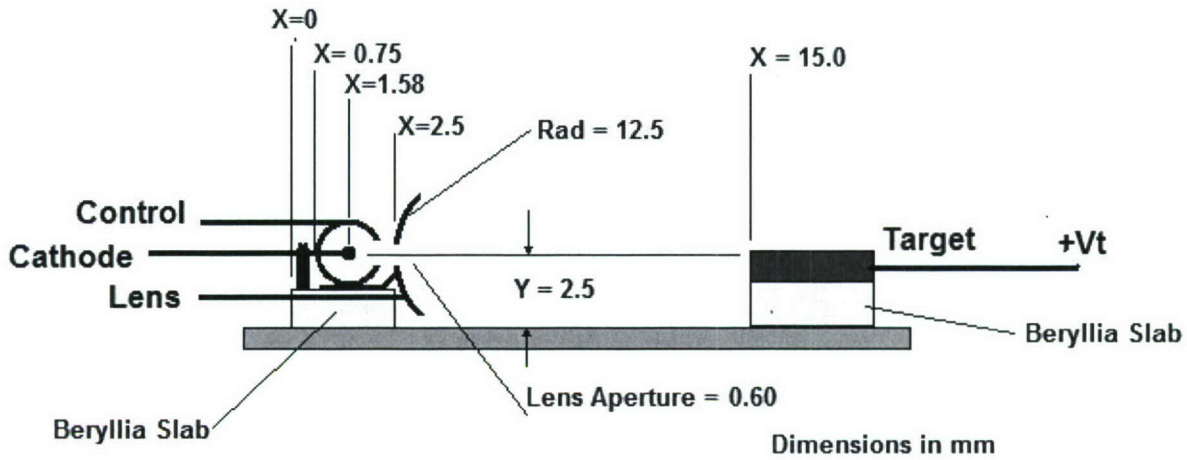

Figure 85a *Elevation view of miniature E-Gun. Note all dimensions are in mm. Component mounting detail is not shown. Fastenings must compatible with sound high vacuum design (e.g. vented threads), to eliminate virtual leaks.*

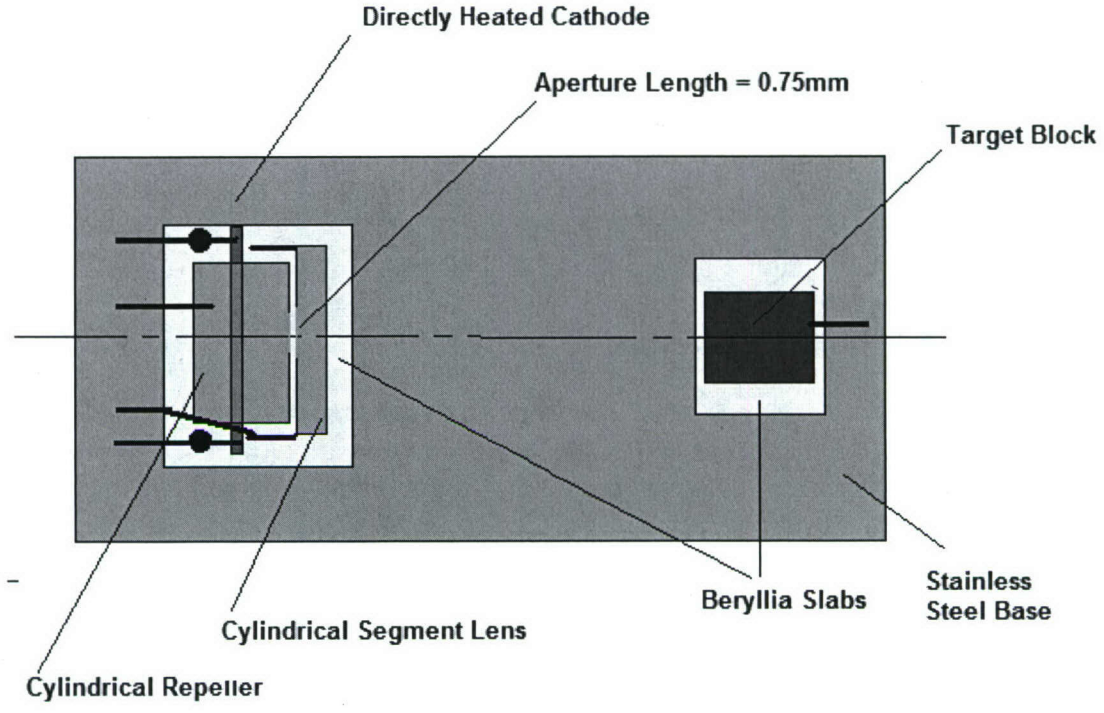

Figure 85b. *Plan view of miniature E-gun. The repeller electrode is concentric with the cathode /heater. The slot in repeller is shown slightly shorter in length than the aperture in the lens. This dimension is not critical, but lens aperture must be at least 0.75 mm in length to fill target.*

Table 8
Design Values for the Thermionic Electron Gun

Parameter	**Short Focus**	**Long Focus**
Cathode:		
Type:	Directly Heated	Directly Heated
Material:	Tungsten w/2%th	Tungsten w/2%th
Diameter:	0.5 mm	0.5 mm
Length:	12.0 mm	12.0 mm
Heater Voltage	0.9 – 1.06 V	0.9 – 1.06 V
Heater Current	26 – 28.8 A	26 – 28.8 A
Cathode Voltage	+21.2 V	-17 V
Repeller:		
Diameter:	0.75 mm	0.75 mm
Aperture:	0.60 x 0.75 mm	0.60 x 0.75 mm
Normal Voltage	0 V	0 V
Cutoff Voltage	-5.5 V	-5.5 V
Current	0.0	0.0

Lens:		
Aperture	0.60 x 0.75 mm	0.60 x 0.75 mm
Voltage	+84.5 V	+730 V
Current	0.0	0.0
Target:		
Voltage	+7500 V	+7500 V
Performance:		
Focal Length	~ 5.00 mm	~12.50 mm
Beam width	~2.6 um	~ 3.2 um
% Total Beam on target	70.5	80.3

G. Summary and Conclusions

A study of the factors affecting the design and operation of a thermionic electron gun and target has been presented. Charts and tables for a variety of cathode materials have been presented so that variations to the specified design of the device can be determined with relatively little additional work. The simulations and electron trajectory models indicate that the specified beam profile at the target is just within reach using the relatively simple design presented here.

The entire device can be housed in a volume approximately 1 by 1 by 1.5 cm^3 .
Several important conclusions can be drawn from the results of the study. First is that this cathode design, poses severe, possibly insurmountable thermal management issues for a compact self-contained device. The robust tungsten, directly heated cathode, 0.5 mm in diameter, will dissipate a large amount of heat despite the thorium enhancement. At its normal temperature of 1500 C, the tungsten cathode requires about 5 times the heating power, as would a tri-oxide cathode of identical geometry, operating at 1000 C.

For a demonstration class device, operating in a large continuously pumped system, the cathode heat should be manageable, and thus poses no real impediment to testing. The miniature device with the same cathode, would require careful attention to heat removal, to avoid overheating.

For a miniaturized device, a thermionic source *may* be practical, but would require a design optimized to yield the required emission current density at the absolute minimum cathode heater power. A compact "coiled coil" source, with tri-oxide coatings may be possibility. But a cold cathode source is the preferred choice, altogether, although present source materials may not yet be capable of the required current density. Design of such a device should be considered after a successful demonstration of optical generation using the current design.

3.4.5 Raman and native fluorescence detection and identification methods development

Deep UV resonance Raman and native fluorescence methods have been developed under this contract, primarily at Photon Systems but also under a subcontract with the University of Rhode Island. Following is a summary of that effort.

3.4.5.1 Photon Systems Results

1. Introduction

A number of instrumental techniques are available for laboratory testing of biological or chemical materials if the quantities are plentiful, if sample handling, preparation, and use of reagents are possible, and if the size, weight, power consumption and cost of the instrument are not of concern. In situ detection and identification of trace levels of biochemical agent contamination in air, water and on surfaces typically requires instruments for which no consumables or sample handling is allowed, and which are light weight and low power consumption. Instruments will eventually be needed that cover a wide range of sensitivity, specificity, size, weight, power consumption and cost. But generally the sensitivity and specificity requirements for in situ instruments are high and the size, weight, power consumption and cost are low.

When searching for trace levels of organic or biogenic materials, as required for hazardous biochemical agent detectors, an *in situ* instrumental methodology is needed that includes a high sensitivity *trigger phase* that can process relatively large amounts of sample material quickly, followed by a high specificity *confirmation phase* capable of obtaining detailed compositional information about samples identified as possible hazardous materials during the trigger phase. In the trigger phase it is sufficient to eliminate those particles or materials that are clearly non-organic or non-biogenic from those materials that are biological in nature including intact organisms, residues from organisms, virus', or other potentially harmful materials. Sensitivity is more important than specificity in this phase of detection. In the confirmation phase it is important to give high levels of specificity in identification of the organic or biogenic material. More than one level of triage of a sample may be desired or required in order to formulate a response to an event. Confirmation sensors may take the form of a series of increasingly specific sensors, each of which provides more detailed information about a threat.

2. Background

Instruments based on optical methods offer the greatest opportunity to achieve the goals of simple, miniature, trigger and confirmation sensors for hazardous biological and chemical materials. Optical methods include measurement of elastic and inelastic scattering, fluorescence, phosphorescence, and absorption. Elastic scattering includes Raleigh and Mie scattering and inelastic scattering includes Raman and Brillouin scattering. For reasons described below, instruments based on elastic scattering in combination with laser induced native fluorescence (LINF) (auto-fluorescence) and ultra-violet resonance Raman spectroscopy (UVRRS) can provide the needed sensitivity and specificity in biochemical agent detection and identification without the need for consumables or sample preparation[11i]. Techniques also based on LINF and UVRRS can be applied to more invasive detection methods such as surface enhanced Raman and various wet chemistry sample separation or segregation methods to yield even higher levels of

[11] Cary, P.R. *Biological applications of Raman and resonance Raman spectroscopies*, (Academic Press, New York, 1982)

specificity. Laser induced *native* fluorescence is differentiated from traditional laser induced fluorescence since it employs stimulation of fluorophors which are endogenous or native to the biological or chemical targets of interest and do not require derivatization with dye tags or other sample preparation or handling. Derivatization with dye tags offers great advantages if the chemical compounds to be detected are known and sample handling or preparation are not a problem. Elimination of the need for derivatization broadens the range of chemical groups that can be detected and expands the ability to find unexpected compounds or composites in complex mixtures.

When monochromatic light is incident on a gas, liquid or solid, it will be transmitted, absorbed or scattered. The forms of interaction of light with a molecule are shown in the Jablonski energy level diagram in Figure 1. The absorbed light will either be converted to light in the form of fluorescence or phosphorescence, or into thermal energy. The scattered light will occur either at the same energy, called elastic scattering, or shifted and called Raman scattering. Elastic scattering occurs when the oscillating electric field of the incident light wave interacts with the electron cloud of a molecule in a short-lived virtual state, which is not a true quantum state of the molecule[ii]. During elastic scattering there is no absorption or loss of photon energy or change in molecular vibration or rotational energy. Elastic scattering efficiency, or scattering cross-section, is greater in the blue than the red with dependence proportional to the

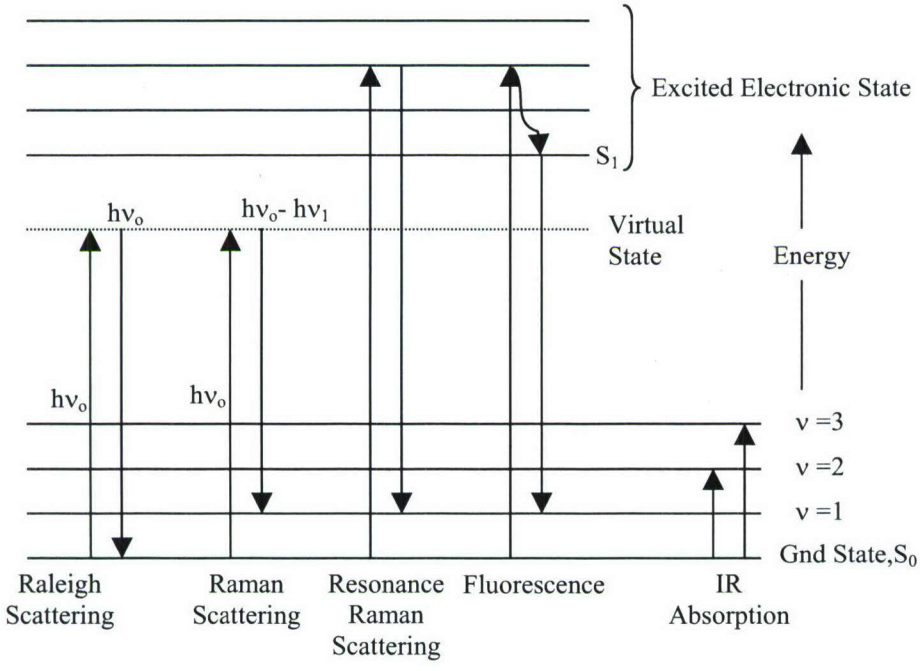

Figure 1. Optically induced molecular transitions

fourth power of frequency, ν^4.

2.1 Raman Scattering.

Internal vibrations also perturb the electron cloud surrounding a molecule. The interaction of the external electromagnetic field and internal molecular vibrations give rise to an inelastic scattering process called Raman scattering, wherein the internal vibrational or rotational energy of the molecule is changed. Conservation of energy requires that the scattered photon

also be changed by an equal energy, the corresponding frequency of which is known as the Raman shift. If the molecule gains energy, the scattered photon loses energy and is Stokes shifted from the incident photon. If the molecule loses energy, the scattered photon gains energy and is anti-Stokes shifted from the incident photon. The phenomenon was predicted by Smekal[12] and demonstrated by Krishna and Raman[13] in 1928 and has been well developed and documented in a wide range of books, research papers and monographs well described in McCreery[14]. Raman spectroscopy offers a non-contact method of extracting information on molecular structure and dynamics that does not suffer from many of the problem with infrared or near-infrared absorption spectroscopy, especially with measurements in aqueous solutions. In addition, Raman spectra can be obtained without "looking" through the sample. So the sample can remain in its natural, unperturbed, location. Stokes scattering is shown below in Figure 1, where the molecule gains and the scattered photon loses energy by an amount, $h\nu_o - h\nu_1$. The number of vibrational or rotational modes or resonance frequencies of a molecule is given as 3N-6 (3N-5 for linear molecules), where N is the number of atoms in the molecule[15]. For simple, linear, diatomic molecules, there is only a single mode or resonance. Examples are H_2 where the resonance occurs at 4159 cm^{-1}, N_2 at 2331 cm^{-1}, and O_2 at 1556 cm^{-1}. Complex molecules, including biological macromolecules, can have very large numbers of atoms and can have subsequently very complex spectra.

Raman spectroscopy can be employed at a wide range of excitation wavelengths from the deep UV to the near infrared. Generally, dispersive Raman spectroscopy does not use excitation wavelengths above 790nm since the normal Raman shift range of interest (to about 4000 cm^{-1}) would extend beyond the spectral sensitivity range of typical silicon-based CCD array and may other types of common detectors. Normal Raman spectroscopy is a very inefficient process, with scatter cross-sections for typical "strong" Raman scattering bands in the range of 10^{-30} cm^2/molecule/steradian. To put this in perspective, in order to collect one Raman scattered photon/sec from a sample with 10^6 molecules within the field of view of a 532nm laser using an optical system with a collection solid angle of one steradian would require an incident laser flux of 10^{24} photons/sec/cm^2. This corresponds to a laser output nearly $4x10^5$W/cm^2 irradiating the sample for 1 second. When a laser is focused to a small spot of perhaps 30μm square, the required laser power is nearly 4W for one second to obtain one Raman scattered photon per second. Normal Raman spectroscopy is therefore conducted in the visible or near infrared using very powerful, high intensity lasers to provide sufficient excitation photon flux to generate a measurable number of scattered photons. Prior to the introduction of lasers, Raman spectroscopy was a curious phenomenon with little practical use.

---

[12] A. Smekal, *Naturwissenschaften* 11, 873, 1923
[13] C.V.Raman and K.S. Krishnan, Nature 121, 50, 1928.
[14] R.L.McCreery, *Raman Spectroscopy for Chemical Analysis* (Wiley Interscience, 2000).
[15] N.B. Colthup, L.H.Daly, S.E. Wiberley, *Introduction to Infrared and Raman Spectroscopy* (Academic Press, 1990).

Since the introduction of visible and later ultraviolet lasers and a variety of modern detectors, the usefulness of the process has dramatically increased and continues to increase. One technique that has made a dramatic impact on the use of Raman spectroscopy in the measurement of biological material has been the use of pre-resonance and resonance Raman spectroscopy. Pre-resonance Raman occurs as the excitation photon energy approaches the first electronic excited state of the molecule and the Raman scattering cross-section begins to increase above its normal value. When the excitation photon energy occurs within the molecular manifold of the first electronic excited state, Raman scattering cross-sections and resulting scattering efficiency can dramatically increase in a process called resonance Raman. Resonance Raman has been demonstrated to yield scatter cross-section and signal improvement up to 10^8 over normal Raman. Resonance enhancement occurs dominantly within the electronic manifold of the absorbing species, greatly simplifying the ability to interpret the Raman spectra. Pre-resonance and resonance Raman spectroscopy as well as surface enhanced Raman spectroscopy have enabled dramatic increases in scatter cross-sections to values approaching 10^{-22} cm^2/molecule/steradian, enabling dramatic reductions in the required laser power to values in the microwatt range. This is making Raman methods of increasing value for practical uses, such as biochemical agent detection and identification as well as a host of other government and industrial applications. Excitation in the UV additionally enhances Raman scattering with dependence proportional to the fourth power of frequency, ν^4.

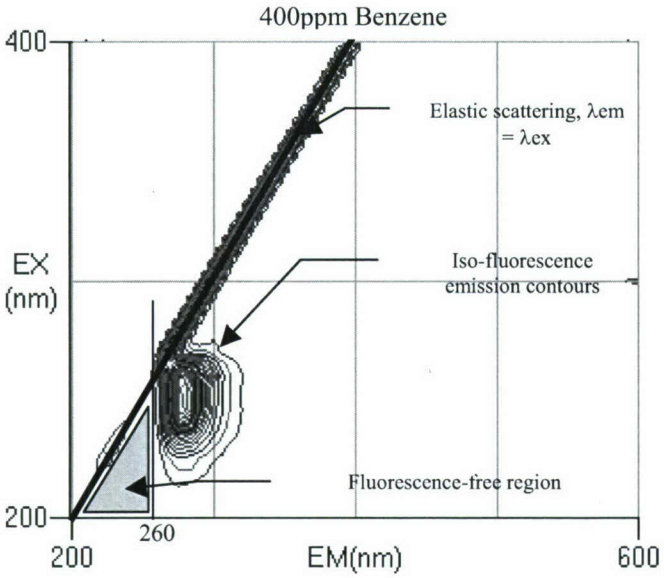

Figure 2. Excitation-Emission-Matrix diagram of benzene

2.2 Native Fluorescence.

A challenging problem to the use of Raman spectroscopy has been the ubiquity of fluorescence, which can be emitted by the sample under investigation or by impurities or background materials within the field of view of the laser. Fluorescence is normally a much more efficient process than Raman and even weak fluorescence can be much stronger than Raman, overwhelming and masking the Raman emissions. Fluorescence is not a scattering process. Fluorescence emission spectra do not have the vibrational fine structure observed in Raman spectra. When a molecule is irradiated at an excitation wavelength that lies within the absorption spectrum of a molecule, it will absorb the radiant energy and be activated from its ground state (S_0) to an excited singlet state (S_1), with the electron in the same spin as the ground state. The molecule can then relax back from the excited state to the ground state by giving up excitation energy either non-radiatively or radiatively, depending on the local environment. In a nonradiative transition, relaxation occurs by thermal generation. In a radiative transition, relaxation occurs via fluorescence at specific emission wavelengths. Fluorescence generation occurs in three steps: thermal equilibrium is achieved rapidly (10^{-9}s) as the electron makes a

non-radiative transition to the lowest vibrational level of the first excited state; the electron then makes a radiative transition to a vibrational level of the ground state (10^{-7}s); and finally the electron makes a non-radiative transition to the lowest vibrational level of the ground state[16]. When there is inter-system crossing, in which the spin of the electron is flipped in the excited state, the time for the radiative transition from the excited state to the ground state is longer because the transition must occur with a spin change. This excited state is termed the triplet state. Radiative transition from the excited triplet state is termed phosphorescence with a decay time constant often in the range of milliseconds[17].

Many molecules and most organic and biological molecules have fluorophors or electronic states corresponding to energy in the ultraviolet. Figure 2 shows an excitation-emission matrix (EEM) diagram of benzene over a range of excitation wavelengths from 200nm to 400nm and emission wavelengths from 200nm to 600nm. Shown are iso-intensity contours resulting from elastic scattering and fluorescence. This diagram illustrates several important features of the relationship between elastic and Raman scattering and fluorescence. The diagonal line in the diagram represents elastic scattering where the emission and excitation wavelengths are equal: $\lambda em = \lambda ex$. Fluorescence emission is always Stokes-shifted to longer wavelengths. The amount of Stokes shift varies from one compound to another and as a function of excitation wavelength. In 1984 S.Asher[18] showed that that no fluorescence is observable below 260nm for any sample, even with excitation at wavelengths as low as 220nm. This is also illustrated in Figure 2, where a fluorescence-free region is shown for excitation wavelengths below about 250nm and extending down to 200nm and below. Asher's explanation was that the smallest conjugated polyene or aromatic molecule to show significant fluorescence from its first excited state is benzene, shown in Figure 2, which shows fluorescence only at wavelengths longer than 260nm. Larger aromatics show absorption bands below 260nm but excitation into these bands results in fast internal conversion of this energy into the lowest energy singlet or triplet excited state, and fluorescence or phosphorescence occurs at much longer wavelengths. As illustrated in Fig 2, shorter excitation wavelengths provide a wider range of fluorescence-free wavelengths in which to observe weak Raman scattering emissions without interference from fluorescence. At wavelengths below about 240nm, Raman scattering up to about 4000 cm^{-1} can be observed without interference from fluorescence. Figure 2 also clearly illustrates the fact that the fluorescence efficiency and Stokes shift is strongly dependent on excitation wavelength. At excitation wavelengths below about 220nm benzene shows little or no fluorescence at any wavelength. S. Asher's 1984 paper opened up the field of ultraviolet resonance Raman spectroscopy, which is especially valuable for the elucidation of biological materials.

When excitation wavelength is increased above about 240nm, fluorescence begins to interfere with Raman emissions occurring at larger Raman Stokes shifts. At excitation wavelengths above 260nm, fluorescence emissions will always overwhelm weak Raman emissions, even at small Raman Stokes shifts. A wide range of material fluoresces between about 260nm and 750nm, severely restricting the variety of samples for which Raman spectra can be obtained without fluorescence interference. For this reason, Raman spectroscopy is commonly performed in the near infrared or ultraviolet to avoid fluorescence interference.

---

[16] Nirmala Ramanujam, *Fluorescence Spectroscopy In Vivo*, in Encyclopedia of Analytical Chemistry, R.A Meyers (Ed.), pp.20-56, John Wiley & Sons Ltd, Chichester, 2000.

[17] J.G.Winans, *Fluorescence and Phosphorescence*, in Handbook of Physics, E.U. Condon and H. Odishaw (Ed.), pp.6-131 to 6-157, McGraw Hill Book Co., 1967.

[18] S.A.Asher, C.R. Johnson, *Raman Spectroscopy of a Coal Liquid Shows That Fluorescence Interference Is Minimized with Ultraviolet Excitation,* Science, 225, 311-313, 20 July 1984.

3. Sensitivity and Specificity of Sample Detection and Identification Using Laser Induced Native Fluorescence

All microorganisms require continual input of free energy through cellular metabolism. The source of this energy input is electrochemical potential between electron donors and acceptors. The primary carrier of free energy is adenosine triphosphate (ATP), which is derived from the oxidation of fuel molecules such as carbohydrates and fatty acids. Typical molecules responsible for the transport of energy within cells are porphyrins, quinones, flavins, NADH, etc. Other essential building blocks of living organisms are nucleic acids, amino acids and peptides, sugars and lipids, and polysaccharides. Amino acids are the most common chemical group in biological materials, characterized by an amino group (NH_2) and a carboxyl group (COOH) and link to each other to form peptides and proteins. Phenylalanine, tyrosine, and tryptophan all have aromatic side chains with one or more benzene or phenyl rings. The aromatic side chains cause ultraviolet absorbance and fluorescence properties. When excited at an appropriate wavelength, these materials will provide a signature that can give a good indication of the general class to which the microorganism or organic material belongs. Many other organic and inorganic materials also fluoresce that are not harmful to humans. However, when the excitation and emission wavebands are carefully chosen, these can be discriminated against with high reliability.

Figure 3 shows excitation-emission matrix (EEM) diagrams over a range of excitation wavelengths from 200nm to 400nm and emission wavelengths from 200nm to 600nm of four materials: Bacillus subtilis cells in the vegetative and spore form and tryptophane and tyrosine. The double fluorophors are a characteristic of the fingerprint of these materials, which have excitation maxima near 230nm and 280nm. Below about 270nm there is a fluorescence-free region between the elastic scattering line and the region of fluorescence of tyrosine. Resonance fluorescence of biological agents is likely the only technique sufficiently sensitive to discover, *in situ* without any sample preparation, the presence and rough classification of a single or few numbers of microorganisms. It is the only viable method of performing non-contact biological classification of aerosols in situ[19] because of the small dwell time for observation in an aerosol stream. It is important to note that both the spores the vegetative cells have two optimum excitation wavelengths, one near 230nm and one near 280nm. Emission maxima vegetative cells at both excitation wavelengths are the same, at about 330nm, as expected. The EEM diagram for Bacillus subtilis in spore form (@10^4 per ml) is also shown in figure 3. Optimum excitation wavelengths for detection of bacteria and cellular residues will be described later. However, the optimum emission wavelength for spores is close to 305nm compared to 340nm for vegetative cells. This is a clearly distinguishable marker feature of spores.

[19] Faris, G.W., R.A. Copeland, K. Mortelmans, and B.V.Bronk, *Spectrally resolved absolute fluorescence cross sections for bacillus spores*, App.Opt.,Vol.36, No.4, pp.958-967, 1 February 1997.

The data in Figure 3 were obtained in water and it known that there are some difference between organisms in a wet versus dry condition. However, the relative response is illustrated in this figure.

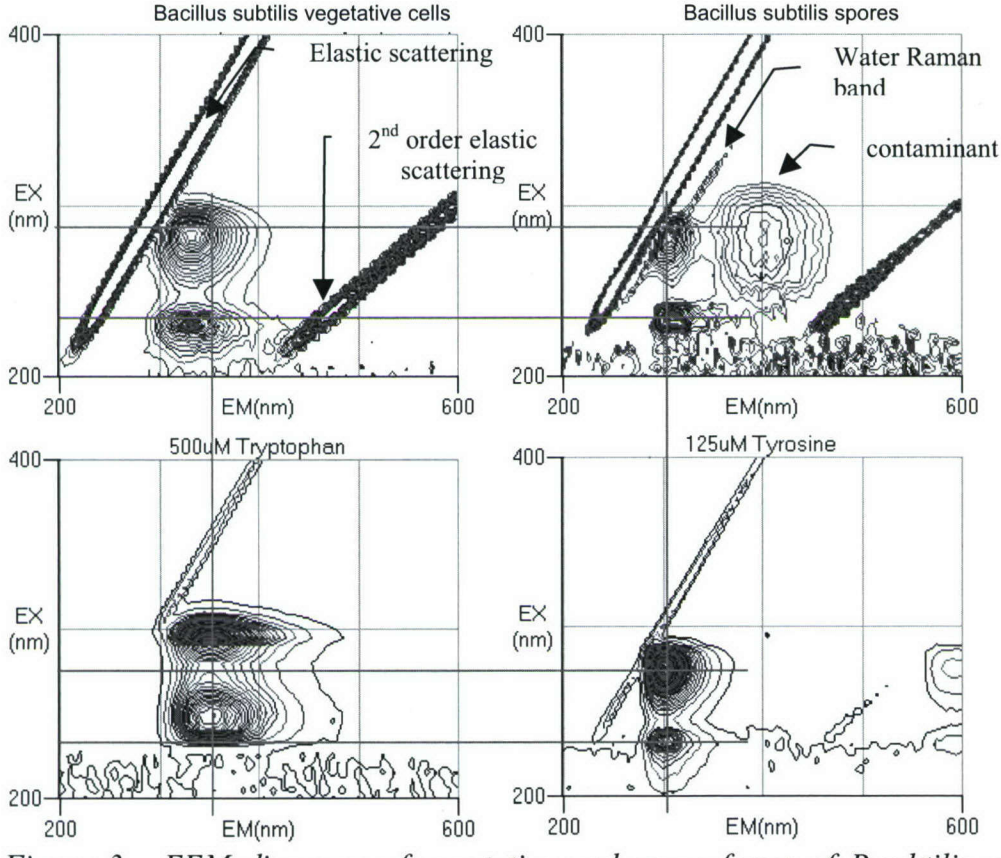

Figure 3. EEM diagrams of vegetative and spore forms of B.subtilis and tryptophan and tyrosine

Driks[20] shows that the spore coat for B. subtilis is dominated by tyrosine, whose fluorescence signature peaks near 300nm rather than the tryptophan, whose peak is near 350nm. This is shown by comparison with the TRP and TYR EEM diagrams shown below the B. subtilis in Fig. 3 above. A secondary optima occurring at Ex=280nm and EM=400nm is a result of a denatured alcohol contaminant in the sample. From the above EEM diagrams it is evident that B.subtilis vegetative cell fluorescence occurs at shorter wavelengths than pure Trp and long wavelengths than pure Tyr. The spore form is very closely related to Tyr as described by Driks.

The double fluorescence maxima in Figure 3 correspond to the double absorption maxima shown in Figure 4[21] for major aromatic amino acids. Trp absorption at 225nm is 5 to 10 times stronger than in the traditional excitation wavelength at 280nm. The fluorescence cross-section and related efficiency is similarly higher when excited near their optima. It is a common notion that excitation at shorter wavelengths causes more interference with background materials. This is incorrect since each material has a unique fingerprint with the fluorescence

[20] Driks, A., *Bacillus subtilis spore coat,* Microbiology and Molecular Biology Reviews, Vol.63, No.1, pp.1-20, Mar. 1999.
[21] T.E. Creighton, *Proteins: Structures and Molecular Properties* ,(W.H. Freeman and Company, 1984)

cross-section and subsequent emission intensity functions of both excitation and emission wavelength, as illustrated in figures 2 and 3 above, and 5 below.

EEM diagrams in Fig. 5, below further illustrate the broad variation of fluorescence fingerprints of many common background materials. Fluorescence of most materials normally occurs between about 270nm and 700nm. Fluorescence at the shorter end of this wavelength range results from molecules that have single phenyl rings while fluorescence at the longer end results from molecules that have several phenyl or benzene rings, such as polyaromatic hydrocarbons. Most fluorescent materials exhibit one to three fluorescence peaks. Paper has strong peaks in the blue/green due to doping of paper with fluorescent dyes to enhance "whiteness". Minerals typically have only one.

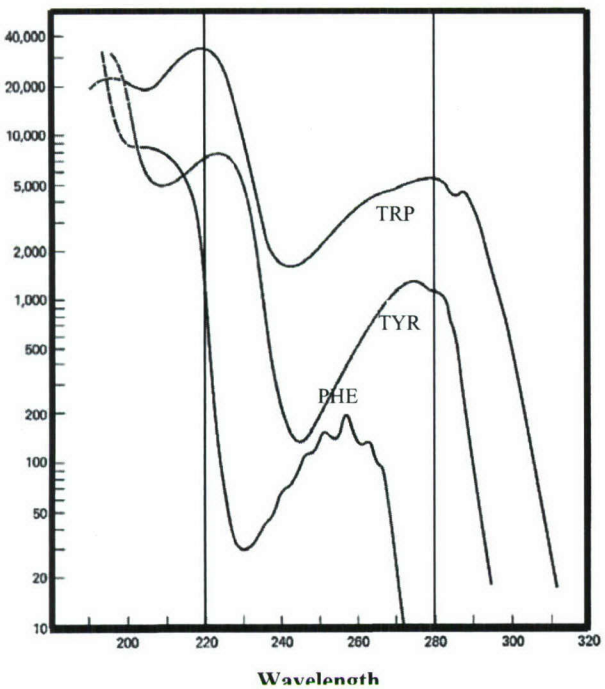

Figure 4. Molar absorptivity of amino acids

It is of interest to understand the ability to differentiate materials based on fluorescence alone. Later, in combination with elastic scattering for particle size determination, biological particles can be further differentiated. Target materials can include spores, vegetative cells, or biological residue materials such as aromatic amino acids, peptides or proteins, or nucleic acids, virus', etc. Background materials can include polyaromatic amino acids (PAH's), minerals, etc. The EEM fingerprint of most background materials is significantly different from a biological cell in either the spore or vegetative form. But even when a signature is similar, it is rarely similar enough that it cannot be differentiated, depending on the resolution of the spectrum obtained.

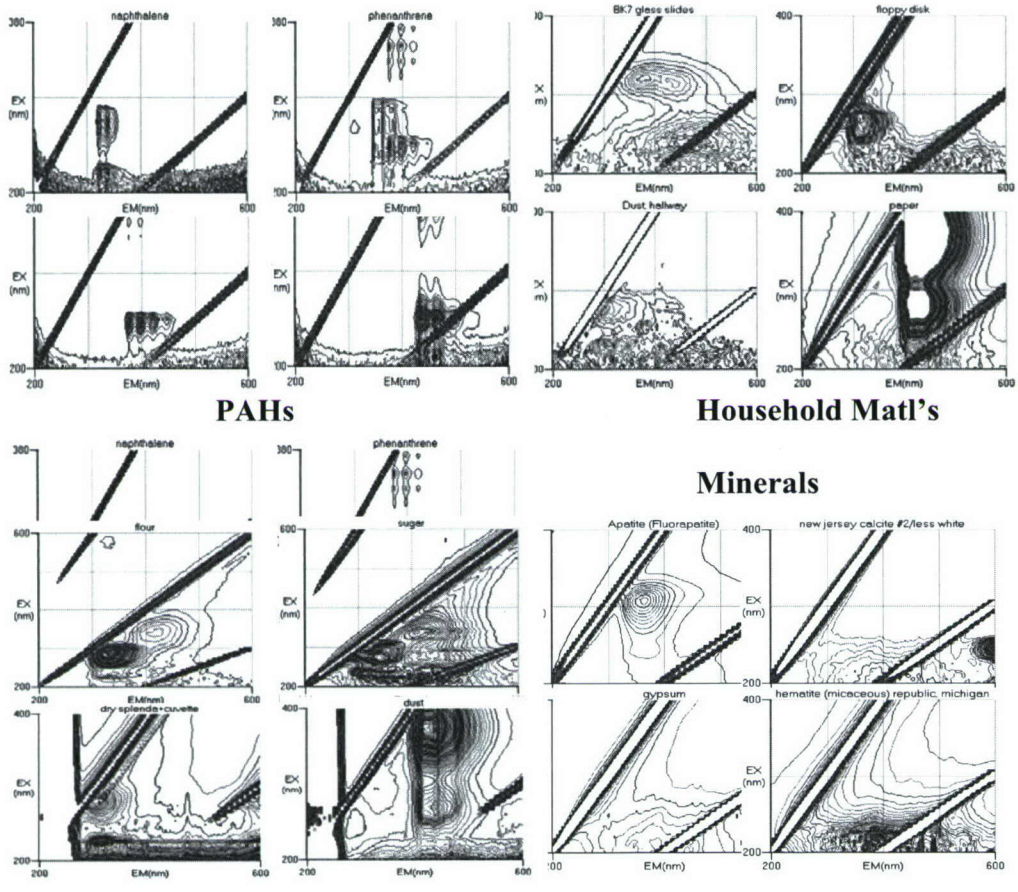

Figure 5. EEM diagrams of background materials

Figure 6, illustrates the ability to differentiate ten (10) groups (A through I) of pure samples excited at 235nm. Each group is made up of similar component materials which include organic and biological materials but which could also include minerals and other materials. High-resolution excitation-emission matrix (EEM) data sets of 61 pure samples were obtained using a Hitachi F4500 spectrofluorimeter where excitation ranged from 200nm to 400nm and emission ranged from 200nm to 600nm. Examples of these data sets are shown in Figs. 2, 3, and 5 above. At selected excitation wavelengths the relationship between the native fluorescence spectra of each material sample was compared using principal component analysis (PCA), although other analysis methods are also being investigated.

Table I. Samples compared: 61 samples in 10 groups according to basic composition

A. One ring compounds (black spheres) A1. 1-2 methyl groups incl. Phe phenylalanine-1Equal in nanopure1-1 b contains phenylalanine Gly phe ala Gly phe ser xylenes-1 **A2. Electronegative groups incl. Tyr** Tyrosine (dil1)-1Carpetaid-1ß contains benzene compounds toluene-1 dichlorobenzene-1 Glu tyr glu Gly tyr gly Leu tyr leu Lys tyr lys Nicety tyr eth ester **B. Spores (gray diamonds)** b atropheus-8b pumilis-8C. sporogen -8 (strain 1)C. sporogen -8 (strain 2)G. stearothermophil-8 **C. Whole cells and fractions (grey spheres)** 119 membrane,anaerobic 119 supernatent, " 120 membrane, " 120 supernatent, " b.pumilus membrane, aerobically grown b.pumilus supernatant, " b.pumilus whole cells, " b.atropheus membrane, " b.atropheus supernatant, " b.atropheus whole cells, " MR1 whole cells, "	**D. 2 ring compounds (open spheres)** 1,2 dimethnaph-21,3 dimethnaph-21,4 dimethnaphthalen-21ethyl naphthal-2acenaphthene-2dibenzothiophene-2 **E. Indole containing compounds (crosses)** carbazole-6 Indole-6tryptophan-6 **F. 3 ring compounds (bent) (open cubes)** 10 phenanthroline-3 'phenanthrene-3 **G. 4 ring (compact) and 3 ring (straight) (grey cubes)** 1 methylanthracene1-71methylpyrene-7pyrene-7anthracene3-7 **H. 5 rings(folded), 4 ring (straight), complex organics (small open cubes)** fluranthene-5 NADH-5perylene-5riboflavin-5 **I. Contaminants (black diamonds)**pink hibiscus pollen-0marigold pollen-0yellow hibiscus pollen-0 mech pencil lead-0drywall-0 corn starch (lush)-0crayola chalk-0ceiling tile-0 sweetnlow-0 splenda-0

Samples illustrated in Figure 6 are grouped according to their general composition as illustrated in Table I. Table I is a list of the 61 samples and how they were grouped. Group A materials represent variants on single phenyl ring materials and are divided into two subgroups: 1 ring with 1-2 methyl group and phenylalanine and 1 ring with electronegative groups and tyrosine. Group B materials are bacterial spores of a variety of types. Group C materials are bacterial cells as well as lysates (supernatant and membrane fractions). Group D materials are two ring materials with or without R groups. Group E are indoles including tryptophan. Group F materials are 3 ring materials with bent conformation such as phenanthrene. Group G include

folded 4 ring and straight 3 ring materials such as pyrene. Group H includes 5 ring and larger ringed organics such as perylene, NADH, etc. Group I materials are common household materials and pollens.

Figure 6 clearly illustrates that microbial spores and vegetative cells are clearly differentiable from each other as well as all of the other chemical groups. The spore group was made up of a variety of spores which all clustered together. Whole vegetative cells and cell fractions from a variety of cell types also clustered together in a distinct group.

To quantify the ability to differentiate these materials the 3D PCA centroid and spherical standard deviation of each group was determined. Using a spherical standard deviation should be very conservative since all materials except household contaminants lie close to a line and are not distributed in a spherically symmetric cluster. In the following figures we define the ability to differentiate materials by two methods:

- Overall differentiability factor, OD_f, is the distance between the centroids of the two closest of the 10 groups, minus the sum of the standard deviations of these two groups.
- Spore differentiability factor, SD_f, is the distance between the spore group centroid and any other material, minus the standard deviation of the spore group.

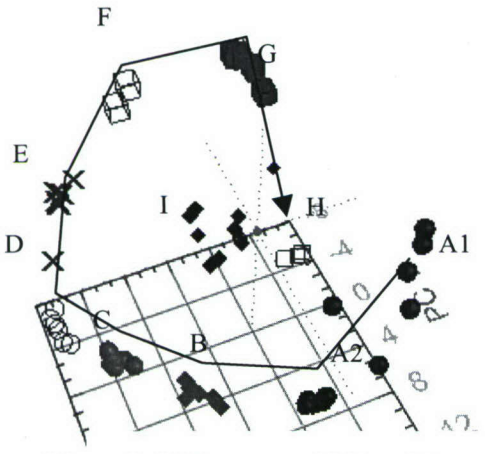

Figure 6. Full spectrum PCA positions of 61 samples in 10 groups. 235nm

The ability to differentiate between groups or individual materials is dependent on several factors including excitation wavelength, spectral resolution, and the number, bandwidth, and location of detection wavebands in sensors employing non-contiguous detection wavebands. Figure 7a shows the overall ability to differentiate all 10 groups, OD_f, identified in Table I as a function of wavelength for three confidence levels, corresponding to 1, 1.645, and 1.96 standard deviations of the group size. The optimum excitation wavelength for differentiating the groups of material selected is near 235nm. However, the shape and absolute values of OD_f with wavelength depends on the set of materials chosen for differentiation as well as the method of grouping materials. As an example, if spores or biological materials were not included, the resulting OD_f spectral distribution would be different. If a set of target and background materials were chosen which represented a specific situation in an industrial or municipal waste stream, in an ocean farming operation, or in a product or chemical factory, the choice of optimum excitation wavelength would be different. Optimum excitation wavelength is based on the choice of materials and groupings. For the materials and groups in Table I, 235nm is the optimum excitation wavelength.

The Spore Differentiability Factor, SD_f, is defined differently than OD_f and results in a different wavelength dependence, as shown in Figure 7b. The Spore Differentiability Factor, SD_f, is defined as the distance from the outer edge of the spore group to the nearest other chemical, since for this case all other chemicals are considered background chemicals and need not be grouped. The outer edge of the spore group is the centroid minus the spherical standard deviation of the group. SD_f is not as sensitive as OD_f to excitation wavelength below 235nm.

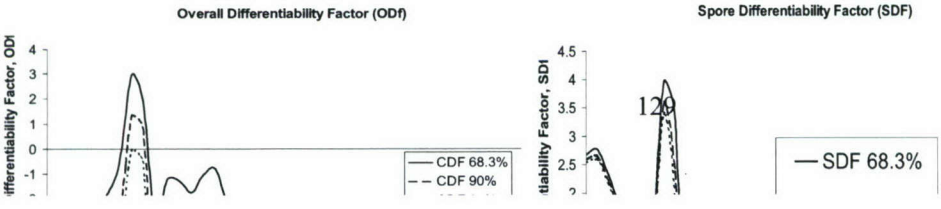

(a) (b)

Figure 7. Overall Differentiability Factor, OD_f (a) and Spore Differentiability Factor, SD_f (b) for 10 groups of samples

Figure 8 provides a more graphical illustration of the wavelength dependence of the Spore Differentiability Factor where PCA diagrams for excitation at 235nm and 280nm show how the spore group merges with other groups of materials as the wavelength is increased from 235nm to 280nm. The PCA diagram for an excitation wavelength of 370nm shows most of the material samples merging into the origin (PCA = 0,0,0) since most materials offer little fluorescence signature when excited at 370nm, and not much differentiation is possible. Therefore this figure is not shown.

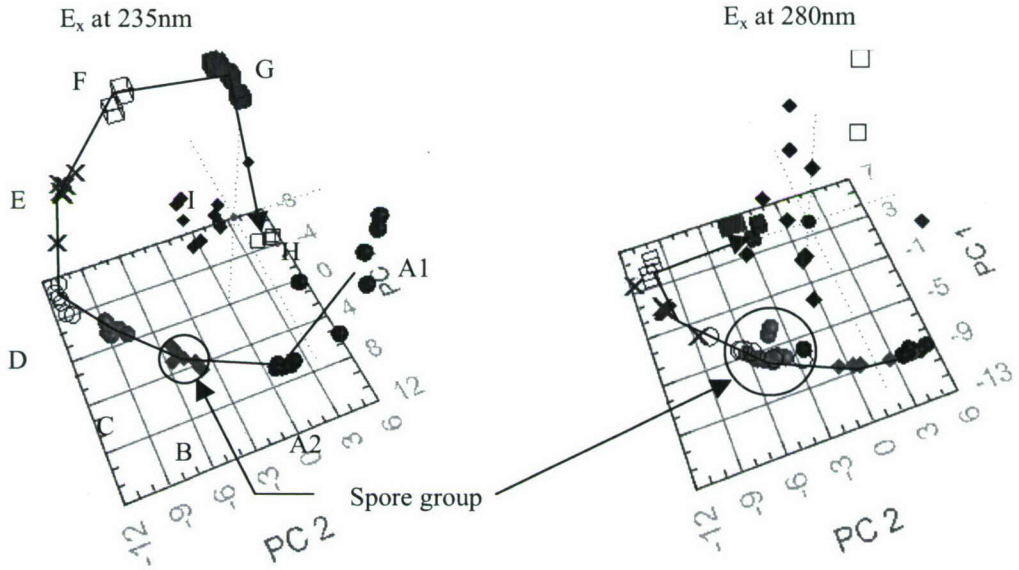

Figure 8. Comparison of PCA diagrams for 10 groups excited at 235nm versus 280nm, illustrating the merging of groups at non-optimum excitation wavelengths.

The results in Fig. 8 are based on data with a spectral resolution of 2nm. Overall as well as Spore differentiability is dependent on the spectra resolution at which the spectra are being compared. Figure 9 below illustrates the effect of spectral resolution for contiguous and non-contiguous spectral bands. The diamonds of Fig. 9 show the Overall Differentiability Factor for contiguous spectral bands. The circles show the OD_f for detection using non-contiguous, targeted, spectra bands. By targeted is meant that spectral bands are selected which enhance the OD_f. It is clear that targeted non-contiguous bands enable higher levels of differentiability than contiguous bands.

Fig. 9 illustrates that spores can be differentiated with significant fidelity using low spectral resolution. Since the sensitivity of detection is proportional to the bandwidth of each detection band, lower spectral resolution dramatically improves detection sensitivity.

Figure 9. Spore differentiability factor versus spectra resolution

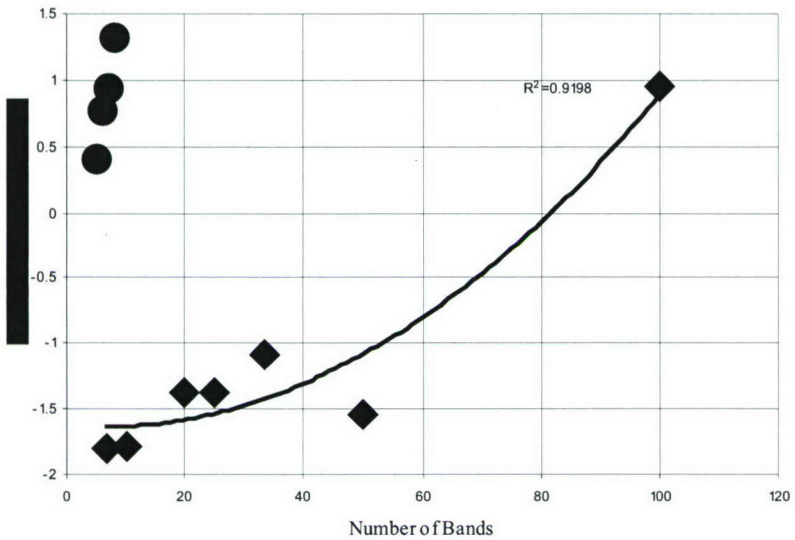

Figure 9. OD_f versus spectral number of detection bands within the 270nm to 550nm spectral region: Comparison of contiguous (diamonds) and targeted, non-contiguous (circles), detection bands

The simplest description for the sensitivity of detection for either fluorescence or Raman emission is $P_c = P_o\sigma\rho d^2/16f^2$, where P_c is the number of photons collected by the detection (objective) lens, P_o is the number of excitation photons delivered by the laser beam onto the sample, σ is the fluorescence or Raman scatter cross-section of the molecule or particle of interest (cm^2/mol) within a specific line or over a defined spectral bandwidth, ρ is the arial density of molecules or particles of interest (mol/cm^2), d is the diameter of the detection (objective lens) aperture and f is the distance of the sample from the detection aperture. Below in Table I are listed the fluorescence cross-sections of a whole B. subtilis spore and a single tryptophan molecule, both measured per nm of bandwidth at the peak of fluorescence emission at 330nm.

Table I. Fluorescence and Raman cross-sections for molecules and whole organisms.

Mode	Target	Detection Band	Comment	Cross-section $cm^2/sr/nm/particle$
fluorescence	B.subtilis spore[iii]	330 Fluor. band	whole spore	6.00E-14
fluorescence	TRP molecule[23]	330 Fluor. band	single molecule	2.75E-21
UV Raman	Adenosine[21]	1336 cm^{-1}	whole line	3.04E-22
UV Raman	Guanosine[21]	1575 cm^{-1}	whole line	1.56E-22
UV Raman	Guanosine[21]	1485 cm^{-1}	whole line	3.30E-22
UV Raman	B. Subtilis (Lag Phase)[21]	1615 cm^{-1}	whole line whole spore	1.04E-16

Also shown, as discussed later, are the UV resonance Raman scatter cross-sections of a single Raman band of a whole B. subtilis spore as well as single molecules. It is noted that the laser induced native fluorescence cross-section in a single nm of bandwidth is about 575 times larger than the strongest (1615 cm^{-1} Tyr) UV resonance Raman band. For a typical fluorescence

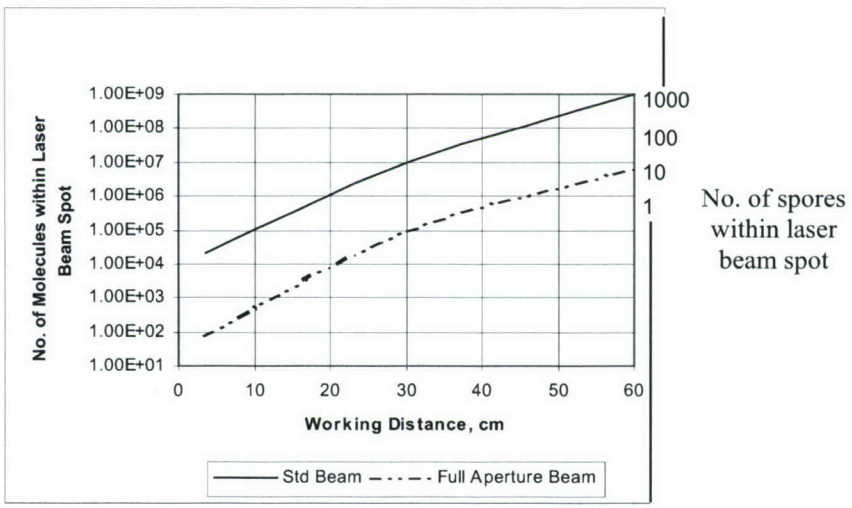

Figure 10. Fluorescence Limit of Detection (FLOD) ~~for~~ tyrptophane molecules and whole microorganisms

detection system where the detection bandwidth is 50nm, the fluorescence signal is 28,000 times stronger than the Tyr Raman band signal. For this reason, laser induced native fluorescence must always precede Raman in any detection and identification scheme.

An illustration of the sensitivity of detection of biological spores and residues from cells is shown in figure 10, below, for a specific surface sensor instrument as a function of the

working distance of the instrument. In this specific instrument configuration a UV laser dose of 10^{13} photons at 224nm was focused onto the target surface and detection was accomplished using 1.2cm diameter excitation and collection optics and a 50nm band-pass fluorescence detection filter centered at 330nm. Other features of the detection systems are: optical systems transmission of 80%; bandpass filter transmission of 25%; elastic scatter blocking filter transmission in the detection bandpass of 80%; PMT quantum efficiency of 25%; and a PMT gain of 10^6. The fluorescence limit of detection (FLOD) determination made here includes only the dark current of the PMT and does not include any background radiation from ambient lighting (i.e detection done in a dark enclosure). Figure 10 shows that the FLOD for tryptophane ranges from about 100 molecules at a working distance of 3.6cm to about 100,000 molecules at 30cm. Using the same full-aperture beam, a single microbe can be detected at a distance about 45cm. The focused laser spot diameter ranges from 9μm at 3.6cm to 70μm at 30cm to 100μm at 60cm for the full aperture beam. Under-filling the objective lens using a 3mm diameter laser beam instead of 12mm for the full aperture beam causes the LOD to increase about 2 orders of magnitude for all cases. The focused spot diameter for this case ranges from 34μm at 3.6cm to 300μm at 30cm to 500μm at 60cm.

4. Sensitivity and Specificity in Biochemical Identification using UVRRS

A molecule has 3N-6 (or 3N-5 for a linear molecule) normal Raman modes or bands. For simple molecules this leads to relatively simple Raman spectra. For large macromolecules, such as biological molecules, the number of atoms within the molecule is large and so is the number of normal modes. For normal, non-resonant, Raman this can lead to very complex, and hard to analyze, spectra. Fortunately, biological molecules are made up of large numbers of a few identical molecular subgroups, which makes their Raman spectra somewhat easier to interpret. UV resonance Raman spectra of bacteria contain a number of bands arising primarily from bacterial protein subunits, various nucleic acids, and other species absorbing strongly in the ultraviolet. Resonance Raman simplifies the interpretation of spectra since it permits the specific million-fold enhancement of the vibrational spectrum of this one particular molecular subgroup within a complex solution or mixture, as occurs in biological organisms. Raman emissions from the non-resonant species are relatively attenuated. For bacterial protein, the most appropriate choice of excitation wavelength is between about 220nm and 240nm because it selectively enhances UVRRS bands of aromatic side chains of phenylalanine, tyrosine, and tryptophan[22]. For nucleic acids, the most appropriate choice of excitation wavelength is between about 240nm and 255nm because of the strong absorption of these molecules in this range.

Over the past ten years UV resonance Raman spectroscopy has been increasingly used for detection and identification of microorganisms and study of cellular function[23], S. Asher and

---

[22] N.Cho, S. Song, and S. Asher., Biochemistry, 33, 9940-9951, 1994.

[23] S. Chadha, W. H. Nelson and J.F. Sperry, *Ultraviolet micro-Raman spectrograph for the detection of small numbers of bacterial cells*, Rev. Sci. Instrum. 64 (11), pp.3088-3093, Nov. 1993

[23] Z. Chi and S. A. Asher, *UV resonance Raman Determination of Protein Acid Denaturation*, Biochemistry, 37, pp.2865-2872, 1998.

[23] F. Sureau, et.al., *An ultraviolet micro-Raman spectrometer: Resonance Raman spectroscopy within a single cell*, App.Spect., 44, No.6, pp.1047-1051, 1990

[23] N.Cho and S.A. Asher, *UV resonance Raman studies of DNA-Pyrene interactions*, J.Am. Chem.Soc. 115, pp.6349-6356, 1993

[23] Sparrow, M.C., J.F. Jackovitz, C.H. Munro, W.F. Hug, and S.A. Asher, *A New 224nm Hollow Cathode UV Laser Raman Spectrometer*, J. App. Spectroscopy, Vol. 55, No. 1, Jan 2001.

W. Nelson are well known for their groundbreaking work in UV resonance Raman spectroscopy, especially as it applies to characterization of organic molecules and the molecules of life. It has been clear for several years that unique ultraviolet resonance Raman spectral signatures can reliably be measured in as few as 20 bacterial cells with low power consumption and low photon flux levels (Nelson, 1993[24]; Nelson, et.al.1993[25]; Chadha, et.al., 1993[26]). The literature in this area continues to grow[27]. The goal is characterization of single cells.

4.1 Taxonomic Raman marker bands for microorganisms

A summary of the major taxonomic marker bands of highly degenerate molecular subgroups occurring within microorganisms is shown below in Table II.

Table II. Major Taxonomic Raman marker bands for biological agents

Material	Raman Band Locations
Tryptophan	753 879 **1011** 1353 **1555** 1615
Tyrosine	831 852 **1180** 1210 **1615**
Guanine	1320 1365 **1485** 1577 1603
Adenine	**1337** **1485** 1580
Cytosine	**1530**
Dipicolinic Acid	**1017** **1195** **1396** **1446**

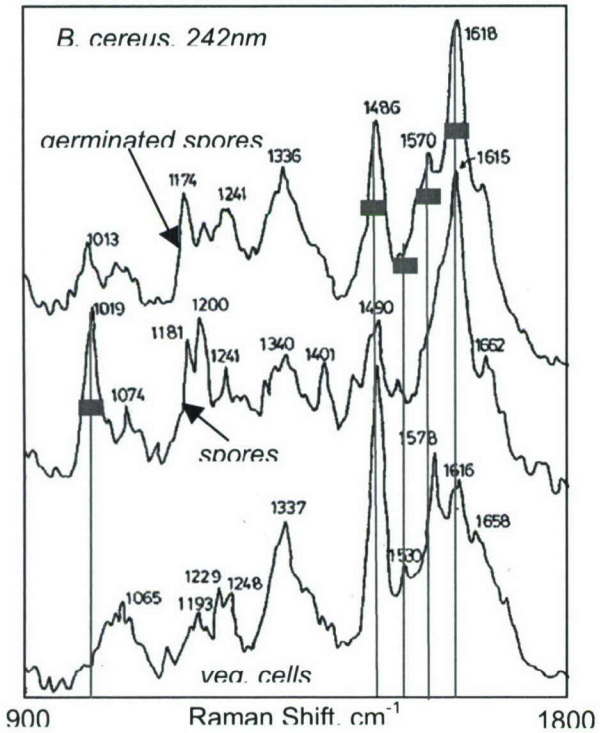

Figure 11. Raman spectra of B. cereus cells (adapted from Ref. 25)

Identification of biopolymers or organisms using UV Raman spectroscopy depends on the ability to produce interpretable, reproducible spectra. DNA and cell surface antigens are the most attractive targets as potential markers for cellular or bacterial identification. Identification of organisms using UV Raman spectroscopy has focused on the ratio of a few taxonomic marker bands (Ref. 14). These band markers are based on ratios of tryptophan and tyrosine and DNA base pairs that can be characteristic of an organism. As mentioned previously, most biological materials have repeating functional groups that are highly degenerate[iv]. These include nucleic acid base pairs and aromatic amino acids. These repeating units have Raman spectra that are very similar to the spectra of the monomers upon which they are based.

[23] Asher, S.A., *UV Resonance Raman Spectroscopy*, Anal. Chem., 65, 2, Jan. 15, 1993.
[24] Nelson, W.H. *Rev Sci. Inst.* (11):3088-3093, 1993
[25] W.H.Nelson, R. Manoharan and J.F. Sperry, "UV Resonance Raman Studies of Bacteria", App. Spect. Reviews, 27 (1), pp67-124, 1992
[26] Chadha, S., Nelson, W.H., Sperry, J.F. *Rev. Sci. Inst.* (11):3088-3093, 1993
[27] Q. Wu, W.H. Nelson, S. Elliot, J.F. Sperry, M. Feld, R Dasari and R. Manoharan, *Intensities of E. coli Nucleic Acid Raman Spectra Excited Selectively from Whole Cells with 251- nm Light*, Anal. Chem. **72**, 2981-2986 (2000).

Raman spectra of B. cereus in several forms is shown below in Fig. 11 in using 242nm excitation: vegetative, spore and germinated spore (Ref.25). Major Raman marker bands are shown at 1019 cm^{-1}, 1485 cm^{-1}, 1530 cm^{-1}, 1555 cm^{-1}, and 1615 cm^{-1}. The measurement bandwidth illustrated is about 25 cm^{-1}. The bands shown below in figure 10 are 50 cm^{-1} wide.

4.2 Raman spectra of biological particles

Bacteria can be characterized as Gram positive versus Gram negative based on the 1555 cm^{-1}/1615 cm^{-1} intensity ratio. Gram negative bacteria have a much higher ratio of the tryptophan intensity at 1011 cm^{-1} or 1555 cm^{-1} compared to the Tyr + Trp intensity at 1615 cm^{-1}. In general, this ratio is described as the intensity in broad spectral regions centered near the 1555 cm^{-1} and 1615 cm^{-1} Raman bands. However, the exact position, center of gravity, band width, and other features of each band can provide more detailed identification of bacteria. However, the relationships are presently unknown. It is believed that these marker bands primarily describe the surface composition of an organism.

Within Gram positive organisms such as spores, or vegetative cells there is further sub-classification G+C percentage. This is determined by the 1530 cm^{-1}/1485 cm^{-1} Raman band intensity ratio. The intensity of the 1485 cm^{-1} peak is taken as closely proportional to the total amount of nucleic acid on a molar basis (DNA + RNA) in the cell. The intensity of the peak at 1530 cm^{-1} can be assumed to be proportional to the moles of cytosine in the nucleic acids. It follows that the mole fraction of G+C in the bacteria should be proportional to the ratio of the 1530 cm^{-1} and 1485 cm^{-1} peaks.

Within Gram positive organisms such as spores, or vegetative cells there is further sub-classification G+C percentage. This is determined by the 1530 cm^{-1}/1485 cm^{-1} Raman band intensity ratio. The intensity of the 1485 cm^{-1} peak is taken as closely proportional to the total amount of nucleic acid on a molar basis (DNA + RNA) in the cell. The intensity of the peak at 1530 cm^{-1} can be assumed to be proportional to the moles of cytosine in the nucleic acids. It follows that the mole fraction of G+C in the bacteria should be proportional to the ratio of the 1530 cm^{-1} and 1485 cm^{-1} peaks.

Following is a graph of the 1530/1485 cm^{-1} ratio versus the known percentage of G+C of DNA in 14 different bacterial species grown on TSA and in TSB, respectively (Ref.14). The peak intensity ratios versus molar percent G+C are linear dependent, as shown in Fig. 12. Three lines are shown in Fig. 11 which represent the mean and ± one standard deviation of the data. This preliminary estimate illustrates the potential to identify an organism within about ± 3 to ± 5 mole percent G+C. In combination with identification of the Gram polarity and whether the organism is a spore, the G+C content can provide significant specificity in identification or biological agents. The organisms employed in Fig. 11 are tabulated below in Table III.

4.3 Biological agent identification specificity

One possible detection and identification strategy for biological agents using laser induced resonance fluorescence and UV Raman spectroscopy is as follows:

a. Determine if a particle is biological or non-biological based on laser induced resonance fluorescence measured in the 300nm region.
b. If particle is biological, measure the relative UV Raman intensity at five (5) Raman bands centered at 1017 cm^{-1}, 1485 cm^{-1}, 1530 cm^{-1}, 1555 cm^{-1} and 1615 cm^{-1}.

c. Determine if the particle is Gram positive or negative based 1555 cm^{-1} /1615 cm^{-1} ratio.
d. Determine if the particle is a spore based on the 1017 cm^{-1} /1615 cm^{-1} ratio.
e. Determine the GC% based on the 1530 cm^{-1} /1485 cm^{-1} ratio.

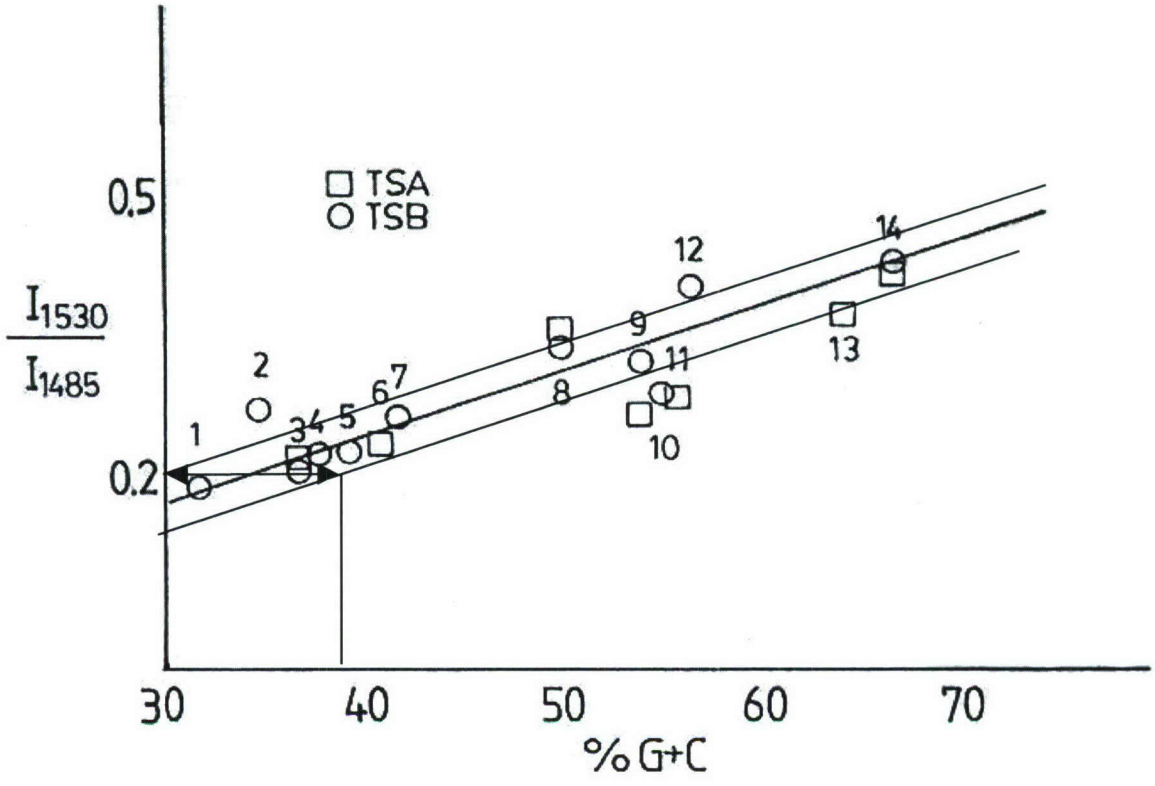

Figure 12. Plot of 1530 cm^{-1}/1485 cm^{-1} versus known G+C for 14 bacterial species. 242nm excitation See Table III on next page for list of organisms displayed above (adapted from Ref.25)

Measurement of the Raman scattering in only five (5) broad (≈50cm^{-1}) bands ***provides knowledge of the: Gram polarity; form of organism; and G+C percent***. These measurements can be made rapidly and correlated using any of several artificial neural net or PCA/PCO algorithms to give a relatively high degree of confidence in identifying organisms within a narrow range. These measurements could be made in sub-second time scales and possibly as short as a millisecond or faster.

Using this fast and simple 5-band Raman technique, it would appear that it is unlikely this method would be able to specifically differentiate B. antracis against a background containing a wide range of other similar spore interferants since the detection accuracy corresponds to only about ± 4 % in G+C concentration. The closest spore to B. antracis at GC=35.2% is B. cereus at 32% (Δ=3.2%) and B. magaterium at 37% (Δ=1.8%). All three are spore formers and all are Gram positive. So none of the discriminators would have differentiated between these organisms with a low false alarm rate. However, this fast method will probably enable discrimination of B.subtilis from B.antracis. In addition, this method would be able to discriminate anthrax from a wide range of other bacterial spores and other microorganisms and identify them within a small range.

Table III. DNA mole fraction for Guanine + Cytosine for bacteria in Fig. 12

Plot No.	Organism	Mole% G+C	*Gram*	Spores	Virulence class[g]
	Clostridium botulinium	28.2[i]	+	X	2
	Rickettsia prowasecki	28.9[i]	-		3
	Staphylococcus aureus	32.8[b]	+		2
1	Bacillus cereus	32[a]	+	X	1
2	Enterococcus faecalis	34-36[a] 37.5[b]	-		1
	Staphylococcus simulans	34-38[a]	+		1
	Bacillus antracis Ames	35.2[b]	+	***X***	2
	Streptococcus agalactiae	35.5[b]	+		1
4	Proteus vulgaris	36-40[a]	-		1
3	Bacillus magaterium	37[a]	+	X	1
5	Proteus mirabilis	39.5[a]	-		1
6	Bacillus subtilis	41[a]	+	X	1
7	Acinetobacter calcoaceticus	42[a]	-		2
	Bacillus subtilis	43.5[b]	+	X	1
	Shewanella oneidensis MR1	45.9[b]	-		1
	Yersinia pestis.	47.6[i]	-		3
	Vibrio cholerae	47.6[i]	-		3
8	Escherichia coli, K12-MG1655	50.7[b]	-		2
	Shigella dysenteriae	50[i]	-		2
	Samonella tphi	52.1[i]	-		2
9	Enterobacter aeroqenes	54.3[a]	-		1
10	Alcaliqenes faecalis	54.8[a]	-		1
11	Enterobacter cloacae	55.4[a] 57.2[b]	-		1
12	Aeromonas hydraphila	55.7[a]	-		1
	Brucella suis 1330	57.2[b]	-		3
	Brucella melitensis	57.2[c]	-		3
	Aeromonas hydrophila	59-62[c]	-		1
	Pseudomonas putida	61.4	-		1
13	Pseudomonas aeruqinosa	64[a],66.4[b]	-		1
14	Micrococcus luteus	66.3[a]	+		1
	Alcaligenes faecalis	66.7-69.9	-		1
	Burkholderia pseudomallei	68.06[i]	-		3

a=A.I.Laskin & H.A.Lechevallier(eds), CRC Handbook of Microbiology, Vol.II, CRS Press, Cleveland, 1973. b=tigr, i=Sanger Inst.

The above measurements and correlations were done at an excitation wavelength of 242nm. The effect of employing other excitation wavelengths is shown in Fig. 9 below. It is clear from this figure that excitation wavelengths need to be between 230nm and about 255nm. Excitation wavelengths below this range would not clearly distinguish the dipicolinic acid peak at 1019 cm^{-1}. Wavelengths above 255nm would run into fluorescence background for high Raman shift marker bands.

There are many UV Raman spectroscopic options that have yet to be evaluated to reduce the false alarm rate in identifying B. antracis or other virulent microorganisms. The fast and simple approach described above does not take advantage of the much larger wealth of information contained in UV Raman spectra. Substantial differences in taxonomic marker band intensity, peak position, center of gravity, and band shape occur for each of the basic Raman marker bands. These are a result of environmental and conformational differences between organisms as well as more subtle compositional and environmental differences. In addition, there are other Raman marker bands that are clearly measurable which may give further discrimination to microorganism identification. It is not yet clear whether higher resolution spectra are needed to provide a higher level of biological agent specificity. A reasonably way to triage a target would be to follow the laser induced resonance fluorescence and few-broadband UV resonance Raman with higher numbers of broadband measurements, and possibly followed by high resolution UV resonance Raman. Each of these techniques is successively more time consuming, less sensitive and more specific. At present there is no clear model to provide higher specificity based on more subtle nuances of the Raman spectra such as peak position or center of gravity variations due to difference is microorganisms. This is the subject of a continuing study.

4.4 Biological agent detection sensitivity for resonance Raman

The Raman Limit of Detection (RLOD) for the 1336 cm^{-1} band of a single Adenosine molecule (from Table I) is 625 times lower than the FLOD for a TRP molecule per nm of bandpass or about 6.2×10^4 molecules. The RLOD for this line is less than the content of a single microorganism. A typical cell (E. coli) has 32×10^6 molecules of Adenosine. Thus, at a focal length or working distance of the instrument of 3.6cm, the instrument will be able to detect the 1336 cm^{-1} band of the cellular residue of less than one cell or certainly one, intact, cell.

4.5 Photochemical damage

Much of the biological UVRRS data published to date have been on cells in a flowing aqueous solution where the spectra result from an aggregate of the cells flowing through a UV laser beam focused into a flow cell during data accumulation times ranging up to several minutes. This was done to reduce photochemical damage and degradation of the samples during data accumulation. Careful attention was paid to culturing homogeneous samples so that spectra obtained were from well-characterized cells under well-known conditions. For the purposes of this development it is intended that spectra be taken on immobile samples on dry substrates, or flowing in aerosol or liquid streams where the spectra are accumulated from a small but fixed sample of cells during data accumulation. The ultimate goal is characterization of single cells. To do this, the total excitation photon dose needs to be limited to a value for which the spectroscopic characteristics of the cell are not altered during data accumulation.

The UV resonance Raman scattering cross-section of the tyrosine (Tyr) 1615cm^{-1} Raman band for a whole Bacillus subtilis spore is about 1×10^{-16} cm^2/sr. Assuming the objective lens of the optical system of a sensor collects one steradian of solid angle, it would take an excitation

dose of 10^{16} photons/cm^2 on a spore to collect a single photon in the optical system. This dose corresponds 8mJ/cm^2 of exposure. Since the physical cross-section of a typical spore (1x4μm) is about $4x10^{-8}$ cm^2, about 10^8 photons are incident on a single spore to enable collection of the single Tyr Raman band photon. Put in other terms, an 8mW laser exposing an area of 1 cm^2 would require a 1 second exposure to collect a single photon, or 8mW in a 30μm square area for 10μs. Since a typical optical system is at best 50% efficient, the typical actual dose to collect a single photon into a PMT would be at least double these values. The number of photons incident on the spore during this period would be about $2x10^8$ photons.

One log of inactivation (i.e. 90% kill) of wild-type B. subtilis spores requires the same dose[v]: 10^{16} photons/cm^2. As the dose is increased, the emitted and collected number of photons in the 1615cm^{-1} TYR Raman band increases proportionally. However, so does the level of spore inactivation. At the dose level of one or two logs of inactivation, it is not anticipated that much spectroscopic alteration of a single spore would occur. This is because at one or two logs of inactivation, the total number of photons incident on the spore is still less than 10^9 photons, a relatively small number compared to the number of bonds in a spore. It is likely that several orders of magnitude greater dose can be accepted before significant photochemical alteration occurs in the Raman spectra of a whole organism. A significant literature exists on the requirement for spore inactivation, an excellent survey of which is in Ref. 29[vi]. Little literature has been found on the subject of photochemical alteration of the spectral signatures of UV Raman spectra. However, from this cursory analysis it appear possible to obtain adequate signal from a single microorganism without producing so much photochemical damage as to cause spectral alteration.

3.4.5.2 Subcontract with U. Rhode Island:

The statement of work under the URI subcontract follows.

The University of Rhode Island Phase II SBIR subcontract will be directed towards the development of a biological agent identification algorithm. This comprises Task 5 of the program as proposed to DARPA.

This task will be conducted at University of Rhode Island under the direction of Profs. Wilfred Nelson and Chris Brown. This work will follow the direction that Prof. Nelson has pioneered for over 10 years in the use of UV Raman to identify microorganisms. Resonance fluorescence will be included in addition to the UV Raman studies. With regard to resonance fluorescence measurements, we will attempt to quantify the relationship between microorganism classification false alarm rate and the excitation wavelength and observation waveband locations, bandwidths and numbers of bands.

In this task we will also attempt to determine the robustness of the ability both to measure specific UV Raman taxonomic marker band intensity ratios and the relationship between signal to noise in this measurement and the false alarm rate of identification of specific biological agents or their categories.

While resonance fluorescence measurements are known to be possible for detecting single biological agent particles in an aerosol, UV Raman cannot, even with the advantage of resonance enhancement. This is a result of the substantially smaller scatter cross-sections for UV resonance Raman. We will study various methods of in situ sample accumulation, especially

for UV Raman, such as liquid concentrators, air-to-liquid concentrators, or surface contaminant measurements.

Summary of U. Rhode Island Results

By the time this contract started, Prof. Nelson was essentially retired. His effort was taken up by Prof. Chris Brown and a student. Prof. Brown with the help of Prof. Nelson attempted to recover much of the original UV Raman spectral data used in many of Prof. Nelson's prior publication. Much of the spectral data were lost, but some were recovered from old hard drives, etc. The purpose of recovery of this data was because this data set was the most self-consistent data set existing on bacterial organisms of various types and in various points is a life cycle. Development of these sample would have been a very large endeavor.

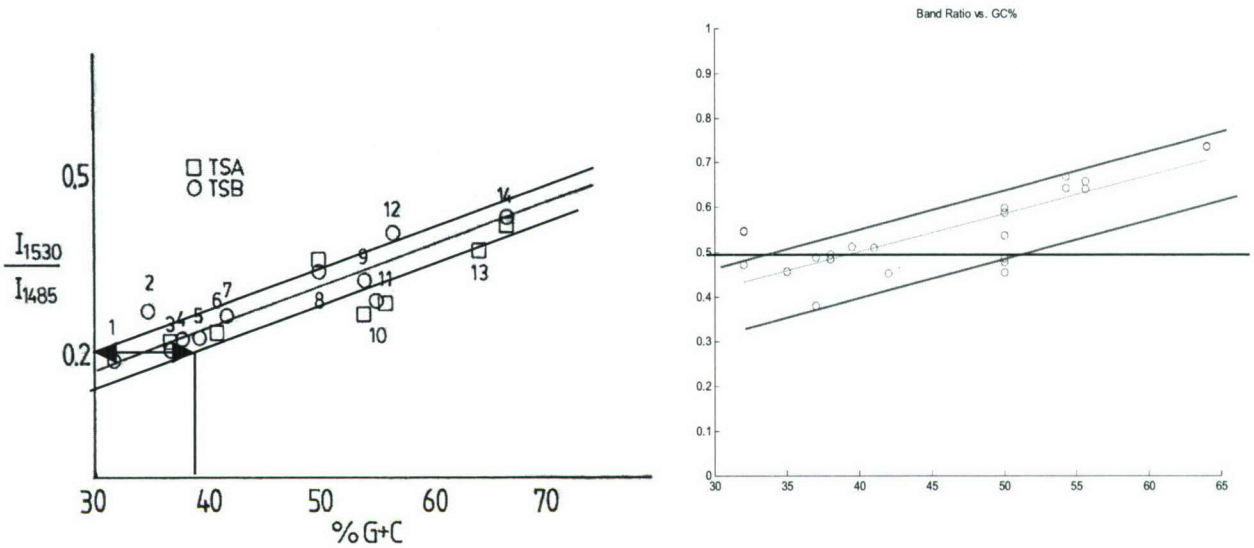

Figure 13. Reproduction of Fig. 12 on left. Re-analysis of data of 1530 cm^{-1}/1485 cm^{-1} ration versus known G+C for 14 bacterial species. 242nm excitation. (adapted from Ref.25)

The spectra on the right of Fig. 13 above employed recovered raw spectral data from Prof. Nelson but reprocessed. The spectra were smoothed with a Savitsky-Golay 9- or 11-point cubic function; thus, there was some degradation of the resolution, but not a lot. The results are similar in both slope but with a somewhat wider statistical distribution. Compared to the earlier published results by Prof. Nelson the statistical spread for a given 1530/1485 band ratio is closer to ±10% than the earlier ±4% value. The offset in Raman band ratio between the two data sets is believed due to the selection of the baseline for determining the peak heights. Prof. Brown's graduate student, Kevin, used the minimum for the entire spectral region as the baseline.

Unfortunately, all of the data recovered from Prof. Nelsons original studies were analyze regarding how the spectra related to GC content in organisms, and this correlation did not bear fruit. This is not to say that whole spectra at various levels of spectra resolution would not yield the ability to differentiate organisms better than the GC content method using the 1530/1485 Raman band ration method.

3.5 Boston University Results

The following results from Boston Universities effort has it's own numbering systems for figures, equations, etc.

1. OVERVIEW

The work at Boston University was directed at development of laser structures based on III-Nitride materials, which upon electron-beam pumping would show emission at wavelengths below 250nm. We have successfully developed laser structures that exhibit wafer level sub-threshold emission at 233-250nm. These structures have been designed such that the laser cavity can be formed by crystallographic cleaving.

In addition, we have developed a versatile system to measure the cathodoluminescence and photoluminescence from bulk films and device structures grown during this program. The luminescence measurements can be obtained using various excitation geometries, at temperatures from room temperature down to 80K.

A major part of the efforts involved materials development; these devices being primarily based on AlGaN alloys with Al content ranging from 70 to 100%, a relatively unexplored class of materials. It has been reported in the literature, that AlGaN alloys in this composition range show very strong sub-bandgap luminescence, which can be much more intense than the band-edge emission. We have successfully demonstrated that with the optimization of MBE growth parameters, AlGaN alloys can be deposited which show a band-edge luminescence three orders of magnitude stronger than the sub-bandgap emission.

Laser structures based on the GRINSCH design, and using AlGaN/AlN MQWs were deposited onto C-plane sapphire. These structures show wafer level sub-threshold emission at 233nm. However, for this structure the formation of laser devices require the generation of facets by reactive ion etching (RIE), as there are no common crystallographic cleavage planes between C-plane sapphire and C-plane AlGaN. The RIE process, which is generally used for the fabrication of blue lasers, produces sidewalls with a high degree of roughness. This is a problem in the case of deep-UV lasers as the smoothness requirement is greatly enhanced with the reduction of emission wavelengths.

A suitable method for generation of cleaved-facet cavity in the III-Nitrides is to use an A-plane (11-20) sapphire as the substrate for deposition. In this case, the nitride film grows with its C-axis parallel to the substrate and the R-plane of the sapphire substrate is aligned with the A-planes of AlGaN epitaxial films, and crystallographic cleaving can be accomplished. However, almost all published literature of growth onto A-plane sapphire has been limited to GaN and InGaN materials. We found that it is necessary to develop a new buffer layer deposition technique in order to obtain epitaxial AlGaN films with high structural and optical quality. AlGaN bulk films deposited onto A-plane sapphire was successfully cleaved to form atomically smooth facets.

Laser structures incorporating a GRINSCH configuration for optical confinement were deposited onto A-plane sapphire. Either an AlGaN double heterostructure or AlGaN/AlN MQWs were used as the active region. These structures show wafer level sub-threshold luminescence at 233nm to 250nm range. The luminescence intensity and spectral purity for these structures are similar to those deposited onto C-plane sapphire.

In order to improve the structural properties of AlGaN alloy bulk film, Indium was tested as a surfactant during the growth. TEM images indicate that under optimized deposition conditions, the introduction of indium causes a significant reduction of dislocation densities.

Since dislocations in these materials are non-radiative recombination centers, such films also show strong increase in luminescence intensity. In the later part of the program, GRINSCH laser structured were deposited onto A-plane sapphire using these techniques for improvement of crystal quality.

Several of the laser structures were delivered for facet formation. In addition, laser structures were cleaved at Boston University, and the cleaved bars were tested by e-beam pumping at room and low temperatures.

2. MAJOR ACCOMPLISHMENTS

1. Reduction of sub-bandgap luminescence in high Al-content AlGaN alloys
2. Reduction of dislocation density in AlGaN bulk films by use of Indium as a surfactant.
3. Optimization of AlN buffer layers for growth of AlGaN alloys on A-plane sapphire
4. Crystallographic cleaving of AlGaN bulk film deposited onto A-plane sapphire leading to extremely smooth facets
5. Growth of parabolically graded AlGaN cladding layers by use of digital alloys.
6. Development of laser structures on C-plane sapphire with wafer level sub threshold luminescence at 233nm
7. Development of laser structures on A-plane sapphire with wafer level sub threshold luminescence ranging from 233nm to 250nm
8. Development of cathodoluminescence / photoluminescence system for testing bulk films and laser structures.

3. DETAILS OF RESEARCH EFFORTS

3.1 Growth of AlGaN alloys onto C-plane sapphire

3.1.1 Reduction of deep level luminescence in High Al content AlGaN alloys

We have correlated the growth conditions of AlGaN films grown onto the C-plane of sapphire with 70% AlN mole fraction, with their cathodoluminescence (CL) spectra as well as their structure, determined by X-ray and TEM-SAD (selective area diffraction). The results show that the CL spectra depend strongly on the ratio of group-III to group-V fluxes. Specifically, when III/V is larger or smaller than 1, a significant fraction of radiative recombination occurs through centers in the middle of the gap. On the other hand when the ratio of III/V is equal to 1, the recombination occurs primarily across the band-gap. The XRD and electron diffraction studies show superlattice lines, consistent with the presence of atomic ordering. This alloy ordering results depends also strongly on the ratio of III/V. These results suggest that the radiative recombination through centers in the middle of the gap is related to the structural differences in the films rather than oxygen incorporation as suggested in the literature.

A. Kinetics of growth of AlGaN films

Our group has demonstrated earlier [1] that the kinetics of AlGaN growth is different than the kinetics of AlGaAs growth by MBE. This is due to the difference in the strength of the Al-N and Ga-N bonds versus the relative similarity of the strengths of the bonds Al-As and Ga-As. We find that Al incorporates with unity incorporation probability in both the group-III and Nitrogen rich growth regimes at the usual growths temperatures of 750 to 800 C. In contrast the incorporation probability of Ga atoms is constant (but less than 1) only under N-rich conditions of growth. Under group-III rich conditions of growth, there is a competition between the

incorporation of Al and Ga atoms. Due to the stronger Al-N versus Ga-N bond, the incorporation of Ga is controlled solely by the available nitrogen flux that is not consumed by the Al atoms.

As a result the Ga flux can be chosen to be high enough without affecting the AlN mole-fraction in the films. The excess Ga forms a thin layer on the surface during growth, whose steady state thickness is determined by the Ga arrival and evaporation rates, the latter being strongly dependent on the substrate temperature. Even though the Ga in the surface does not incorporate and hence does not alter the alloy composition, the presence and the thickness of this Ga film plays an important role in the structural, electronic and optical properties of the AlGaN alloy.

B. Incorporation of Oxygen

The incorporation of chemical impurities such as oxygen into AlGaN alloys is also influenced by the group III- group V ratio. Oxygen is present in AlGaN alloys grown by either MOCVD or MBE, and the density increases with the increase of Al content due to the affinity of Al for oxygen. In MBE systems such as the one used in the current work the presence of oxygen in the ambient is negligibly small. However oxygen enters the system as chemical impurities in the process gas (NH_3 or N_2). It has been reported that the incorporation of oxygen into AlGaN alloys decreases with the increase of the Ga flux [2]. This is because oxygen reacts with the Ga adlayer formed under these conditions and the resultant Gallium-Oxide being fairly volatile, quickly leaves the surface. A number of authors have attributed sub-bandgap luminescence in AlGaN alloys with high AlN mole fraction to the presence of oxygen in the films [3-4]. Fig 1 shows the luminescence spectra of AlGaN alloys published recently by the Santa Barbara group. As can be seen from data the sub-bandgap luminescence for the AlGaN film with 75% AlN mole fraction is significantly higher than the band-gap luminescence and it was attributed to complex centers associated with oxygen.

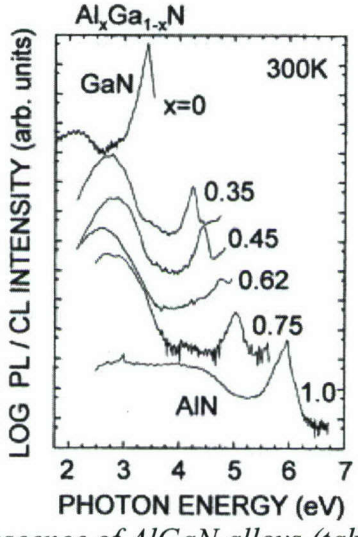

Fig 1: Luminescence of AlGaN alloys (taken from ref 4).

C. Experimental Results of AlGaN alloys with 70% Al

Three AlGaN bulk films were deposited by PA-MBE with AlN mole fraction ~70%. The conditions of growth of these samples are described in Table 1. All films were grown at 770 C using an AlN buffer and KOH etching studies indicate that all films have the [0001] polarity.

During the growth of these films the nitrogen-plasma was the same, and thus the amount of oxygen that is brought into the UHV chamber with the process gas (molecular nitrogen of six 9 purity) during the growth is identical for all films.

Table 1: Conditions of growth of AlGaN alloys with 70% Al

Sample #	Conditions of Growth
1369	Group III-rich
1373	Group V-rich
1416	III/V ratio ~1 (slightly group III-rich)

The crystal structure of the four samples was examined by X-ray diffraction using the Synchrotron source at the Brookhaven National laboratories. Also the samples were examined by Selective Area Diffraction (SAD) TEM studies. Cathodoluminescence measurements were conducted using a probe current of about $1x10^{-8}$ A and an acceleration voltage of 10 KV. In the following we discuss the optical properties of these films and correlate the results with their structure.

1. <u>Sample # 1369: (Grown under Ga-rich conditions):</u> CL spectra at room temperature for this sample show the presence of a band-edge peak at 276nm and a strong deep-level peak at 376 nm. As shown in Fig 2, the intensity of the two peaks is comparable as has been reported in Fig 1 by the Santa Barbara group. Based on ref [2], oxygen incorporation in this film should have been minimized, since this film was produced under extreme Ga-rich conditions. Therefore the mid-gap radiative recombination at 376 nm cannot be attributed to oxygen incorporation as proposed in reference (4) to explain the data of Fig. 1. Furthermore, the transmission spectra (Fig 2b) show the presence of long tails for this sample.

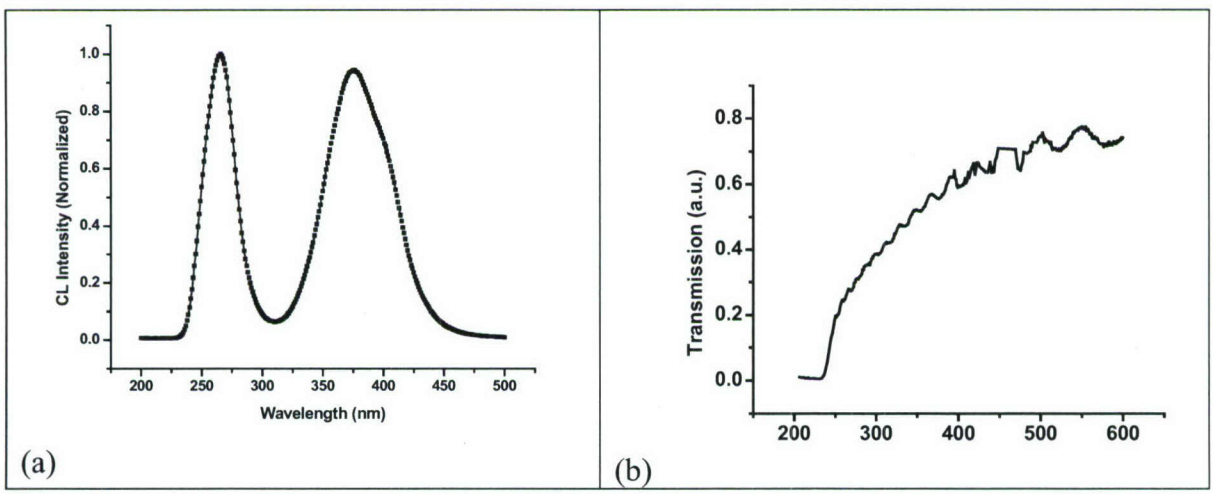

Fig 2: CL spectrum (a) and Transmission Spectrum (b) from sample 1369

2: <u>Sample #1373: (grown under Nitrogen rich conditions)</u>: The CL spectra for this sample are more complicated and show both band-gap luminescence as well as transitions in the mid-gap region. This film, based on the findings of ref [2], could potentially have oxygen and thus some

of the mid-gap transitions may be due to oxygen related defects. This would not however account for the presence of band-tails in the transmission spectrum, as seen for the sample.

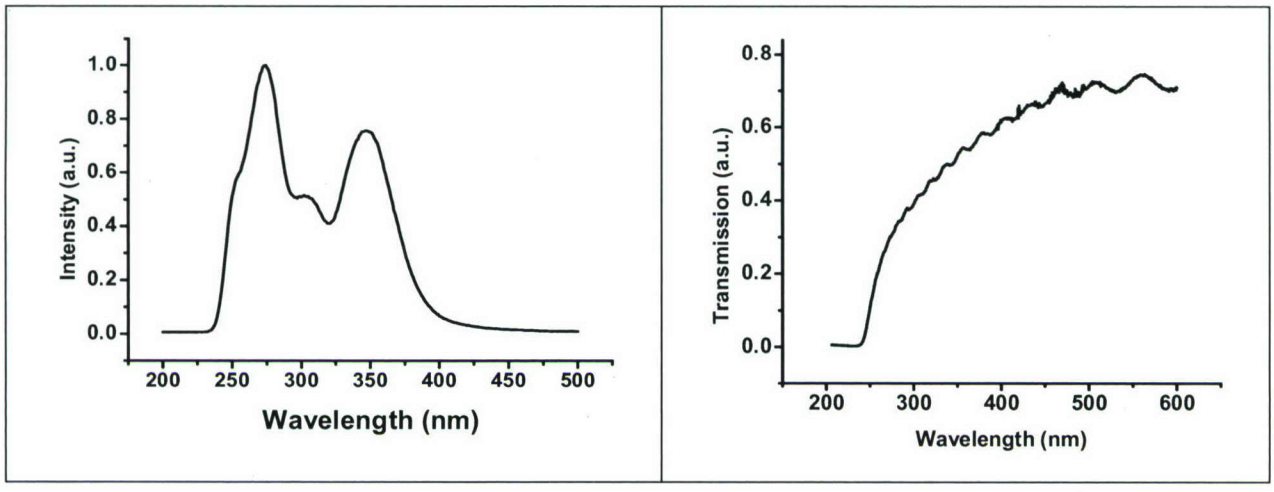

Fig 3: CL spectrum (a) and Transmission Spectrum (b) from sample 1373

3: Sample #1416: (Grown under III/V ratio close to 1): The CL spectra for this film (see Fig. 4) show that the luminescence occurs primarily across the gap and the sub-bandgap luminescence is orders of magnitude lower in intensity. Furthermore this sample shows a more abrupt absorption edge, as seen in Fig 4(b).

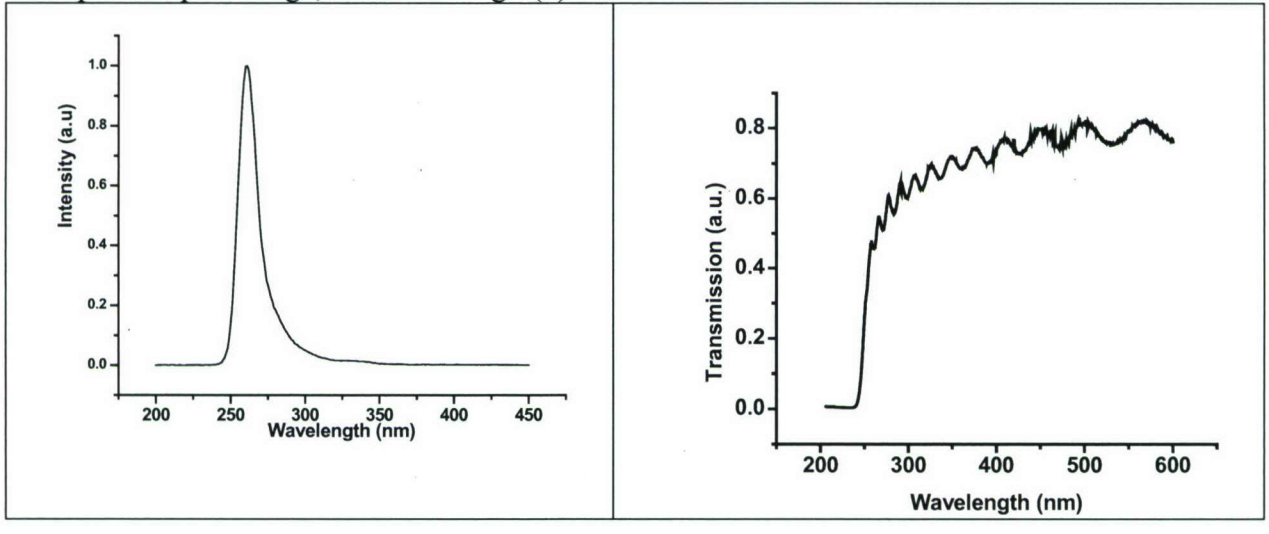

Fig 4: CL spectrum (a) and Transmission Spectrum (b) from sample 1416

In order to understand the origin of these findings XRD and TEM studies were carried out. In this report we present only a brief summary of the results. The X-ray diffraction patterns for all three samples show the presence of superlattice peaks that arise due to the presence of long-range atomic order. Similar superlattice peaks have also been observed in the TEM electron diffraction pattern. The nature and the degree of the ordering however is strongly dependent on the growth conditions. The sample grown under nitrogen rich conditions show the strongest

ordering with 4 monolayer periodicity. Sample #1369, which was grown under excess group III, show complex ordering patterns with several periodicities being simultaneously present. The sample #1416 which was grown under optimized conditions, show weak long-range atomic order.

We believe that the presence of long-range order plays a significant role in determining the optical properties of AlGaN films. [5]

D. Cathodoluminescence Spectra at 240 nm from an Optimized AlGaN alloy

A bulk AlGaN film (BU-1452) was grown by MBE with ~85%AlN mole fraction. Optimized growth conditions, as described in the previous section, were employed. The room temperature CL spectra taken in a scanning mode with a 10 KV acceleration voltage is presented in Fig 5 in linear as well as log scales.

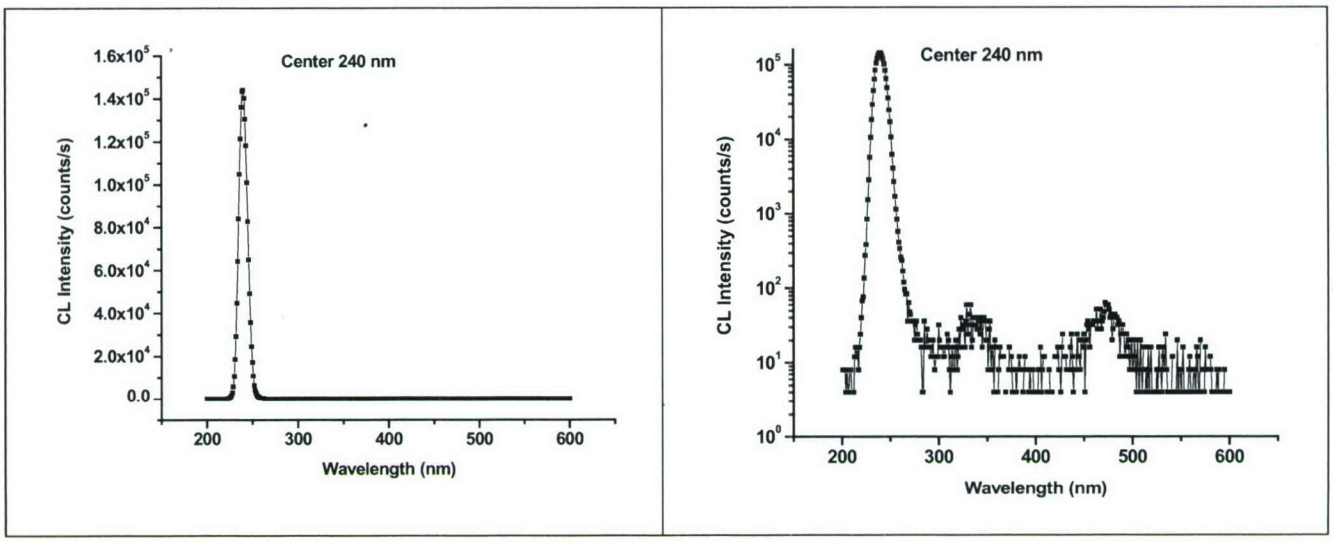

Fig 5: CL spectra for AlGaN film with ~85% AlN mole fraction deposited under optimized Group III / Group V ratios.

The room temperature CL spectra show a band edge peak at 240 nm that is more than three orders of magnitude more intense than the sub-bandgap emissions. The low temperature (80K) luminescence spectra show a peak at 227nm.

3.2 Growth of AlGaN alloys onto A-plane sapphire

3.2.1 Formation of laser facets in AlGaN based structures

The formation of facets in order to define the cavity is an important step in the fabrication of laser devices. For lasers based on the III-Nitride system this is a challenging. C-Plane AlGaN alloys deposited onto C-plane sapphire cannot be cleaved crystallographically as the two crystal planes are rotated by 30 degrees with respect to each other. Moreover, these materials are resistant to most chemical etchants. This problem can be overcome as follows:

Reactive Ion Etching:

AlGaN alloys can be etched using a high density plasma reactive ion etching processes. The RIE usually leads to certain degree of roughness (striations). Most importantly there is a slope of about 6° off vertical (ref 9), which will have implications for a long cavity {see Fig. 7(a)}.

Crystallographic cleaving using an A-plane sapphire substrate:

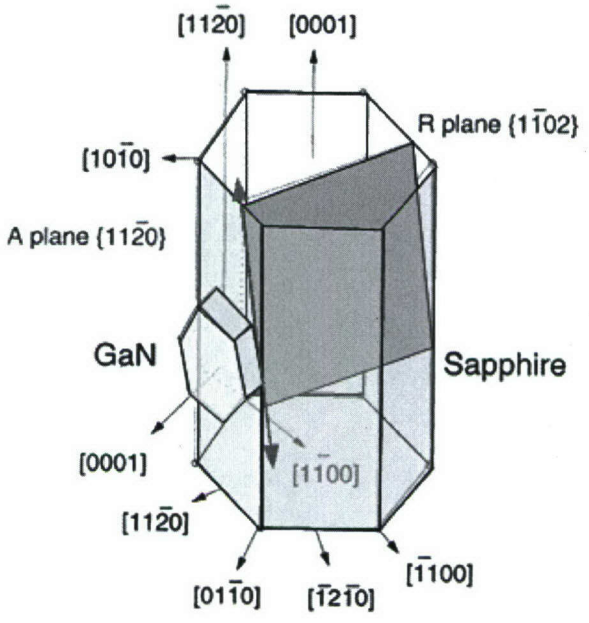

Fig 6: Crystallographic planes for A-Plane sapphire and C-plane GaN showing the common cleavage planes (from Ref 6)

The major crystallographic planes [6] of GaN deposited onto A-plane sapphire are shown in Fig.6. The cleavage plane in sapphire (1-102) (R-plane) extends to the GaN lattice as the (11-20) (A-plane). The R-plane of sapphire is perpendicular to the A-plane of sapphire. Therefore there is enormous incentive of growing the AlGaN based laser structures on (11-20) sapphire (A-plane) due to the ability to form cleaved facets.

In the literature, however, only a few references exist on the growth of GaN onto A-plane sapphire [7-10]. It was reported in ref [9] that , the facet that is cleaved along the sapphire R-plane shows fractures in the GaN layer {see Fig 7 (b)}. This fracturing is caused by a 2.4° difference in the orientation of the R-planes of the A-Sapphire and the A-planes of the C-GaN. This fracturing shown in Fig 9 (b), which is shown in 20 μm scale, is probably not a problem, as the width of the excitation e-beam source is expected to be as small as 2 microns.. In Fig 7 (c) we show the smoothness of the surface on a smaller scale (from our own publication [10]). Most importantly the facet is perfectly vertical.

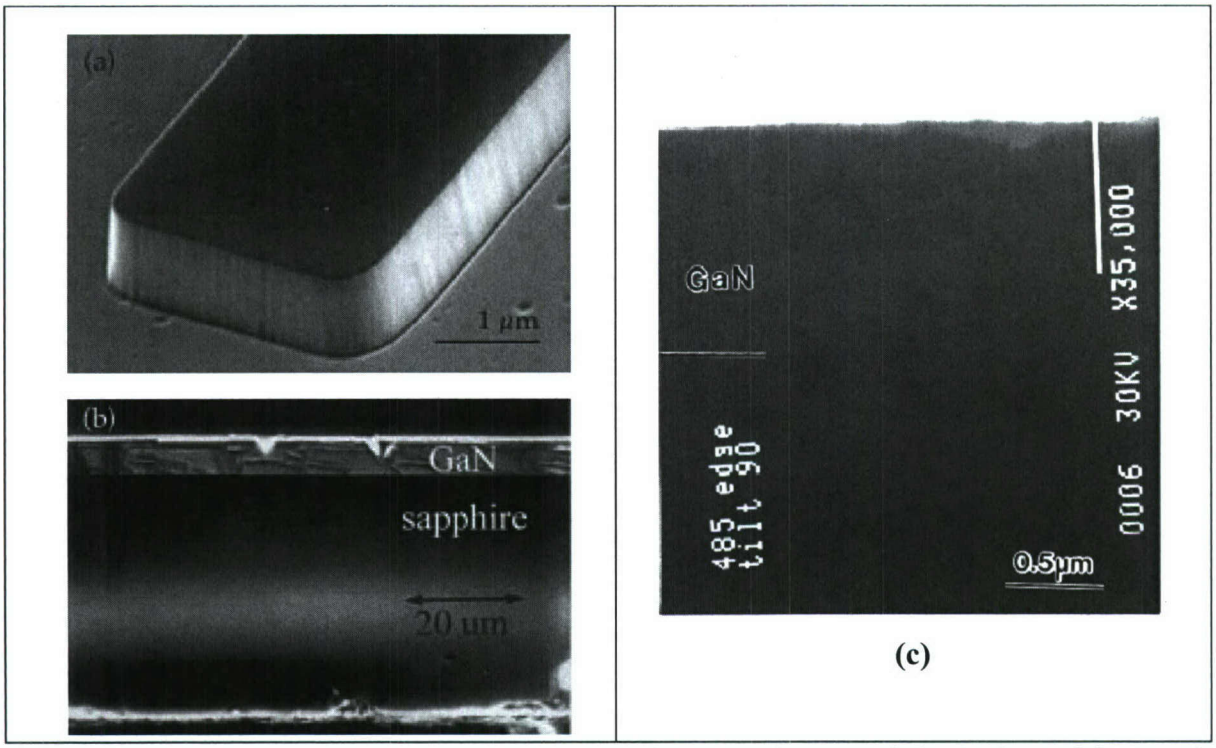

Fig 7: SEM micrograph of (a) RIE GaN on C-plane sapphire and (b, c) cleaved facets of GaN on A-plane sapphire.

Due to these advantages in the cavity formation, all effort in the latter part of the program was directed towards the development of laser structures onto A-plane sapphire.

3.2.2: Growth of GaN using a different buffer layers

The growth of GaN on A-plane sapphire has been already reported in the literature using both MOCVD and MBE methods. In all these cases, the GaN film was deposited using a GaN buffer layer. This led in almost all cases to the growth of C (0001) plane GaN films.

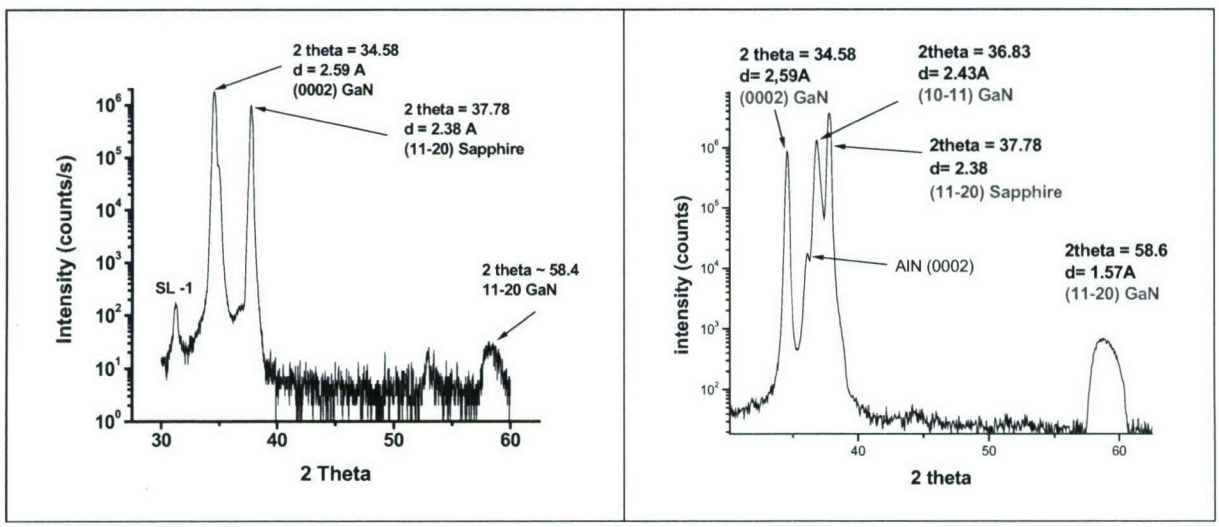

Fig 8: Growth of GaN onto A-plane sapphire using (a) GaN and (b) un-optimized AlN buffer

Fig 8 (a) shows the XRD diffraction pattern from a set of GaN/AlGaN MQWs deposited on top of a thick GaN bulk film grown onto A-plane sapphire. A low temperature GaN buffer layer was used for this sample. The XRD pattern shows the peaks corresponding to the C-plane GaN, the A-plane sapphire, as well as the first order superlattice peak corresponding to the MQW structure. This establishes that using a GaN buffer layer leads to growth of C-plane GaN..

The development of deep UV laser structures require the growth of films which are primarily AlGaN alloys with very high Al content. Therefore, it is preferable to use AlN buffer layers, due to the better lattice match with these AlGaN alloys to AlN than to GaN. Fig 10 (b) shows the XRD pattern of GaN bulk film deposited onto A-Plane sapphire using an AlN buffer layer under conditions similar to those employed for deposition onto C-plane sapphire. It can be seen that both the (0002) peak of C-plane GaN as well as the (10-11) peak of the pyramidal plane GaN are present. Therefore two different oriented epilayers are simultaneously present in this film. A similar result has been reported earlier by Razeghi et. al. (Fig 9) where the (10-10) and (0002) peak corresponding to the M-plane and C-plane GaN was seen simultaneously in GaN films deposited onto A-plane sapphire by MOCVD[11]. Such a growth is obviously not appropriate for device development.

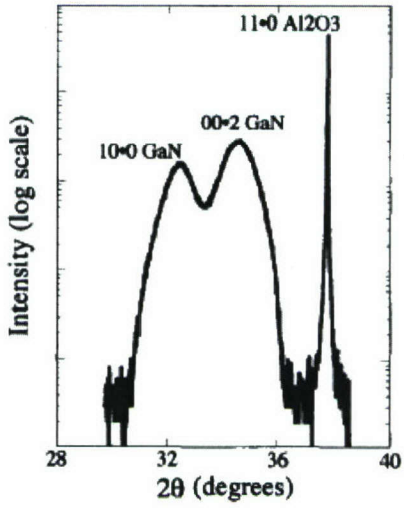

Fig 9: XRD pattern from GaN film deposited onto A-plane sapphire showing multiple crystallographic phases (ref 11).

3.2.3 Growth of AlGaN alloys: Optimization of Nucleation steps

Since the AlN buffer deposition conditions usually employed for growth on C-plane sapphire was found to be not appropriate for growth on A-plane sapphire, it was necessary to develop new buffer layer deposition conditions that were more suitable. A series of films were deposited onto A-plane sapphire in order to optimize the nucleation steps. Figure 10 shows the XRD pattern and optical transmission spectra for un-optimized (a), partially optimized (b) and optimized films (c). With the improvement of nucleation steps, the (0002) peak corresponding to the C-plane growth becomes dominant and the absorption edge becomes abrupt with reduced band-tailing.

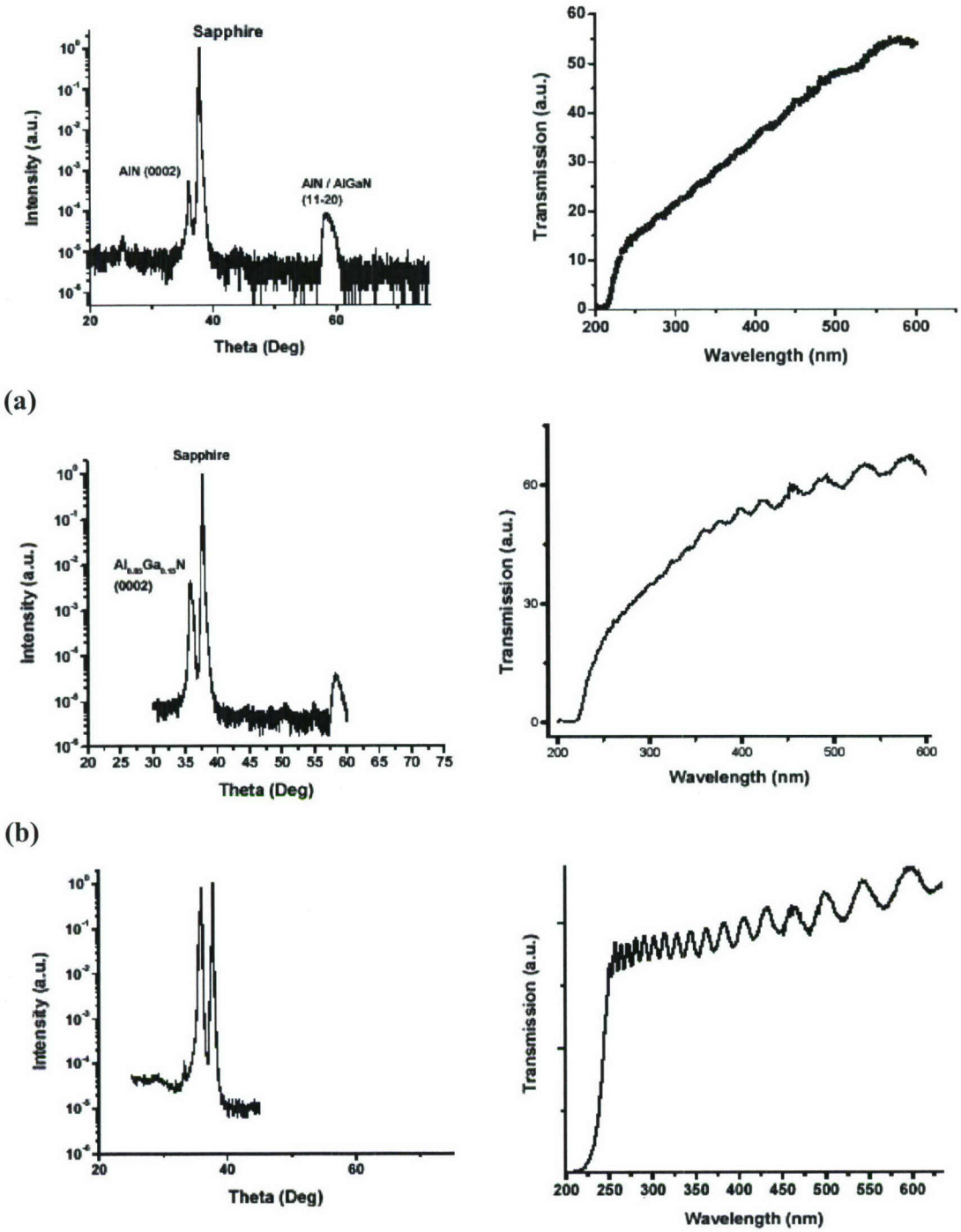

Fig 10: XRD pattern and optical transmission spectra of AlGaN alloys deposited onto A-plane sapphire using un-optimized (a), partially optimized (b) and optimized AlN buffer (c) layers

3.2.4 Luminescence from AlGaN alloys (sample #1641)

Room temperature cathodoluminescence spectrum for bulk $Al_{0.7}Ga_{0.3}N$ bulk film deposited under optimized conditions is presented in Fig 11. A sharp luminescence peak is seen at 254 nm. The FWHM of this peak is 10 nm. The transmission spectrum for this sample, as seen in Figure 10 (c) shows an absorption edge at 243nm. Thus the Stokes shift for this sample is 11nm, which is relatively small when compared with those for AlGaN alloys deposited onto C-plane sapphire. Fig 11 (b)) shows the same spectra in a logarithmic scale. No deep level luminescence peaks are seen. This reduction is possible by careful control over the group III to group V ratio, as in the case for AlGaN alloys deposited onto the C-plane sapphire.

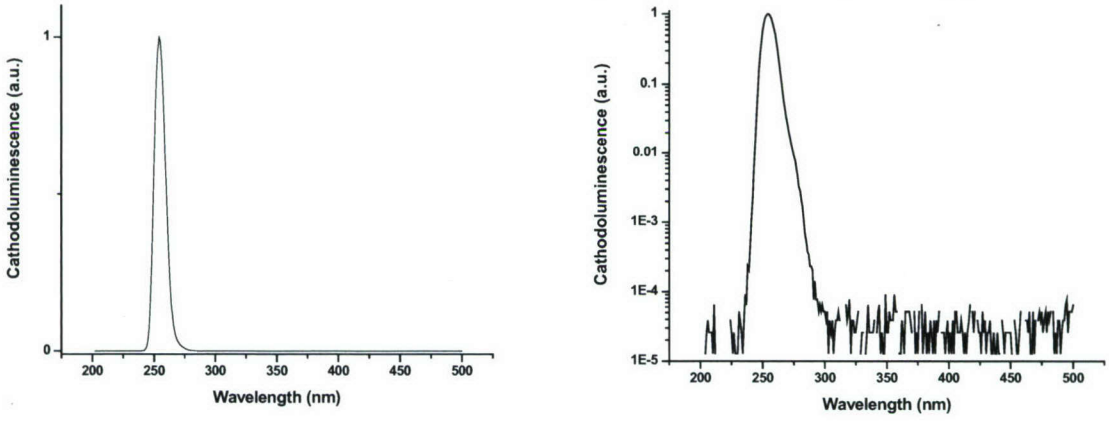

Fig 11: Room Temperature CL spectra for AlGaN alloys deposited onto A-plane sapphire using AlN buffer type A.

3.2.5 Crystallographic Cleaving

From Fig 6, it is apparent that the growth of III-Nitrides needs to be along the C-direction in order for the cleavage planes, the A-plane for the AlGaN and the R-plane of the sapphire to line up. Fig 12 (a) shows the cross-section of an A-plane sapphire substrate cleaved along the R-plane. The cross-section of the cleaved facet is atomically smooth. However when the same procedure was conducted on a sapphire substrate onto which AlGaN alloys have been deposited, the results depended on the buffer layer conditions employed during the deposition.

Fig 10(b) shows the cleaved edge for an AlGaN layer deposited onto A-plane sapphire using an un-optimized buffer layer. We see that even thought the sapphire surface is atomically smooth, the AlGaN shows a high degree of roughness. For a sample deposited using an optimized buffer layer, as given in Fig 12 (c), it was seen that both the sapphire and the AlGaN layer have smooth cross-sections, indicating that crystallographic cleavage has taken place.

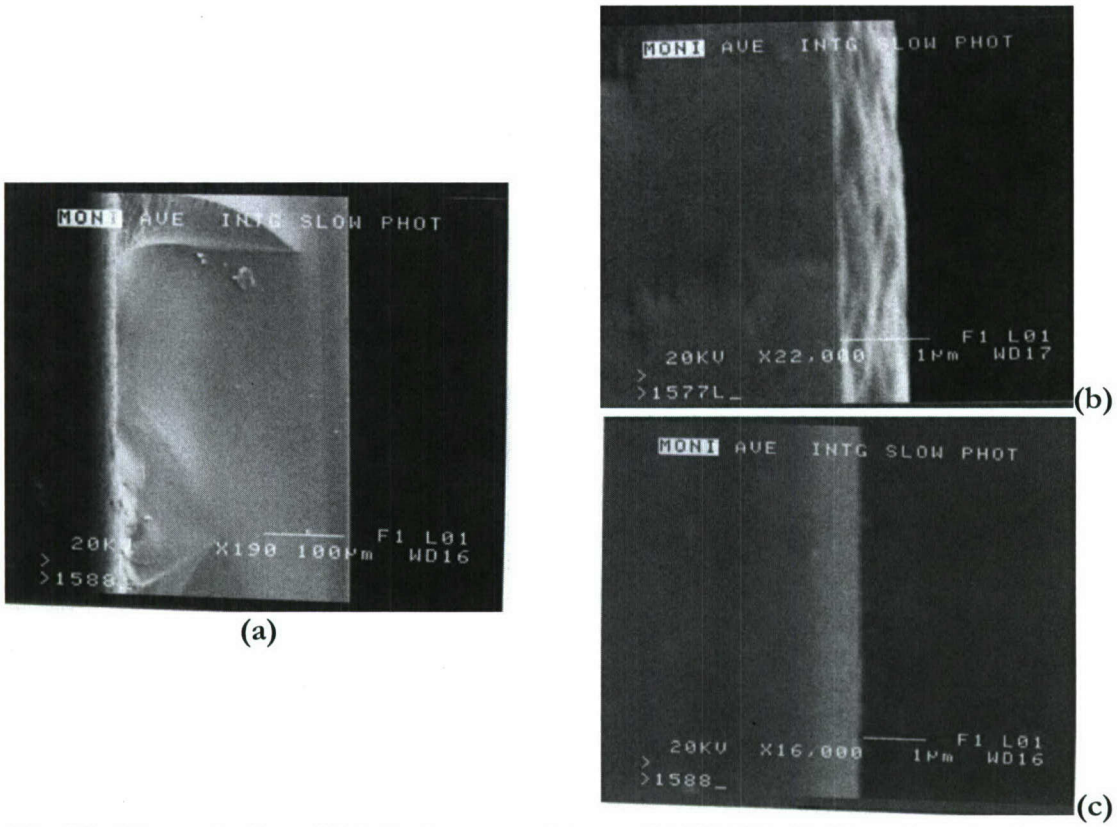

Fig 12: Cleaved edge of (a) A-plane sapphire and AlGaN bulk films deposited onto it using different buffer layer conditions (b, c)

3.3. Development of Laser Structures

3.3.1 Laser Structures on C-plane sapphire

A GRINSCH laser structure deposited onto C-plane sapphire (sample #1584) is described schematically in Fig 13. The active region consisted on 50 MQWs, where the wells are nominally $Al_{0.7}Ga_{0.3}N$ alloy 1nm thick and the barriers consisted of AlN 3nm thick. The cladding layers were graded AlGaN alloys where AlN mole fraction was changed from 100 to 70% continuously over 70nm. The outer cladding layers consist of AlN. A thicker AlN layer was used at the bottom in order to reduce defects, while the top AlN layer was only 50 nm thick to reduce the electron absorption during e-beam pumping.

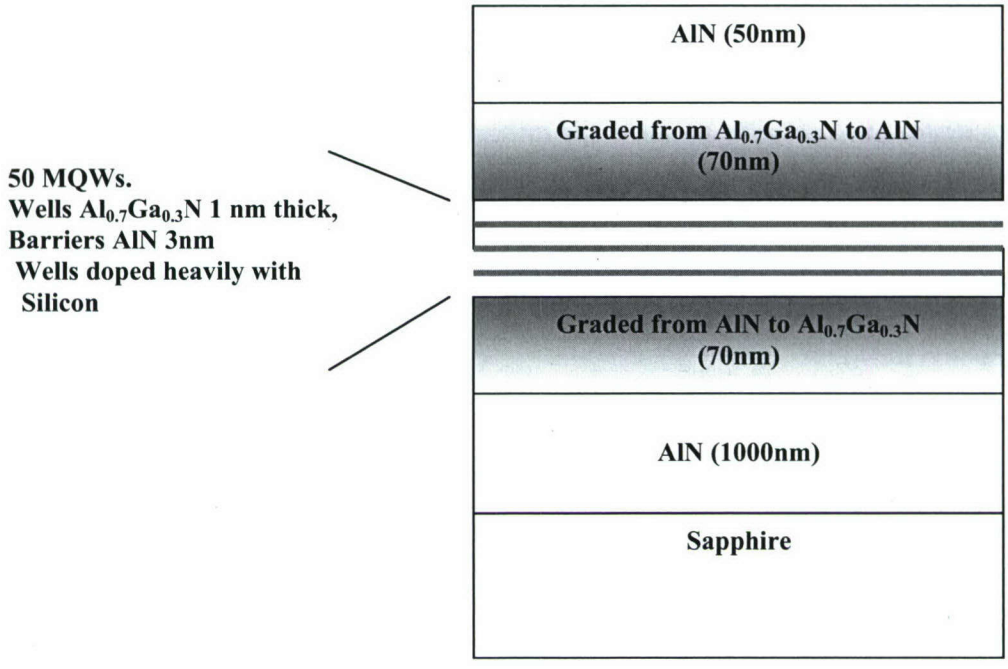

Fig 13: Schematic of GRINSCH structure on C-plane sapphire

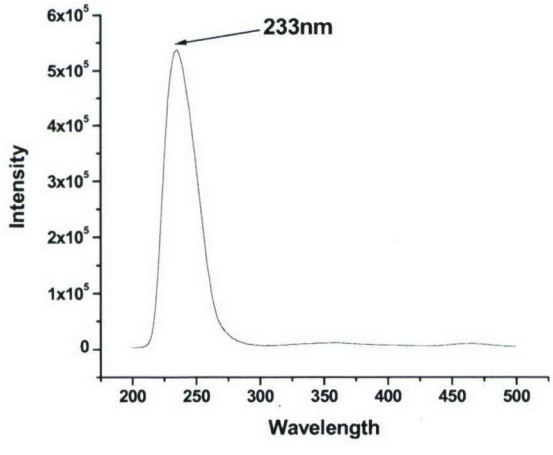

Fig 14: CL spectra at RT from sample 1584

The Cathodoluminescence spectra for the structure described in Fig 6 are presented in Fig 14. The acceleration Voltage employed was 5kV, and the luminescence was collected from the top, i.e. through the 50nm AlN layer. The spectrum shows a strong single peak, without sub bandgap luminescence. The peak position is at 233nm for a large area of the sample, but near the edge of the wafer, the peak position shifts to 245nm.

3.3.2 Laser Structures on A-plane sapphire

After the optimization of the nucleation layers that lead to deposition of bulk AlGaN alloys with good structural and luminescence properties, efforts were made to deposit edge emitting laser structures onto A-plane Sapphire substrates. Two types of laser structures were developed, employing either AlGaN/AlN MQWs, or a bulk AlGaN film, as the active region.

1.GRINSCH Emitters employing an DH-based active region

A: Dependence of deposition conditions on the luminescence properties

In section 3.1, the dependence of the III/V ratio on the materials properties of AlGaN bulk films with high AlN mole fraction has been discussed. It is seen that for high III/V ratio, the luminescence spectrum shows the presence of deep-level peaks. This result is also valid for the growth onto A-plane sapphire. A series of samples were deposited having identical structures, except for the Ga flux used in the AlGaN layer in the active region. The schematic for the three structures are presented in Figure 15.

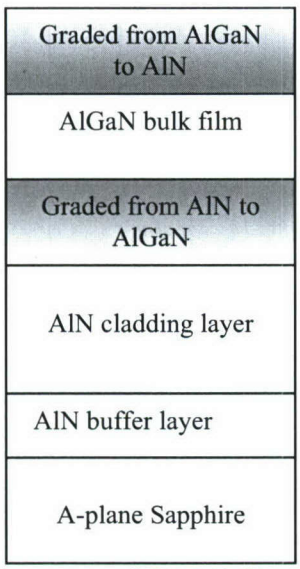

Figure 15: Schematic of GRINSCH-DH structure

The nucleation scheme for all samples was carried out using optimized conditions. A thick AlN bulk film and a graded AlGaN cladding layer was first deposited. This layer was graded from AlN to $Al_{0.75}Ga_{0.25}N$ over 500Å.. The active region consists of a bulk $Al_{0.75}Ga_{0.25}N$ film, which has been deposited for three structures using three different Group III/V ratios, from very group III-rich (a), moderately III-rich (b) to group III/V ratio ~1 (c). This thickness of this AlGaN layer was 2500Å. Finally a graded AlGaN cladding layer was deposited, with the Al percentage increasing from 75 to 100%. No bulk AlN film was deposited on top, to prevent absorption of the electron beam. The room temperature CL spectra from the structures are shown in Figure 16 (a-c). The deep-level luminescence peak decreases as the Ga flux is decreased. This is similar to the results for the growth of AlGaN onto C-plane sapphire, where the samples grown with group III/V ratio close to 1 show the best luminescence properties. This shows that the understanding of AlGaN growth, as has been detailed in section 3.1, for films deposited onto C-plane sapphire, can be transferred to growth on A-plane sapphire.

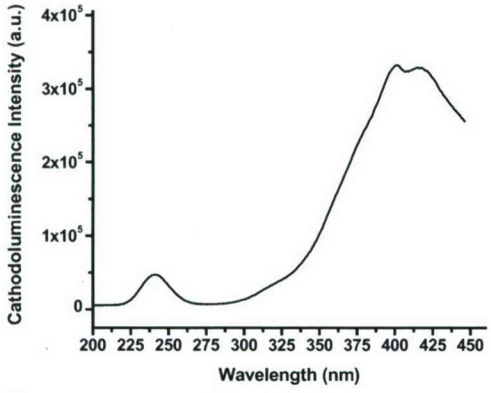

(a) Extreme group III-rich

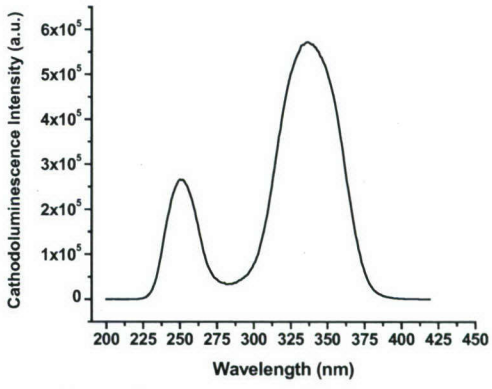

(b) Moderately group III-rich

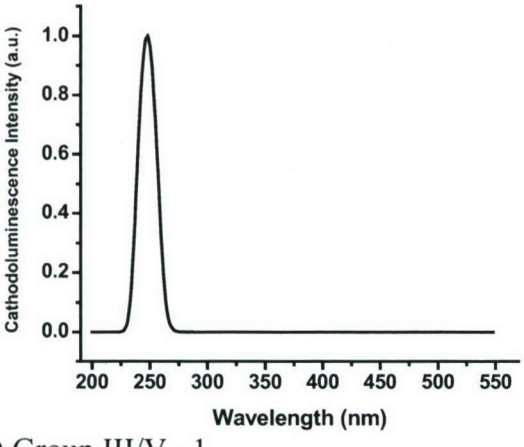

(c) Group III/V ~1

Fig 16: Room Temperature CL spectra from Graded-index Double heterojunction Structures with active region deposited under different group III /V ratio

B. GRINSCH-DH laser structures grown under optimized conditions, and delivered for processing.

(a) . GRINSCH Laser structure 1 (sample #1644)

Figure 17 shows the sequence of the various nitride layers configured in the form of a GRINSCH structure. The active layer in this structure is a 300 nm bulk film with composition $Al_{0.75}Ga_{0.15}N$. In either side of the active region there are 25 nm AlGaN cladding layers, graded from 75% AlN mole fraction to pure AlN

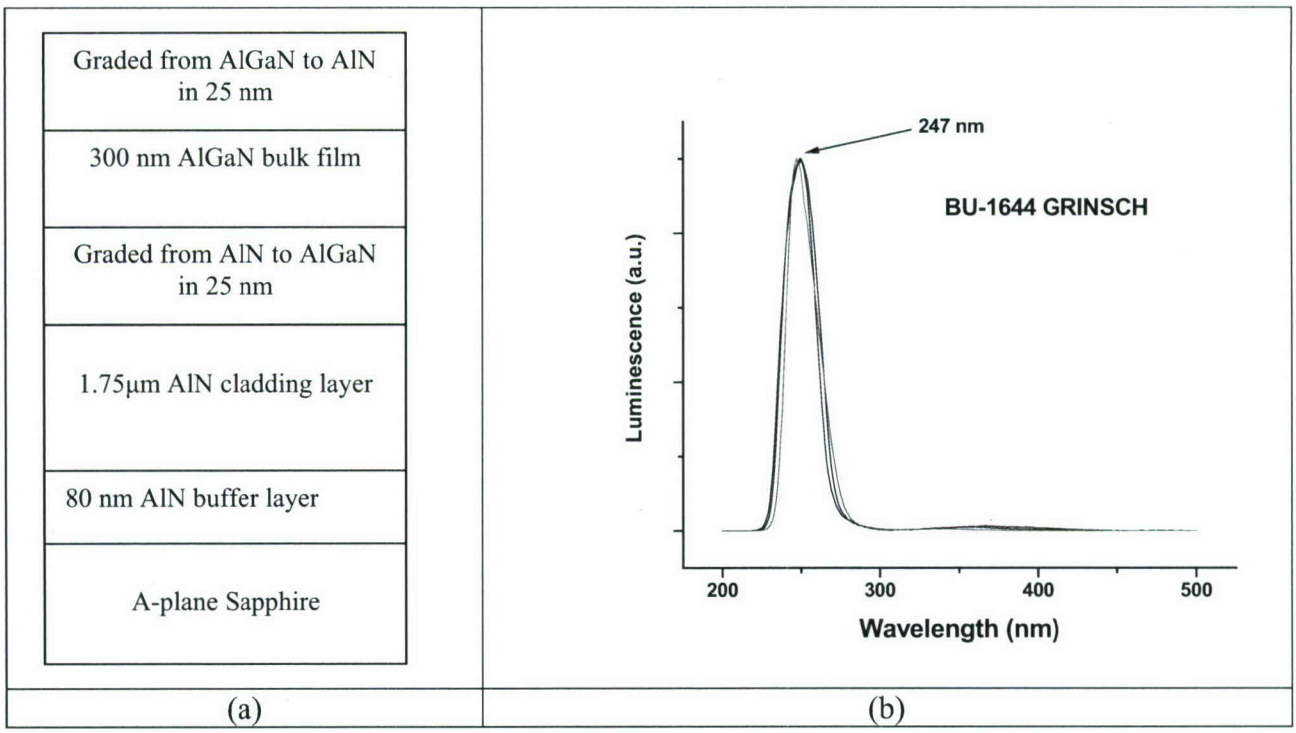

Fig 17: (a) Structure and (b) RT luminescence spectra of sample #1644

CL measurements at room temperature on this sample were conducted using an acceleration voltage of 3KV, and a probe current of 10nA. We see that the band-edge luminescence peak is at 247-249nm and there are no deep-level luminescence peaks. This indicates that the optical properties of the device structures deposited onto A-plane sapphire are not inferior to that deposited onto C-plane sapphire.

(b) . GRINSCH Laser structure 2 (sample #1683)

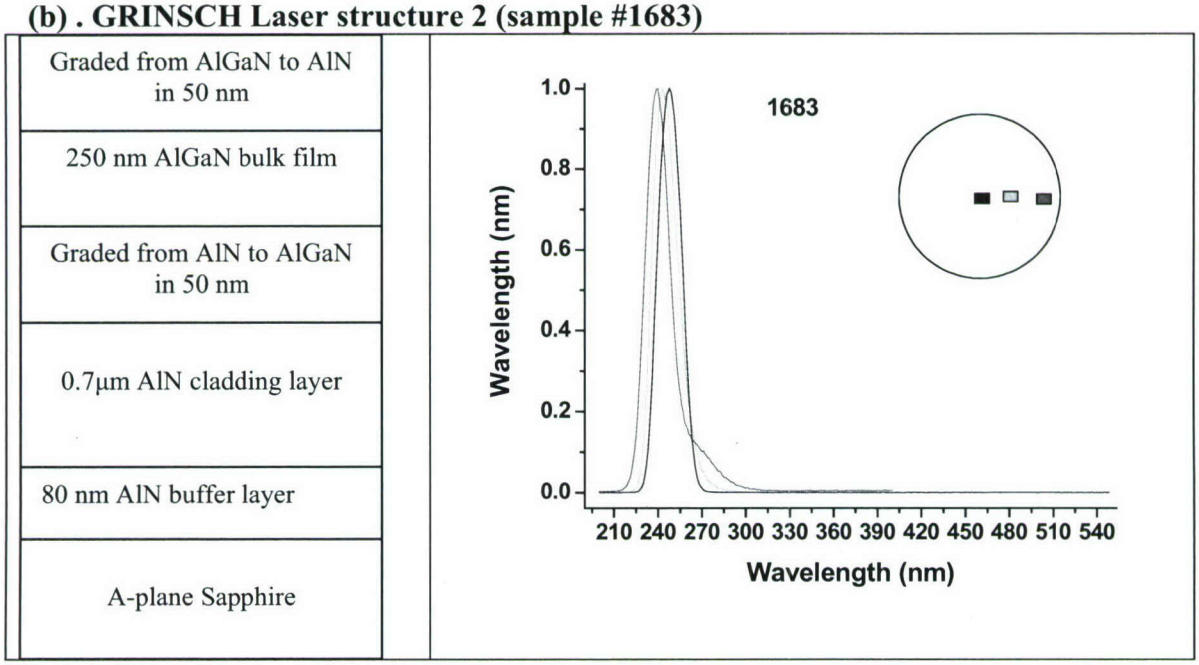

Fig 18: Room Temperature wafer level CL spectra from optimized Graded-index Double heterojunction laser Structures

For this structure, the AlN cladding layer was 0.7 microns thick, and was reduced in thickness compared to #1644. The AlGaN cladding layer was graded from an Al content of 100% to 80% over 500Å. . The nominally 80% AlGaN active layer was 2500Å thick The RT CL spectra shows a peak position that varied form 247 to 239 from the center to the edge of the 2-inch wafer

(c) GRINSCH Laser structure (sample #1787)

Figure 19 (a) shows the schematic for sample #1787, a GRINSCH laser structure deposited onto A-plane sapphire. The active region is a bulk AlGaN film with nominally 78% AlN mole fraction. Figure 19 (b) shows the CL spectrum from sample #1787 at room temperature. The data was obtained using an electron acceleration voltage of 3KV. The luminescence peak is at 238-240nm range.

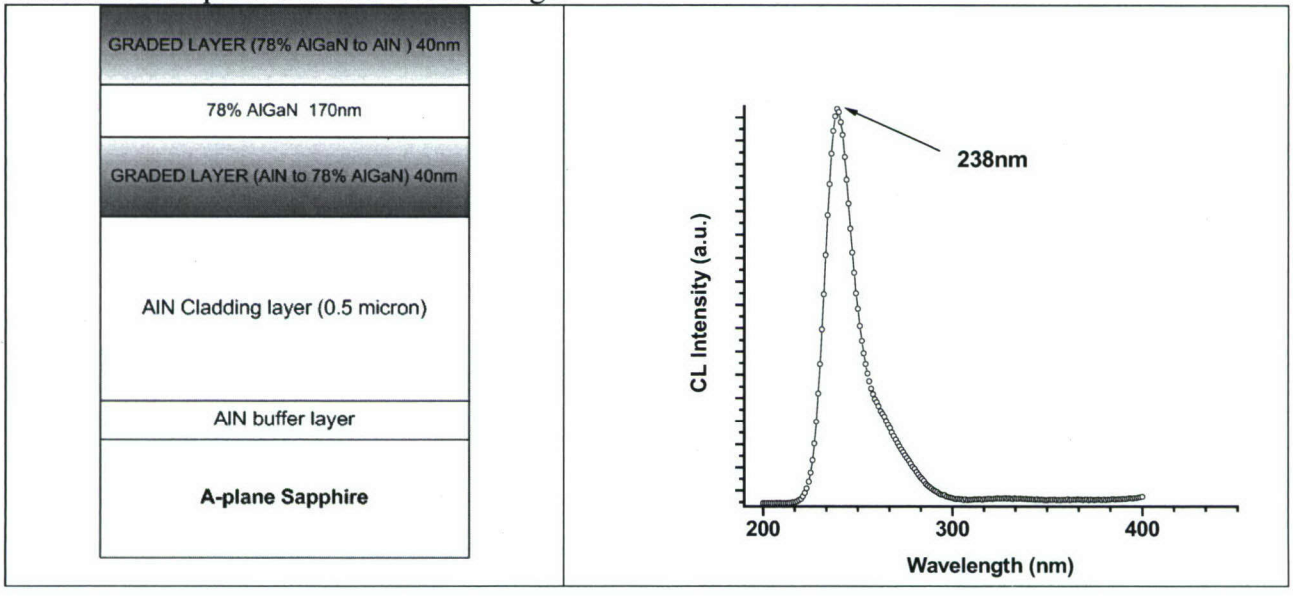

Fig 19 (a): Schematic of sample #1787, a GRINSCH laser structure. (b) RT CL spectra

1.GRINSCH Emitters employing an MQW-based active region

The schematic of the a laser structure employing AlN/AlGaN MQWs (sample #1671) is given in fig. 20. The active region consists of 50 MQWs, with 70%AlGaN wells and AlN barriers. The wells are heavily doped with silicon. It is expected that the doping will increase the luminescence intensity of the MQWs by charging the dislocations which does not then act as recombination centers.

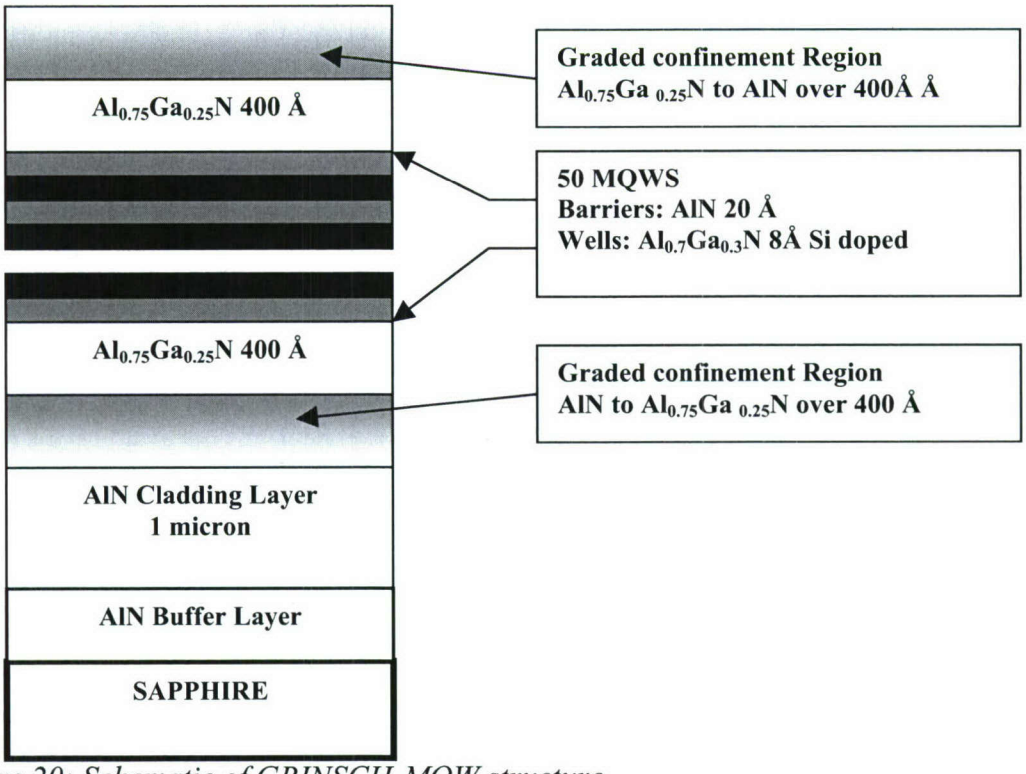

Figure 20: Schematic of GRINSCH-MQW structure.

CL spectroscopy at room temperature was conducted across the 2-inch wafer in order to determine spatial dependence of the spectral profile. The results are presented in Fig 21. From near the center of the wafer to near the edge of the wafer, the peak shifts from 233 to 231 nm. Also the ratio of the intensity of the luminescence from the MQWs to that originating from the cladding layer (~278nm) decreases continuously, possibly due to the roughening of the well/barrier interfaces.

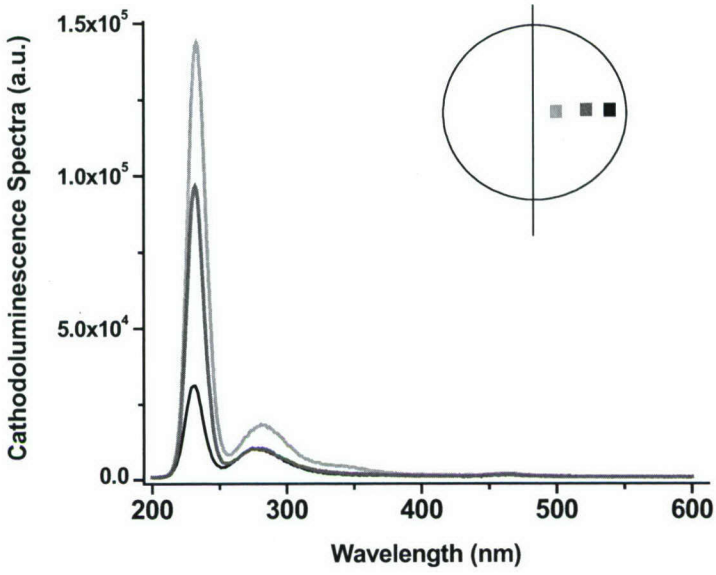

Fig 21: CL spectra across the 2-inch wafer for sample #1671

It is apparent that the presence of cladding layers adds to unwanted peaks in the luminescence spectrum. However, in order to absorb effectively the e-beam excitation, it is possibly necessary to have the thickness of the active region (MQWs) and the cladding region (GRINSCH + the bulk cladding region) ~500 to 700 nm. One option is to use a very large number of MQWs, but that can lead to a broadening of the peak due to inhomogeneities in the well widths. It may also be that under the intense pumping excitation that will be finally employed; the MQW peak to cladding region peak intensity ratio will be significantly higher.

3.4 Use of Indium during the growth of AlGaN alloys

3.4.1 AlGaN bulk films deposited onto C-plane sapphire

III-Nitride films deposited heteroepitaxially onto various substrates are not single crystal, but are polycrystalline films with well-oriented grains grown along the 0001 direction. The size of these grains or domains determines to a large extent the structural and electronic properties of the film.

It has also been reported in the literature that Indium can act as surfactant during the growth of GaN by both MBE and MOCVD techniques, leading to a strong improvement of materials properties. Here we have made an initial attempt to understand the effect of Indium as a surfactant during growth of $Al_{0.1}Ga_{0.9}N$ bulk films on C-plane sapphire. Initially, an AlN buffer layer was deposited onto C-plane sapphire. Then an AlGaN bulk film was grown with ~10% Al content. Halfway during the growth of this layer, an Indium flux was made incident on the film to act as a surfactant.

Figure 22 shows the cross-sectional TEM micrograph of the film, done under a two-beam condition in order to look at dislocations with the Berger's vector (a) $g = (10\underline{1}0)$, (b) $g = (0002)$, and hence discriminate between the screw-type, edge-type and mixed dislocations. The arrow

points out the point at which Indium was turned on during the growth. We can see the presence of the Indium flux causes a drastic reduction of all the different types of defects, and leads to an increase in domain size.

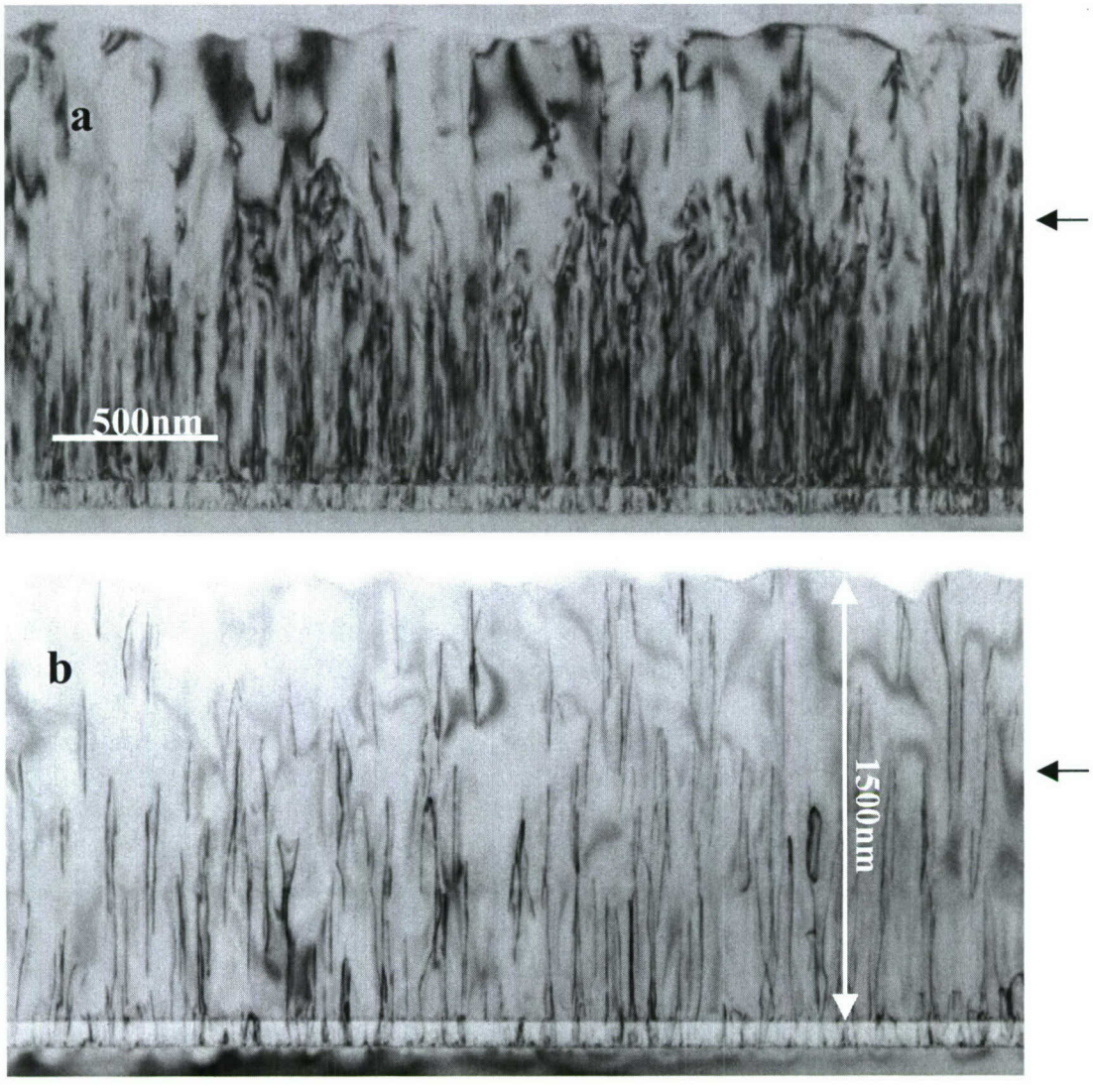

Figure 22: TEM micrograph of (In)AlGaN sample (a) g = (10$\underline{1}$0), (b) g = (0002)

It is to be noted that the amount of Indium incorporation into the film is very small ($<10^{17}$ /cm^3), as found from SIMS measurements. This is expected, as Indium has very high vapor pressure at the growth temperature. Therefore, the Indium mainly acts as a surfactant, increasing the diffusion lengths of the reactant species during growth.

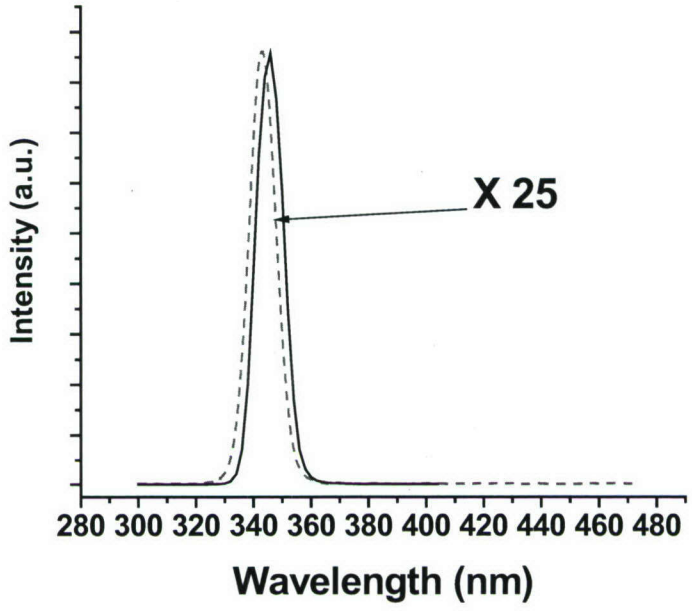

Figure 22: RT CL spectra of AlGaN films growth without (red) and with (black) an Indium flux. The red curve has been multiplied by 25X

The comparative RT CL spectra of the AlGaN samples grown with and without the presence of Indium are shown in Figure 22. We see that the presence of Indium significantly increases the luminescence intensity (by 25 times).

We are going to investigate if the presence of an Indium flux shows a similar improvement in the structural and optical properties of AlGaN alloys with high Al content, deposited onto A-plane sapphire substrates.

3.4.2 GRISNCH-DH structures deposited onto A-plane sapphire

A. Use of Indium as a surfactant

The heteroepitaxial deposition of III-Nitrides onto sapphire substrates usually leads to a columnar morphology. The crystal orientations of individual domains or columns are slightly rotated from each other, leading to generation of threading dislocations, which act as non-radiative recombination centers, thereby reducing luminescence efficiency. These columns can be observed in cross-sectional SEM micrographs.

In order to increase the domain size and thereby reduce the dislocation density in bulk GaN films, the growth conditions are generally chosen to increase the migration length of the reactant species. For MBE growth, this entails choosing gallium-rich conditions of deposition. However, as we have reported previously, growth of AlGaN alloys with high group III (Al+Ga) flux, leads to films that show substantial deep-level luminescence. Therefore, in order to reduce the sub-bandgap luminescence, the e-beam pumped laser structures were deposited using a Group III/V ratio close to one. This however is expected to reduce the domain size, and increase the columnar nature of the growth.

In order to increase the migration length of the reactant species, a surfactant can be used which while not incorporating into the film, causes an enhancement of the surface diffusion. For

AlGaN alloys, Indium can be a surfactant. It was seen (sec 3.4.1) that the Indium increased the domain size, which led to a significant increase in the luminescence intensity.

During this period, we have attempted to use Indium as a surfactant during the growth of the complete e-beam pumped laser structure, and the results are presented in section D.

B. Use of GaN interlayer

Gallium nitride nucleation layers have been used earlier to grow high quality bulk GaN films onto A-plane sapphire. However, during this project, we have almost exclusively used AlN buffer layers for nucleation and AlGaN active regions with very high Al content, which makes AlN the material of choice in the buffer layer in order to reduce lattice mismatch between the buffer layer and final epitaxial growth.

C. Laser device incorporating GaN interlayer and Indium surfactant

The schematic of a laser device structure deposited onto A-plane sapphire using a GaN interlayer and using Indium as a surfactant during growth is presented in Figure 23.

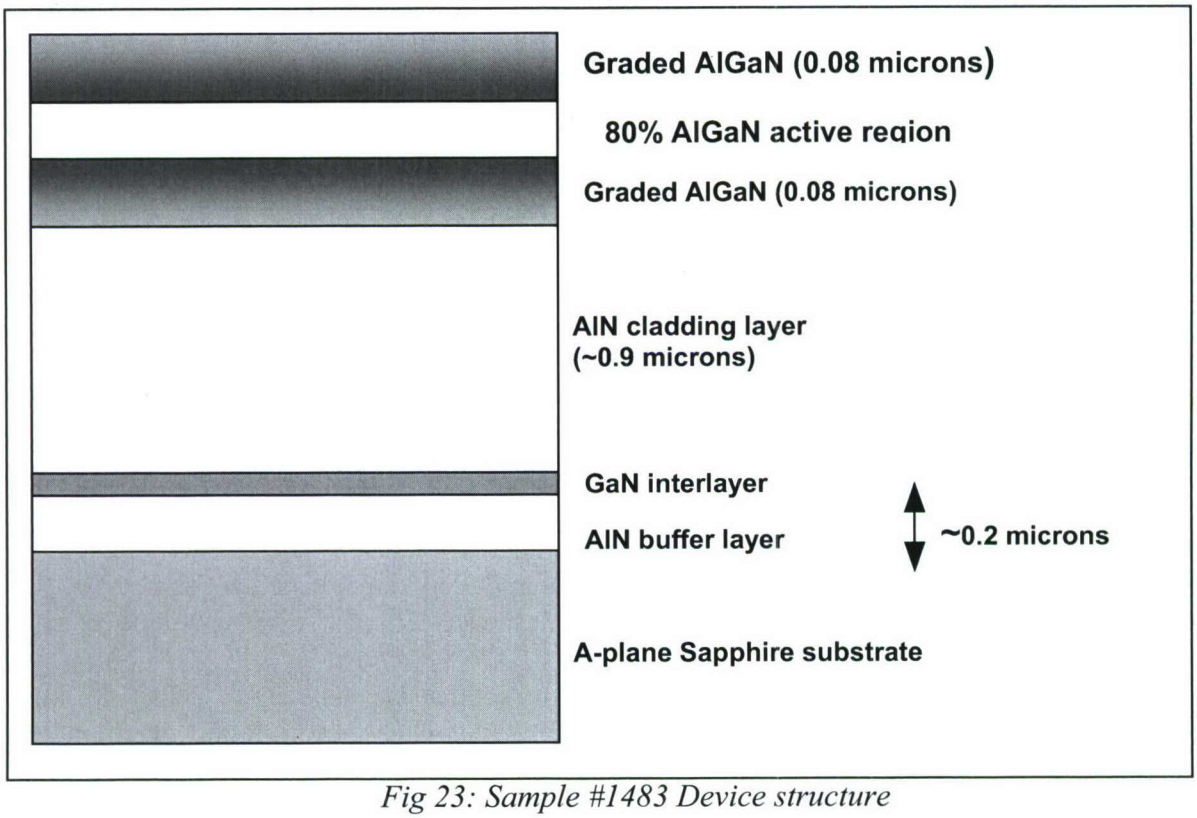

Fig 23: Sample #1483 Device structure

The schematic shows that a thin GaN interlayer was deposited just after the Nitridation and AlN nucleation steps. Furthermore, an Indium flux was present during the growth of the entire device structure.

D. Cross-sectional SEM micrographs

Figure 24 shows the cross-sectional SEM taken after the sample was cleaved along the R-plane of the sapphire (58 degrees from the A-direction). Fig 2(a) shows the cross-section of the sapphire substrate, which is flat with a few fractures that can be seen since the sapphire was cleaved without thinning. The bottom edge is the sapphire back surface is rough because that is where the wafer was scribed.

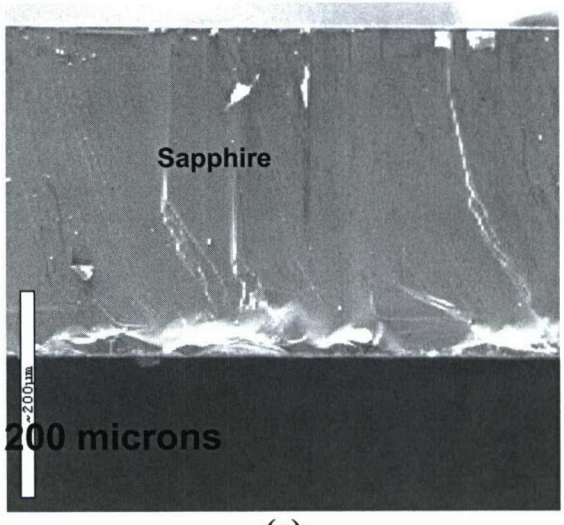

(a)

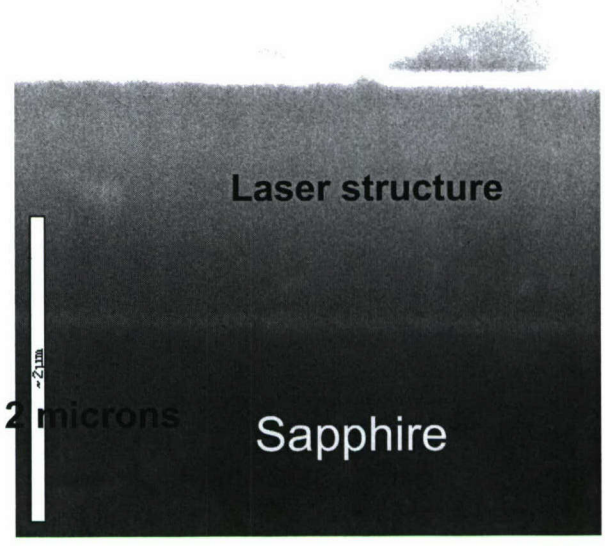

(b)

Figure 24: Cross-sectional SEM of (a) sapphire substrate and (b) Laser structure

Figure 24(b) shows the cross-sectional SEM of the laser structure and sapphire substrate. The lighter band near the interface shows the AlN nucleation layer.

From Fig 24(b) it is apparent that the combination of the interlayer and indium surfactant has significantly improved the smoothness of the sidewalls by increasing the domain size. This is expected to improve the luminescent properties of the final laser structure by (a) reducing the

losses due to facet roughness and (b) by reducing the non-radiative recombination processes at domain boundaries. However, more studies (TEM) are required before we can definitely state the degree of reduction of dislocation densities.

E. Optical Characterization of GRINSCH Laser structure.

Fig 25 presents the optical characteristics of the sample. The room temperature CL spectra taken in a standard SEM-CL setup is presented in Fig 1. An excitation voltage of 5KV was employed, and the luminescence was collected through the top surface.

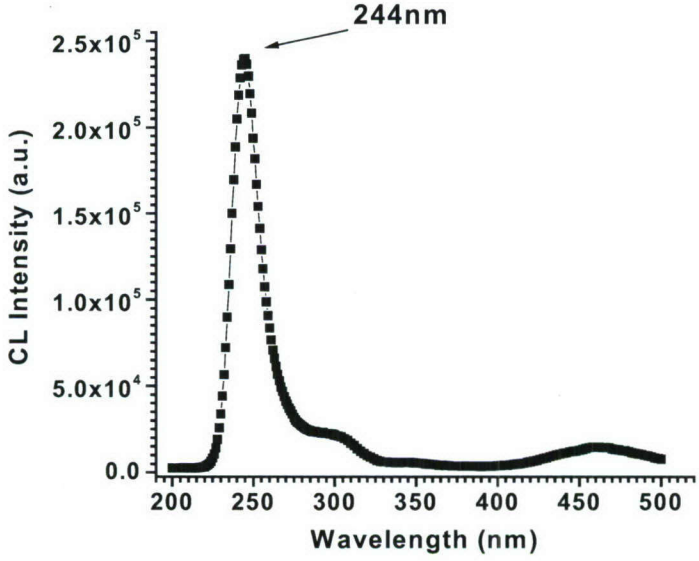

Fig 25: Room Temperature CL spectrum

Fig 25 shows a narrow peak at 244nm, along with weak sub-bandgap luminescence. The intensity of the sample is quite high, as is expected from the results presented in sec 3.4.1, where we show that growth of AlGaN bulk films in the presence of an Indium flux increased the luminescence intensity by a factor of 25. The slightly increased sub-bandgap luminescence is typical of AlGaN films deposited using Indium as a surfactant, but its origins are currently unknown.

It was however also observed that the film has an increased top surface roughness, which causes the film to appear less transparent. This may have been caused by the presence of the indium during growth, or due to the presence of the GaN interlayer. Such roughness is however not expected to affect the working of the laser device.

3.5 Formation of Graded index structures based on digital AlGaN alloys

In the laser structures that have been developed in this program, the active region is confined by two graded AlGaN layers. These layers serve two purposes. Firstly, the excitation electron beam is "funneled" so as to cause a net drift of the generated electrons and holes towards the active region. Furthermore, the refractive index gradient plays a significant role in

confining the optical modes. This has a strong effect on not only the laser threshold, but also on the far field pattern.

Even though the exact relation of the laser parameters with the nature of the grading in the alloy composition is quite complex, it is clear that an accurate control over the grading profile is necessary to obtain the best results.

3.5.1 Digital alloy formation

Ternary AlGaN alloys can be formed by either the analog method or the digital method of deposition [12,13]. In the analog method, the Al and Ga effusion cells are opened at the same time during the growth of the alloy. The alloy composition is determined by temperature of the two cells, along with the operating conditions of the group V emitter, which in our case is the RF power in the Nitrogen Plasma source. In this case, the AlGaN alloy composition can be graded by changing the temperatures of the Al and Ga cells as a function of time. This method is limited by the thermal inertia of the effusion cells. A second method of formation of AlGaN alloys is the digital method, that is, by use of short period superlattices. In this case, thin layers of binary GaN and AlN are deposited with layer thicknesses much shorter than the carrier wave functions. As a result, the composition changes in the individual layers are effectively transparent to the carriers, and the average composition of the layers determines the materials properties. The alloy composition is therefore given by the ratio of the thickness of the two constituent layers. Instead of AlN and GaN, thin layers of AlGaN alloys with two different compositions can be also used. This method allows a greater control over the alloy composition, and graded ternary alloys grown by this method in other materials systems have been extensively reported in the literature. There are additional advantages related to control over strain and alloy disorder

3.5.2 Growth of "bulk" digital AlGaN alloy

Before attempting to form graded alloys, bulk single composition AlGaN films were grown using AlN/GaN short period superlattices... Two such films were deposited using the usual three-step process. In the first sample, the AlN and GaN layers were both 10 Å thick, leading to an average Al content of 50%. For the second sample the GaN layer was 5Å thick while the AlN layers were 15Å thick. In this case the average AlN mole fraction is 75%. In both films 200 bilayers were deposited, leading to a film thickness of 4000Å. The schematics of the films are presented along with their optical transmission spectra in Fig 26. It is clearly seen that the films behave as bulk AlGaN alloys, with absorption edge qualitatively given by the average Al content.

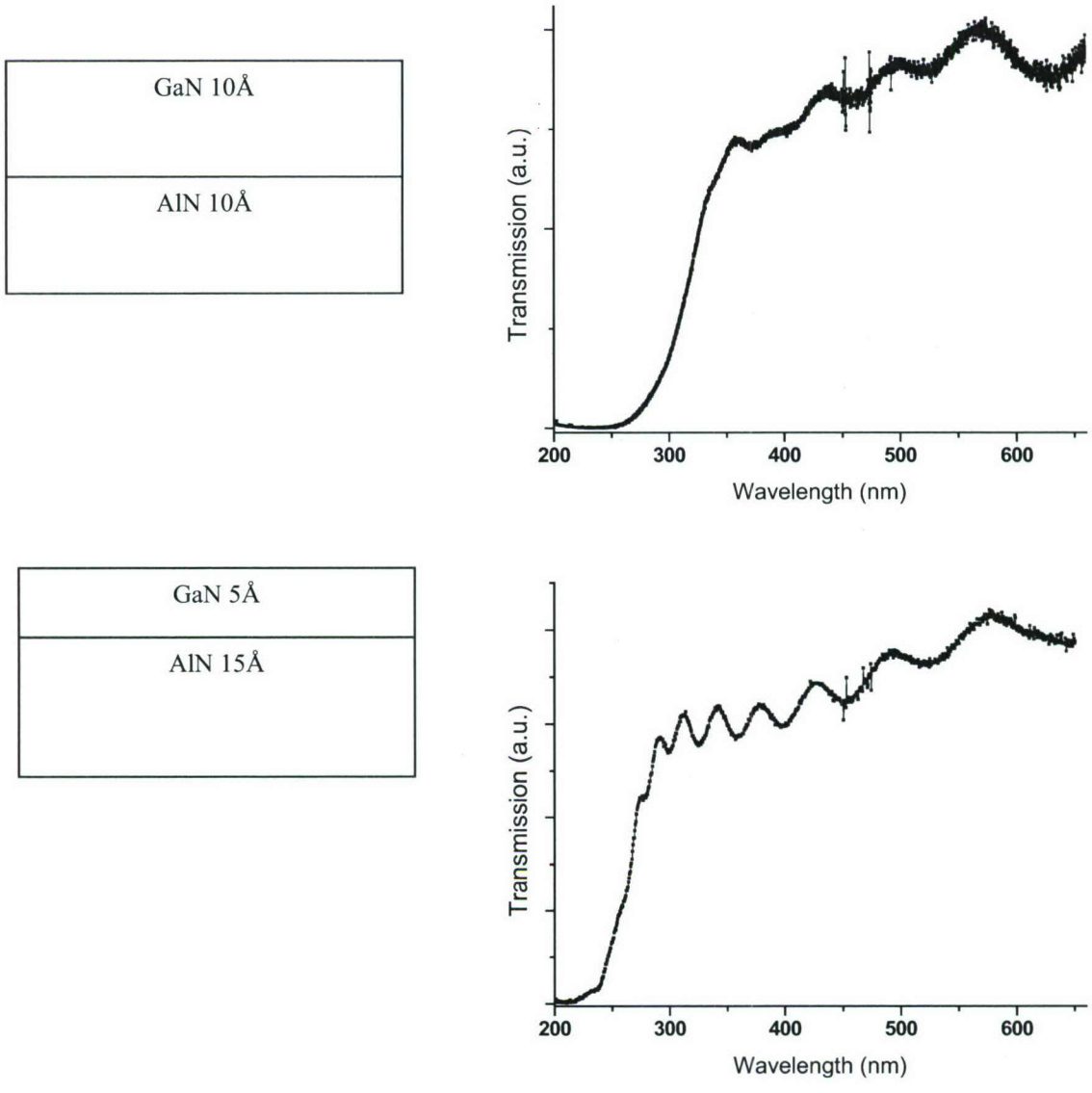

Fig 26: Schematic for bulk short period superlattice structures and their transmission spectra.

3.5.3 Growth of parabolic graded index digital AlGaN alloy

The technique for depositing AlGaN alloys using short period superlattices based on AlN/GaN bilayers has been used to grow a graded AlGaN film where the Al content has been graded **parabolically** from 100% to 50% over 3000Å. The film consists of 100 bilayers each 30Å thick. The thickness of the AlN layer in each bilayer is changed from 30Å to 15 Å in a parabolic fashion. The resultant Al content for each bilayer is presented in Fig 27.

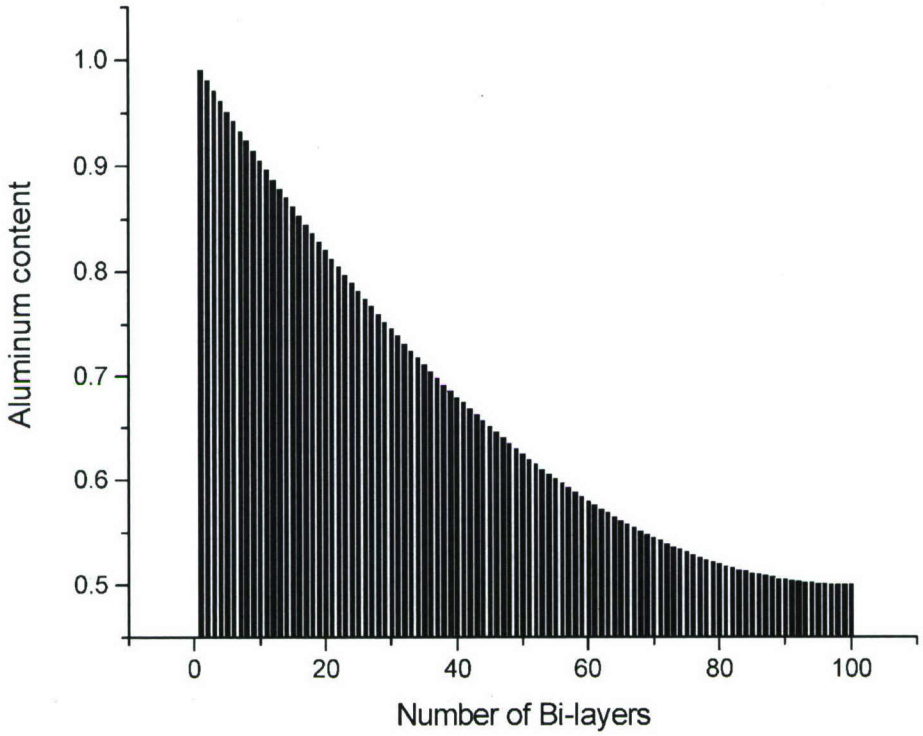

Fig 27: parabolic grading of AlN content in a bulk AlGaN film

The precise control of the AlGaN compositional profile of the graded index optical/electronic confinement regions is expected to cause significant improvement of the laser properties.

3.6 Cross-sectional SEM of cleaved GRISNCH structures

In the course of this program, we have switched form growing AlGaN based laser structures on the C-plane sapphire substrate to A-plane sapphire substrate in order to be able to make facets by cleaving. However, as discussed in previous monthly reports, based on our own work and that reported in the literature, the growth of AlGaN based structures on the A-plane sapphire is not trivial. Specifically, if the nucleation step (AlN buffer) is not done properly, the subsequent growth is a mixed phase. More recently, Astralux has reported that the cleaved facets of GRINSCH AlGaN structures are decorated with vertical striations which were attributed to the columnar nature of the films. As a result of this work, we investigated different deposition conditions to promote lateral growth and increase the size of those columns. In a number of experiments, we have incorporated Indium during the growth of the AlGaN alloy since indium was found to be a surfactant during growth of GaN. In another set of experiments we use GaN thin interlayers during the growth of the AlN cladding layer of the GRINSCH structure. The optical properties of such structures have been reported in previous monthly reports. During the month of August, we focused on studying the surface morphology and cross-section images of cleaved facets in bulk AlGaN and in GRINSCH structures produced under various conditions. The objective was to find out whether these various nucleation approaches affect the cross-sectional smoothness.

A. Experimental results and discussion

Prior to cleaving AlGaN thick films or GRINSCH structures based on AlGaN grown in A-plane sapphire, we practice in cleaving pure A-plane sapphire substrates without thinning of the substrates. We understand that this technique of cleaving thick sapphire substrates may not be suitable for the formation of laser bars. Nevertheless this was adapted in our work for the purpose of examining the surface morphology of the cross-section.

The cleaving was done using a manual scribe and break technique. The scribe mark was made relatively lightly, on the back surface of the sapphire substrate. The mark was made deeper near the edge of the wafer. The wafer was then placed between glass slides, and a shear force was applied. The break that was made tended to deviate slightly from the scribe mark made, as it is difficult to align perfectly the scribe mark along the crystallographic planes. During SEM, the region of the cross-section showing the best smoothness of the cleaved sapphire was generally chosen for evaluation. It should be noted that the evaluation was made at several locations of the substrate, and the pictures presented below are representative of the commonly observed images.

The SEM was conducted using a JEOL machine operating at 20KV. The surfaces were coated with a very thin sputtered gold film in order to reduce charging effects, as the films are very insulating.

Figure 28 shows the cleaved facet of a A-plane sapphire substrate. This is the R-plane of sapphire which is located at 58° from the flat of the substrate.

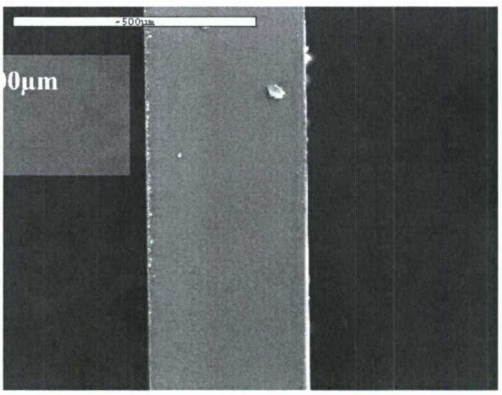

Fig 28: A cleaved facet of A-plane sapphire substrate

Fig 29 shows a cleaved facet of a 0.6 µm thick film of AlGaN with an AlN mole fraction of 60%. This film was grown using the following nucleation steps. First the surface of the substrate was converted from Al_2O_3 to AlN (nitridation) by exposing the substrate to a nitrogen plasma at 870°C, followed by a low temperature GaN buffer.

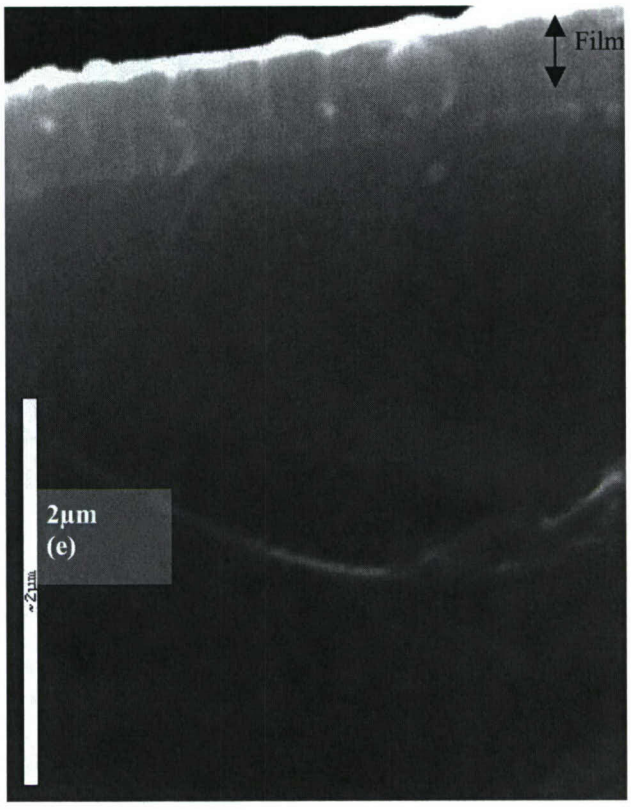

Fig 29: Cross-sectional SEM of AlGaN bulk film deposited onto A-plane sapphire using a GaN buffer layer.

It is apparent from the data of figure 29 that this film shows strong columnar morphology. The data shown in figure 29 represents the state of the limited investigation of growing AlGaN on the A-plane sapphire using the nucleation steps described previously.

Figure 30 shows the cross-section SEM of two AlGaN GRINSCH structures grown on the A-plane sapphire using a AlN buffer layer and a GaN interlayer in the beginning of the AlN cladding layer. Also during the growth of these GRINSCH structures we have used certain Flux of indium to act as a surfactant. These cross-sections have a better surface morphology than that showed in Fig 29.

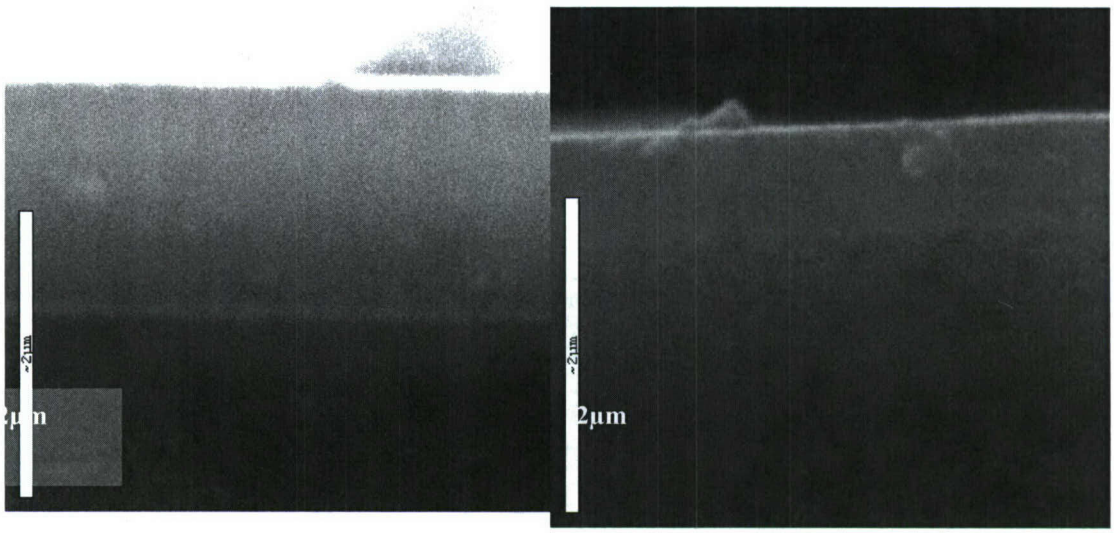

Fig 30: Cross-sectional SEM of GRISNCH structures deposited onto A-plane sapphire using a AlN buffer layer and a GaN interlayer

Finally, Fig 31 shows the cross-section SEM images of GRINSCH AlGaN structures grown only AlN buffer without GaN interlayer in the cladding layer, and without Indium flux during the film growth. During cleaving of the materials we have made the following observations. If the cleaving of the sapphire was done perfectly the AlGaN has a relatively smooth surface morphology with a few fractures (see Fig 4). These fractures are expected since the R-plane of the sapphire does not completely coincide with A-plane of the sapphire, but differ by approximately 1°. On the other hand, in some other cases (see Fig 32) the surface morphology of the cross-section is highly fractured. We tentatively attribute this to slight miss-orientation during the cleaving of the sapphire.

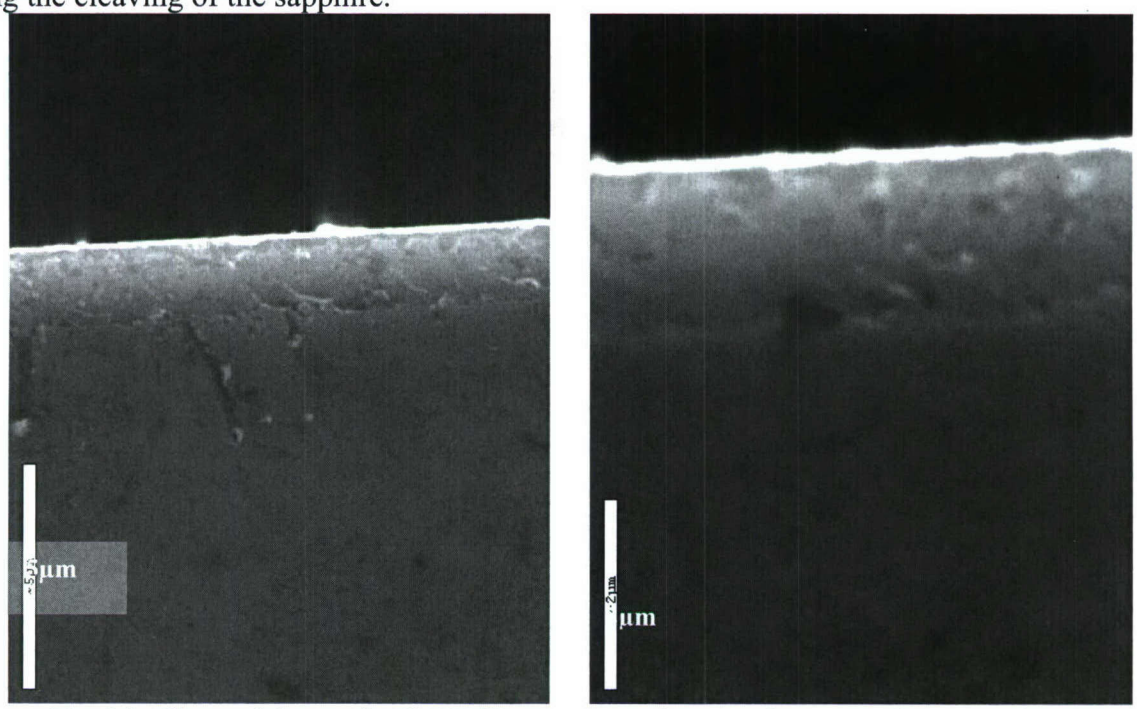

Fig 31: Cleaved facet of a GRINCH structure deposited onto A-plane sapphire.

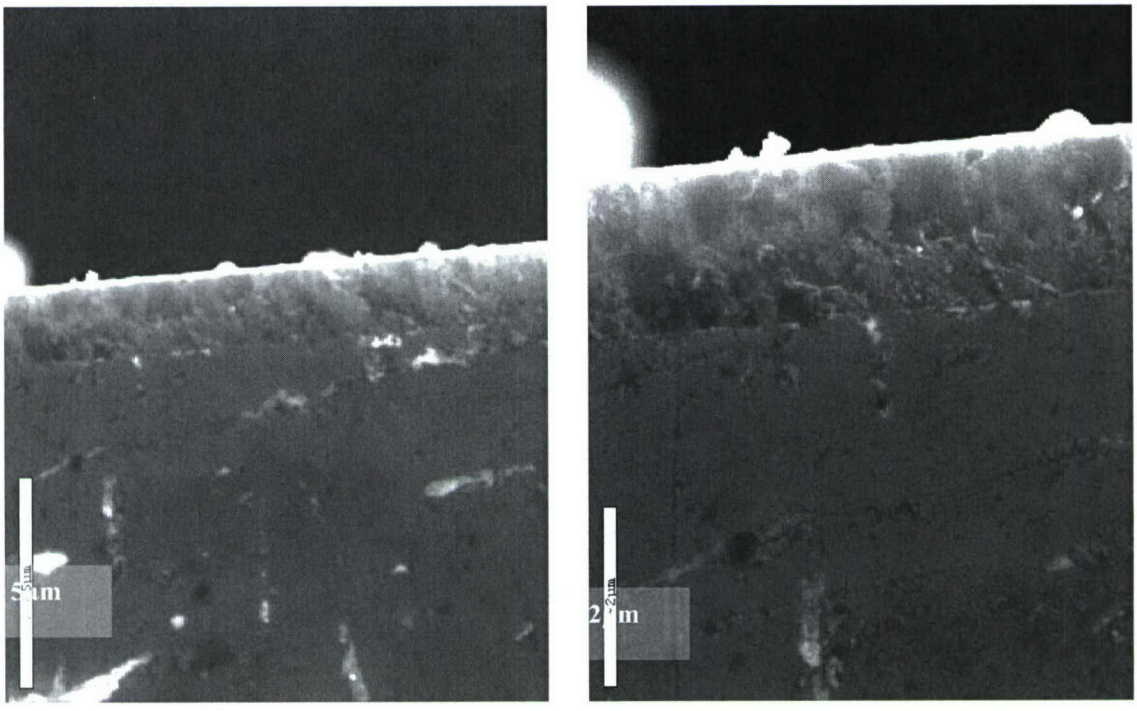

Fig 32: Imperfectly cleaved facet of a GRINCH structure deposited onto A-plane sapphire

B. Conclusions

The surface morphology of cleaved facets depends critically on the nucleation layers during the growth of AlGaN layers on A-plane sapphire. However we have evidence that the surface morphology of the facet may be the result of imperfect cleaving.

3.7 Development of Cathodoluminescence / Photoluminescence Measurement System

In order to study the electron-beam pumping of the laser device structures grown and processed during this program, a custom built cathodoluminescence system was designed and constructed at Boston University. The electron gun, which is capable to providing a slit excitation beam, was provided by Photon Systems Ind. Fig 33 shows the schematic of the CL/PL setup. It has been designed such that both photoluminescence using a He-Ag laser as an activation source, as well as cathodoluminescence using a slit electron-beam can be conducted on the same sample without venting the chamber. Fig. 34.shows the top view of the main chamber, indicating the geometry of excitation, when using either the electron-gun or the deep UV laser as the excitation source.

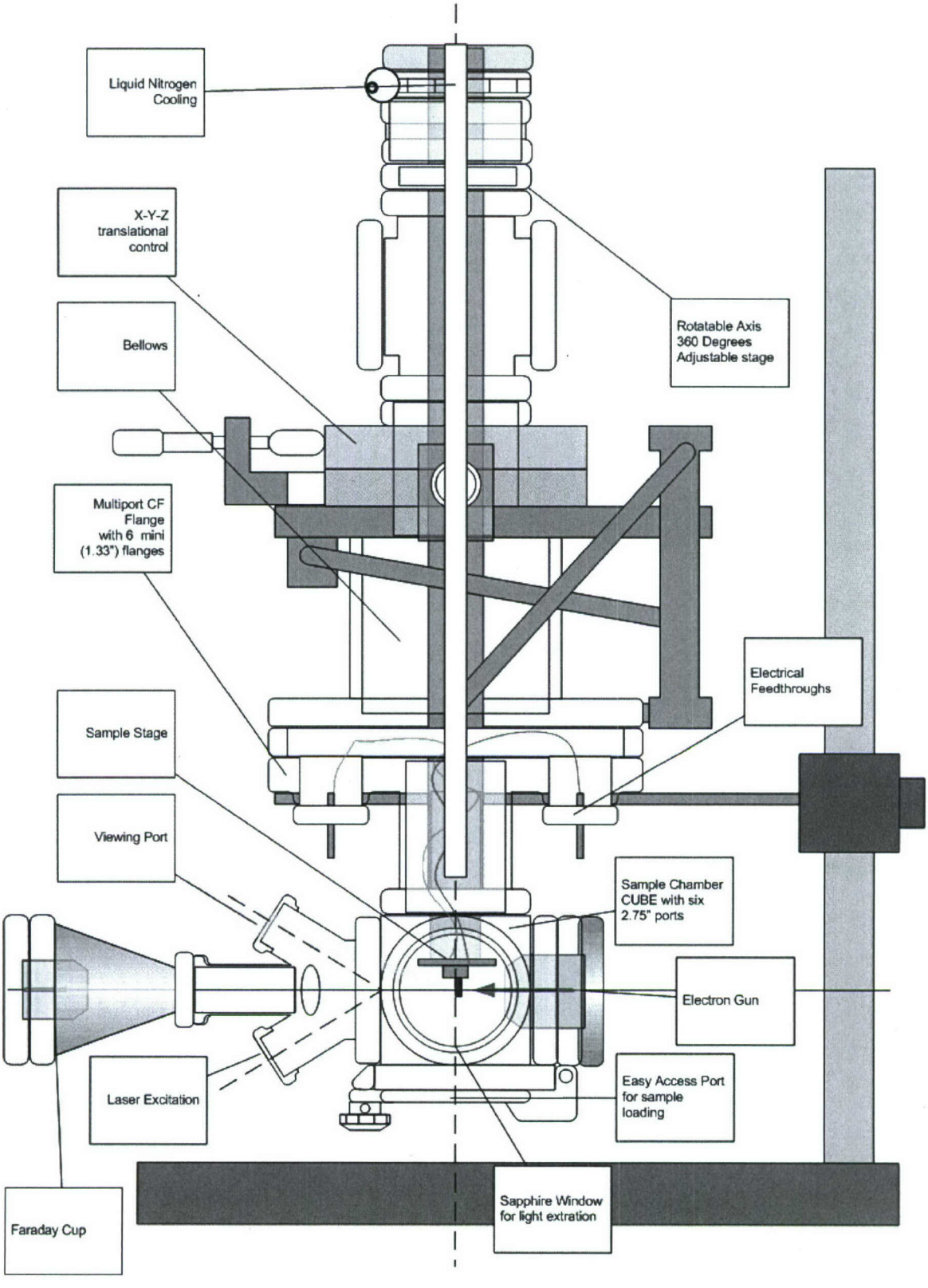

Fig 33: Schematic of custom-built CL/PL system developed at Boston University

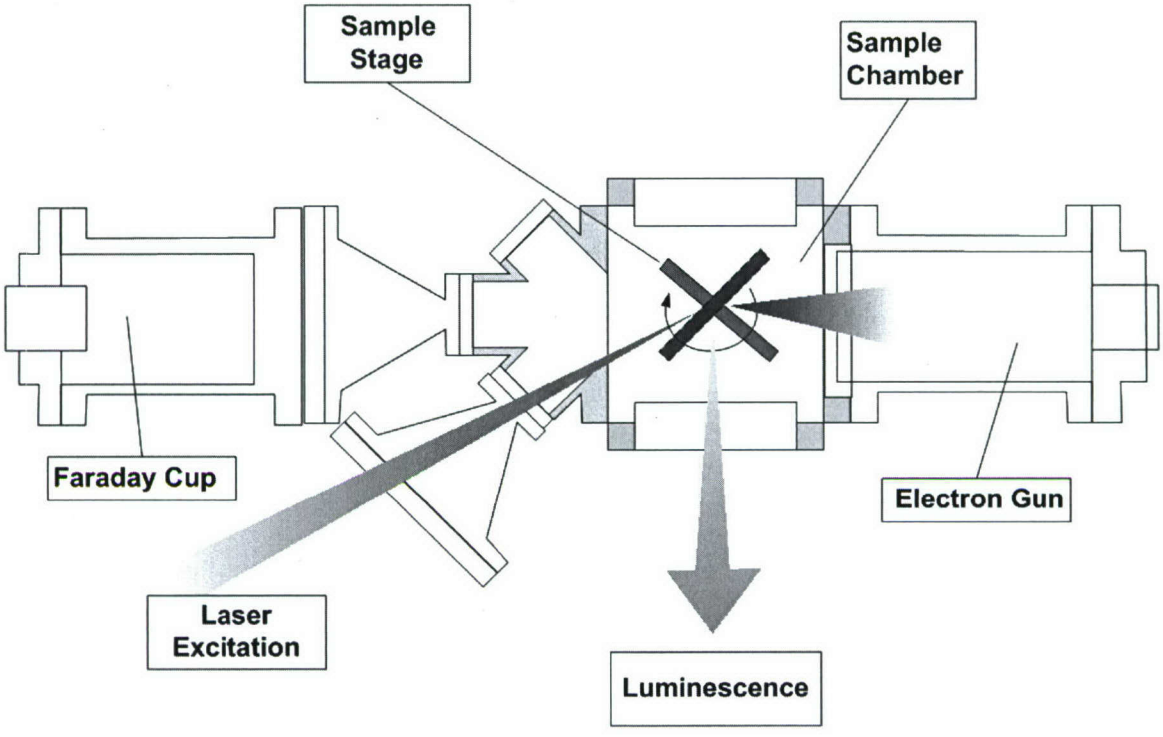

Fig 34: Schematic of CL/PL setup: top view of the sample chamber

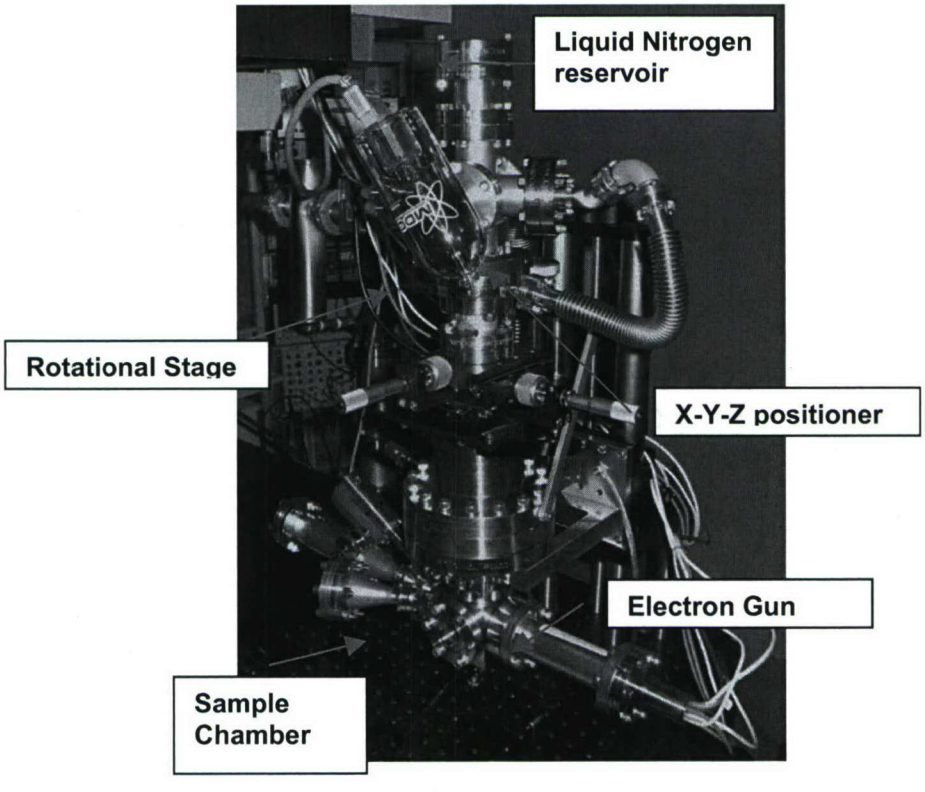

Figure 35: CL /PL setup photograph 1

Fig 35 shows a photograph of the instrument. The sample is mounted inside a cubical vacuum chamber, onto a vertically suspended sample stage, which is attached to a three-axis manipulator thus allowing different positions of the mounted sample to be exposed to the e-beam excitation. A rotational stage allows the sample to be excited by either the electron beam or a deep ultraviolet laser (see fig 4). During excitation of a bulk AlGaN film for surface luminescence, the sample is placed at a small angle from the electron beam, while for edge emission measurements, the sample surface is placed perpendicular to the excitation.

Fig 36(a) shows the setup from a different angle. The optical window for laser excitation, the Faraday cup, which is placed opposite to the electron gun; and the high voltage, feed thorough for sample bias can be seen. The sample is loaded and unloaded through the bottom port of the sample chamber. The shaft onto which the sample stage is mounted, shown in fig 36(b), is a hollow tube into which liquid nitrogen can be poured to cool the sample to a temperature of 80K. The sample holder is electrically isolated from the cold stage by a thin sapphire plate. This holder is appropriate for luminescence testing at the wafer level. For cleaved substrates a different holder, provided already by Photon Systems will be used.

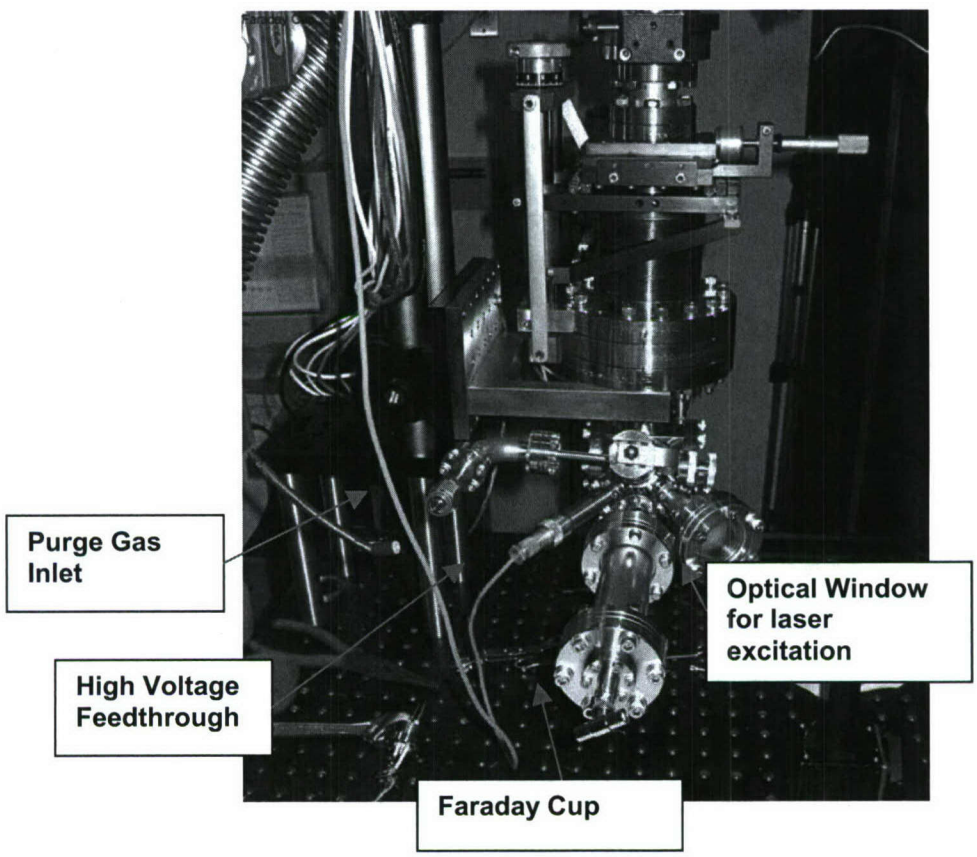

Figure 36(a): CL /PL setup photograph 2

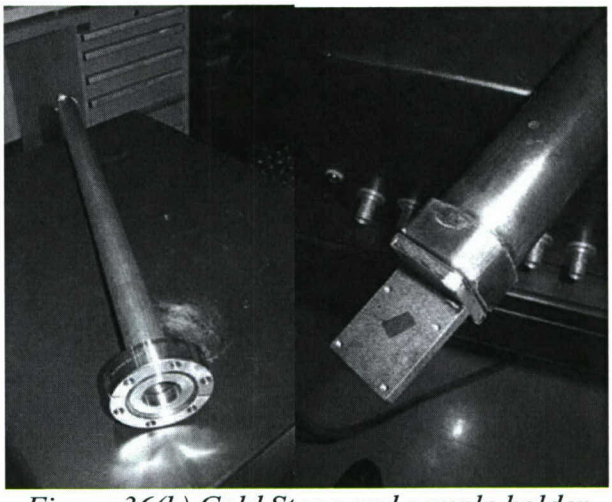

Figure 36(b) Cold Stage and sample holder

3.8 Cathodoluminescence measured from bulk films and structures using custom-built setup

3.8.1 Initial Photoluminescence / Cathodoluminescence Data obtained

In order to test the CL/PL setup, an AlGaN sample that was previously characterized by a commercial system was measure. Figure 37 shows a room temperature photoluminescence spectrum from this bulk AlGaN film with 85% AlN mole fraction, obtained using a He-Ag laser as excitation source. The CL spectrum of the same sample obtained using a commercial setup is shown for comparison.

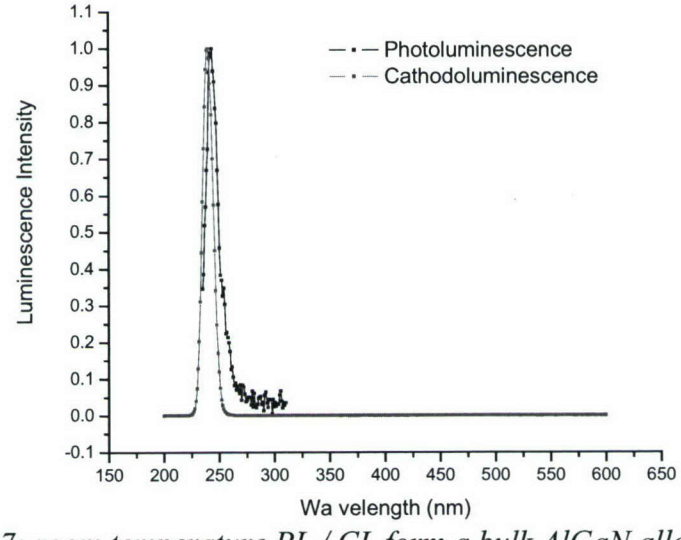

Fig 37: room temperature PL / CL form a bulk AlGaN alloy film

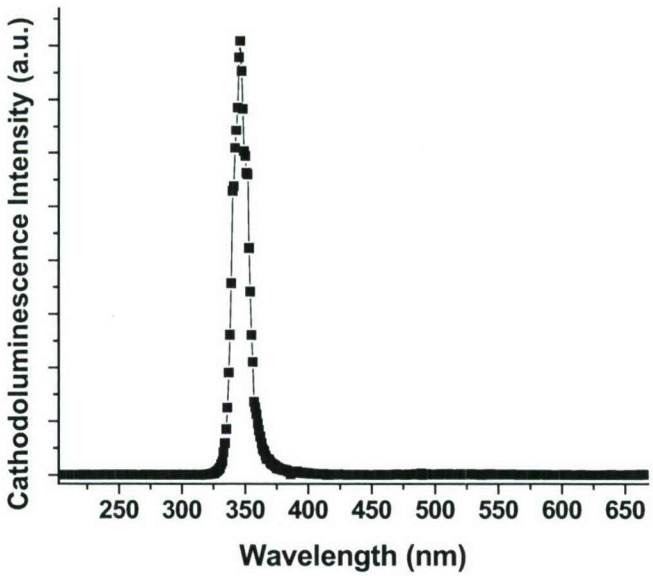

Fig 38: room temperature CL form a bulk AlGaN alloy film

Fig 38 shows the room temperature CL spectrum form a bulk ~10% AlGaN alloy film obtained from the setup described in section 3.7. This sample, which was grown under N-rich conditions using indium as a surfactant has been described in sec 3.4.1. The data was obtained using an ARC 0.5m monochromator and a photomultiplier tube.

3.8.2 Description of the investigated samples.

The investigated samples were all grown in the edge emitting GRINSCH configuration and some of them employ a double heterostructures, and some employ AlGaN/AlN MQWs as the active region of the device. The CL spectra from all of these structures were investigated previously using a commercial CL system (Oxford Scientific). The CL spectra in this system are collected by illuminating the sample at normal angles and collecting the luminescence at normal angles (surface emission) as shown in Fig 39. The identification, the structure and the peak emission of these samples are shown in table II.

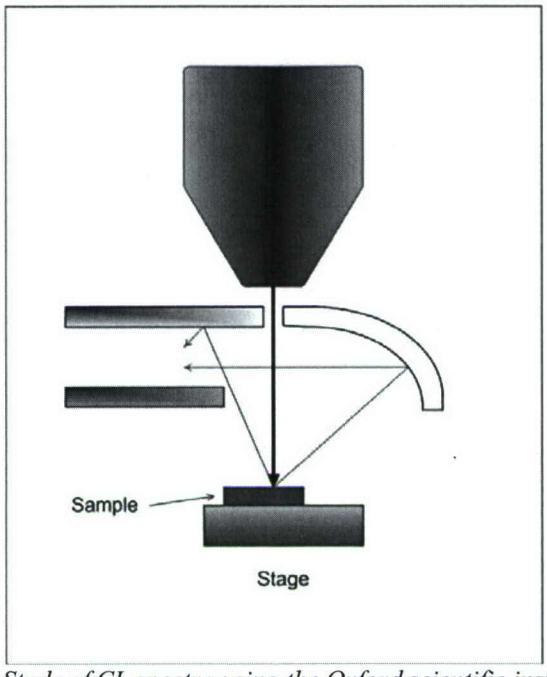

Fig 39: Study of CL spectra using the Oxford scientific instrument.

Table II: Investigated edge-emitting laser structures

Sample Number	Type	Sample Description	CL peak (nm)
1644	GRINSCH DH	Graded index double heterostructure	247
1683	GRINSCH DH	Graded index double heterostructure	239-247
1671	GRINSCH-MQW	GRINSCH Structure with 50 AlGaN/AlN MQWs	233
1787	GRINSCH-DH	Graded index double heterostructure	240
1843	GRINSCH-DH	Graded index double heterostructure grown with Indium as surfactant	244

By employing the scribe and break technique, several laser stripes were formed form each of these wafers. Fig 40 shows a photograph of several of these cleaved structures. It can be seen that these structures were between 1 and 2 mm in width. The slit electron beam was placed perpendicular to the cleaved edges.

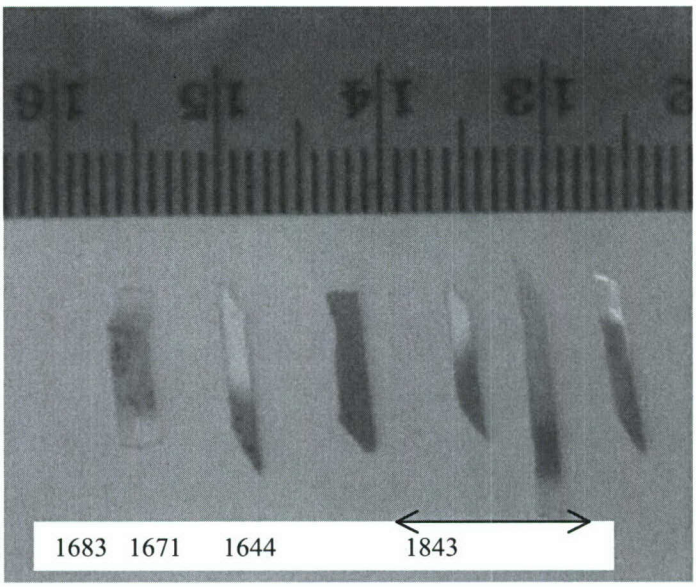

Fig 40: Cleaved laser structures formed by scribe and break technique. A cm scale is

3.8.3 Experimental results

The cleaved samples were mounted on the cold finger, and CL measurements were conducted using various excitation schemes, as indicated in Fig 41. First, in order to ascertain that the electron beam was incident on the sample, and to focus the spot, the sample was placed such that the top surface faced the exit window, and the electron beam was incident at a glancing angle, as shown in Fig 41 (a). In this case, the majority of the luminescence collected was from the surface of the sample. Subsequently, the sample was tilted so that the angle of incidence was less than 20 degrees from normal (setup b). In this case, it was still possible to observe the spot size and nature of the focusing. Even in this second setup, as the sample was not completely perpendicular to the output window, a component of the luminescence emitted from the surface was also collected along with luminescence emitted from the edge of the sample. For setup C, only the edge emission was measured.

In addition, the penetration depth of the electron-beam excitation was different in the three setups. For most of the measurement done, the acceleration voltage was 5KV. This value of the voltage causes the electron beam to penetrate deeper than that active region, when the electron beam is incident normal to the surface. For oblique incidences, as in (a) and (b), the excitation is more efficiently absorbed in the active region.

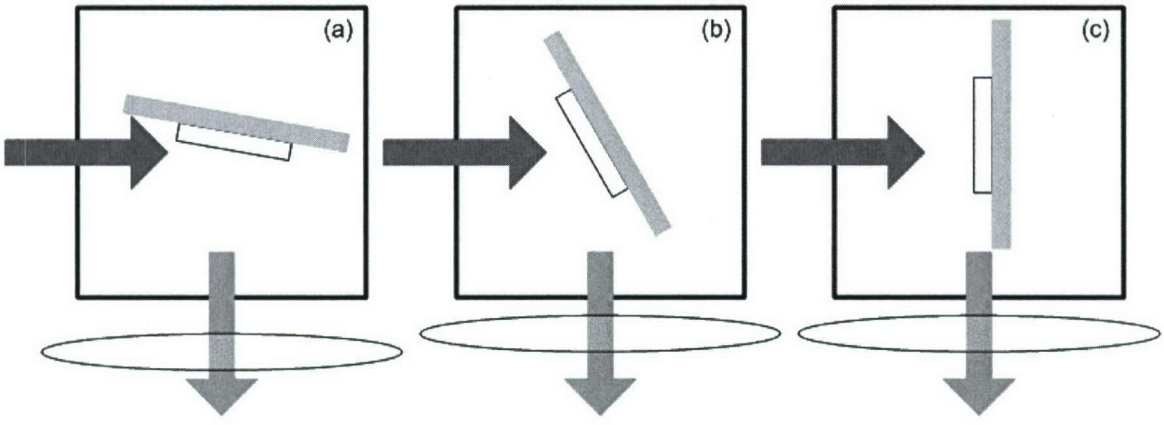

Fig 41: (a) sample orientation for surface and (b), (c) edge emission measurements

A. Sample #1671:GRINSCH(MQW)

The schematic of the sample BU #1671 has been shown in section 3.5. The active region consists of 50 MQWs, with 70%AlGaN wells and AlN barriers. The wells are heavily doped with silicon.

A small piece of the sample several mm wide was cut from the wafer by the scribe and break technique. The sample was mounted onto the CL setup, as shown in Fig 41. Two sets of spectra was obtained, the first, as shown in Fig 41(a), with the wafer surface facing the optical window so as to collect the light in a surface emission mode, and the second with the cleaved edge facing the window.

1. Surface emission measurements:

The room temperature surface emission form sample BU #1671, as obtained using a set-up described schematically in Fig 41 (a) is presented in Fig 42 The e-gun parameters used in obtaining the luminescence are as follows: The filament was in the BOOST mode, the PW and freq switches were set to 500 and 150 respectively. The voltages applied to the grids G1, G2, G4, G3/5 and G6 are 0, 332V, 0, 6.3KV and 1.8KV respectively. These parameters were obtained from the "E-gun installation and operation" manual provided by Photon Systems. The target voltage was 5KV. At these settings, a bluish white light spot was observed where the e-beam impinges on the sample, and visual inspection of this spot was used to determine whether the beam is tightly focused or not. However, we do not have yet any quantitative measurements of the spot geometry or the size.

The spectrum obtained from a GATAN commercial system is also presented for comparison. We clearly see that the two spectra are practically identical. These measurements generate confidence in the accuracy of the CL set-up. The inset in Fig 42 however shows that the line-width of the spectrum, as obtained from the new set-up, is slightly narrower. This narrowing of the line may be linked to the increased electron beam current in the current setup.

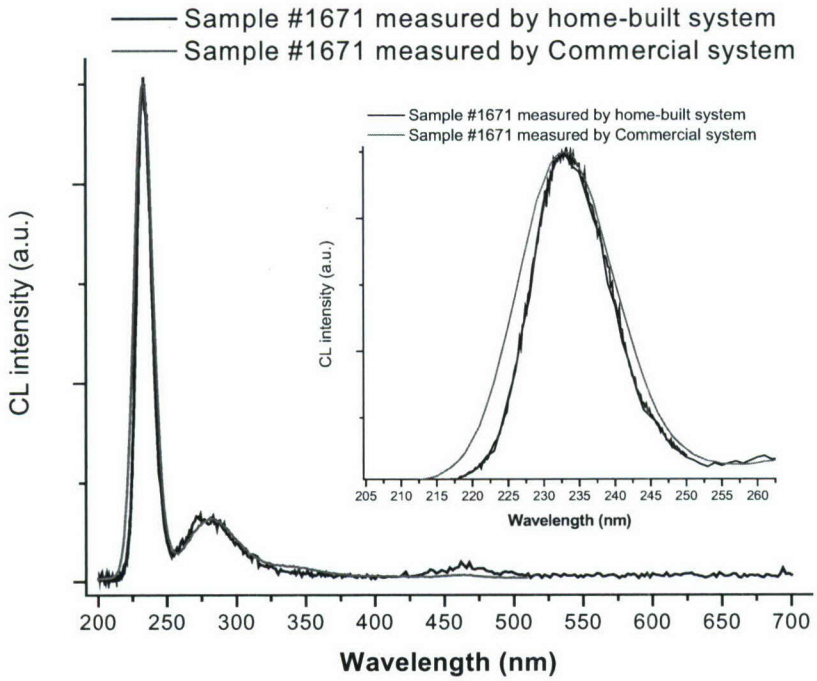

Fig 42: RT CL spectrum from sample 1671 obtained in surface emission mode using the CL set-up developed at BU and its comparison with spectrum obtained from a **commercial system.**

2. Surface/ Edge emission measurements

Subsequent to the surface emission measurements, the sample holder was rotated to the position as described in Fig 41(b). Using the e-gun parameters as described in the previous section, several CL scans were conducted, and the data from two scans obtained using slight variations of the excitation angle are presented in Fig 43.

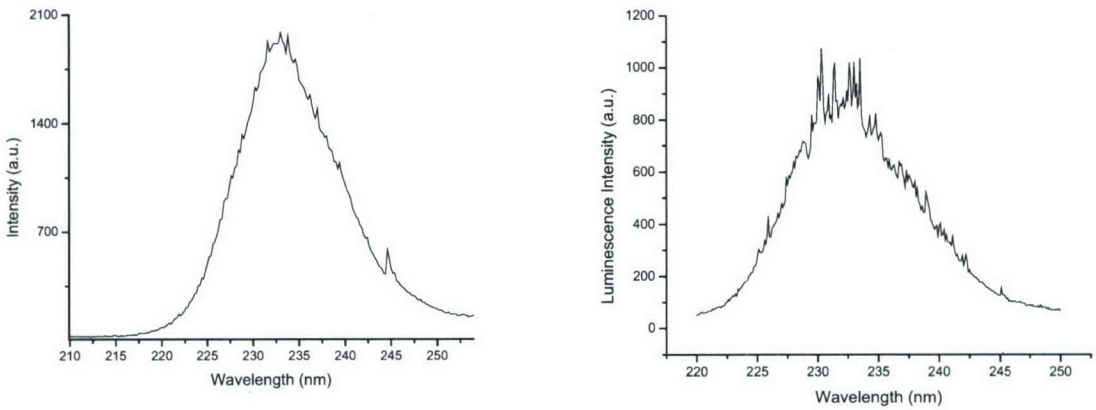

Fig 43: CL spectra from sample #1671 obtained in the edge emission mode

The spectra 43(a) were obtained using a monochromator step size of 0.1 nm and a sampling time of 0.5 second per step. The scan 43(b) and all subsequent scans were obtained using a monochromator step size of 0.1nm and a sampling time of 1 second per step.

After these scans were conducted, the grid voltages G2 and G3/5 were increased to produce more target current. However, this also caused to beam to defocus, as seen from the size of the visible spot. A CL scan was conducted at these conditions, and the spectrum is presented in Fig 44(c). Then the grid voltage G4 was adjusted to decrease the spot size. The CL obtained at these conditions are presented in Fig 5 (b). Finally, the G4 was further adjusted to produce a sharper spot, and the spectrum obtained is presented in Fig 44 (a).

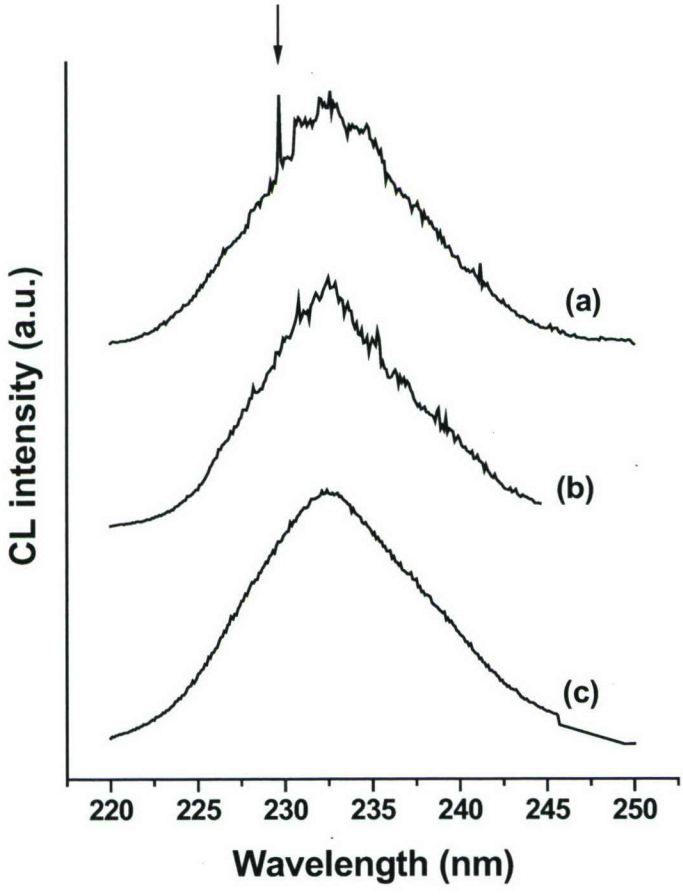

Fig 44: Edge emission CL spectra from sample #1671 under different conditions of e-beam focus.

These results were obtained recently and have not been completely understood. However, there is a strong possibility that the sharp lines obtained in the spectra of Figures 44(b) and 44(a) are cavity modes produced by stimulated emission. The broad peaks seen in Figures 43 and 44 possibly originate from surface emission, which has not been eliminated completely in the setup used.

For comparison, we reproduce in Fig 6 the stimulated emission obtained in ZnCdSe/ZnSe GRINSCH heterostructures using a single QW as the active region, by micro-gun pumping at low temperatures [Herve et. al. Appl. Phys. Lett, 67, 2144 (1995)] .

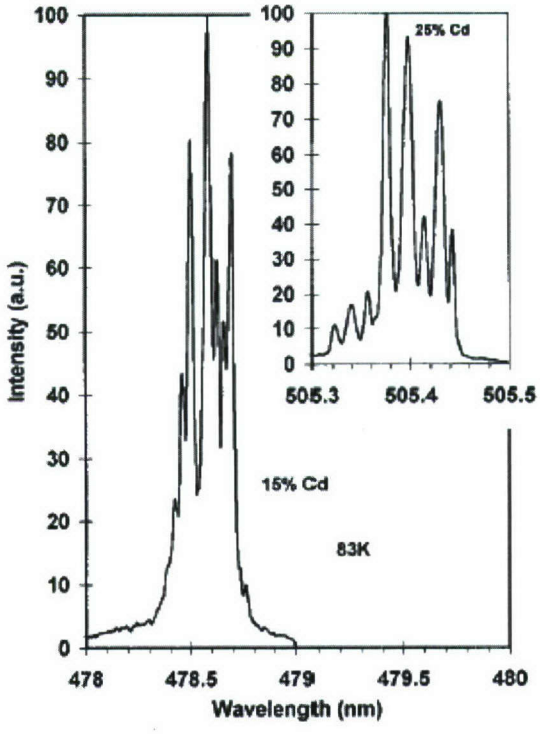

FIG. 3. Stimulated emission spectra at 83 K from a blue laser which included a $Zn_{0.85}Cd_{0.15}Se$ single-QW GRINSCH with $L_W = 8$ nm, and from a blue-green laser which included a $Zn_{0.75}Cd_{0.25}Se$ single-QW GRINSCH with $L_W = 5$ nm (see inset).

Fig 45: Stimulated emission as reported in the literature [Herve et. al. Appl. Phys. Lett, 67, 2144 (1995)]

The cavity in our case may be formed by the two cleaved facets. A second possibility is that the cavity is formed by one of the facets and the length of the e-beam spot.

3. Edge emission (setup C).

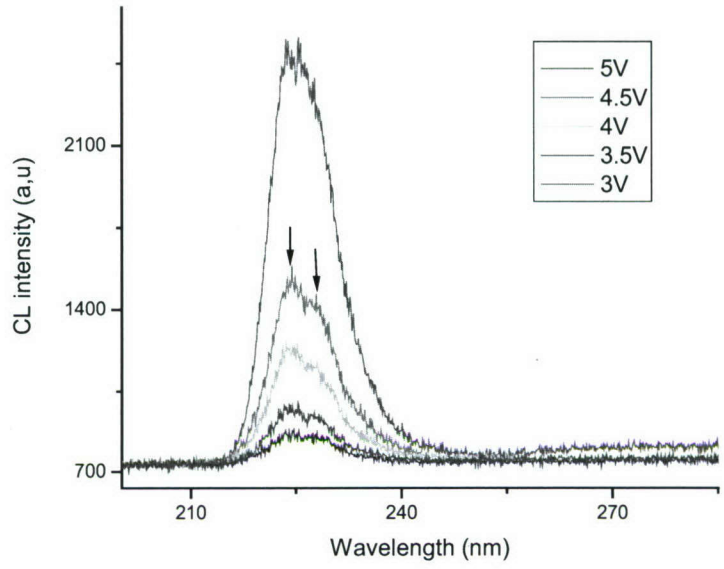

Fig 46: edge emission from sample 1671 as a function of acceleration voltage

The spectra of Fig 46 have the following characteristics: First there are two peaks at all excitation levels. We are currently in the process of fitting these data in order to understand the nature of these two peaks. Second, the peak CL intensity increased by a factor of 18 as the acceleration voltage increased from 3KV to 5KV. At this point, since we do not have an absolute measurement of the electron beam current as a function of acceleration voltage we are unable to plot the CL intensity vs. excitation beam current.

B. Sample #1644 (GRINSCH structure employing a Double Heterostructure as the active region)

1. Room temperature surface emission

This sample was excited at room temperature using various acceleration voltages in the surface emission mode. It should be noted that during these excitations, the beam current also varies, as shown Fig 47. This beam current has been obtained from the ammeter reading of the power supply and not using a Faraday cup, which would be probably a more accurate method of measurement. It can be seen that with the increase in acceleration voltage, (and corresponding beam current) the peak intensity increases significantly.

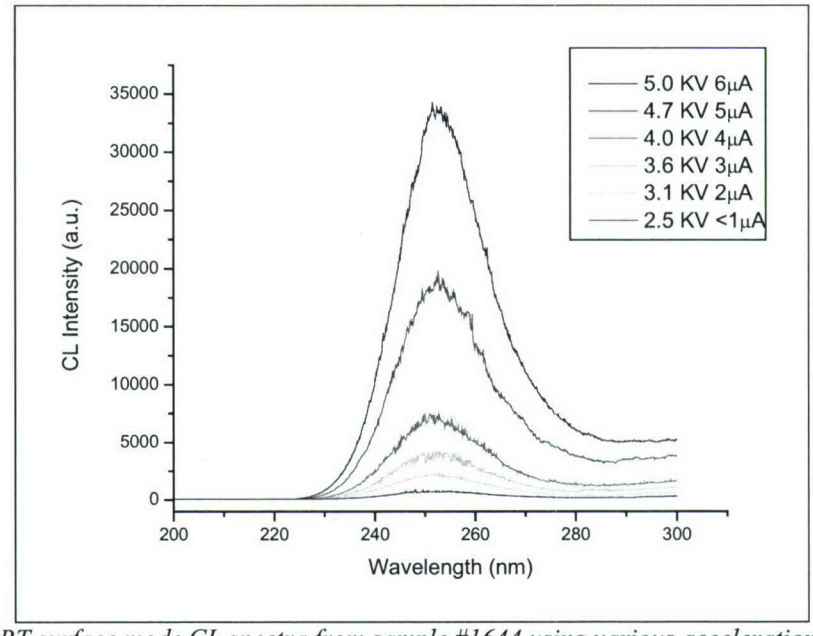

Fig 47: RT surface mode CL spectra from sample #1644 using various acceleration voltages

In order to observe more clearly the nature of the change in luminescence peak with the acceleration voltage, the spectra in Fig 47 have been re-plotted in Fig 48 after being normalized and vertically shifted for easier comparison.

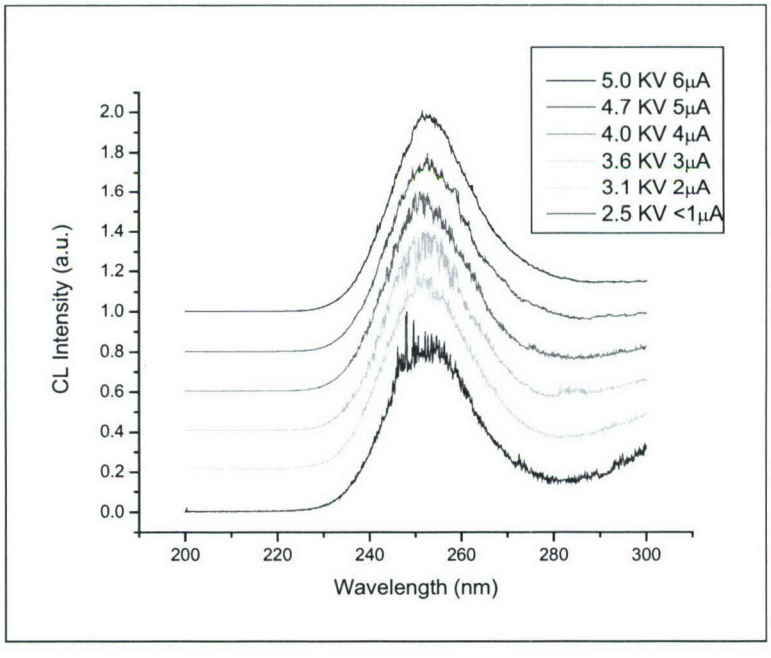

Fig 48: RT surface mode CL spectra (normalized) from sample #1644 using various acceleration voltages

Temperature dependent CL measurements were conducted on sample 1644, and the normalized CL spectra are presented in Fig 49. The CL intensity shows a blue shift from 252 to 247 nm due as the sample temperature decreases from room temperature to Liquid nitrogen temperature..

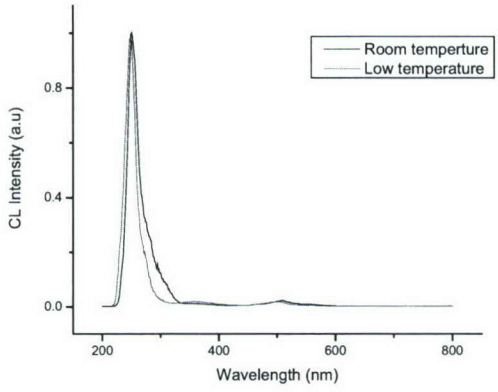

Fig 49: RT and low temperate CL spectra from sample 1644

2. Low temperature edge emission

This sample was also investigated in the edge emission configuration, and the data at room and low temperature are presented in Fig 50. The measurements were taken at 5KV acceleration voltages and with long integration times to reduce random noise in the data. The peak shows a slight blue shift and a increase of luminescence intensity with reduction in temperature.

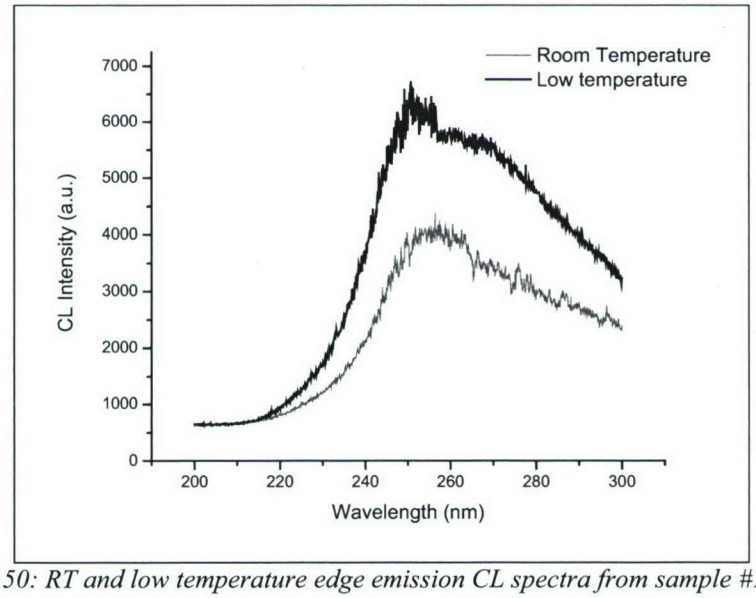

Fig 50: RT and low temperature edge emission CL spectra from sample #1644

In addition, sharp features in the CL spectra are also seen at ~250 nm for the measurements conducted at low temperature. These features are similar to those described in Figure 44 and 45/

C. Sample #1843 (GRINSCH structure employing a Double Heterostructure as the active region)

Laser stripes produced from sample #1843 was mounted onto the CL stage and room temperature luminescence measurements were conducted using the mode. In this mode described in Fig 41 (b), the luminescence from both the surface and the edge is collected simultaneously.

The room temperature measurements taken at different points of the stripe are presented in Fig 51.

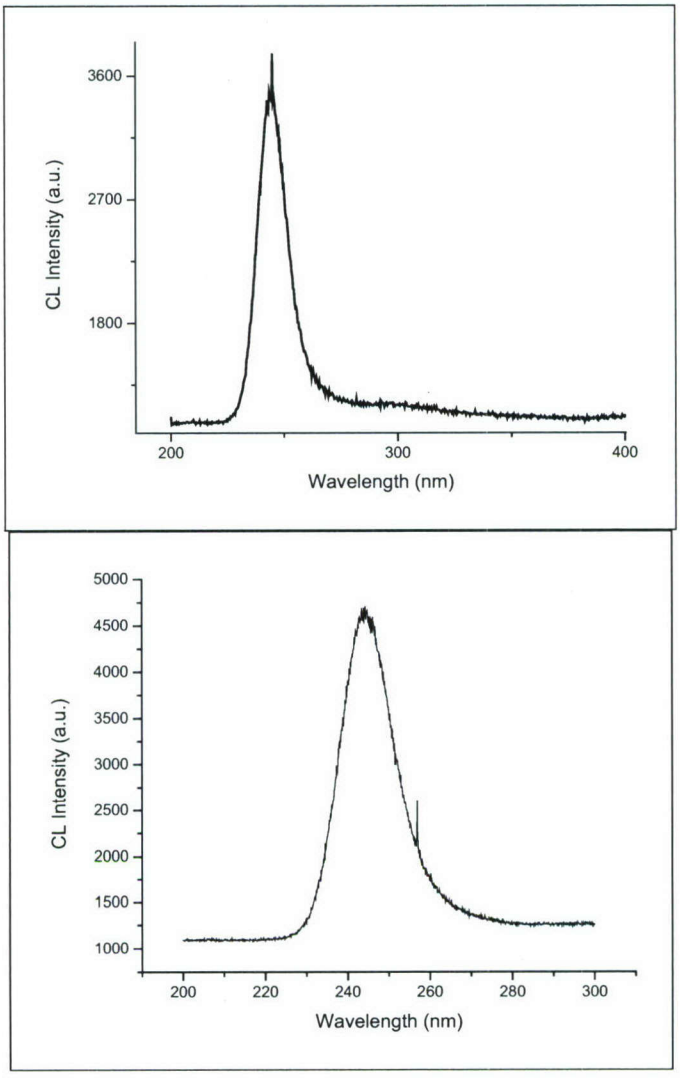

Fig 51: RT CL spectra from sample #1843

D. Sample #1787 (GRINSCH structure employing a Double Heterostructure as the active region)

Figure 52 shows the CL spectrum taken from structure #1787 in an edge emission mode. The black line shows the room temperature data while the other spectra were obtained during the cooling down of the sample. We see a significant increase of the luminescence intensity of the band-edge peak as well as the sub-bandgap luminescence.

This device shows a room temperature CL peak at 235 nm which blue shifts to 230nm at low temperature. This is the lowest wavelength achieved during this program in laser structures employing a bulk film (DH) as the active region.

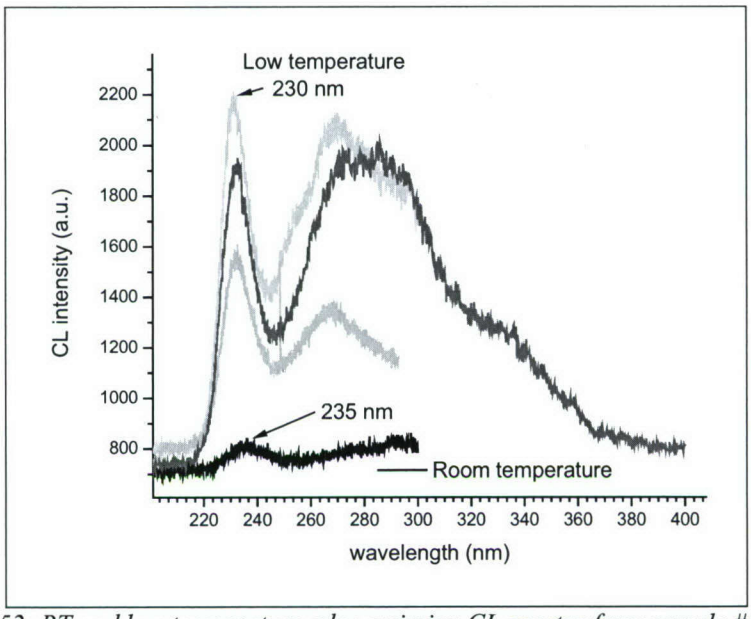

Fig 52: RT and low temperature edge emission CL spectra from sample #1787

Conclusion on electron-beam pumping of laser structures.

Several edge emitting laser structures have been studies using room and low temperature CL measurements. The important observations are:

1. For surface emission, the samples indicate results similar to those obtained using a commercial CL system
2. For edge emission, specially at low temperature, the CL spectra shows the presence of sharp features. These features are likely to be due to the mode-hopping at the onset of stimulated emission from the sample.
3. The absence of a clear lasing action from these samples can be attributed to the inadequate strength of the electron beam.

- The spot size was large, visual inspections indicate that it is about 1 mm in diameter. With a beam current of 6μA, the beam current density is only 0.6mA/cm^2. Our previous results indicate that much higher current densities are necessary for the stimulated emission from these materials
- The current density is dependent on the acceleration voltage. For lower acceleration voltages, the current density drops significantly. This is a problem, because the laser structures were designed to have the active region very close (less than 1000Å) from the top surface. Thus for efficient coupling of the electron energy to the active region, it is necessary to use a lower acceleration voltage, while still maintaining the beam currents.

Reference:

[1] E. Iliopoulos and T. D. Moustakas, Appl. Phys. Lett., **81,** 295, (2002).
[2] C. R. Elsass, T. Mates, B. Heying, C. Poblenz, P. Fini, P. M. Petroff,, S. P. DenBaars, and J. S. Speck, Appl. Phys. Lett, **77,** 3167 (2000).
[3] S. T. Bradley, S. H. Goss, L. J. Brillson, J. Hwang and W. J. Schaff, J. Vac. Sci. & Tech. **B 21**, 2558 (2003).

[4] Takeyoshi Onuma, Shigefusa F. Chichibu, Akira Uedono, Takayuki Sota, Pablo Cantu, Thomas M. Katona, John F. Keading, Stacia Keller, Umesh K. Mishra, Shuji Nakamura, and Steven P. DenBaars, J. Appl. Phys, **95,** 2495 (2004).
[5] S. V. Dudiy and Alex Zunger, Appl. Phys. Lett., **84**. 1874, (2004).
[6] Andenet Alemu, Michel Julier, Javier Campo, Bernard Gil,1, Denis Scalbert, Jean-Paul Lascaray, Shuji Nakamura Mat. Sci & Engg. **B59**, 159 (1999)
[7] D.S. Li, H. Chen, H.B. Yu, H.Q. Jia, Q. Huang, J.M. Zhou J. Crystal Growth **267,** 395,(2004)
[8] V. Darakchieva, P. P. Paskov, T. Paskova, E. Valcheva, B. Monemar and M. Heuken Appl. Phys. Lett., **82**. 703, (2003).
[9] A.C. Abare, M.P. Mack, M. Hansen, R.K Sink, P Kozodoy, S Keller, J.S Speck, J.E Bowers, U.K. Mishra, L.A Coldren, S.P DenBaars, IEEE J. of Selected Topics in Quantum Electronics, **4**, 505 (1998)
[10] D. Doppalapudi, E. Iliopoulos, S. N. Basu, and T. D. Moustakas, J. Appl. Phys, **85**, 3582 (1999)
[11] Tomohisa Kato, Hitoshi Ohsato, Takashi Okuda, Patric Kung, Adam Saxler, Chien-Jen Sun b, Manijeh Razeghi J. Crystal Growth **173,** 244,(1997)
[12]. *GaN / AlN digital alloy short-period superlattices by switched atomic layer metalorganic chemical vapor deposition* M. Asif Khan, J. N. Kuznia, and D. T. Olson, T. George and W. T. Pike, Appl. Phys. Lett. 63, 3470, 1993
[13] . *InGaAs/InAlAs SCH-MQW lasers with superlattice optical confinement layers grown by MBE.* Kawamura, Y; Asai, H; Sakai, Y; Kotaka, I; Naganuma, M IEEE PHOTON. TECHNOL. LETT. Vol. 2, no. 1, pp. 1-2. 1990

3.6 Astralux Contract Summary

This section will have it's own subsection, figure, and table numbers.

Introduction

Astralux Phase II work was focused on the production of faceted laser dies from $Al_xGa_{1-x}N$ and characterization/optical measurements to assist in the development and optimization of the processes involved. The production of faceted laser dies from $Al_xGa_{1-x}N$ is a critical step in the fabrication of an electron beam semiconductor UV optical source (ESUVOS) laser for operation in the 220 nm to 250 nm band. Production of the faceted die involved cleavage along crystal planes for facet formation, deposition of optical mirror coatings on the facets, and attachment to a customized thermally and electrically conductive submount. During this program a total of thirteen mounted $Al_xGa_{1-x}N$ die were produced from four $Al_xGa_{1-x}N$ wafers having different structures and distributed between Photon Systems, Boston University, and Astralux for emission measurements. Details of the production and characterization of these die, and supporting optical measurements, are discussed below.

Production and Characterization of Cleaved Facet $Al_xGa_{1-x}N$ Laser Dies

Die Fabrication and Mounting Process Flow

The die dimensions that were decided upon with Photon Systems after discussion of various testing and vacuum packaging issues for the ESUVOS prototype are 5 mm x 750 μm x 80-100 μm (thickness). It was decided to keep the facet length 5 mm to allow electron pumping along the entire length and also for ease of handling the die. The die will be attached, as shown in Figure 2, to a custom-made 1 x 5 x 10 mm CuW submount, supplied by Photon Systems. These submounts are electroplated with Ni and Au to a thickness of 1-2.5 μm if die attachment via eutectic solder is to be done. For attachment via conductive silver adhesive this is not necessary. We have access to electrolytic and electroless Ni plating solutions from Transene, Inc. at CU along with the proper electrochemical apparatus. For Au plating, we use 24k Hard Acid Immersion Gold from Gold Plating Services, Inc. 5-6 submounts were plated for the initial cleaved die production runs.

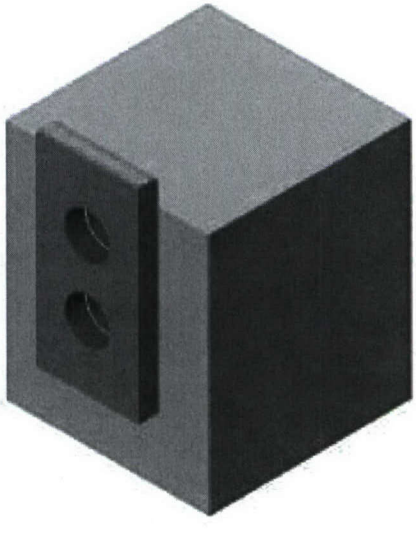

Figure 1. Laser die (blue-green), CuW submount (brown), and submount holder (yellow) for eutectic die attachment.

Details for eutectic die attachment are as follows. The dies are mounted using Au/Sn preform having a 300 C process temperature. Due to the unusual aspect ratio of the submount, the assembly is done by hand using a custom-made block to hold the submount, as shown in Figure 2. The die positioning tolerance is approximately +/- 0.005". The eutectic bonding requires a backside wetting metallization on the die. This metallization is Cr/Au having thicknesses on the order of 100 nm. This backside metallization is done after the sample is thinned. However, it is most convenient to do the metallization on larger pieces rather than the individual dies. Therefore, the metallization is done before cavity cleavage to form the dies. This is the main reason we thin the samples in-house

at Astralux.

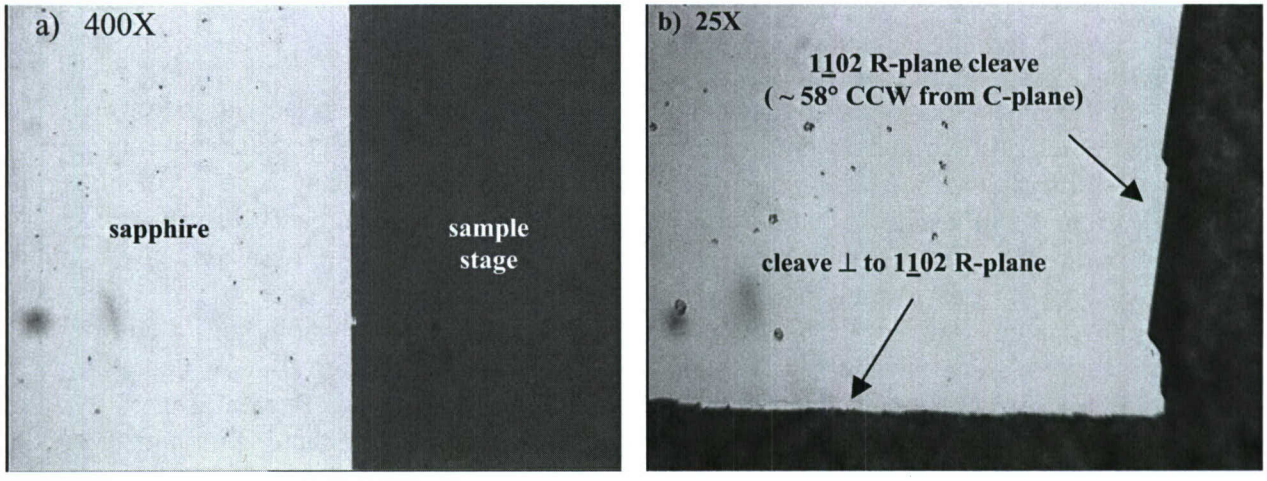

Figure 2. Optical micrographs of a) R-plane cleave and b) R-plane and ⊥ to R-plane cleaves in A-plane sapphire.

The process flow for die fabrication and mounting is summarized below:

1) Reference cleave formation and dicing to produce 6 x 5 mm samples
2) Thin 6 x 5 mm samples from 330 μm to 80-100 μm
3) Backside Cr/Au metallization
4) Cavity cleavage to form 6 laser dies from each 6 x 5 mm sample
5) Submount electroplating with Ni/Au
6) Die attachment to submount using 80/20 Au/Sn preform solder or conductive Ag adhesive

Further details of the development and optimization of each process step are given in the sections below.

Cleavage Optimization using A-plane sapphire

We began practicing cleavage of A-plane sapphire for facet formation using a diamond hand scribe to create a stress line along the 1102 R-plane in the wafer, which is then cleaved with large-area contact. A-plane sapphire having the standard thickness of 0.33 mm was obtained from Saint-Gobain Crystals for these initial cleaves. The sapphire cleaves

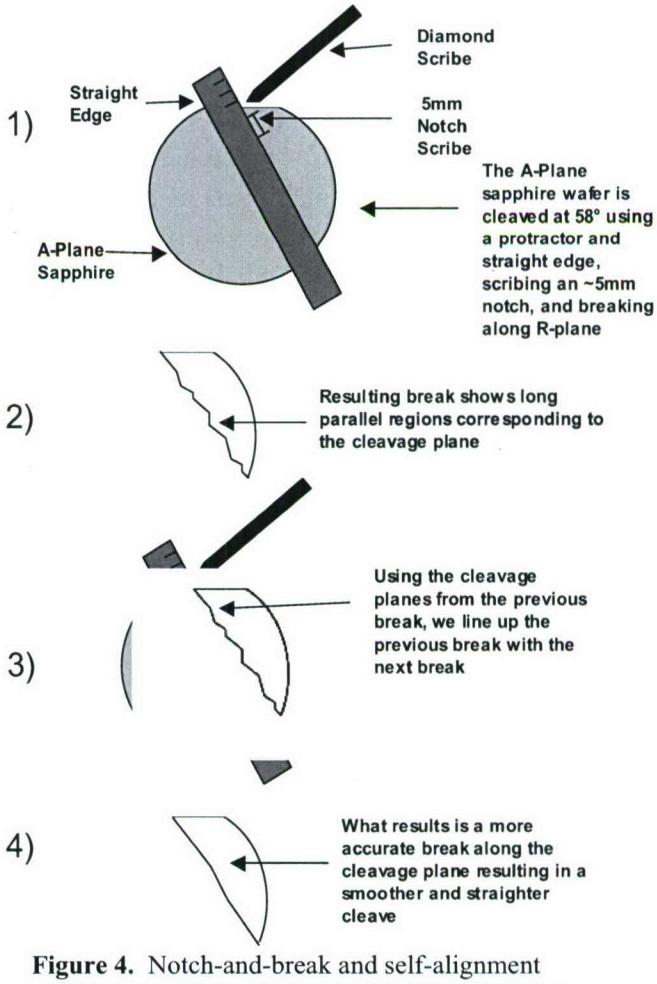

Figure 4. Notch-and-break and self-alignment techniques used for cleavage of A-plane sapphire.

readily in this direction as expected, and after some optimization of the pressure applied to the hand scribe, nice cleaves such as the one shown at 400X magnification in Figure 2a were obtained. One challenging aspect of the process is due to the angular orientation of the R-planes with respect to the wafer flat. The wafer flat is parallel to the C-plane, whereas the R-planes are 57.6° to either side of the C-plane. The (1$\underline{1}$02) R-plane is 58 degrees counterclockwise from the flat, therefore a simple plastic protractor was used to measure this angle. However, with this protractor it is difficult to measure the angle precisely, and it would be easy to be ~ 1-2 degrees off the desired angle. Figure 2b shows what we think is the result of a slight deviation from the desired 58° angle. The cleave on the right in this figure is initially irregular and then can be seen to abruptly line up with the R-plane as it travels up from the lower right hand corner of the sample. This figure also shows that the cleave perpendicular to the R-plane is irregular and of poor quality as expected. Figure 3 is an optical micrograph showing a comparison of the edge quality for the R-plane cleave versus a sample cut using a moderate quality Resinoid wafer saw blade. On the cleaved sample there is no evidence of the chipping apparent on the sawed sample.

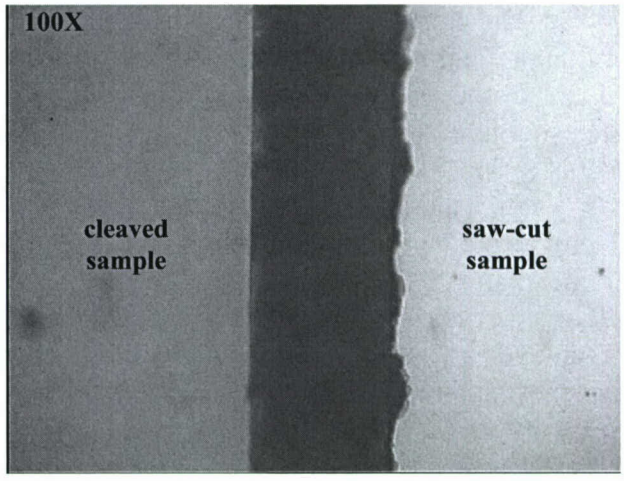

Figure 3. Comparison of edge quality for R-plane cleave vs. a saw-cut edge.

After the initial test cleaves described above, some refinements were made which are illustrated in Figure 4 and include the utilization of a notch-and-break technique and a self-alignment procedure. Both are intended to ensure propagation of the cleave exactly along the R-plane. In the notch-and-break technique, the wafer is lightly scribed for only a short distance (~ 5 mm) from the edge creating the 'notch'. Then, pressure is applied at the edge of the wafer parallel to the notch line to cleave the wafer. The advantage of this technique is that cleave should propagate naturally along the R-plane in the crystal, rather than having a tendency to follow the scribe mark some of the time, which may be 1-2□ off the R-plane. The self-alignment procedure, also shown in Figure 4, consists of using the R-plane edge of one cleaved piece to measure the R-plane angle with respect to the wafer flat (C-plane) in the next cleave more accurately than using the protractor.

The cleaves resulting from an earlier scribe-and-break method and the more recent notch-and-break and self-alignment methods were examined with both optical microscopy and SEM. Figure 5 shows topviews and sideviews of the resulting cleaves. In Figures 5a and 5b, undesirable features due to the width and depth of the scribe can be observed. The notch-and-break technique does not leave these features, as shown in Figures 5c and 5d. However, the edge has 'jags' that can be seen from both the top and sideviews. We believe these are the result of reorientations of the cleave as it propagates. The best results were obtained when the notch-and-break was combined with the self-alignment described above. Images of this cleave are shown in Figures 5e and 5f. A straight cleave was produced without the jags present in the previous attempt. Figures 5d and 5f also show the presence of horizontal striations. There was also evidence of these features in other images of the scribe-and-break sample of Figure 5b. Whether these striations are natural to sapphire cleaves and/or bad for device performance will be researched further.

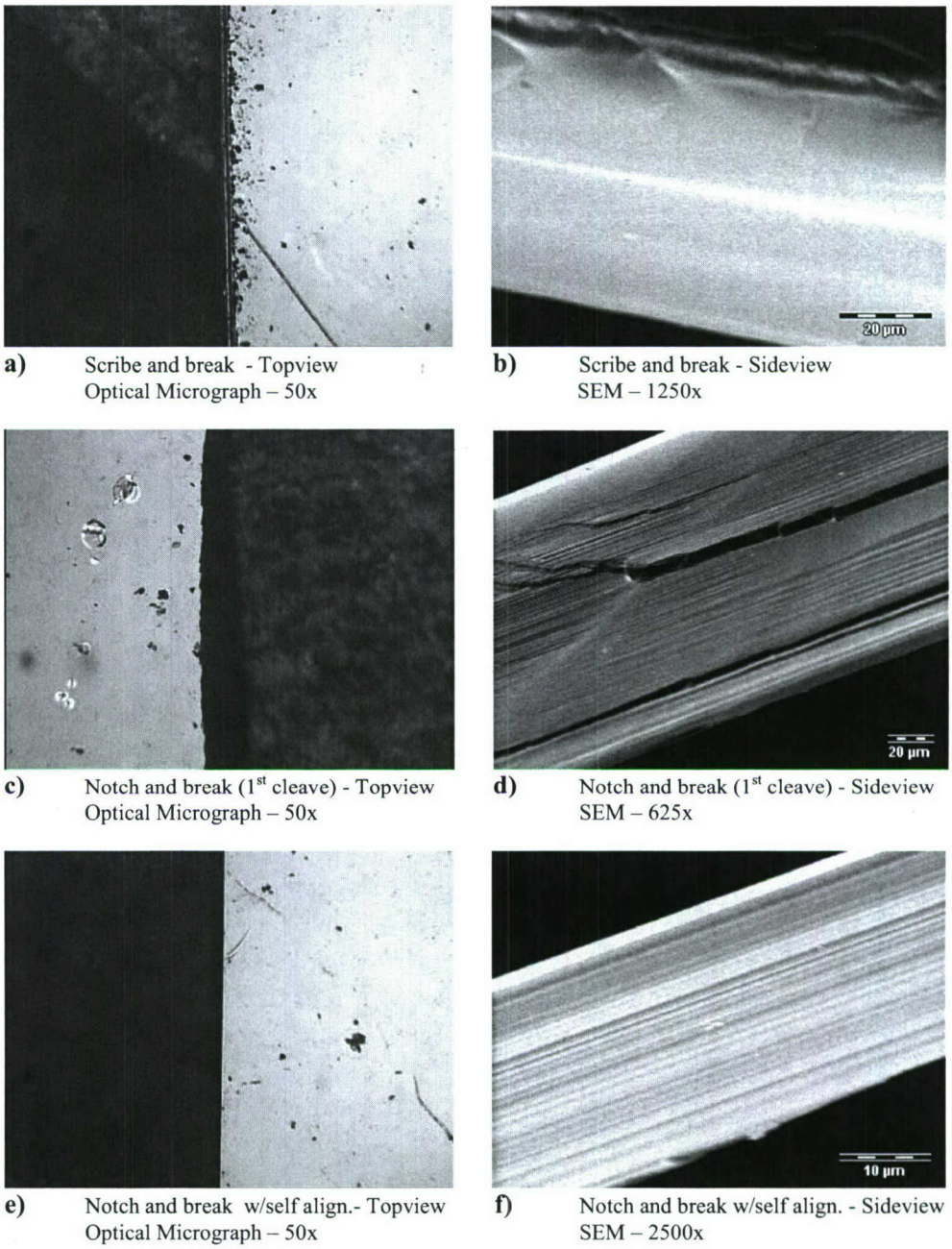

a) Scribe and break - Topview
Optical Micrograph – 50x

b) Scribe and break - Sideview
SEM – 1250x

c) Notch and break (1st cleave) - Topview
Optical Micrograph – 50x

d) Notch and break (1st cleave) - Sideview
SEM – 625x

e) Notch and break w/self align.- Topview
Optical Micrograph – 50x

f) Notch and break w/self align. - Sideview
SEM – 2500x

Figure 5. Optical micrographs and SEM images of cleaved facets produced in A-plane sapphire using various techniques.

Sample Thinning to Enhance Cleave Quality and Reliability

From discussions with our partners at Colorado State University (CSU), who have experience in the production of cleaved facet GaAs lasers, and also various reports in the literature, we learned of the benefits of sample thinning prior to cleave formation. These benefits include the formation of a consistent high quality cleave over a longer cleave length and more reliable propagation of the cleave along the proper plane. Therefore, we decided to test sample thinning prior to cleave formation for our die production.

We began our testing with a 5 mm wide bar from a 2" A-plane sapphire wafer, which we had previously cleaved utilizing a hand scribed notch-and-break. We also used the self-alignment technique to cleave this bar. CSU normally cleaves samples that are < 5 mm long. Therefore, we diced a rectangular sample to similar dimensions of 6 mm (cleaved edges) by 5 mm (diced edges). Then, to form laser dies we simply cleave parallel to these initial cleaved edges.

The 6 x 5 mm sample was thinned from 330 □m down to 110 □m via hand polishing. A 45 □m diamond grinding disc from Buehler was used for most of the thinning, followed by the use of diamond lapping films having several grit sizes for final thinning and scratch removal. It is necessary to polish the sample to a relatively fine finish because scratches can affect cleave formation or lead to cracking if they are deep enough.

Cleavage to Form Die with Sub-Millimeter Cavity Length

After the die dimensions discussed above were decided upon, it became a high priority to locate and evaluate a scriber/breaker system capable of forming edge emitter cavities on the order of 750 μm long. Our partners at CSU have such a system, which is capable of accurately cleaving cavities well under 1 mm in length. We went to CSU with some A-plane sapphire to evaluate their equipment and techniques to assess if they will work for our material. The cleavage of a practice 'cavity' from A-plane sapphire turned out to be quite successful as discussed below.

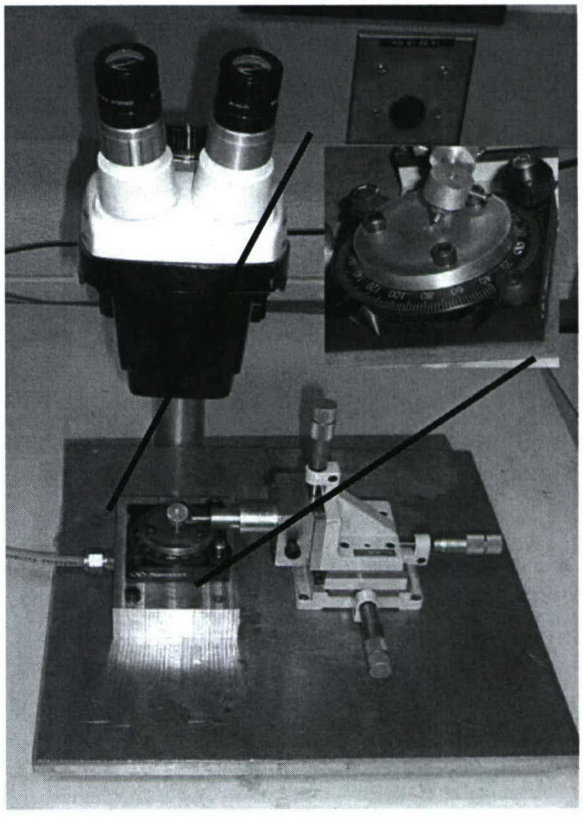

Figure 6. Frontview of the CSU edge emitter scribing tool. Inset shows a closeup sideview of the sample stage and diamond scriber.

The CSU scribing tool is shown in Figure 6. The main components are an xyz micrometer stage, a diamond scriber held at an adjustable angle relative to the sample, a rotatable vacuum chuck to hold the sample, and a long-working distance stereoscope. The diamond scriber was obtained from a jeweler and has a 60 degree tip angle. Our thinned sample was mounted on a small square of dicing tape, which is then held by the vacuum chuck. Then, the sample was aligned on the stage so that the scribe traveled parallel to one of the previously cleaved edges, as seen under the stereoscope. After this, a ~ 700 μm long notch was made at the edge of the sample using

the z adjustment on the xyz stage. Multiple passes are necessary to ensure the notch is deep enough to result in easy cleave propagation. After 2-3 scribes were made, we observed that the scribe tip was damaged due to the hardness of the sapphire. The diamond tip is held to a metal shaft with some sort of binder, and it is likely that this binder became damaged. Therefore, a new tip was mounted and the scribe angle was changed from ~ 30 degrees to 45 degrees. After these adjustments no further tip damage was observed for the remaining scribes. After ~ 10 passes were made the notch was deemed to be deep enough to permit cleavage.

The sample was taken off the scribing tool and without removing it from the dicing tape was placed between two ~ 1 x 1 inch mylar sheets. The sandwiched sample was then placed on a glass microscope slide and the notch is lined up with the edge of the slide under a long-working distance microscope. Then, the cleave was formed by simply pressing down gently on the mylar. The cleaves formed quite easily and looked quite good. To form a 650 μm practice 'cavity' a second cleave was made using same process described above.

The cleaved edges were then examined under the optical microscope and found to be quite straight, as shown in Figures 7. A calibrated eyepiece was used to measure the distance between the cleaves.

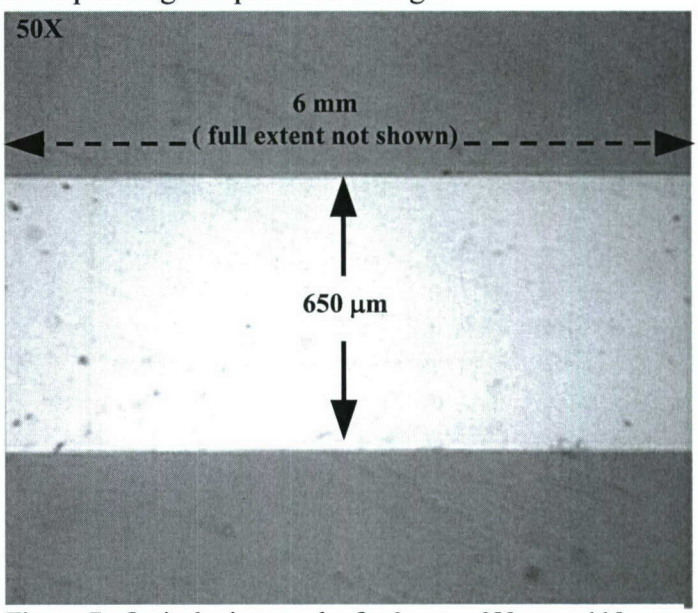

Figure 7. Optical micrograph of a 6 mm x 650 um x 110 μm thick bar of A-plane sapphire. The two sides that are 650 μm apart were formed using the notch-and-break technique utilizing the CSU scribe tool to form the notch.

Die Formation from $Al_xGa_{1-x}N$ on A-plane Sapphire Samples

Samples from two $Al_xGa_{1-x}N$ on A-plane sapphire wafers were prepared and thinned as described above. The backsides of these samples were then metallized with Cr/Au (50 nm/100 nm) via thermal evaporation. The samples were then cleaved using the CSU scriber/breaker system, also described in a prior report.

The formation of straight cleaves was not achieved as easily as during the practice runs using A-plane sapphire. The majority of the cleaves produced did not turn out straight. However, one of the 6 x 5 mm samples from wafer #1644 gave enough straight cleaves to produce three laser dies we believe are suitable for mounting and testing. The cleaves for one of these dies are shown in Figure 8.

The cause of the difficulty we encountered is unknown, although we believe

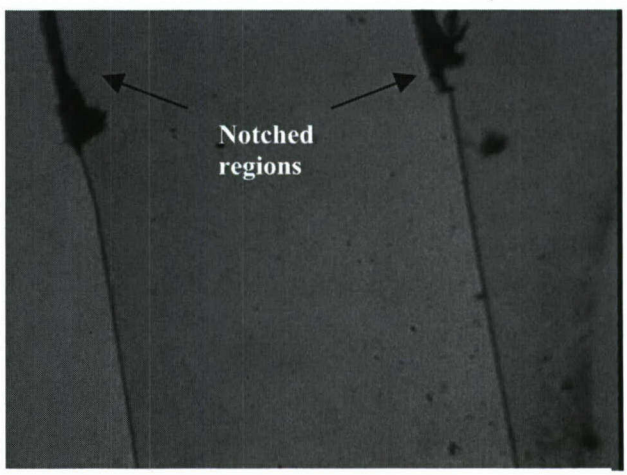

Figure 8. Optical micrograph of the cleaved edges on one of the dies formed from #1644.

there are several possibilities. In order to protect the epi surface, the notches were made on the metallized backsides of the samples. Previous trial runs were done without this metal layer. The metal made notch formation more difficult because the scribe tip had a tendency to wander sideways in the soft Au layer. The metal also made it difficult to see the depth of the notch using the stereoscope because of the metal reflectivity. Another possibility is nonuniformity in the sapphire crystalline orientation of the wafers. Evidence which suggests this possibility includes the difficulty in reference cleave formation in these materials encountered earlier and also the fact that the three best cleaves came from the same square sample. A third possibility is that the samples were too thick even after the thinning we did. Due to the indirect method we use to measure sample thickness during thinning, there is uncertainty in the final thickness on the order of +/- 20 μm. We do not measure the actual thickness of the finished thinned pieces in order to prevent scratching the $Al_xGa_{1-x}N$ epi surface.

Examination of Cleaved Facet Quality for $Al_xGa_{1-x}N$ Dies

Test cleaves were made on materials from three BU wafers having various $Al_xGa_{1-x}N$ structures on A-plane sapphire substrates. These cleaves were then examined under high optical magnification using Normaski contrast. A typical facet is shown in Figure 9. A thin layer having vertical features is observable at the top (epi side) of the sample. These features appear to be striations or roughening. Dark vertical bands can be observed which have irregular spacing, although the spacing often appears to be similar to the layer thickness. *In contrast to the top layer, the sapphire sidewall below the striated layer is very smooth and featureless, indicating*

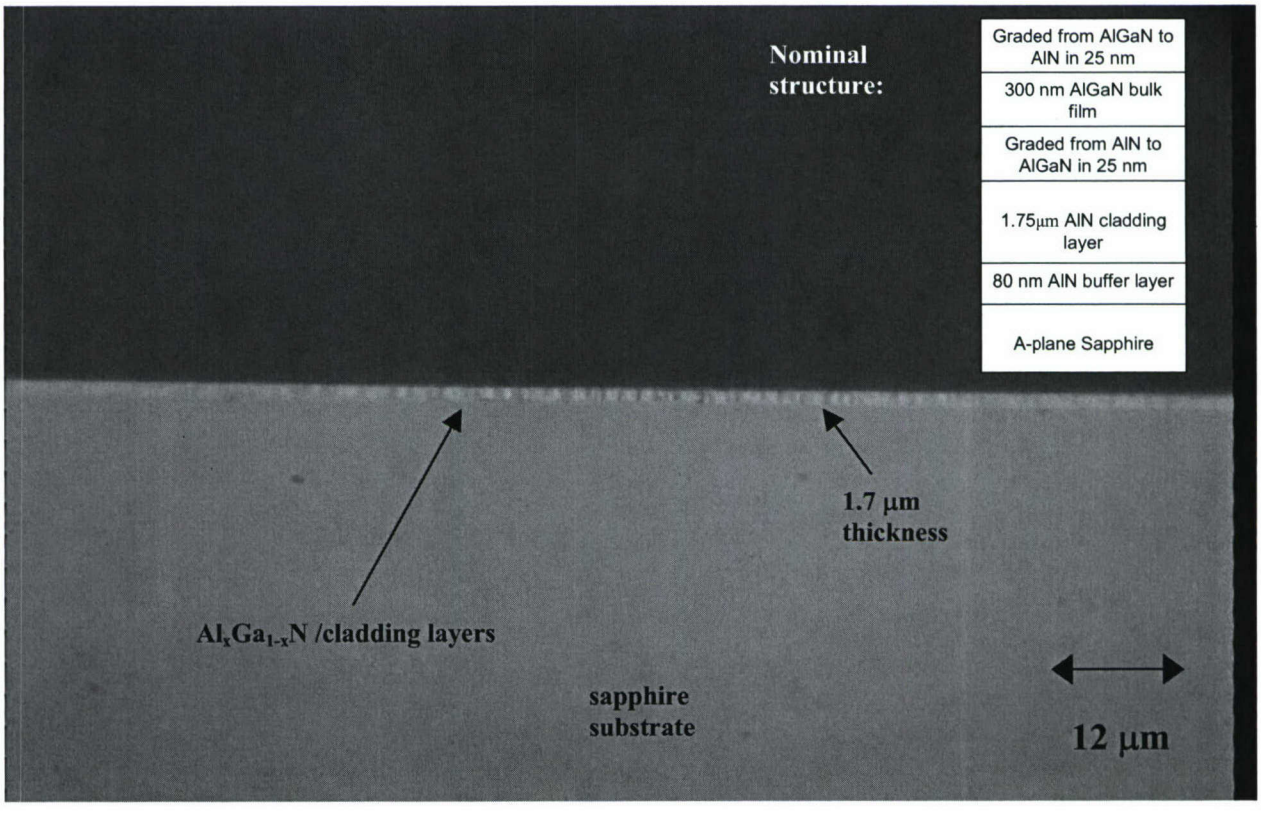

Figure 9. 1000X optical micrograph of a cleaved facet (sideview) formed from wafer #1644 and nominal layer structure for this wafer.

that the sapphire has been cleaved along one of the proper vertical r-planes. From a calibration of the length scale at 1000X, the thickness of this striated layer is determined to be 1.7 +/- 0.2 μm from the image. This value is in reasonable agreement with the nominal total thickness of 2.1 μm reported for the active and cladding layers in this sample (see inset in Figure 9). The 300 nm thickness of the active bulk AlGaN layer for this sample is comparable to or under the resolution limit of the microscope at 1000X, and therefore the individual layers are not resolved. A striated layer at top is observed for samples from two other wafers as well, although in some regions the striations appear less prominent.

The cleaved facet from sample #1644 was also examined under the SEM, to better resolve facet detail in the active and cladding layers. Two images obtained from different regions along the facet (and at different magnifications), are shown in Figure 10. As for the optical micrograph above, there is a clear interface between the sapphire and the active/cladding layers, although there is some variation in the measured thicknesses of this layer. The thin bright layer which appears in both images is likely due to charging of high Al-content surface and/or upper cladding layer. These images were taken without metallization of the die, in order to preserve the die for further optical measurements. In both images, the sapphire appears fairly smooth with the exception of some limited areas in Figure 10b. The active/cladding layers appear fairly smooth in the image at left, with some vertical shading just barely visible, while the active/cladding layers at right exhibit more roughening. Some nonuniformity of facet quality was anticipated during the design of laser die, and is the reason that the first die prototypes are 5 mm long, which will allow electron excitation of various areas along the cleave.

Finally, various optical and SEM images of cleaves made from thinned versus unthinned material show that the facet quality is higher and more uniform for the thinned samples. Therefore, we will continue to thin samples prior to cleavage for die formation.

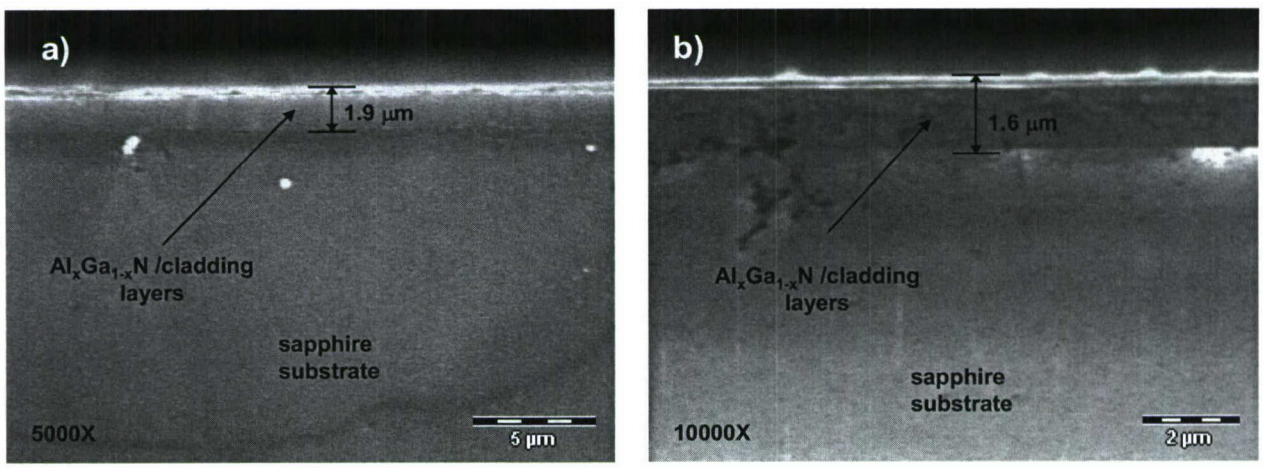

Figure 10. SEM images of two different locations of the cleaved facet (sideview) formed from wafer #1644.

A-plane Sapphire Processing Yields

Due to problems encountered with the first cleaves to form AlxGa1-xN die, we decided to cleave more A-plane sapphire bars having similar dimensions. These practice cleaves allowed us to accomplish the following:

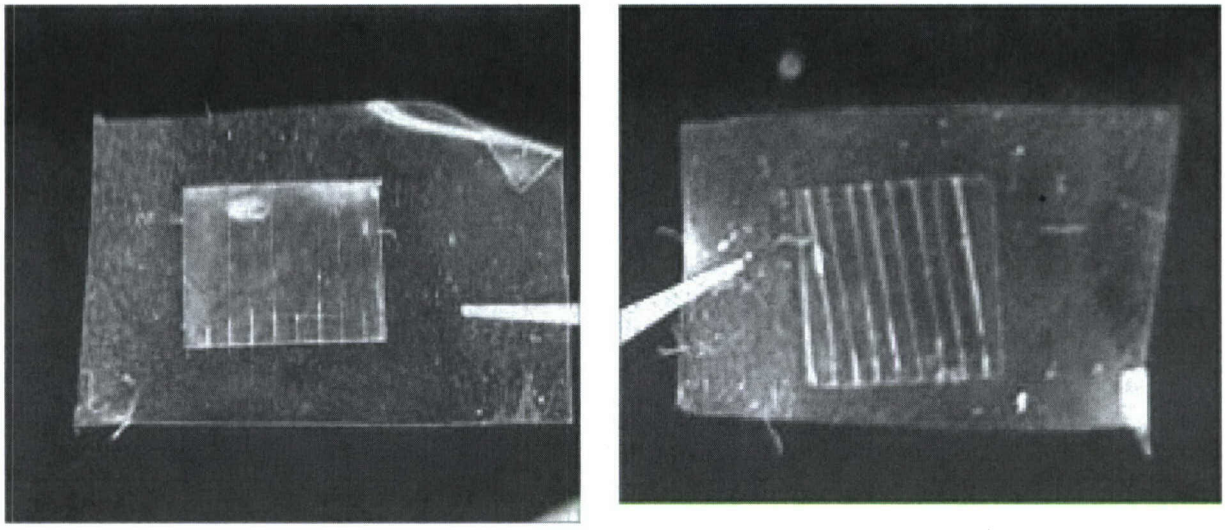

Figure 11.a. Typical cleave results obtained for A-plane sapphire sample. **b.** Undesirable result obtained for one of twelve A-plane sapphire samples processed.

- Further optimize cleave technique for sub mm die widths without using up the very limited amounts of $Al_xGa_{1-x}N$ material
- Better quantify yields for each step of die processing

The yields obtained for each step are summarized below in Table 1. The straightness of the cleaves formed was assessed quickly under a 5X illuminator. Several samples were lost during the thinning step and in handling after thinning. The samples are extremely fragile after being thinned down to 80-100 μm, so some loss in handling appears to be likely. Although the yield for straight cleaves was close to 50%, the yield of satisfactory dies having two straight sides was much lower. This is illustrated by the sample shown in Figure 11a, which shows typical cleave results. The straight cleaves can be easily seen, while the cleaves which propagated off-plane frequently occur in between the straight cleaves and can be seen faintly (especially on left side).

We believe part of the reason for our low die formation yield is due to a lack of precise control of some of the critical cleave parameters. With a commercial scriber-breaker machine, the notch/scribe pressure and break wheel pressure are under precise machine control. In our method, we attempt to control these parameters by hand, with low success rates, as seen in the table above. However, there are some variations in our cleave method that we have not tried yet, which we will pursue to determine if they increase the die formation yield.

Table 1. Yields for each stage of die processing using A-plane sapphire.

Process	# obtained	# initial	Yield
Thinning	15 samples	18 samples	83%
Handling post-thinning	12 samples	15 samples	80%
Die formation	13 dies	72 dies	18%
		Overall yield	12%
Formation of straight cleave	42 cleaves	88 notches	48%

There was also more scatter in the measured widths (cavity length) of the 13 dies we produced than desirable for the goal of producing spacers for facet coating which are 20 μm shorter than the actual dies. The standard deviation of the die widths for the 13 dies was ~ 50 μm. Therefore, only several dies from this current batch of A-plane sapphire are suitable for use as spacers. However, there is an alternate source to obtain a large numbers of spacers having precise dimensions in a short period of time. Cutting Edge Optronics, a division of Northrop Grumman, sells unmounted GaAs bars as an off-the-shelf item. The dimensions we require are a custom job for them, but they can deliver 100 spacers with the dimensions we require for $1200 with a 1 week delivery time ARO.

Another undesirable result which occurred for one of the twelve samples cleaved is shown in Figure 11b. It can be seen that all of the cleaves did not propagate along the notch direction but rather at a considerable angle (perhaps ~ 10°) relative to the notch direction, which was parallel to the two edges of the sample. Since great care was taken to ensure that the notch and sample edges were oriented properly at a 58° angle from the wafer flat, it seems likely that the orientation of the crystal planes in the region of the wafer where this piece came from differed from the remainder of the wafer.

The low yield and problems described above may be at least partially due to inherent limitations in material quality. This idea is supported by the following information from the Emcore website referring to cleavage of III-V substrates[28]: "...the inherent structural qualities of sapphire substrates, such as crystal structure and orientation and hardness and materials strength, inhibit this method from working well. Another obstacle using scribe-and-break is the inability to cleave the wafer on the crystal planes, which reduces the usable area of the wafer and results in device yields that are only in the range of 70% to 80%." However, our current yields are considerably lower than this, so improvement is likely possible.

To summarize, we believe that the low yield and other problems encountered above are likely due to two main factors: lack of precise control of some critical cleave parameters and inherent limitations in material quality.

Preparation of $Al_xGa_{1-x}N$ dies for Facet Mirror Coating

Next, eight more die were produced from $Al_xGa_{1-x}N$ on A-plane sapphire wafersA summary of the relevant details for the cleaved-cavity $Al_xGa_{1-x}N$ dies produced last month, as well as previously during the Phase II program, are shown in Table 2. Processing yields for the most recent round of die formation were similar to that observed previously. From brief low level characterization, a total of 8-9 of the unmounted dies appear to be the best candidates for facet coating and are identified as such below. The dies at the bottom of the table are not suitable for facet coating because the cavity length is less than the spacer cavity length or one side is very irregular and/or has significant chipping. A brief explanation of the several items listed in the Table is given below.

Table 2. Summary of cleaved-cavity $Al_xGa_{1-x}N$ dies ready for facet mirror coatings with relevant details.

[28] Emcore press release, July 15, 2003, www.emcore.com/news.

Wafer #	Cavity Length (μm)	Backside Metallization	Attachment to Submount	Current Status / Intended Use
Processing completed in January 2005:				
1644	not measured	yes	Au/Sn solder	sent to Photon Systems
1644	not measured	yes	Au/Sn solder	sent to Photon Systems
1644	not measured	no	Au/Sn solder	CL studies at Astralux
Processing completed in March 2005:				
1671	823	no	pending	ready for facet coating
1671	754	yes	pending	ready for facet coating
1671	792	no	pending	ready for facet coating
1671	777	no	pending	ready for facet coating
Processing completed in May 2005:				
1644	831	yes	pending	ready for facet coating
1683	1146	yes	pending	ready for facet coating
1683	777	yes	pending	ready for facet coating
1683	823	yes	pending	ready for facet coating
1683	1046	yes	pending	ready for facet coating
Not suitable for facet coating:				
1644	577	yes	Ag paste	for characterization / test mounting
1644	715	yes	pending	for characterization / test mounting
1683	785	yes	Ag paste	for characterization / test mounting

The dies have been inspected from the top under low magnifications. The edges are reasonably straight and parallel, although some imperfections were observed (typically 1-3 per 5 cm facet length excluding the notched region). Further characterization at higher magnifications for 1 or 2 typical dies is ongoing. There is quite a bit of variation in cavity length due to wobble in the diamond tip used for creating the notch to initiate cleavage. However, most of the dies have a cavity length of ~ 800 +/- 30 μm.

The majority of the dies have a backside metallization of Cr/Au 100/200 nm to facilitate eutectic die attachment and to allow ready identification of the top- and back-sides of the die. Several do not have backside metallization in order to test the effect of omitted the metallization on die cleavage. Since the backsides of these dies have been lapped to a fine finish, the epi side and backside can not be distinguished under an optical microscope. It will be necessary to identify the epi side prior to attachment of the die to the submount. PL spectroscopy would be a convenient method to accomplish this identification since it does not require fixing the die within a vacuum chamber, which is difficult for the very small unmounted die bars. However, the bandedge peak measured by BU for the wafer used to cleave these dies was at ~ 233 nm, which is higher in energy than the 325 nm HeCd laser line available at Astralux. The 224 nm Photon Systems DUV laser would be suitable to

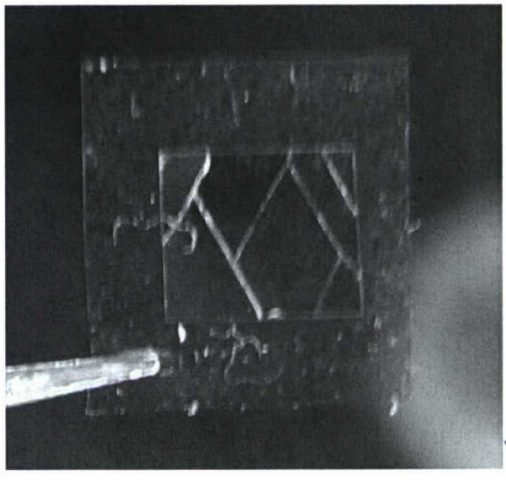

Figure 12. Undesirable cleave pattern obtained from one $Al_xGa_{1-x}N$ on A-plane sapphire sample.

excite the bandedge emission.

The dies at the bottom of the table are not suitable for facet coating because the cavity length is less than the spacer cavity length or one side is very irregular and/or has significant chipping.

An undesirable result obtained from one cleaved sample is shown in Figure 12. A triangular or diamond pattern of cleaves was obtained for this sample, rather than the intended series of parallel cleaves. This result would appear to indicate poor crystal quality since the weakest crystallographic planes are not the desired R-planes (parallel to the edges of the sample). It is not known whether the crystal quality was poor as-received, suffers significantly during lapping, or both.

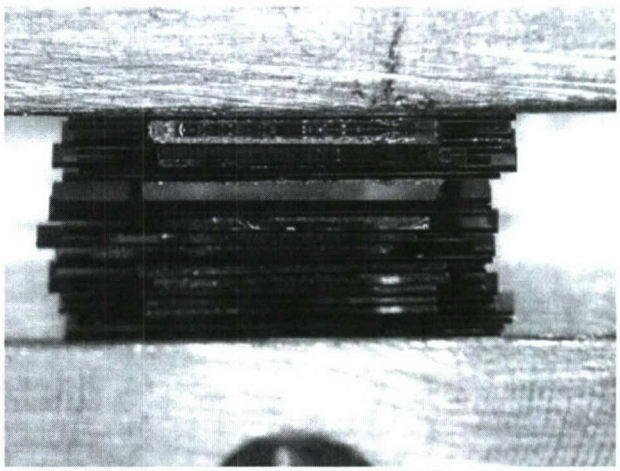

Figure 13. Sideview of the $Al_xGa_{1-x}N$ dice and GaAs spacers held within the coating tooling prior to mirror coating deposition at MLD. Some metallic contamination is observed on the facets for a few of the dice near the top.

One hundred cleaved-cavity GaAs bars which are 7 mm in length x 710 μm in cavity length x 110 μm thick were ordered and received from Cutting Edge Optronics. The cavity lengths of twelve representative dies were measured under the optical microscope and determined to be ~ 710 +/- 2-3 μm. These will be sent to MLD Technologies along with the candidate $Al_xGa_{1-x}N$ dies for coating. The $Al_xGa_{1-x}N$ die and GaAs spacers are held within a customized coating tool, shown in Figure 13, for mirror coating deposition. A total of 11 $Al_xGa_{1-x}N$ die from various wafers were sent to MLD Technologies for coating.

Further Characterizations of Cleaved Facets via SEM Microscopy

While waiting for MLD Technologies to complete the coating deposition, we decided to do further characterization of cleaved facets via SEM. In optical images at 1,000X, such as Figure 14a, and SEM images at 10,000X and higher magnification, such as Figures 14b and 14c, a region was observed at the top of the facet having vertical bands of varying shading. At SEM

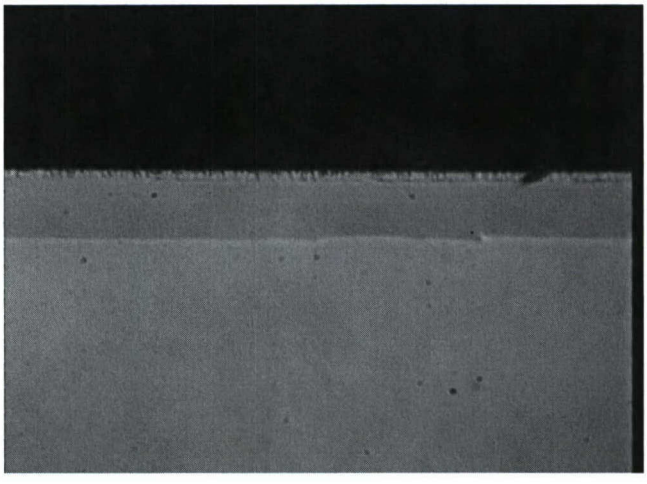

(a) 1,000X optical micrograph of a die from BU

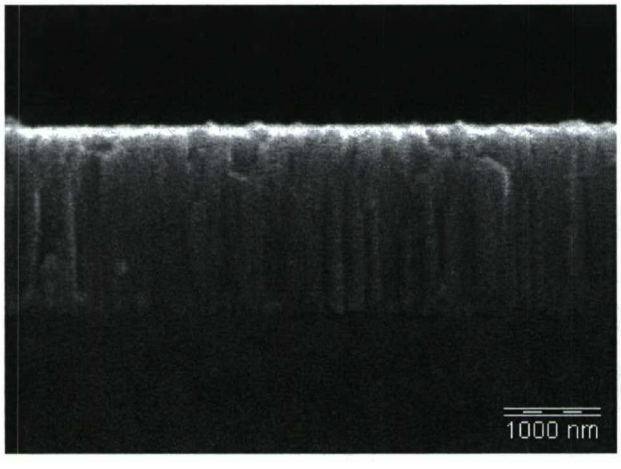

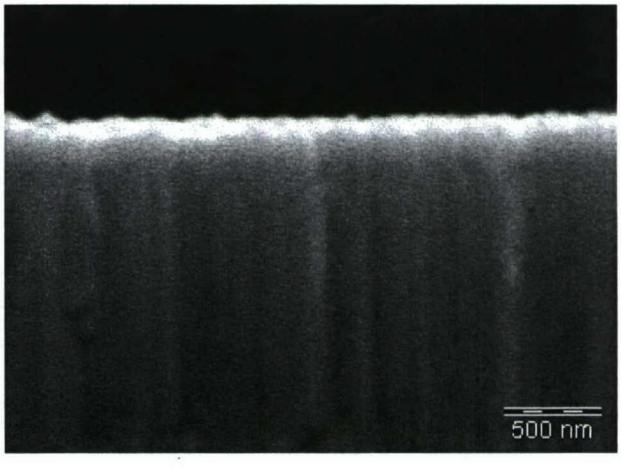

(b) 20,000X SEM micrograph of a die from BU 1644 (c) 40,000X SEM micrograph of a die from BU 168

Figure 14. Optical and SEM micrographs of recently cleaved facets.

magnifications these features appear columnar in nature. The thicknesses of the layer containing these features determined from the images (~2μm) correspond fairly well to the nominal thickness of the epilayers and associated growth buffer layers. These banded regions at the top of the facet were observed for cleaves done on all $Al_xGa_{1-x}N$ on A-plane sapphire epiwafer samples (1641, 1644, 1671, 1683), although in some regions they appear less prominent, as mentioned previously. These features were present along the entire length of the facet. In contrast to the top layer, the sapphire sidewall below the banded region is generally smooth and featureless, as shown in Figures 14a and 14b, indicating a high quality cleave. Therefore, we believe that the columnar features were present prior to cleaving. In a crude effort to determine an order of magnitude of the diameter of the columns, we used the images from each

magnification to estimate the average widths of these columnar bands. We determined the average widths to be ~ 660 nm from the optical micrograph and ~ 150 nm from SEM micrographs. There is significant uncertainty in both of these values because the features are barely resolvable in the optical image at 1000X and it was difficult to determine which areas were columns and/or voids due to variations in shading.

The columnar features we observed appear similar to features shown in Figures 15a and 15b from an APL article on growth behavior of GaN surfaces during MBE.[29] They described the features in these SEM micrographs "as a presence of a porous columnar structure with the presence of voids between columns in the GaN epilayers".

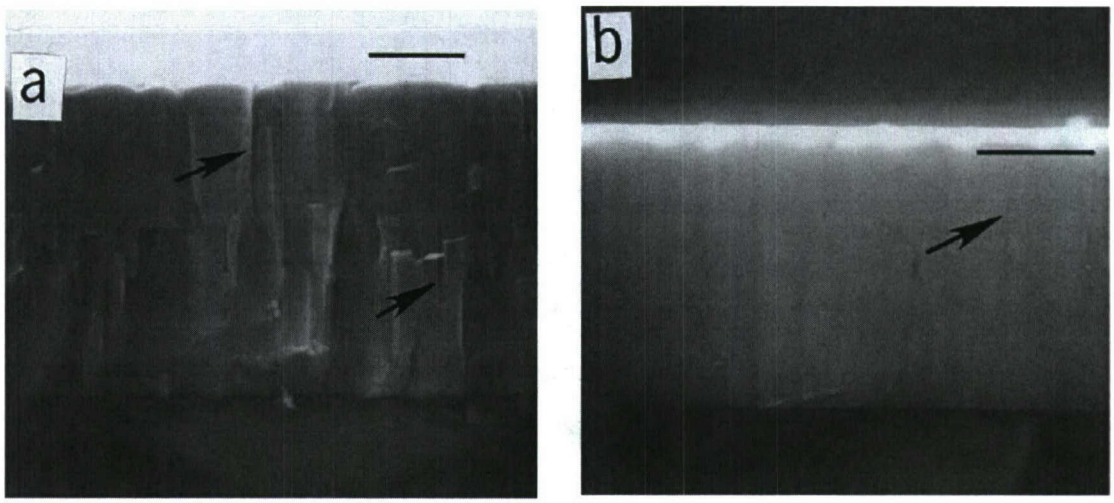

Figure 15. SEM micrographs from reference 1 of cross sections of MBE-grown GaN epilayers showing columnar growth structures. The marker indicates 0.5 μm.

We do not know whether these columnar features will be detrimental to facet reflectivity or to signal gain. However, since the widths of these features are comparable to the emission wavelength it would seem that scattering within the layer and off of the facet surface could be a possibility. Prof. Moustakas suggested that the column packing is likely to be more dense than it appears from the cleaved facet SEM images and therefore scattering within the plane of propagation should be minimal. Perusal of the literature we have on hand suggests that GaN and AlGaN films typically have columnar microstructure.

Summary of Key Parameters for Coated-facet $Al_xGa_{1-x}N$ Dice

During the last month, the cleaved-cavity $Al_xGa_{1-x}N$ dice were received back from MLD technologies after the edge facets were coated with a UV mirror layer. In preparation for bonding of these laser die candidates to submounts to facilitate CL testing, a review of key growth, spectral, and processed parameters was performed.

A summary of key parameters for all coated-facet $Al_xGa_{1-x}N$ dice produced in Phase II is shown in Table 3. The die identification numbers correspond to the wafer numbers assigned by BU. The growth parameters are nominal values reported by BU. λ_{max} values were measured by

[29] S. Guha, N.A. Bojarczuk, and D.W. Kisker, *Appl. Phys. Lett.*, **69**, 2879 (1996).

CL spectroscopy at BU and/or Astralux for wafer samples prior to die processing. Cavity lengths were measured at Astralux using a calibrated length scale under an optical microscope.

Table 3. Summary of key growth, spectral, and processed parameters for the coated-facet $Al_xGa_{1-x}N$ dice produced to date in Phase II.

Die #	Layer Structure	Active Layer Al Content (%AlN)	Active Layer Thickness (nm)	CL λ_{max} (nm)	Approx. Cavity Length (μm)	Backside Metallization
1644e	GRINSCH	75	300	247-256	804	yes
1671e	GRINSCH-MQW	70	140 (50 MQWs)	231-233	824	no
1671m	GRINSCH-MQW	70	140 (50 MQWs)	231-233	766	yes
1671n1	GRINSCH-MQW	70	140 (50 MQWs)	231-233	773	no
1671n2	GRINSCH-MQW	70	140 (50 MQWs)	231-233	796	no
1683b	GRINSCH	80	250	240-250	1032	yes
1683c	GRINSCH	80	250	240-250	827	yes
1683d	GRINSCH	80	250	240-250	787	yes
1683e	GRINSCH	80	250	240-250	1150	yes
1787v	GRINSCH	78	170	238-240	773	no
1787w	GRINSCH	78	170	238-240	823	no

A total of eleven dice from four wafers had edge facets coated at MLD Technologies. The AlN content ranged from 70-80%, resulting in λ_{max} values from 231-256 nm. Some variation in λ_{max} for each wafer was observed as a function of position on the wafer and also excitation conditions. There is a significant amount of variation in cavity lengths due to poor control during notch formation, with most of the dice having lengths ~ 800 +/- 30 μm. Six of the dice have Cr/Au backside metallizations for identification of the epitaxial-side of the die, as well as to facilitate possible eutectic die bonding. From topview inspection under low magnification, the dice labeled 1671m and 1671n1 have the best cleaved edges with no significant imperfections visible at 100X magnification.

After the die came back from MLD Technologies, they were attached to CuW submounts supplied by Photon Systems. Further details for die attachment are given in the following section. The facets were inspected under an optical microscope after die attachment to map the facet conditions. These maps will be used as a guide to determine what regions on the die to avoid probing with the electron beam during emission testing. After attachment, nine of the mounted die were distributed to Photon Systems and Boston University for emission testing using the specialized line-output electron gun developed by Photon Systems.

Die Attachment to Submount

Both Au/Sn solder and conductive adhesive were investigated for die attachment. Au/Sn solder was used for die attachment of the earliest dies produced, however, something in the solder/flux system was apparently not compatible with high-vacuum. Therefore, for most of the die produced in the program, a conductive adhesive (Ag paste suspension) was used for attachment.

Electroplating of Die Submounts for Eutectic Attachment

To facilitate eutectic attachment it was necessary to electroplate the submounts as described below. Submounts received from Photon Systems were deburred and cleaned in preparation for electroplating. The submounts are rather fragile; one was cracked as received. Therefore, they were deburred by dragging with light pressure across 400 grit paper and then cleaned up by soaking in acetone. Immediately prior to the Ni electroplating, the submounts were immersed in a 5% HCl:DI H_2O solution for 3 minutes for final cleaning and removal of oxides. Prior to the Au plating, the submounts were immersed in a 5% H_2SO_4:DI H_2O solution for 1 minute to activate the surface and ensure good adhesion of the second metal layer.

An electroless Ni plating solution from Transene (Ammonia type) was used for the first layer. To confirm the success of the plating runs, the pieces were inspected for color changes, profiled with a Dektak profilometer, and measured for resistance changes. A scrap CuW plate, as well as the cracked submount, were used for calibration runs to determine optimum plating times. Metal thicknesses were difficult to measure precisely using the Dektak, due to the high degree of roughness of the surfaces being measured. However, it was found that 5 minutes in the Ni plating solution heated to 70°C resulted in approximately 2μm of metal. Resistance measurements showed a reproducible drop in the resistance, as expected for Ni versus CuW.

For the Au plating, 24k Hard Acid Immersion Gold Plating Solution from Gold Plating Services was used. Electrolytic plating using 11 mA, 2 V for 11 minutes resulted in Au layers between 2-3 microns thick.

Die Attachment via Solder

An 80/20 Au/Sn eutectic solder preform, which reflows at 280 C, was used for die mounting. From practice runs on the dummy die, it was determined there were inorganic salt residues present on the submounts from the electroplating, which were causing foaming and interfering with the die attach. These contaminants were then removed from the remaining submounts with scrubbing. Also, the reflow properties were not satisfactory, so the die attach faces on the remaining submounts were polished to reduce the roughness of the electroplated layers and improve reflow. This did improve the reflow on the next attempt.

After some practice runs, a die from #1644 was mounted. Figure 16 is a topview of the die positioned on the submount prior to solder reflow. Figure 17 shows the bond profile obtained after reflow. It is reasonably level. Figure 18 shows a topview of the mounted die after reflow. It can be seen that partial delamination of the backside metallization occurred. We will work to solve this delamination problem by further optimization of the backside surface and metallization.

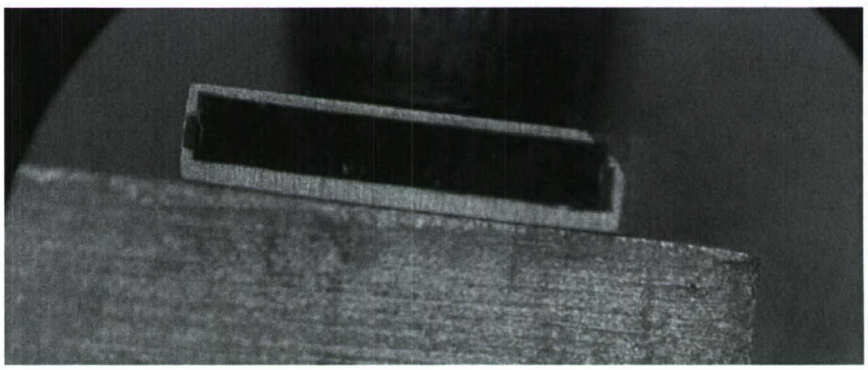

Figure 16. Magnified topview of die in place prior to reflow.

Also, it is possible that there may be some flux and/or flux smoke on the sidewalls, although I didn't see any evidence of this. A rinsable flux which is soluble in acetone was used, so if you want to you could soak or scrub (very gently) in acetone. However, it might be good to first test the die without doing this.

A modified die attachment procedure to eliminate the delamination problem described above. Previously, the solder preforms, flux, and laser die were all placed on the submount prior to heating and reflow. For the modified build, the solder and flux were placed on the mount and then heated until solder reflow was observed. Then, the die was placed on the molten solder on the submount using the die bonder pickup tool and the entire assembly was immediately removed from the hot plate. This modified procedure minimizes the time the backside metallization spends at reflow temperatures. A comparison of the bond results obtained using the original and modified procedure is shown in Figure 18. No evidence of delamination or consumption of the backside metallization can be seen for the modified build.

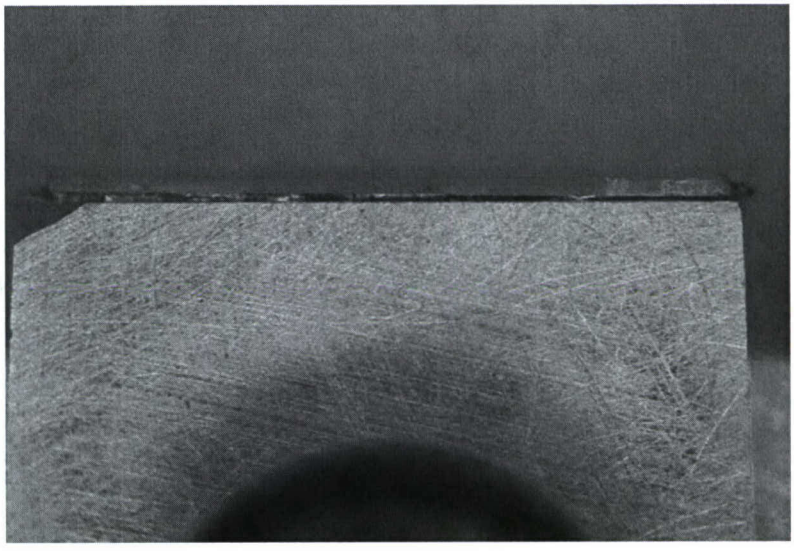

Figure 17. Magnified sideview showing bond profile.

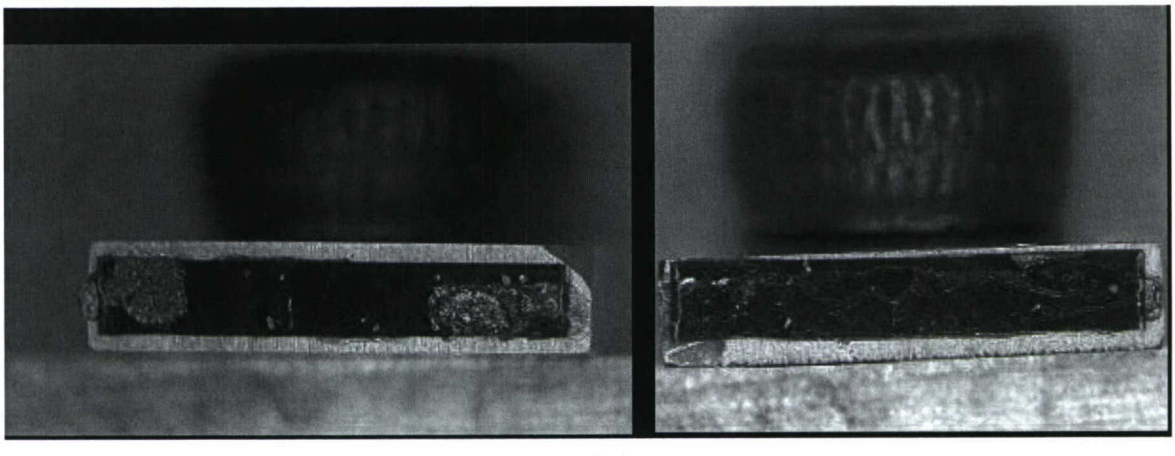

Figure 18. Comparison of bonds obtained using the original die attachment procedure (left) and a modified procedure (right).

Die Attachment via Conductive Adhesive

Several practice die attachment trials were made using 'dummy' sapphire dice. The procedure consists of attaching a submount to a holder with the bonding area facing up, applying the Ag alloy adhesive to the bonding area, and then placing the die on top of the adhesive with a

small amount of pressure to ensure good adhesion. The main challenge is due to the difficulty in applying a controlled, uniformly thick layer of the Ag paste. If too much Ag paste is applied it can flow over the faceted area after the die is placed. Best results were obtained using special pen-style applicators having a microtip, but problems still can occur. Out of 4 trials, 3 were totally successful with no evidence of contamination of the facet with Ag adhesive. The other had only a very small amount of Ag adhesive on the faceted surfaces.

After the trial runs, we then attached three of the $Al_xGa_{1-x}N$ dice using the same procedure. The results were mixed:

1683c – perfect bond with no Ag adhesive on side walls after attachment (see Figure 19).

1644e – fairly good but some Ag adhesive on the side walls covering approx. 30-40% of the faceted region

1671m – poor bond which cracked the die in half with approx. 50% coverage of the faceted region with Ag adhesive.

One additional die, 1683d, was attached to a submount. Upon inspection of the facet on this die after attachment, areas having metallic contamination were observed, as shown in Figure 20, as well as areas where the mirror coating has been damaged or is missing. Therefore this die was deemed unsuitable for further testing.

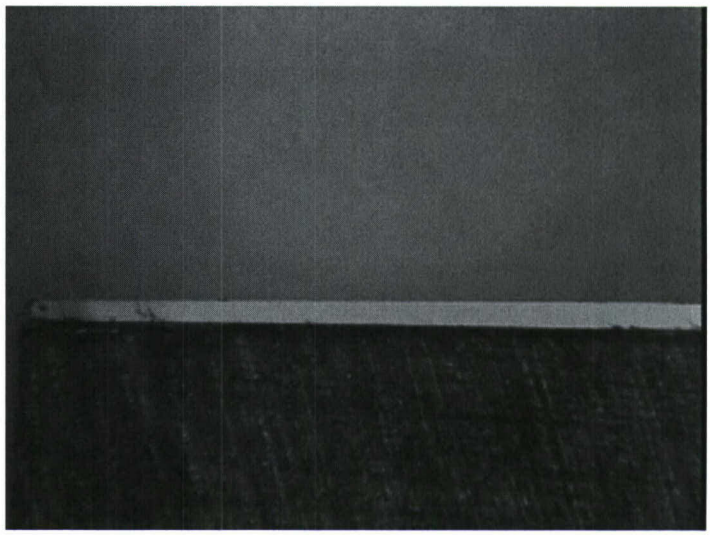

Figure 19. 50X sideview of die 1683c attached to submount (bottom) with Ag adhesive.

Due to the mixed results in bonding the $Al_xGa_{1-x}N$ dice we decided to test how easy it would be to remove the die from the submount by soaking 1683d in silver paint thinner (a mixture of acetone, ethyl acetate, N-butyl acetate, toluene). According to MLD, the mirror coatings should withstand standard cleaning solvents such as acetone and isopropanol, but they had no information about other solvents. We were successful in removing the die; however, it appeared there was more damage to the coating after the soak.

In light of this, we feel it would be best to perform optical measurements on the partially-successful bonded dice prior to attempting detachment and rebonding.

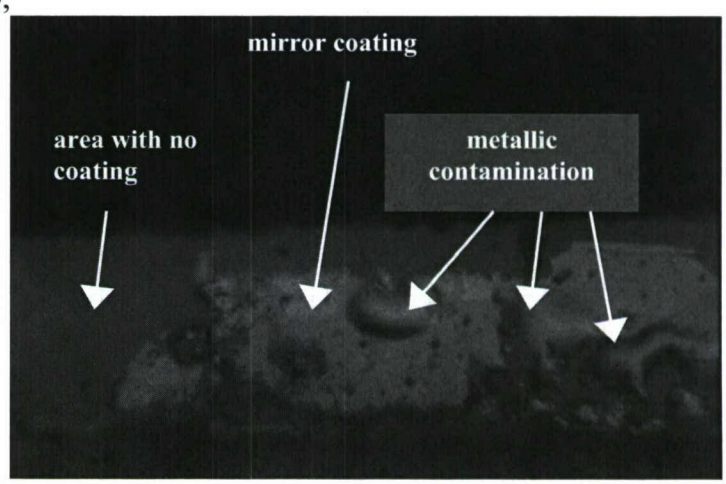

Figure 20. 400X optical micrograph of the facet on die 1683d, showing damage to the mirror coating and areas of metallic contamination.

Optical Measurements

Optical measurements performed at Astralux in Phase II took advantage of improvements to our CL characterization setup which provided the flexibility to conduct several different types of measurements. The improvements we made to the setup early in Phase II are discussed below, followed by discussion of the measurements performed and their significance for the program. These measurements included calibration of electron excitation current delivered to target, testing for stimulated emission from a faceted die, and measurement of the absolute radiant power from a bulk $Al_xGa_{1-x}N$ film.

Improved Apparatus for CL Spectroscopy

During various CL measurements conducted during Phase I, several key limitations of the experimental setup for edge emission measurements and CL mapping were discovered. These limitations were due to the small size of vacuum chamber and the lack of a vacuum feedthrough for external control of sample positioning and angle. Therefore, the first major task at Astralux during Phase II was to design and construct a new vacuum chamber having capabilities for CL mapping spectroscopy of sample edge and surface emission from samples having a wide range of shapes and dimensions. The UV grating spectrometer, collection/focusing optics, and electron gun have been described previously in Phase I reports. Therefore, only the key modifications to the CL setup are described below.

After an inventory of our vacuum hardware and consideration of various requirements for the instrument, we decided to use a 6-way cross with 4.5" CF flanges that we had on hand for the central chamber of the new instrument. The relatively large interior and large-diameter viewports allow viewing and collection of edge emission. This interior is also large enough to accommodate a Faraday cup for calibration of electron excitation currents. The port configuration we use for CL measurements is shown in Figure 21. For external control of sample positioning, a linear/rotary stage feedthrough, which was also on hand, will be used. This feedthrough also allows control of electron beam angle of incidence on the target sample. Samples are mounted to the feedthrough rod through the use of metal clips or silver paste depending upon sample dimensions and shape. Samples ranging in size from sub mm to 2" wafers can be mounted and tested within the chamber.

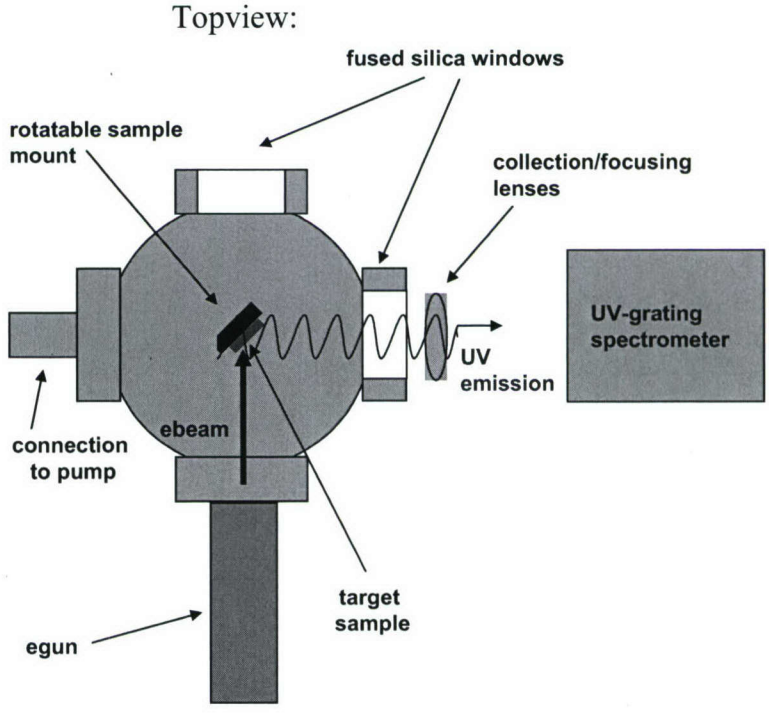

Figure 21. Improved setup for CL measurements at Astralux.

Calibration of Electron Excitation Currents

A Faraday cup from Kimball Physics was placed in the center of the Astralux CL chamber where samples are mounted for optical measurements. Absolute current measurements were then performed over a range of accelerating voltages, and the results of these measurements are shown in Figure 22. Significantly lower values were measured relative to the filament emission meter on the filament high voltage power supply. For example, at emission saturation at 15 kV, the filament emission meter indicated on the order of 25 μA, compared to 1.9 μA measured at the Faraday cup, indicating significant attenuation or loss of current. These measurements will be used as a calibration of the incident current for stimulated emission testing.

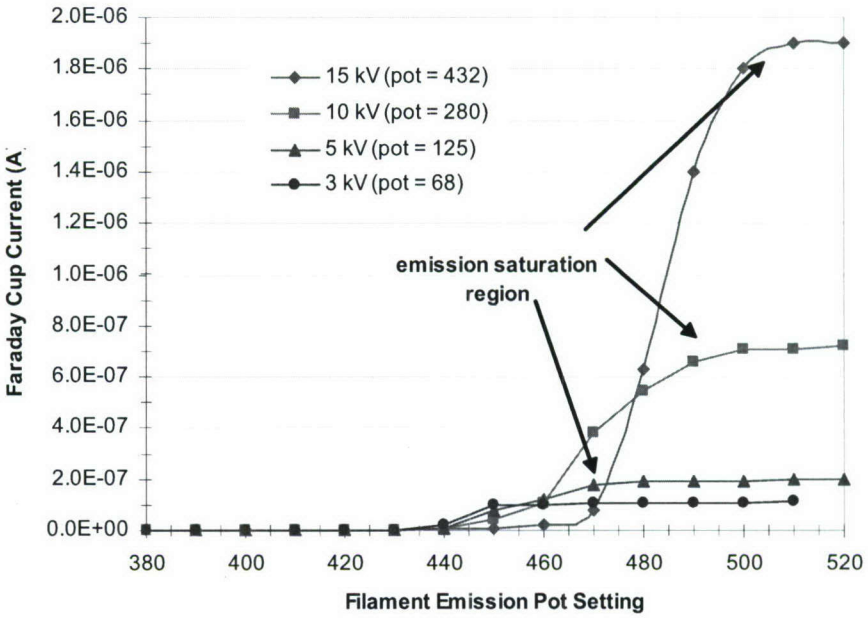

Figure 22. Faraday cup measurements of ebeam current at center of Astralux CL test chamber.

Stimulated Emission Testing of Faceted Laser Die

One of the faceted laser dies from wafer #1644 was placed in the Astralux CL test chamber for emission measurements and stimulated emission testing. A series of *surface orientation* (45° ebeam angle of incidence) CL spectra were acquired at 15 keV and various filament emission pot settings. 15 keV excitation, rather than a lower voltage, was used to obtain as large a range of currents as possible, as illustrated by the data in Figure 22 above. A typical spectrum we measured is shown in Figure 23. A bandedge peak at 252 nm was

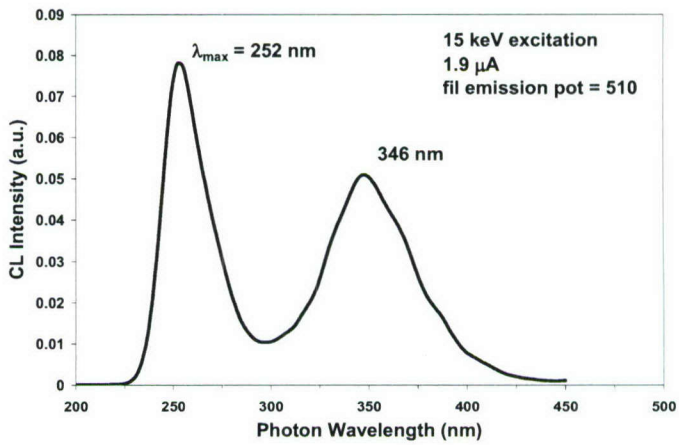

Figure 23. Surface CL spectrum of a faceted $Al_xGa_{1-x}N$ die.

observed, as well as a deep level band from the cladding or buffer layers.

Two series of measurements were conducted to obtain the maximum bandedge intensity as a function of emission pot setting, and this data is plotted in Figure 24. From the calibration of measured excitation current versus filament emission pot setting, the CL intensity data in Figure 24 can be replotted as shown in Figure 25. From this plot, *a nonlinear increase of CL intensity with increasing excitation current is observed for both series of measurements, which is suggestive of a stimulated emission process.* The data point density in this plot is insufficient to identify a clear threshold where nonlinearity starts. Figure 26 shows the same data as Figure 25 in a log-log plot, which

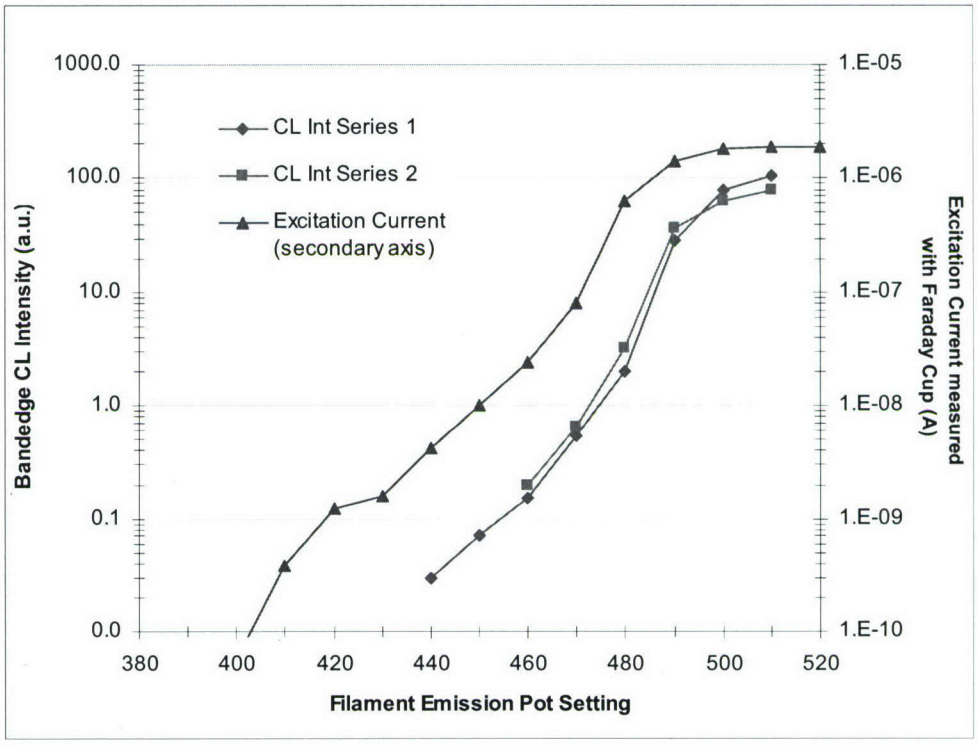

Figure 24. Bandedge CL intensities and excitation currents versus filament emission pot setting.

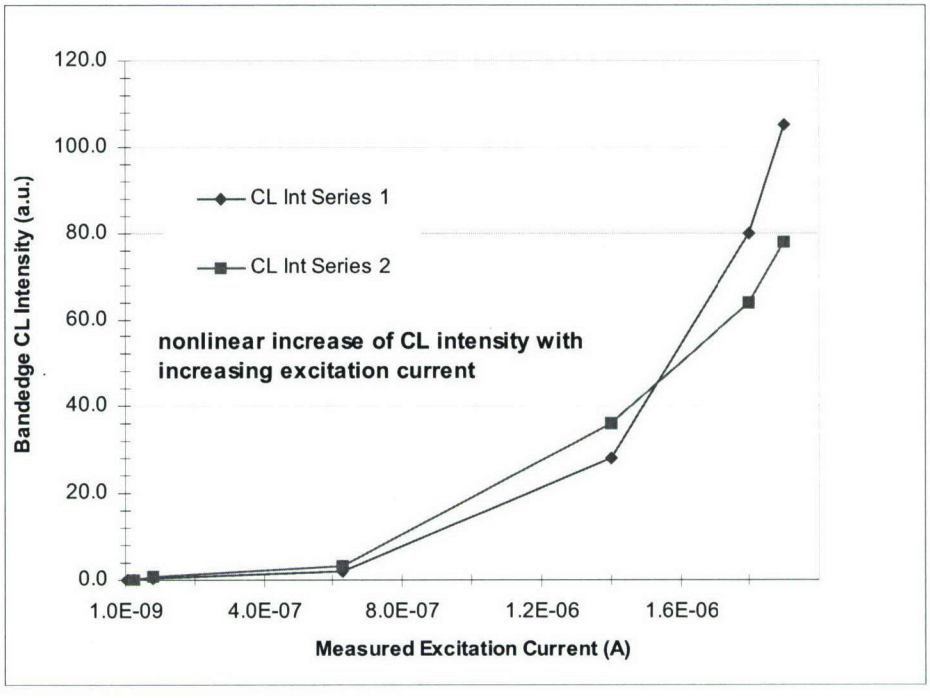

Figure 25. Bandedge CL intensities versus excitation current for the $Al_xGa_{1-x}N$ die.

more clearly shows the changes in magnitude for CL intensity versus current.

The need for careful calibration of excitation currents during stimulated emission testing is shown by a comparison between Figure 26 and Figure 27, below. In Figure 27, the CL intensity data is plotted versus the filament emission current gauge readings on the electron gun HV supply. A much more dramatic increase in CL intensity versus current is observed compared to Figure 26.

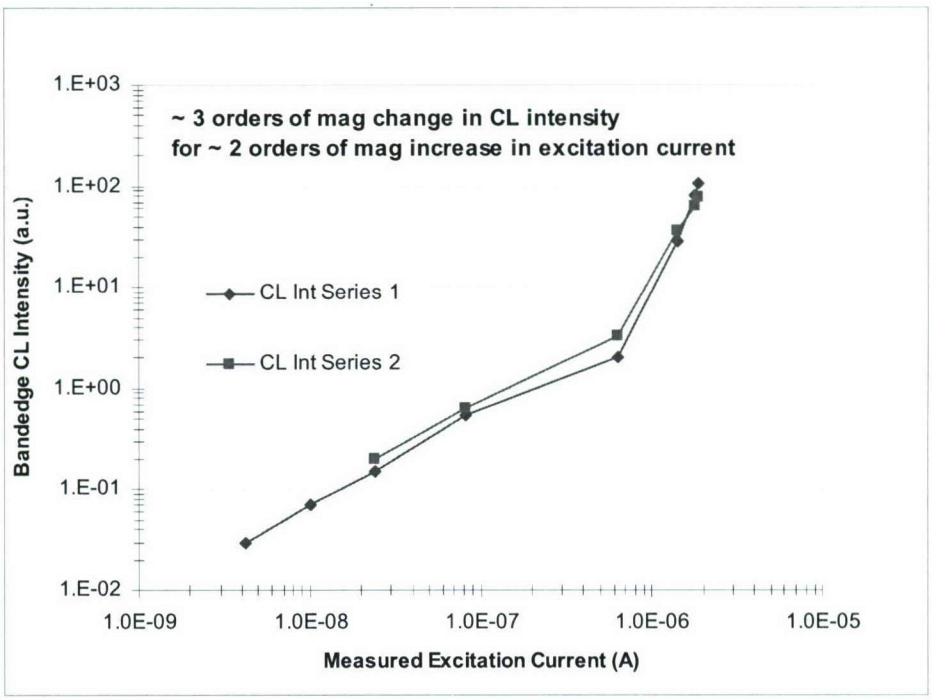

Figure 26. Bandedge CL intensities versus excitation current for the $Al_xGa_{1-x}N$. die.

The CL spectra acquired as a function of excitation current were also examined for evidence of line narrowing with increasing excitation current. However, with the data point density and resolution that were used, there was no apparent trend in FWHM versus excitation current. However, more measurements are necessary to determine if there is any line narrowing.

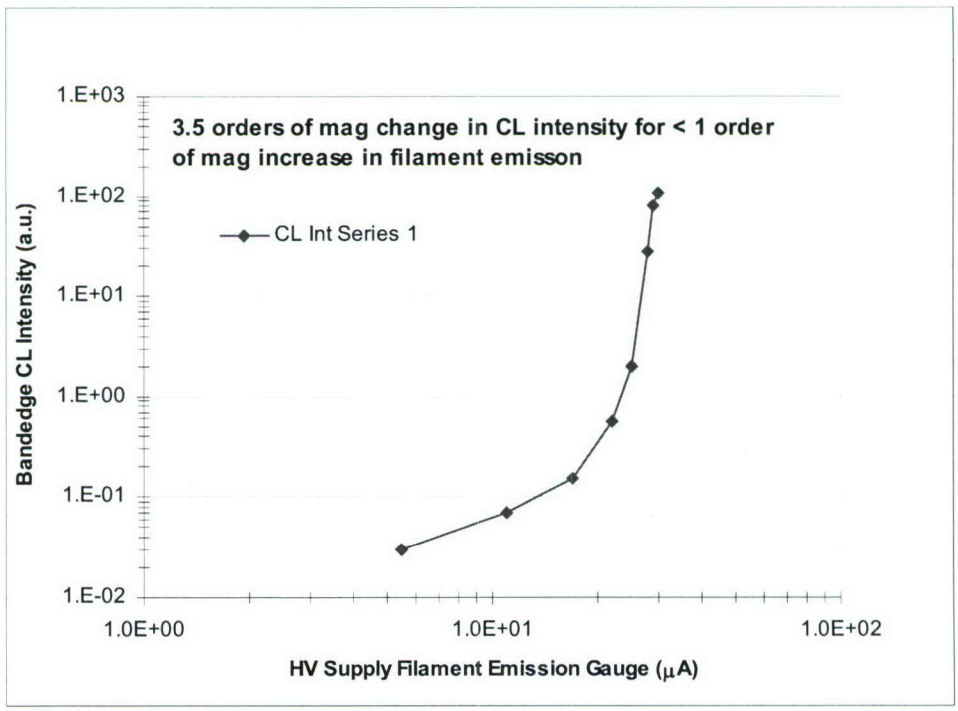

Figure 27. Bandedge CL intensities versus filament emission gauge currents for the $Al_xGa_{1-x}N$ die.

Setup and Methodology for Power Measurements

A Newport Optical Power Meter (Model 2832-C) and a UV-rated Si photodiode detector (Model 818-UV) were used for the power measurements. The detector responds to wavelengths ranging from 190 to 1100 nm and was calibrated in March 2002 to NIST-traceable standards. The power meter was mounted on an xyz micrometer stage to allow optimization of the detector position for collection of UV emission.

Measurements were conducted with the power meter in two different positions. In one configuration, the power meter was positioned so that it was touching the window port of the CL vacuum system to minimize the emitter-to-detector distance. This window port is a 2 ¾" CF-flanged Suprasil-2 window, which transmits nearly all of the UV except for ~ 8% reflection losses. In the other configuration, a Suprasil lens (F/2, 50 mm FL) coated for > 99% transmission from 220 to 330 nm, was positioned immediately next to the window port, and the detector was positioned ~ 1 cm behind this lens. Power readings were approximately a factor of two higher for the configuration without the collection lens. Therefore, no lens was used for the measurements described below.

During setup for the power measurements, a green phosphor screen was used to examine far-field radiation patterns and ensure that the active area of the detector surface was uniformly illuminated and to avoid focusing of the light on the detector. The screen luminescence was too faint to be captured with a digital camera and normal exposure lengths, therefore, a typical radiation pattern observed is indicated in a sketch shown in Figure 1. Two primary spots ranging in diameter from ~ 5-10 mm were observed near the center on top of a faint circular glow pattern corresponding to the window dimensions. One of the primary spots was more off-center and irregular in shape than the other one. This spot appears to arise from a reflection of the filament glow off the polished sample, as explained below. This filament glow appeared golden in color and has been observed previously (see Figure 1 in Monthly Rpt. #6). The spot due to filament glow remained on the screen as the sample stage was translated so that the ebeam was striking the polished sapphire carrier wafer used to mount the samples, rather than striking the emitter sample. The smaller, centered spot and large-area circular glow disappear under these conditions, indicating that these components originate from sample CL.

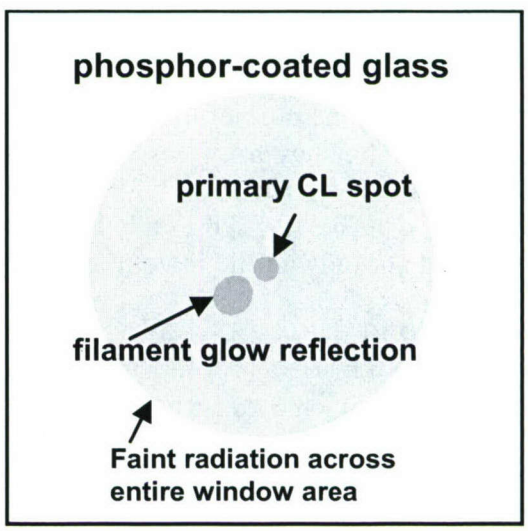

Figure 28. Sketch of the far-field radiation pattern observed on the phosphor screen.

The presence of the filament glow made accurate measurement of the UV power emitted by the sample more difficult, since the detector responds to a broad wavelength range. With the configuration used and tools available it was not possible to ensure the detector was positioned to capture only the CL emission and exclude all filament glow. Therefore, the power meter reading of 122 nW when the ebeam was striking the sapphire carrier was zeroed prior to measurement of the CL from the sample. The sample stage was then translated so that the ebeam would strike

the emitter sample and the power meter reading under this condition was then recorded as the 280 nm power

Results/Analysis of Power Measurements

Measurements of the 280 nm emission (bandedge emission maximum) from BU sample #1278 were performed. This is a bulk $Al_xGa_{1-x}N$ film (approx. 72% AlN content) grown in Phase I, which exhibited stimulated emission at BU. The sample was mounted at a 45° angle with respect to both the incident ebeam and the detector. Under excitation with ~ 2 μA of 15 keV electrons, 0.111 μW of 280 nm radiation was measured for a sample-to-detector distance of 12.8 cm after zeroing the meter as described above.

Assuming the detector was positioned to capture all of the CL emission at this distance, this reading corresponds to a measured irradiance of 0.111 $\mu W/cm^2$, since the active area of the detector is 1.00 cm^2. At this distance, the detector collects the radiation over a solid angle of 6.1 x 10^{-3} sr, corresponding to 0.097% of the hemisphere of CL emission. Therefore, the radiant intensity, *I*, at the 45° detector angle is 0.111 μW / 6.1 x 10^{-3} sr = 18 μW/sr. Assuming the emission is Lambertian, the radiance, *B*, from the sample can then be calculated from

$$B = I / A_p$$

where *Ap* is the projected area of emission. The nominal excitation spot diameter on the sample was 100 μm. From this diameter, a source area of 7.8 x 10^{-5} cm^2 and a projected area of 5.6 x 10^{-5} cm^2 (7.8 x 10^{-5} cm^2 x cos 45°) were calculated. Thus, the radiance determined from the power measurement and the preceding calculations is 0.32 W sr^{-1} cm^{-2}. The sample emittance, *M*, (power emitted per unit area of the source) can now be determined from the following relation:

$$M = \pi B$$

Thus, a radiance of 0.32 W sr^{-1} cm^{-2} gives an emittance of 1.0 W/cm^2.

Finally, the ratio of the emittance to the ebeam power density is the cathodoluminescence conversion efficiency from this emitter sample. The ebeam power density on the sample was 15 kV x 2 uA / 7.8 x 10^{-5} cm^2 = 380 W/cm^2. Thus, 1.0 W/cm^2 / 380 W/cm^2 gives a conversion efficiency of ~ 0.3%. While this efficiency is quite low compared to conventional LEDs, it is comparable or only a little lower than x-ray tube efficiencies.

Conclusions

To summarize, Astralux accomplishments during the Phase II program included:

- Designing and constructing an improved CL spectroscopy apparatus, with capabilities for edge/surface CL mapping spectroscopy and stimulated emission testing of samples having a wide range of shapes and dimensions.
- Producing a total of thirteen $Al_xGa_{1-x}N$ die bars (750 μm x 5 mm) having high-reflectivity cleaved facets from four high quality emitter wafers grown by MBE at BU. Processing of these dies involved thinning, cleaving, and deposition of mirror coatings on the facets. These dies have been attached to custom-made CuW laser mounts using a conductive adhesive. The compact dimensions of these dies are a key feature enabling the production of the *miniature* ESUVOS laser.
- Characterizing cleaved facet quality by Normaski contrast microscopy and SEM.
- Conducting preliminary CL emission measurements on a cleaved facet laser die, which are suggestive of stimulated emission. A nonlinear increase of 252 nm bandedge CL intensity versus excitation current (measured with a Faraday cup) was observed

- Measuring the radiant CL power produced by a $Al_xGa_{1-x}N$ film and calculating the cathodoluminescence conversion efficiency from this measurement

The compact dimensions of these dies are a key feature enabling the production of the *miniature* ESUVOS laser. However, issues related to cleaving and handling sub-millimeter die, as well as inherent material limitations, presented significant challenges during the production of the die, resulting in quite low yields. Nonetheless, thirteen $Al_xGa_{1-x}N$ die were successfully produced, mounted, and distributed between Photon Systems, Boston University, and Astralux for emission measurements.

4.0 Distribution List - Final Report

a. Director, — 1 Copy
Defense Advanced Research Projects Agency
Attn: MTO (Dr. Henryk Temkin)
3701 North Fairfax Drive
Arlington, VA 22203-1714

b. U.S. Army Aviation and Missile Command — 2 Copy
Attn: AMSAM-RD-WS-DP-SB (Martin Soprano, Tech Monitor)
Bldg. 7804, Room 222
Redstone Arsenal, AL 35898-5248

c. U.S. Army Aviation & Missile Command — 1 Copy
Attn: AMSAM-RD-WS
Bldg. 7804, Room 247
Redstone Arsenal, Alabama 35898-5248

d. Director
Defense Advanced Research Projects Agency — 1 Copy
Attn: CMO/SBIR
3701 North Fairfax Drive
Arlington, VA 22203-1714

e. Director — 1 Copy
Defense Advanced Research Projects Agency
Attn: OMO/DARPA Library
3701 North Fairfax Drive
Arlington, VA 22203-1714

f. Defense Technical Information Center — 2 Copies
ATTN: Acquisitions\DTIC-OCP, Rm-815
8725 John J. Kingman Rd., STE 0944
Ft. Belvoir, VA 22060-6218

Interim copy:
Dr. Michael Wraback — 1 Copy
U.S. Army Research Labs
2800 Powder Mill Road
Adelphi, MD 20783

---

[i] Cary, P.R. *Biological applications of Raman and resonance Raman spectroscopies*, (Academic Press, New York, 1982)
[ii] R.L.McCreery, *Raman Spectroscopy for Chemical Analysis* (Wiley Interscience, 2000).
[iii] G. Faris, et.al. , App. Opt. 36, 4, Feb.1997.
[iv] W.H. Nelson, R.R. Dasari, M. Feld and J.F. Sperry, *Intensities of Calcium Dipicolinate and Bacillus Subtilis Endospore Raman Spectra Excited with 244 nm Light*, (In press, Applied Spectroscopy)
[v] N. Bunakata, M.Saito, and K.Hieda, *Inactivation Action Spectra of B.Subtilis Spores from 50nm to 300nm*, Photochemistry and Photobiology, 54, 5, pp.761-768, 1991

[vi] K. Warriner, et.al., *Inactivation of Bacillus subtilis spores on packaging surfaces by UV excimer laser irradiation,* J. App. Microbiology, 88, 678-685, 2000.